Thermocline study of packed-bed thermal energy storage system

Baoshan Xie

DOCTORAT BRETAGNE LOIRE SCIENCES POUR L'INGENIEUR

Nantes Université

THESE DE DOCTORAT DE

NANTES UNIVERSITE

ECOLE DOCTORALE N° 602
Sciences pour l'Ingénieur
Spécialité : Energétique – Thermique – Combustion

Par
Baoshan XIE

Etude des systèmes de stockage thermique par thermocline avec garnissage

Thèse présentée et soutenue à Nantes, le 20/09/2022
Unité de recherche : Laboratoire de Thermique et Energie de Nantes (CNRS UMR 6607)

Rapporteurs avant soutenance :

Jean-Pierre BEDECARRATS	Professeur, LATEP, Université de Pau et des Pays de l'Adour
Kévyn JOHANNES	Maître de conférences(HDR), CETHIL, Université Claude Bernard Lyon 1

Composition du Jury :

Président :	Régis OLIVES	Professeur, PROMES, Université de Perpignan Via Domitia
Examinateur :	Christian CRISTOFARI	Professeur, SPE, Université de Corse
Examinateur :	Yilin FAN	Chargé de recherche CNRS(HDR), LTEN, Nantes Université
Directrice de thèse :	Lingai LUO	Directrice de recherche CNRS, LTEN, Nantes Université
Co-directeur de thèse :	Jérôme SOTO	Chercheur associé, LTEN, Nantes Université & Enseignant, ICAM
Co-directeur de thèse :	Nicolas BAUDIN	Maître de Conférences, LTEN, Nantes Université

Thermocline study of packed-bed thermal energy storage system

PhD thesis

Baoshan XIE

Supervisor:

Lingai LUO

Co-supervisors:

Jérôme SOTO, Nicolas BAUDIN

Supporter:

Yilin FAN

Committee:

Christian CRISTOFARI, Régis OLIVES, Kévyn JOHANNES, Jean-Pierre BEDECARRATS

Specialty:

Energy – Thermal – Combustion

Thesis defense:

On 20 September 2022, at 9:30 AM

In Nantes, France

To my family.

(致我最爱的家人)

Acknowledgments

Thesis work is certainly an individual work, but it cannot be fruition without the corporation and assistance of groups. I would like to thank to people in this group that support me to construct this 'building'.

First of all, I have greatly appreciated my supervisor —Prof. Lingai LUO, for her everlasting guidance during my three-year study. Her knowledge, motivation and numerous advices are of importance to my thesis work and to my future work.

I am also deepest grateful to my co-supervisor —Dr. Nicolas BAUDIN, having accompanied me from the beginning of this thesis. His constant encourage inspires when I depressed and his instruction give me direction on solving troubles in thesis.

I would like to give thanks to my co-supervisor —Dr. Jérôme SOTO, for guiding me and enriching me with his individual expertise. His profound knowledge and patience facilitated the realization of this thesis.

I am very grateful for my support —Dr. Yilin FAN, who helped me in professional and in personal, and always be present in my study. His patience and positive attitude for each problem encountered were of great help.

I would like to thanks to members of my individual monitoring committee —Prof. Régis OLIVES and Prof. Gilles FLAMANT, for monitoring my thesis in regular and give useful suggestions and comments. I also thank the experts reviewing this paper and members attending my thesis defense.

I would like to express my thank to Mr. Julien AUBRIL, Mr. Arnaud ARRIVE, Mr. BIOTTEAU Gwenaël, and Mr. Jorge FERNANDEZ-PACHECO ARMENTEROS for their technique supports during the experiments.

I would like to say thanks to member of LTEN, especially the director of Steven LE CORRE and Cathy CASTELAIN (former). Thanks to Michèle-Anne AUDRAIN and Amandine BOUHIER to provide continuously help in authority assistances and registration of language.

At last, greatly thankful to the Chinese Scholarship Council for funding me (No. 201908430177) to finish my PhD study.

Abstract

The thermocline packed-bed tank with sensible heat or latent heat fillers is a cost-effective option for thermal energy storage (TES). Its thermal performance is very dependent on the packing configurations to each fluid flow and temperature situation. The principal objective of this PhD dissertation is to study the influence factors for different configuration of fluid flow and tank design, and then to conduct multi-layered packing configuration optimization of the storage tank. It starts by exploring the wall impact on thermocline and global thermal performance in dynamic conditions. Then, various influences, including the inlet configuration, the insulation, the filler size, and the operating parameters, on the thermocline in radial and axial direction based on a basic sensible heat filler tank are investigated. After that, the multi-layered configuration optimization of phase change material storage tank using a multi-objective genetic algorithm in multiple cycling is carried out by integrating the tank into an agriculture greenhouse application. The thermal performance of optimal tanks in seasonal operations is studied to find the potential for improvement of future work.

Keywords: Thermal energy storage (TES), packed bed, thermocline, packing configuration, storage media, multi-objective optimization

Résumé

Un réservoir thermocline avec un garnissage constitué de matériaux pour du stockage thermique sensible et/ou latent est une solution prometteuse pour le stockage d'énergie thermique (TES). Les performances d'un tel réservoir sont très dépendantes de la configuration physique, et des matériaux du garnissage. Ainsi, il existe un optimum pour chaque cas d'usage même si quelques règles générales sont conservées. L'objectif de cette thèse consiste à d'abord étudier l'effet de ces différents paramètres géométriques, physiques et thermo-hydrauliques sur l'efficacité du stockage. Une étude d'optimisation est réalisée afin de déterminer la meilleure configuration des paramètres pour un objectif donné. La première partie du manuscrit traite de l'impact des parois sur l'évolution de la thermocline et sur l'efficacité globale de la charge/décharge du réservoir, au moyen d'un modèle numérique simplifié prenant en compte ces effets tout en restant rapide à résoudre. Ensuite, les effets de la configuration du diffuseur d'entrée/sortie, de l'isolation thermique et des paramètres de charge/décharge sont étudiés expérimentalement sur un banc de tests dédié. Cette expérience a permi également de valider le modèle numérique. Ce modèle numérique est ensuite utilisé pour mener une optimisation avec une configuration multi-couches et multi-matériaux du garnissage grâce à un algorithme génétique multi-objectifs pour différents types de cycles de charge/décharge. Cette méthodologie est notamment mise en œuvre pour une application de stockage thermique dédiée à une serre horticole. Le manuscrit décrit, enfin, des pistes à développer pour des travaux futurs.

Mots clés : Stockage d'énergie thermique (TES), garnissage, stratification thermique, configuration de garnissage, média de stockage, optimisation multi-objectifs

Table of contents

Nomenclature

Abbreviations

ANR	l'Agence Nationale de la Recherche
CSP	Concentrated Solar Power
GH	Greenhouse
HDPE	High-density Polyethylene
HHTPB	Heterogeneous Heat Thermocline Packed Bed
HTC	Heat Transfer Coefficient
HTF	Heat Transfer Fluid
IEA	International Energy Agency
KPI	Key Performance Indicators
LCA	Life Cycling Assessment
LHTPB	Latent Heat Thermocline Packed Bed
MOGA	Multi-objective Genetic Algorithm
PCM	Phase Change Material
RMS	Root Mean Square
SD	Standard Deviation
SHTPB	Sensible Heat Thermocline Packed Bed
TC	Thermocouple
TES	Thermal Energy Storage
TR	Thermal Resistance

Latin symbols

a	Surface area per unit volume [$m^2 \cdot m^{-3}$]
A	Superficial area [m^2]
Bi	Biot number [-], $Bi=h \cdot (V/A)/\lambda$
C_p	Specific heat capacity [$J \cdot kg^{-1} \cdot K^{-1}$]
C_{ratio}	Capacity ratio [-]
D_p	Diameter of particle [m]
D_{tank}	Diameter of tank for free bed region [m]
E	Energy [J]
E_{in}	Inlet/input energy [J]
E_{out}	Outlet/output energy [J]
E_x	Exergy [J]
F_i	Function objectives [-]
f_r	Non-uniformity factor [-]

g	Acceleration due to gravity [m·s^{-2}]
Gr	Grashof number [-], $Gr=g\cdot\beta\cdot H^3\cdot\Delta T/\nu^2$
h	Heat transfer coefficient [W·m^{-2}·K^{-1}]
H	Height of tank for free bed region [m]
H_m	Enthalpy [kJ·kg^{-1}]
ΔH_m	Phase change enthalpy [J·g^{-1}]
I	Radiation intensity [W·m^{-2}]
L	Later thickness [m]
L_c	Characteristic length [m]
m	Mass [kg]
$\dot{m}$	Mass flow rate [kg·s^{-1}]
N, M, F	Node number for height, time, and radius in discrete process [-]
Nu	Nusselt number [-]
P	Power of greenhouse gas heating [W]
ΔP	Pressure drop [Pa]
Pe	Péclet number [-], $Pe=D_p\cdot u_{sup}/\alpha$
Pr	Prandtl number [-], $Pr=C_p\cdot\mu/\lambda$
Q	Stored heat of material for a given temperature range [J]
$\dot{Q}$	Heat transfer rate [W]
r	Radial coordinate of tank [m]
r_p	Radial coordinate of sphere [m]
Ra	Rayleigh number [-], $Ra= Gr\cdot Pr$
Re	Superficial Reynold number, $Re=\rho_f\cdot D_p\cdot u_{sup}/\mu_f$
R_{ext}	External radius of tank, or insulation radius [m]
R_{int}	Internal radius of tank, or bed region radius [m]
R_{mid}	Middle radius of tank, or support wall radius [m]
S	Surface area of solar collector [m^2]
t	Time [s]
T	Temperature [K]
T_0	Reference temperature [K]
T^A	Radial temperature of A position [K]
T^B	Radial temperature of B position [K]
T^C	Radial temperature of C position [K]
T_{amb}	Ambient temperature [K]
T_{ave}	Average operating temperature [K]
T_C	Coldest operation temperature of system [K]
T_H	Hotest operation temperature of system [K]
T_{in}	Fluid inlet temperature [K]
T_m	Melting temperature of PCM [K]

T_{out}	Fluid outlet temperature [K]
TR	Theraml resistance [K·W^{-1}]
u_f	Interstitial fluid velocity [m·s^{-1}], $u_f=\dot{m}/(\rho_f \cdot \varepsilon \cdot \pi \cdot R^2_{int})$
u_{sup}	Superficial fluid velocity [m·s^{-1}], $u_{sup}=u_f \cdot \varepsilon$
U_{ratio}	Utilization ratio [-]
V	Volume [m^3]
V_b	Tank volume based on inner tank diameter R_{int} [m^3]
V_{DES}	Tank volume in initial design [m^3]
$\dot{V}_f$	Volumetric flow rate [m^3·s^{-1}]
V_s	Total volume of solid particles [m^3]
z	Axial coordinate in flow direction [m]

Greek symbols

ν	Kinematic viscosity [m^2·s^{-1}]
α	Thermal diffusivity [m^2·s^{-1}], $\alpha= \lambda/ (\rho \cdot C_p)$
β	Thermal expansion coefficient [K^{-1}]
ε	Porosity [-]
ϵ	Emissivity [-]
η	Energy efficiency [-]
$\eta_{collector}$	Transfer efficiency of solar collector [-]
η_o	Overall energy efficiency [-]
η_x	Exergy efficiency [-]
θ	Outlet temperature threshold coefficient [-]
λ	Thermal conductivity [W·m^{-1}·K^{-1}]
μ	Dynamic viscosity [Pa·s]
Π_i	Dimensionless numbers [-]
ρ	Density [kg·m^{-3}]
σ	Stefan-Boltzmann constant, =5.67×10^{-8} W·m^{-2}·K^{-4}
Υ_o	The combined storage/utilization ratio [-]
ϑ	Uncertainty [-]

Subscripts

amb	Ambient
ave	Average
b	Bed region of inner diameter of tank R_{int}
ch	Charging
cond	Conductive
conv	Convective

DES	Designed
diff	Diffusivity
dis	Discharging
eff	Effective value
ext	External surface of tank
f	Fluid
in	Inlet
ini	Initial
ins	Insulation
int	Internal surface of tank
l	liquid
max	Maximum
mid	Middle surface of tank, or wall surface
o	Overall value
out	Outlet
p	Particle
rad	Radiative
s	Solid
sf	Solid-to-fluid phase
w	Wall

Chapter 1
General introduction

1.1. Context

In coping with issues of the fluctuating and intermittent renewable energy sources in utilization, thermal energy storage (TES) technology is an effective way. It addresses the contradiction between energy supply and demand through smoothing production and shifting peak load [1]. Integrating TES system in various applications like buildings, agriculture, and industries is feasible to improve the system stability and efficiency by replacing the conventional carbon dioxide (CO_2) emission energy backup.

Thermocline packed-bed TES tank (or dual-media thermocline) is a type of cost-effective and potential technology. As a type of one-tank system, it has tank volume investment reduction compared to the two-tank system, and also shows the filler advantages compared to another one-tank system of single-media thermocline (by 45% than two-tank in total) [2]. In this kind of tank, cheap sensible heat fillers and latent heat fillers (or phase change material, PCM) with high energy density are good selections, or even mixing both as fillers through different packing configurations to increase efficiency of system [3].

However, **barriers** still exist:

— Unstable temperature stratification or thermocline in one-tank system is leading to thermal performance degradation.

— The tradeoff between configurations (packing structure, filler types) and high efficiency under various operational parameters is difficult to be achieved, comparing to single-media thermocline system.

It's necessary to propose proper packing configuration in consideration of the influence factors (wall impact, inlet flow, heat loss, etc.) on thermocline in a packed-bed system.

1.2. Research foundation

This thesis work is part of a cooperation project of the 'OPTICLINE' supported by l'Agence Nationale de la Recherche (ANR): *Optimization of high temperature thermal energy storage by the thermocline technology*. Researchers in this project had conducted a lot of interesting and meaningful work in thermocline storage tank, including the single-media thermocline and the dual-media thermocline. Various parameters were investigated and optimized to stabilize the thermocline, as well as improve the thermal performance.

On one side, colleagues of **PROMES laboratory** focus on dual-media thermocline tank and design a large pilot-scale high-temperature experimental tank. Vannerem et al. [4] once investigated the operating parameters of the interstitial fluid velocity cause effect on thermocline performance. Finding that the impact of fluid velocity is too moderate to observe an optimal velocity, especially because of non-ideal inlet temperature conditions. Then, they tried to understand the effect of fluid distribution on the storage tank in experiment [5]. Later, latent heat PCMs were also attempted to be filled at top layer to enhance the thermal performance [6].

On another side, works on **laboratory LTEN** begins from the single-media storage tank. Lou et al. [7][8] built a small lab-scale low-temperature experimental system and aimed at solving the flow distribution problem by designing the inlet/outlet manifold, to enhance the temperature stratification performance. In experimental validation, it was proved that the mixing behavior within the main fluid region doesn't represent obvious anymore after the optimized upper distributor equipping.

This thesis is a supplement of previous works and an extension to the dual-media thermocline (or packed-bed thermocline) tank investigation, focusing on influence factors and packing configuration optimization. Simulation is chosen as MATLAB and the experiment is based and modified on Lou's experimental set-up in LTEN.

1.3. Research objective

The main objective of this thesis is to propose the packing strategy for improving efficiency and utilization in cycles of thermocline packed-bed TES system. Initially, to understand the

influence factors on thermocline system from the wall, insulation, inlet configuration, flow rate, etc. Subsequently, through optimizing packing configuration to obtain a stable and thinner thermocline for alleviating the influence of the unstable temperature input. Accessorily, the experimental methodology is used to clarify some phenomena that were insufficiently explained in the simulation and to validate the developed models for this study.

The present thesis is implemented to combine the scientific methodologies of the theoretical analysis, numerical simulation, and experimental validation to provide a case study for industrial applications.

1.4. Thesis outline

This thesis paper is introduced in several parts:

Chapter 2

This chapter presents a comprehensive review of the thermocline packed-bed TES system, covering the storage mechanisms, packing configurations, and the application temperature ranges. A detailed description of storage media is presented. An introduction of influence factors i.e., operational, geometrical, and thermophysical parameters, on the thermal performance of storage systems, is exhibited. The state of the art of thermocline packed-bed system based on storage media and packing structure is presented in a series of studies. This chapter is objective to offer good guideline to design the initial packing structure, the selection of filler materials, or the operational conditions.

Chapter 3

This chapter systematically explores the wall impact on the thermocline behavior comparing with two typical configurations — a lab-scale low-temperature tank and a pilot-scale high-temperature tank. The amount of energy stored in wall and insulation is quantified to define the influence degree. The dynamic influence of wall stored energy in discharging on thermocline is presented. An adapted transient model that accounting the wall impact and heat loss in governing equation is defined. After that, a wall parametric study is performed to propose an optimal wall design guideline to avoid thermocline degradation.

Chapter 4

This chapter experimental and numerical investigated influence factors on dynamic thermal behavior of thermocline packed-bed tank with sensible fillers. It studied the impact of diffuser and insulation on radial temperature distribution, and clarifies the impact of flow rate and operational temperature on axial heat transfer and diffusion based on parametric study. The developed three-phases model was experimental validated for the temperature gradient inside and particle. At last, a parameter study of influence factors, including inlet temperature and mass flow rate, on thermocline thickness is performed to get a highest energy efficiency.

Chapter 5

This chapter provides an optimization method for packing configuration strategy on maximizing the overall energy efficiency and storage/utilization ability in multiple cycles by using PCM. An initial tank is first designed according to meteorology data of a low-temperature application of the seasonal greenhouse. Adapting a multi-objective genetic algorithm (MOGA) to optimize the layer configuration under PCM property constraints (thermal conductivity, phase change temperature, and layer thickness) and operational constraints (mass flow rate). Based on optimal result, the steady and dynamic inlet temperature input were compared in real greenhouse application to find the influence for improvement.

Chapter 6

At last, this chapter summaries main results in former chapters of this thesis paper and give some prospective for future work.

Chapter 2
Literature review on thermocline packed bed thermal energy storage system

Abstract

The thermocline packed-bed thermal energy storage (TES) system acted as dual-media is an alternative to conventional two-tank storage system, exhibiting excellent cost and heat capacity advantages. This chapter is the literature review that provides an overview of thermocline packed-bed TES systems, covering the storage mechanism, packing configurations, application temperature ranges, etc. It is looking forward to presenting the research progress, identifying the existing challenges, and giving perspective for future work. The objectives of this chapter are as follows:

- Summarize the different storage materials that used in packed bed system and corresponding advantages/disadvantages.
- Analyze the influencing factors on thermal performance, i.e., operational, geometrical, and thermophysical parameters.
- Make a clarification of the state-of-art of various thermocline packed-bed TES system.
- Point out the interesting of improving the system through designing configuration.

Keywords: thermal energy storage, thermocline, packed bed, packing configuration, sensible heat, latent heat

This chapter is published as:

Xie B, Baudin N, Soto J, Fan Y, Luo L. Chapter 10 - Thermocline packed bed thermal energy storage system: a review. In: Jeguirim MBT-REP and D, editor. Adv. Renew. Energy Technol., vol. 1, Academic Press 2022, p. 325–85.

Chapter content

2.1. Introduction

Energy demand is in rapid growth especially for energy sources without environmental issues of global warming and air pollution. The International Energy Agency (IEA) pointed out in "Tracking Report 2020" that the renewable energy counted for about 27% of the global electricity production in 2019. However, the use of renewable power needs to be significantly increased to half of the production to meet the demand of sustainable development scenario by 2030 [9]. Solar energy as a feasible alternative to fossil fuel is one of the promising options due to the large quantities of solar radiation on the surface of earth [10]. However, the solar power source and the power demand are both intermittent, and often in mismatch.

To address these problems, the TES system is integrated in solar energy system, like concentrated solar power (CSP) and domestic solar hot water supply, to promote the system reliability by replacing conventional fossil fuel backup systems [1][11][12][13][14][15]. This economic and CO_2 emission free solution allows buffering transient weather conditions, increases the annual capacity factor and evens the electricity production. More than that, the TES has been applied in various energy systems in order to improve the system stability and efficiency, including building energy conservation, waste heat recovery, cooling system, and many others [16][17][18][19][20][21].

2.1.1. Storage mechanism

There are different ways to store heat: the sensible heat storage based on a change of temperature, the latent heat storage based on a physical status change, and the thermochemical storage based on endothermic/exothermic chemical reactions [22][23]. The latter can potentially store more energy per volume unit (nearly 10^6 kJ m^{-3}) but suffers from high complexity and low technical maturity[24] thus will not be involved in this chapter. In single-media systems, heat storage is achieved using the sensible heat transfer fluid (HTF) only, such as in domestic hot water tanks [25]. However, in CSP, those require high temperatures and thus expensive and non-environmental friendly fluids, which usually shows poor thermal properties. The packed bed or dual-media is then preferred, with solid fillers in the tank acting as main storage media, exchanging heat with HTF through direct contact, decreasing thereby the total amount of HTF required. There are other considerations when conceptualizing a TES system, such as using active or passive, direct or indirect concept (**Figure *2.1***). Such aspect will not be detailed here and the following parts of the chapter will focus on the storage tanks themselves.

2.1.2. Thermocline packed bed technology

Typically, the integrated TES system is designed as a one-tank or a two-tank system [26][7]. In two-tank system, the HTF is stored in two isolated and insulated tanks with two extreme temperatures. One primary example of a two-tank system is a CSP plant, shown in **Figure *2.1* a**. In daytime, the HTF collects solar heat energy from solar receiver and transfers heat to the steam generator for power generation, and extra heat energy is stored in a hot tank. During the night or insufficient sunlight day, the HTF from the hot tank is delivered and used to maintain the power production. The one-tank system (or single-tank) is a substitution of the conventional two-tank system that greatly cuts off investment costs by removing a tank, as shown in **Figure *2.1* b**.

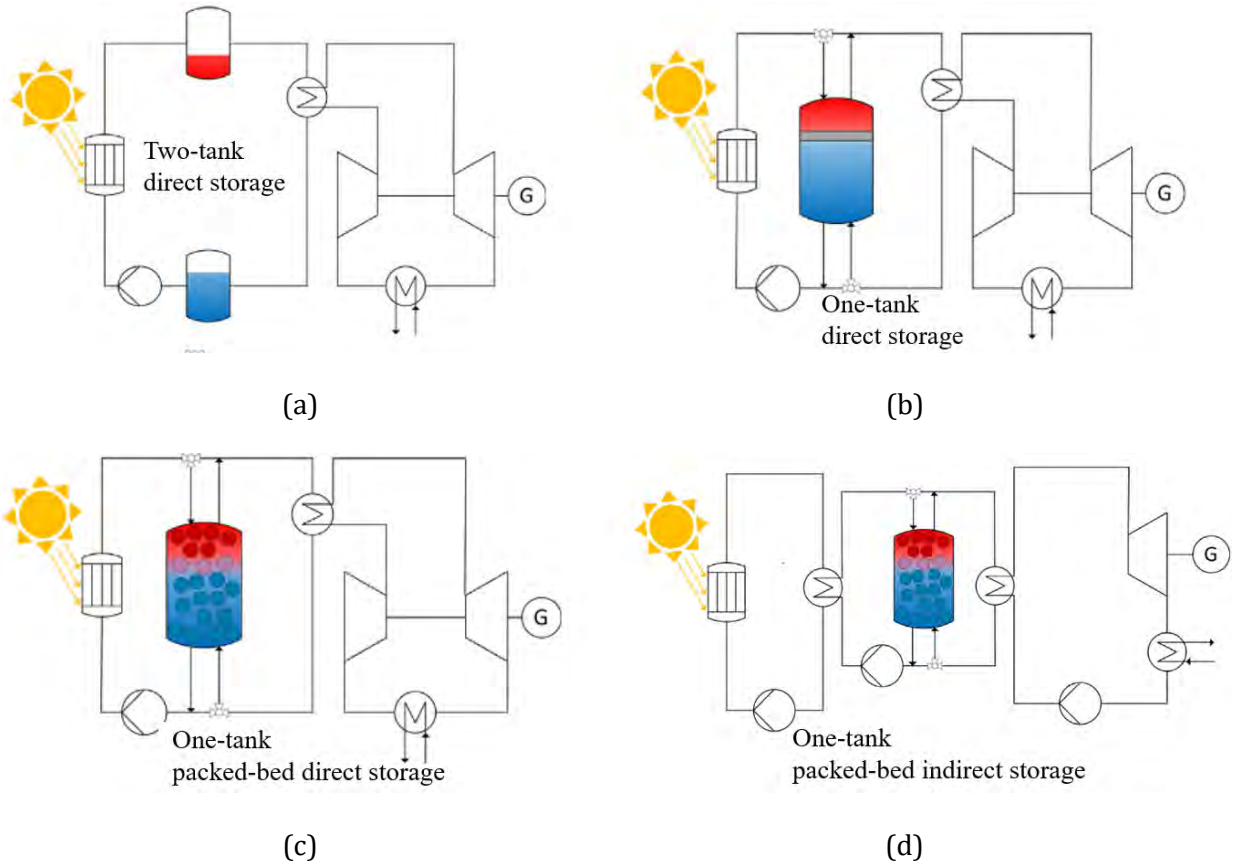

Figure 2.1: CSP plant with Brayton gas cycle: (a) two-tank direct; (b) one-tank direct; (c) one-tank packed-bed direct; (d) one-tank packed-bed indirect storage systems [27].

Adapted from figures that obtained the copyright permission of Elsevier [License No. 5207601058078, Dec 14, 2021].

In this system, the hot HTF is stored at the top, and the cold HTF stays at the bottom of tank. Physical stratification between both HTFs is maintained by buoyancy forces due to the density difference [28]. The zone between the hot and cold HTF, characterized by a temperature gradient,

is called thermocline, and is represented on **Figure 2.2**. With cheap fillers and smaller tank volume, the cost reduction of overall investment can be up to 35% for packed-bed TES tank in comparison to traditional two-tank TES system in CSP plant [29]. For many packing materials used in industry, the energy density in theory is about 180-250 MJ m^{-3} (or 50-70 kWh_{th} m^{-3}) based on a temperature change of about 100 K [30]. Due to these advantages, the thermocline packed-bed TES system is considered to be a promising technology for solar energy application, embracing the low, middle, and high-temperature ranges [31].

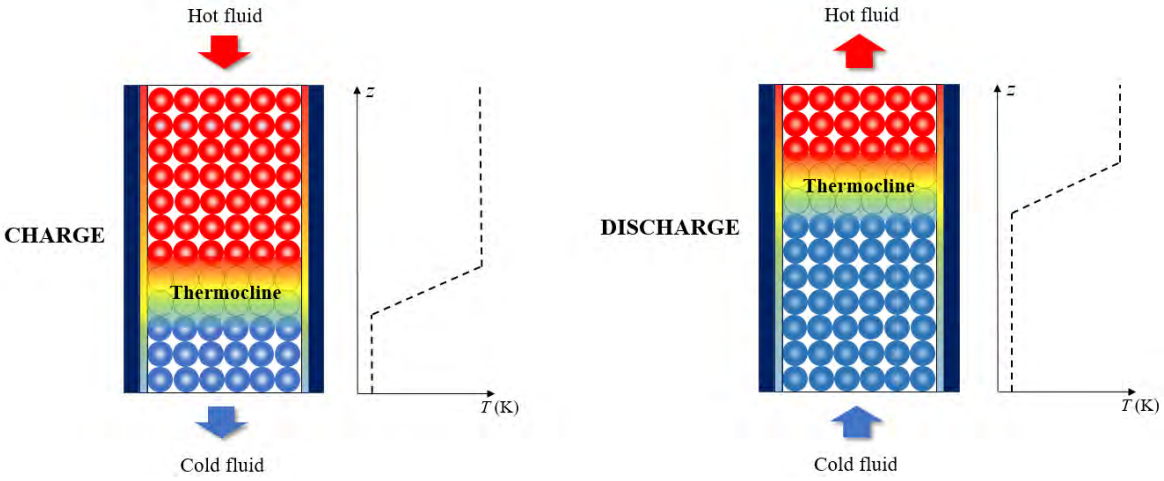

Figure 2.2: Schematic of thermocline during (a) charging and (b) discharging.

2.1.3. Challenges

However, the shortcoming of the present thermocline packed-bed TES system also exists: the useful zone called "**dead zone**" because the heat stored in this region is mostly at a temperature lower than the cutoff temperature, under which the charging/discharging process is hard to be operated (**Figure 2.3**). In theory, the thermocline quality evaluated by its stability and thickness reflects the system performance: *higher level of thermal stratification in the thinner thermocline zone means higher energy and exergy efficiencies* [32][33]. Nevertheless, the thermal stratification tends to become unstable and expanded over dynamic and cycling operations. This thermocline degradation (or decay) can be due to several reasons [34][35].

- Thermal diffusion in the solid fillers and the fluid.
- Heat losses through the walls.
- Heat convection of the HTF itself resulted from fluid flow regimes in porous bed.
- Limited heat convection between solid and fluid causing heat transfer delay.
- Variable operational conditions during charging and discharging.

● Non-uniform flow distribution at the inlet due to sudden fluid injection or near the wall region because of the different porosities.

In addition, this system faces challenges like conflict between high storage capacity per unit volume and low cost, the temperature dropping or heat loss at the end of heat storage/release cycles, pressure drop under high porosity bed, and stability under various operational parameters. Therefore, investigations on the physical phenomena influencing the thermocline thickness and on the performance optimization under techno-economic constraints of the single tank parameters are required. Only through that, the development of the thermocline packed-bed system will become more attractive through designing optimization.

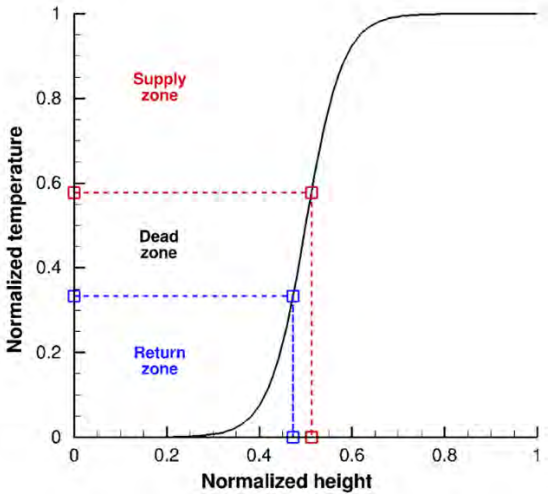

Figure 2.3: Intermediate "dead zone" in conventional rock-filled thermocline tank [36].

Obtained copyright permission of Elsevier [License No. 5207601468200, Dec 14, 2021]

2.2. Storage media

This section presents the different storage materials and the properties considered for the appropriate design, considering the storage media or fillers are the core among other elements of a packed-bed thermocline TES system, including the (sensible heat and/or latent heat) fillers, the HTF, the wall and insulation [37], and the inlet/outlet manifolds or diffusers.

2.2.1. Sensible heat fillers

Sensible heat storage occurs when the temperature of material rises. When choosing the materials, the important thermal properties are the volumetric heat capacity ($\rho \cdot C_p$), which dictates the energy storage density capability, and the heat diffusivity ($\frac{\lambda}{\rho \cdot C_p}$), which reflects the rate of the heat released and absorbed [38].

Table 2.1 lists some sensible material fillers for packed-bed TES system and corresponding thermophysical properties. For most of sensible heat storage materials, the volumetric heat capacity can vary between 900 and 3000 kJ m^{-3} K^{-1} [39]. With favorable features of the proper volumetric heat capacity, low cost, and availability, sensible heat material is commonly used in industrial or lab thermocline tanks. Rocks are interesting fillers in packed-bed TES system since they have a high heat capacity and are cheap. Tiskatine et al. [40] evaluated 52 sensible heat materials of a packed-bed system for high-temperature CSP application. Among those, four types of materials, the dolerite, granodiorite, hornfels, gabbro and quartzitic sandstone were found to be excellent in air-based solar.

The stored heat of material (Q) for a given temperature elevation of sensible fillers is calculated:

$$Q = \int_{T_1}^{T_2} m \cdot C_{p,s} \cdot dT \tag{2.1}$$

where — T_1 and T_2, the initial and final temperature, respectively.

— C_p, the heat capacity.

— , the mass.

— λ, the thermal conductivity.

— , the density.

Table 2.1 Thermophysical properties of common sensible heat fillers for thermocline packed-bed TES.

Sensible fillers	ρ_s **(kg** m^{-3}**)**	$C_{p,s}$ **(J** kg^{-1} K^{-1}**)**	λ_s **(W** m^{-1} K^{-1}**)**	$\rho_s \cdot C_{p,s}$ **(kJ** m^{-3} K^{-1}**)**	**Ref.**
Cast iron	7900	837	29.3	6612	[41]
Steel	7870	565-571	49.8	4447-4494	[42][43]
Magnesia fire brick	1150	3000	5.0	3450	[44]
Coal fly ash brick	2600	735-1300	1.3-2.1	1911-3380	[45]
Castable ceramic	3500	866	1.4	3031	[40]
Blast furnace slag	2980	996	2-3.5	2968	[46]
Alumina ceramic	3750	780	30	2925	[47]
Steatite	2680	1068	2.5	2862	[43][48]
Alumina	3670	750	21	2753	[45]
Granite rock and sand	2643	1020	2.2	2696	[49]
Concrete	2800	916	1.0	2565	[47][40] [50]
Copper slag	3600	683 (300°C)	0.8	2450	[51]
Aluminum	2700	896	204	2419	[43]
Silicon carbide ceramic	3210	750	120	2408	[47]
Quartzite rock and sand	2500	830	5.7	2075	[41]
Silca fire brick	1820	1000	1.5	1820	[44]
Soda-lime glass	2400	760	1.0	1824	[42]

2.2.2. Latent heat fillers

Latent heat storage occurs when a material changes its phase from one physical state to another. When heating/cooling, a material that undergoes this phenomenon and releases/absorbs heat in a narrow temperature range is called phase change material (PCM). Four types of phase transition exist [26]**:** solid-solid (crystalline heat), solid-liquid (fusion heat), liquid-gas (vaporization heat), and solid-gas (sublimation heat). Among them, PCM based on solid-liquid transition is widely used in TES for its simplicity and wide temperature availability [21][52][53][54]. **Table 2.2** lists several candidates of solid-liquid PCM fillers and the corresponding thermophysical properties. As explained in **Figure 2.4**, the material changes its phase from solid to liquid when temperature increases, and more amount of heat is exchanged during the latent storage in comparison to the sensible storage for the same temperature change.

The stored energy of PCM in different heating stages is calculated as:

$$Q = \int_{T_1}^{T_2} m \cdot C_{p,s} \cdot dT \qquad (T_2 < T_m) \qquad (2.2)$$

$$Q = \int_{T_1}^{T_m} m \cdot C_{p,s} \cdot dT + m \cdot \Delta H_m \qquad (T_2 = T_m) \qquad (2.3)$$

$$Q = \int_{T_1}^{T_m} m \cdot C_{p,s} \cdot dT + m \cdot \Delta H_m + \int_{T_m}^{T_2} m \cdot C_{p,l} \cdot dT \qquad (T_m < T_2) \qquad (2.4)$$

where — T_m , the phase change temperature.

— ΔH_m , the phase change enthalpy.

— $C_{p,s}$, the heat capacity of solid phase PCM.

— $C_{p,l}$, the heat capacity of liquid phase PCM.

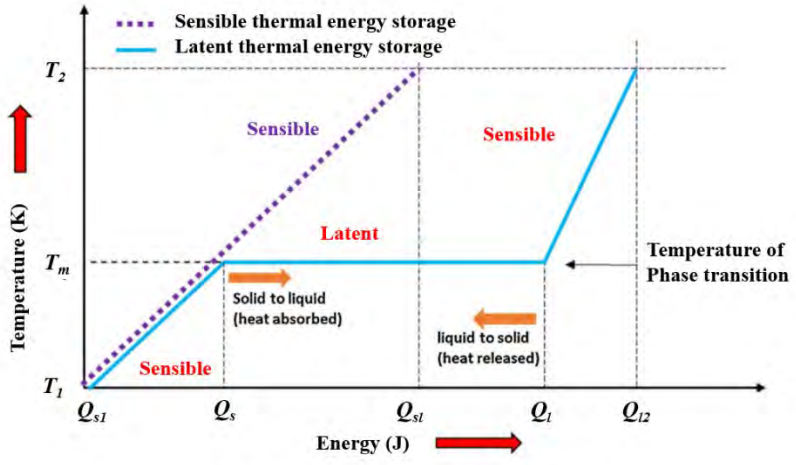

Figure 2.4: Phase change temperature profiles of solid-liquid transition [55][56].

Adapted from the figure that obtained the copyright permission of Elsevier [License No. 5207611412736, Dec 14, 2021]

Table 2.2 Thermophysical properties of some candidate solid-liquid PCM fillers for thermocline packed-bed TES [55].

PCM				Liquid		Solid	
		T_m (°C)	ΔH_m (J g^{-1})	ρ_l (kg m^{-3})	λ_l (W m^{-1} K^{-1})	ρ_s (kg m^{-3})	λ_s (W m^{-1} K^{-1})
Organic (0-200°C)							
Paraffins	n-Tetradecane, $C_{14}H_{30}$	6	230	760 (20 °C)	--	--	0.21
	n-Heptadecane, $C_{17}H_{36}$	19	240	776 (20 °C)	--	--	0.21
	n-Eicosane, $C_{20}H_{42}$	38	283	779	--	--	0.358 (25 °C)
	Polyethylene, CnH_{2n+2}, n up to 100000	110-135	200	--	--	870-940 (20 °C)	--
Fatty acids	Caprylic acid $CH_3(CH_2)_6COOH$	16	149	901 (30 °C)	0.149 (38 °C)	981 (13 °C)	--
	Lauric acid $CH_3(CH_2)_{10}COOH$	42-44	178	870 (50 °C)	0.147 (50 °C)	1007 (24 °C)	--
	Myristic acid $CH_3(CH_2)_{12}COOH$	58	186, 204	861 (55 °C)	--	990 (24 °C)	0.17
Sugar alcohols	Xylitol $C_5H_7(OH)_5$	94	263	--	--	1500 (20 °C)	--
	Erythritol $C_4H_6(OH)_4$	120	340	1300 (140 °C)	0.326 (140 °C)	1480 (20 °C)	0.733 (20 °C)
	Galactitol $C_6H_8(OH)_6$	188	351	--	--	1520 (20 °C)	--
Polyethylen glycols	PEG400	8	100	1125 (25 °C)	0.19 (38 °C)	1228 (3 °C)	--
	PEG1000	35-40	--	--	--	--	--
	PEG6000	55-60, 66	190	1085 (70 °C)	--	1212 (25 °C)	--
Inorganic							
Eutectic water-salts (<0 °C)	$Al(NO_3)_3$ (30.5 wt%) /H_2O	-30.6	131	1283	--	1251	--
	NaCl (22.4 wt%) /H_2O	-21.2	222	1165	--	1108	--
	KCl (19.5 wt%) /H_2O	-10.7	283	1126	--	1105	--
Salt hydrates (5-130 °C)	$LiClO_3 \cdot 3H_2O$	8	155	1530	--	1720	--
	$Na_2HPO_4 \cdot 12H_2O$	35-44	280	1442	0.476	1442	0.514
	$MgCl_2 \cdot 6H_2O$	117	165, 169	1450 (120 °C)	0.570 (120 °C)	1569 (20 °C)	0.704 (110 °C)
Salts (>150 °C)	$NaNO_3$	307	172	1900	0.51	2260	0.50
	$MgCl_2$	714	452	2140	--	--	--
	K_2CO_3	897	236	2290	--	--	--
Inorganic mixtures	4.3 wt% NaCl-0.4 wt% KCl-48 wt% $CaCl_2$-47.3 wt% H_2O	27	188	1530	--	1640	--
	58.7 wt% $Mg(NO_3) \cdot 6H_2O$-41.3 wt% $MgCl_2 \cdot 6H_2O$	58, 59	132	1550	0.510	1630	0.678
	54 wt% KNO_3-46 wt% $NaNO_3$	100	222	1950	--	2050	--

The phase change temperature of PCM commonly maintains at a relatively stable value, allowing a constant temperature heat exchange for process control. But in some real cases, the phase change does not happen in a such stable platform and there is a small temperature range in phase transition actually appears [55]. When calculating the apparent heat capacity, the latent heat depends on transient temperature due to this temperature range [57][58][59][60].“Subcooling” (or supercooling) is another phenomenon that when PCM begins to solidify and release heat, the initial freezing temperature is below the melting temperature, caused by the nucleation rate [61][62]. Decreasing subcooling degree and the difficulty to bed operated.

In TES system, the PCM is commonly encapsulated to obtain a packed bed. Using encapsulated PCM as fillers is helpful to improve the stability and the sharpness of the thermocline in a packed-bed tank owing to the features presented above. Putting the PCM near the ports of tank system can restrict the outlet temperature at a constant value [63]. Ge et al. [64] summarized several types of PCMs that can be used in solar energy storage. Mix molten salt is a promising material for high-temperature CSP plant, showing large melting temperature ranges from 100 to above 600 °C depending on the mixing ratio [65]. The organic PCM shows great volumetric latent heat storage capacity around 128-200 kJ m^{-3} $\times 10^3$, while that of inorganic PCM is even doubled (250-400 kJ $m^{-3} \times 10^3$) [66]. However, the high cost and low thermal conductivity (about 0.2-0.7 W m^{-1} K^{-1} [39]) restrict its wide application. Hence, heat transfer enhancement techniques are widely proposed and implemented to improve the thermal conductivity.

In summary, **Table 2.3** compares the cost of some sensible and PCM materials applied in thermocline packed-bed TES. Sensible materials show cost advantages while PCMs with high energy density and stable phase change temperature can store more energy. **Figure 2.5** shows some examples of sensible and PCM fillers used in real cases. **Figure 2.6** is a typical encapsulated PCM. It is observed that there is natural connection inside capsules when the PCM is melting, so that the thermal conductivity of PCM capsules should be considered in to an effective value in some conditions [67]. While the density variation of PCM in phase change process can be negligible in the constant capsule volume [68]. Moreover, the geometric properties of solid media, including particle size, shape (spherical, cylindrical, or rectangular), shell types, porosity, packing arrangement (random or regular), etc., all have influence on the thermal performance of packed-bed system, especially the level of thermal stratification. Those will be discussed in the later part of this chapter.

Table 2.3 Cost of materials for thermocline packed-bed TES.

Materials	US$ kg^{-1}	Ref.
Sensible heat filler		
Hitec (40 wt%$NaNO_2$-7 wt%$NaNO_3$-53 wt%KNO_3)	1.92	[69]
Solar salt [42 wt%$Ca(NO_3)_2$-15 wt%$NaNO_3$-43 wt%KNO_3]	1.19	[26]
KOH	1.00	[26]
K_2CO_3	0.60	[26]
Solar salt (60 wt%$NaNO_3$-40 wt%KNO_3)	0.46-0.49	[26]
Solar salt (20 wt%Li_2CO_3-60 wt%Na_2CO_3-20 wt%K_2CO_3)	0.41	[26]
KNO_3	0.30	[26]
Na_2CO_3	0.20	[26]
NaCl (solid)	0.15	[26]
Latent heat fillers		
Cast iron	1.00	[70]
Stainless steel	0.63	[28]
Carbon steel	0.38	[28]
Rock and sand	0.15	[26]
Concrete	0.05	[50]
Metal slag	0.005	[70]

(a) (b) (c)

(d) (e) (f)

Figure 2.5: Example of sensible and latent heat fillers used for thermocline packed-bed TES tanks. Sensible heat fillers: (a) demolition wastes, D_p=10 mm, 120-180 °C [71]; (b) sandstone and limestone, D_p=6-50 mm, 25-587 °C [72]; (c) quartzite pebbles, -160-25 °C [73]. PCM capsules fillers: (d) paraffin RT20, D_p=50 mm, 19-28 °C [74][75]; (e) lab-designed PCM, D_p=50 mm, -160-25 °C [73]; (f) paraffin RT 70HC, =15 mm, <40-85 °C [76].

Obtained copyright permission of Elsevier [License No. 5207631127001, No. 5207631305108, No. 5207640003877, No. 5207640830249, No. 5207641236538, Dec 14, 2021]

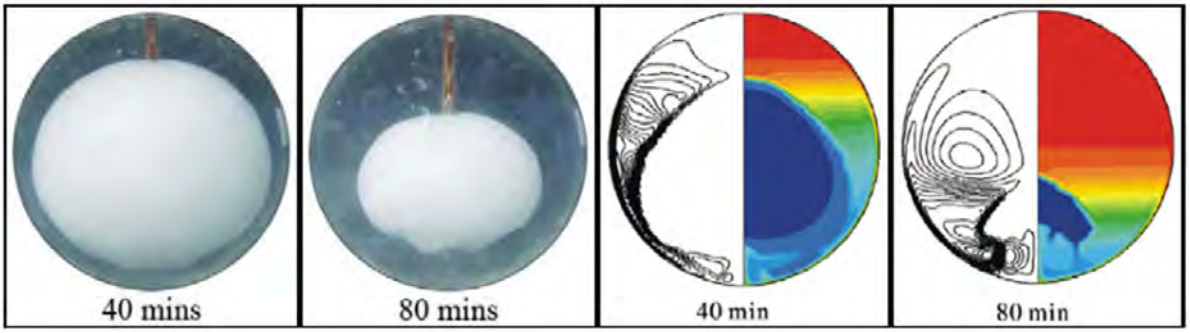

Figure 2.6 PCM capsules melting process in experiment and simulation [77][78].

Obtained copyright permission of Elsevier [License No. 5207630764534, Dec 14, 2021]

2.3. Influencing factors on thermal performance

System thermal performance is mainly affected by three aspect factors (in **Figure 2.7**): operational parameters, geometrical parameters, and thermophysical parameters [79].

The operational parameters are commonly decided by the requirements of certain application. The geometrical parameters include the tank and filler geometries and configurations. The thermophysical parameters are mainly decided by the selected material themselves and are usually temperature and/or pressure dependent. These influences factors are introduced in this sub-section.

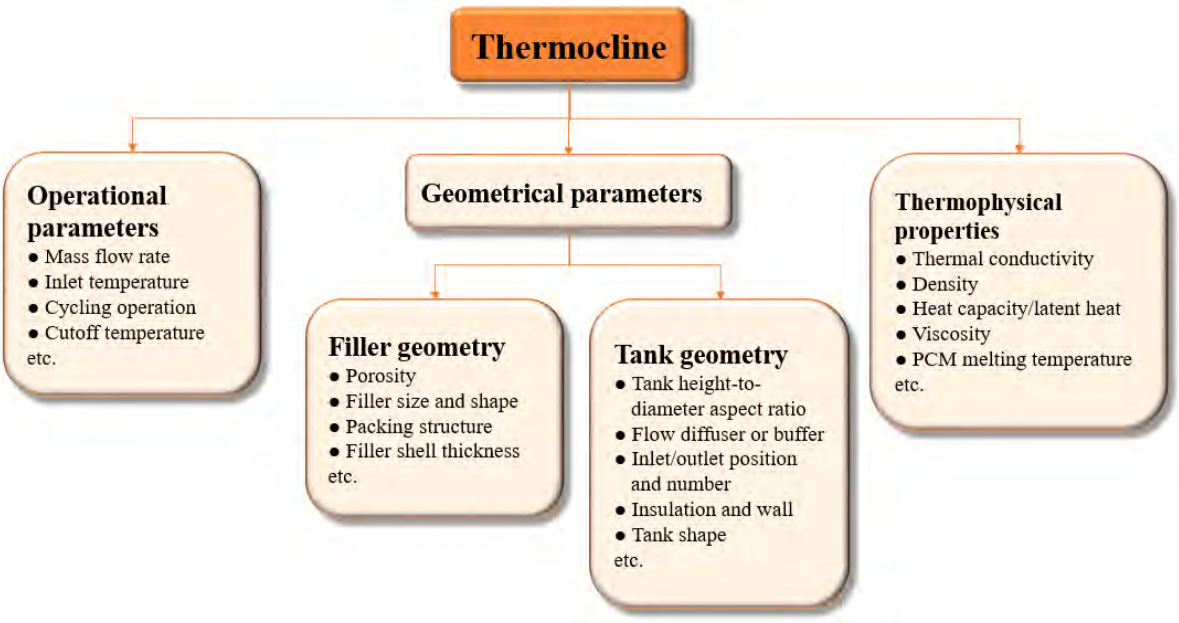

Figure 2.7: Influencing parameters of thermocline packed-bed TES system.

2.3.1. Operational parameters

The HTF mass flow rate, the inlet temperature, the cutoff temperature, and the cycling number are main operational parameters.

2.3.1.1. Mass flow rate

The HTF mass flow rate mainly determines the flow conditions and heat transfer rate between different phases. Commonly, higher flow velocity is beneficial to reduce the charging/discharging time due to the increment of heat transfer rate between HTF and solid fillers [80][34][58]. Nallusamy et al. [81] proved that when the flow rate increased from 2 to 6 kg min^{-1}, the time required for the complete charging decreased by 24% in a PCM thermocline packed-bed system. However, some works found that the total stored energy in the tank [73] and the thermocline development [82][34] were less influenced by the HTF flow rate. In fact, the impacts of the high velocity on uneven flow temperature distribution and stratification cannot be neglected in actual cases. The mass flow rate should be determined by comprehensively considering various factors such as the ending time, the efficiency and the flow distribution uniformity. More discussion on the influence of this parameter can be found in reference [1].

2.3.1.2. Inlet temperature

The inlet temperature is usually decided by application specifications. It determines the temperature difference thus the driving force for the heat transfer between HTF and solid fillers, but also responsible for the heat loss from the storage tank to the ambient. The inlet temperature impacts on heat transfer rate, heat loss, and total stored/released energy should be firstly investigated before system optimization [80]. More information about the influence of this parameter is presented in [1].

2.3.1.3. Cutoff temperature

Likewise, the cutoff temperature referring to the termination condition of operation which is usually decided by application specifications, defined in Chapter 3. It is often set as 0.8-0.95 times to working temperature range in discharging process, and 0.05-0.2 times in charging process [83][84][85]. With lower cutoff temperature, the storage tank cannot be fully charged. In discharging, a lower cutoff outlet temperature will cause more heat loss because of longer operation time, and may be insufficient to drive the power generation or energy supply.

2.3.1.4. Cycling operation

Efficient thermal cycling is closely related to the level of thermal stratification inside the tank [86]. Firstly, the thermocline zone is expanding and stratification degrading after several charging/discharging cycles, causing the declined efficiency [41]. In the end, the thermocline

region could occupy the whole tank volume. Secondly, the heat loss and pumping loss increase as time increase in the cycles [87]. There is no choice on this parameter it is ignored by the application. But of course, the thermocline will change in function of the number of cycles.

As a result, the cycling numbers should be decided when the outlet temperature at the cutoff time seems stable in cycling. Thus, it can be used to optimize the capacity and efficiency of system for long-term operation.

2.3.2. Geometrical parameters

2.3.2.1. Tank wall and insulation

Wall is the main support component of the tank. The selection of wall material is mainly depending on the temperature ranges and tank size. Metals like carbon steel serve as the wall material owing to their high strength and resistance to high pressure in high-temperature applications [83]. But, using this material may result in more heat loss to the ambient because of the high thermal conductivity. Meanwhile, it has a higher volumetric heat capacity than HTF. Therefore, the wall may as the storage media to store/release heat in charging/discharging, leads to a thermocline radial temperature difference between the center and near-wall region. Therefore, the wall impacts should be well considered in designing the thermocline packed-bed tank [88].

Good insulation avoids heat loss and improve system stability. Whereas the energy variation of thick insulation is negligible for different temperature applications. Commonly, insulation is not worth to be considered as storage media.

2.3.2.2. Flow diffuser and buffer and inlet position

The flow distribution and thermocline stability are greatly affected by the injection of the HTF at the inlet. The sudden entering of HTF from the inlet tube will cause high fluid local velocity on the part region inside the bed. Because the inflow jet temperature is comparatively hotter/colder than the surrounding bed. The streamflow leads to the center temperature differing from the temperature in the radial direction of the same high height and may disturb the stratification [25]. Through installing the flow diffuser and buffer at the inlet/outlet position will alleviate this phenonmen to achieve homongenous flow distribution. In packed-bed system, the porous media can serve as the diffuser to a certain extent to eliminate the flow fluctuation. Thus, it may be unnesessary to add a diffuser inside packed-bed tank, especially with the tank diameter to particle size ratio ($\frac{D_{tank}}{D_p}$) larger than 10. Moreover, the inlet/outlet position and numbers can also affect the stratification in non packed-bed TES system [89].

2.3.2.3. Tank diameter-to-height ratio (aspect ratio)

In general, the increasing aspect ratio of tank ($\frac{D_{tank}}{H}$) leads to the decreased heat loss because of the smaller lateral wall surface area for the same bed volume. Zanganeh et al. [87] reported that when the ratio increase from 0.5 to 2, the fraction of the pumping energy strongly decreased from 6.75% to 0.75% due to the shorter bed length. Oppositely, the overall efficiency decreased due to the weaker heat transfer rate caused by the decreased fluid velocity at constant inlet mass flow rate.

2.3.2.4. Particle size

Sensible fillers have a wide range of average particle size, usually varying between 1×10^{-3} m to 0.05 m. Bruch et al. [90] once investigated the fluid flow through a 3 mm sand bed and a 3 cm rock bed in pilot-scale thermal oil bed system. Smaller particle diameter facilitates the flow distribution for better thermal stratification and can increase heat transfer surface area [91], but in the meantime it will cause higher pressure drops. Sometimes, the influence of boundary effect of mass transfer may be alleviated when the bed-to-particle diameter ratio is large [92][48]. Larger particles (with low thermal conductivity) may have a larger temperature difference between solid and fluid, causing the faster expansion of the thermocline [47]. Sorour [93] suggested to use intermediate particle size of 18 mm with low mass velocity instead of small particle size of 12 mm with high mass velocity to increase the storage efficiency.

PCMs use the "capsules" to seal the material to avoid leakage. The encapsulated PCM capsules may be classified based on the diameter into: macro (>1 mm); micro (1-1000 μm); nano (< 1 μm). Macro-encapsulation PCM is a good choice to be applied to packed-bed system. In fact, in actual thermocline packed bed tanks, the particle size is generally above 10 mm considering both the preparation technique and application requirements [94]. However, the phase change time is mostly influenced by the relatively large capsule size of PCM [95]. Gao et al. [96] used the PCM spherical particle with a small size of 40 mm instead of 100 mm to achieve a higher heat transfer rate with a shorter phase change time. Wu et al. [65] decreased capsule diameter from 0.1 m to 0.02 m achieving the effective discharging efficiency from 73.78% to 98.33%.

2.3.2.5. Particle shape

Sensible fillers have including cylinder, sphere, cubic, rectangle or irregular shape, as shown in **Figure 2.8**. For the encapsulated PCM, the basic shapes are nearly the same, like spherical or cylindrical capsules [95]. The sphere shape shows highest the surface area than other regular shapes, facilitating heat exchange with the HTF. Moreover, increasing the surface roughness can increase the pressure drop [97]. The flow condition inside the tank correspondingly changes

when using particles with different shapes, resulting in different heat transfer behaviors between fillers and fluid.

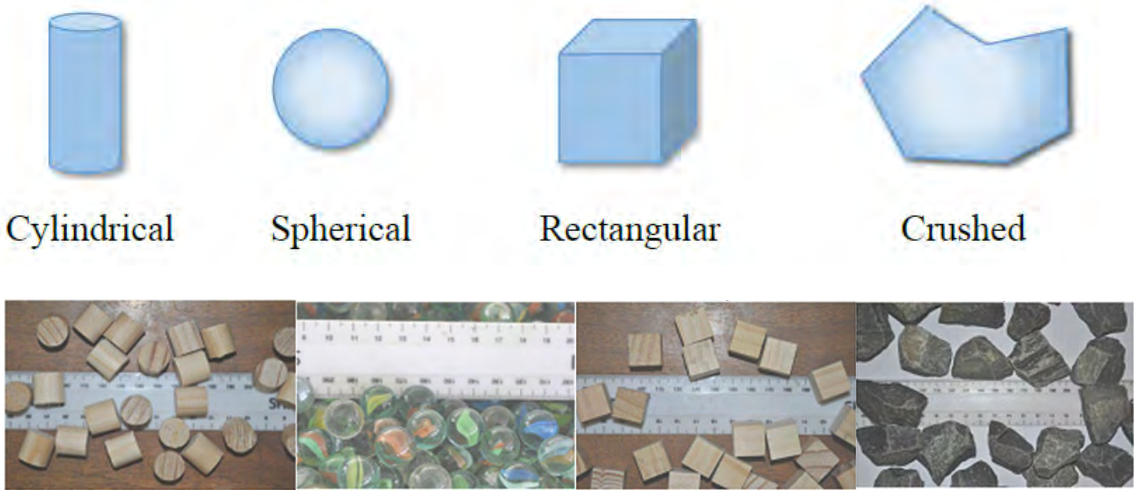

Figure 2.8: Different shapes for sensible material fillers: (a) cylindrical; (b) spherical; (c) rectangular; (d) crushed [98][97].

Obtained copyright permission of Elsevier [License No. 5207671070704, Dec 14, 2021]

2.3.2.6. Porosity and packing structure

Lower porosity means more packed bed region occupied by the solid fillers, usually resulting in a higher pressure drop [99][100][101]. Typically, the porosity is about 0.3-0.4 using uniform spheres [102] and about 0.22 by mixing two size particles [90][103][104]. Nevertheless, the porosity depending on arrangement is hard to be controlled in reality. Cárdenas et al. [105] tested the porosity for the regular sphere particles ranging from 0.660 to 0.259. It was found that the porosity was 0.395 for a hexagonal packing, higher than that of random packing (0.36). Thoenes and Kramers [106] tested the relationship between porosity and regular packing structure. Each cross section is exhibited in sphere center in one layer (**Figure 2.9**). The dense cubic packing in **Figure 2.9 a b** are identical but distinguish in orientation. The body-centered cubic particle packing in **Figure 2.9 f** is in structure but to random packing of spheres, spheres do not attach to each other and only single sphere in the next layer lies in a "pit" formed by four spheres. It was obtained the cubic particle packing structure that nine particles located in body-centered cubic position shows the highest porosity of 0.48 than other packing at the same particle diameter. But, Allen et al. [97] reported that the simple cubic packing was extremely unstable and shifted very easily while random arrangement of irregular-shaped particles was almost not isotropic.

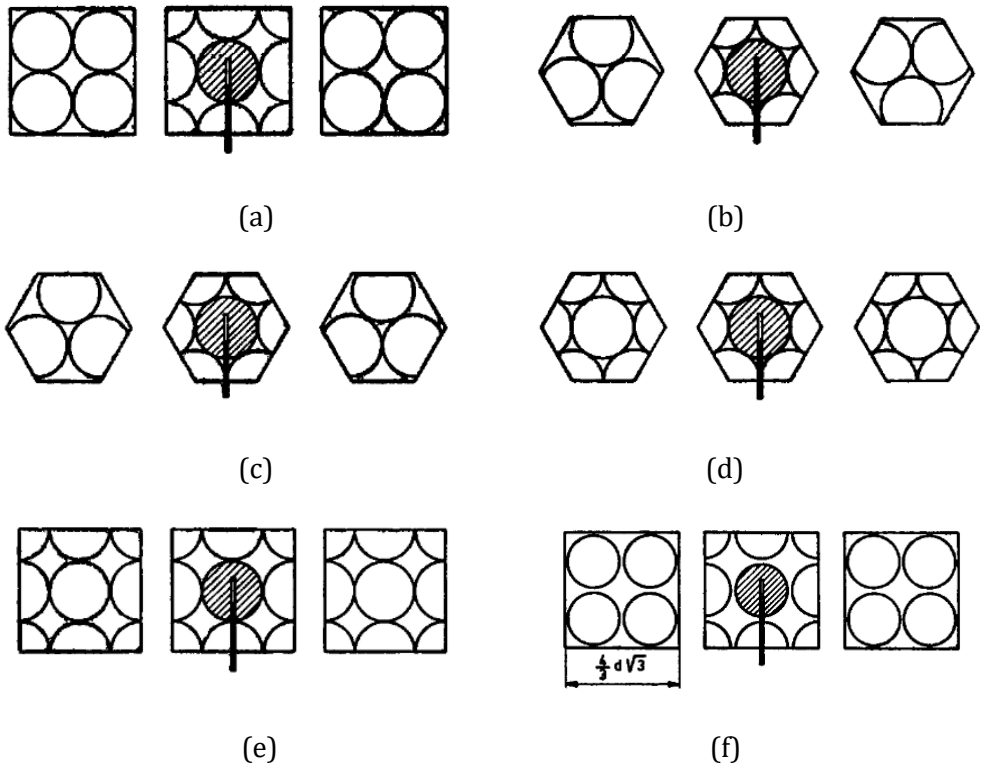

Figure 2.9: Cross section of sphere packing: (a) dense cubic, ε=0.260; (b) dense cubic, ε=0.260; (c) dense hexagonal, ε=0.260; (d) orthorhombic ε=0.395; (e) cubic, ε=0.476; (f) body-centred cubic, ε=0.320 [106].

2.3.2.7. Capsule shell thickness

PCMs can be well sealed in macro capsules using metal or plastic shell, as it shown in **Figure 2.5**. However, the thermal resistance of the shell may hinder the heat transfer process, resulting in slow PCM melting and solidification rate. Bellan et al. [107][108] found when the polymer shell thickness of PCM capsule increases around 66% from 1 to 3 mm, the charging time of storage tank is increased nearly by 15%. Zhang and Wang [109] proposed an optimal core-to-coating weight ratio (wt./wt.) of 75/30 rather than 75/25 for capsulated PCM to avoid the spillage. Therefore, decreasing shell thickness as soon as possible can achieve high heat transfer efficiency for PCM capsule designing, but the mechanical strength should also be considered.

2.4. Types of thermocline packed bed system

The classification of thermocline packed-bed TES system based on different criteria is exhibited **Figure 2.10**.

- According to the storage mechanism of fillers, thermocline packed-bed system can be divided into sensible-heat thermocline packed-bed (SHTPB), latent-heat thermocline packed-bed (LHTPB), and heterogeneous-heat thermocline packed-bed (HHTPB) combining sensible and latent.
- From system temperature range, it covers the low-temperature, e.g., domestic hot water heater, to the high-temperature application, e.g., CSP plant, reflected by the HTF and fillers.
- The layer packing structure is an optimization objective to achieve high performance in recent years.

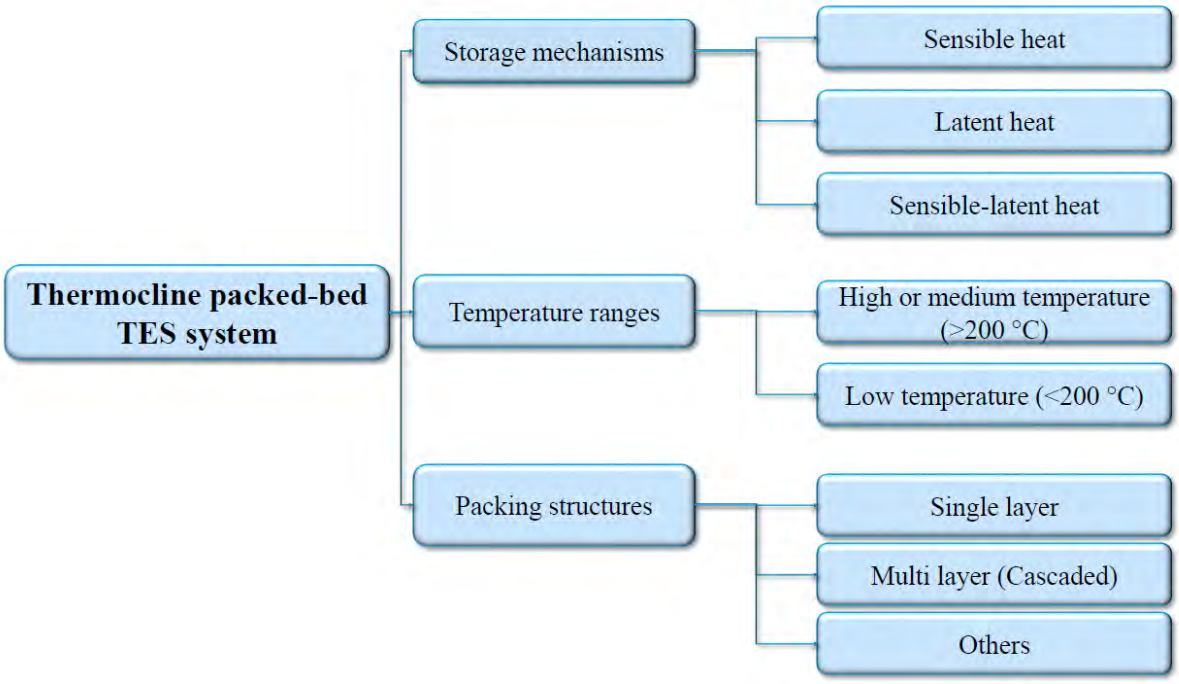

Figure 2.10: Classification of thermocline packed-bed TES system.

2.4.1. Sensible-heat thermocline packed bed (SHTPB)

Packing sensible heat material in full bed is a simple, mature, and cost-effective way for TES with a lot of commercialized applications.

2.4.1.1. Single-layered sensible-heat thermocline

Comparing to the commercial two-tank system, the single-layered dual-media thermocline system is cheaper. Mostafavi Tehrani et al. [110][70] reported that when integrating thermocline systems into a validated 19.9 MWe Gemasolar CSP plant, there is a 62% reduction of specific storage cost for a dual-media thermocline with sensible concrete media of 9.38 US$ kWh_{th}^{-1} compared to the two-tank molten salt system of around 24.5 US$ kWh_{th}^{-1} (**Figure 2.11**). In

addition, Strasser and Selvam [111] conducted cost analysis on two thermocline systems of 2165 MWh storage capacity, including a packed bed and a non-packed bed thermocline system. It obtained the thermocline packed-bed system of around 30 US$ kWh^{-1} is 12.5% costly lower than the structured-concrete thermocline system with axisymmetric and parallel-plate of around 34 US$ kWh^{-1}.

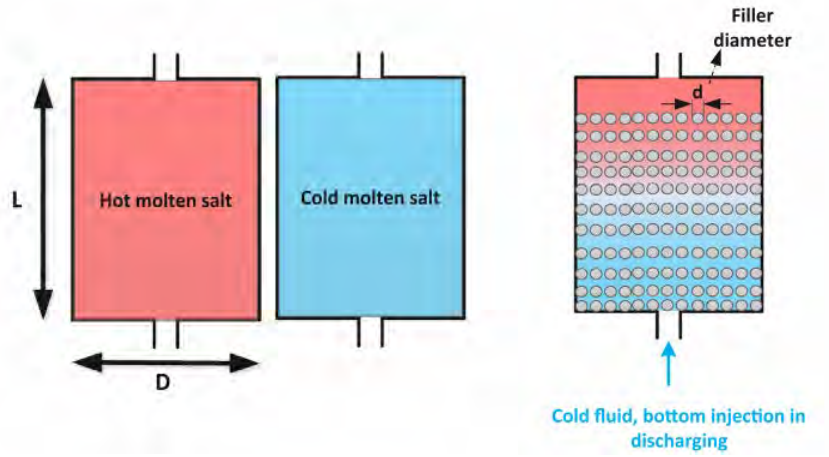

Figure 2.11: Different packing strategies of thermocline systems integrated into a 19.9 MWe Gemasolar CSP: (a) two-tank with specific storage cost of 24.55 US$ kWh_{th}^{-1}; (b) dual-media thermocline tank filled concrete with specific storage cost of 9.38 US$ kWh_{th}^{-1} [70].

For this type of single tank, designing the tank geometrical parameters, like tank height, tank shape, and inside fillers, to improve thermal performance is the main strategy once the solid filler material is determined.

For example, Yang and Garimella [91][112] studied the quartzite rocks (5 cm diameter) - molten-salt thermocline system with small particle Reynolds number (*Re*) from 1 to 50 and where the ratio of the tank height to the particle diameter was 10 to 800. They found the discharging efficiency that is the output energy to the total energy initially stored energy was enhanced with decreasing tank height and increasing *Re*.

Some works focus tank shapes, such as designing the truncated cone shape [113][114][115][116]. Zanganeh et al. [87] studied a 7.2 GWh_{th} rock tank with the varied cone angle. Increasing angle reduces effective storage volume but increases the final outlet temperature degradation in cycling during discharging, thus leading the overall storage efficiency above 95% (**Figure 2.12 a**).

Moreover, the special packing structure that mixes different fillers in one tank as the one-tank system was also investigated. Like, Yin et al. [117] used two representative porous fillers of zirconium ball and silicon carbide (SiC) foam in an experimental cylindrical tank. However, the mixed-filler thermocline system showed a declined effective heat storage capacity than single-phase molten salt thermocline tank due to the conflicts between the low volumetric heat storage capacity and the improved impact of porous structure on thermal performance (**Figure 2.12 b**).

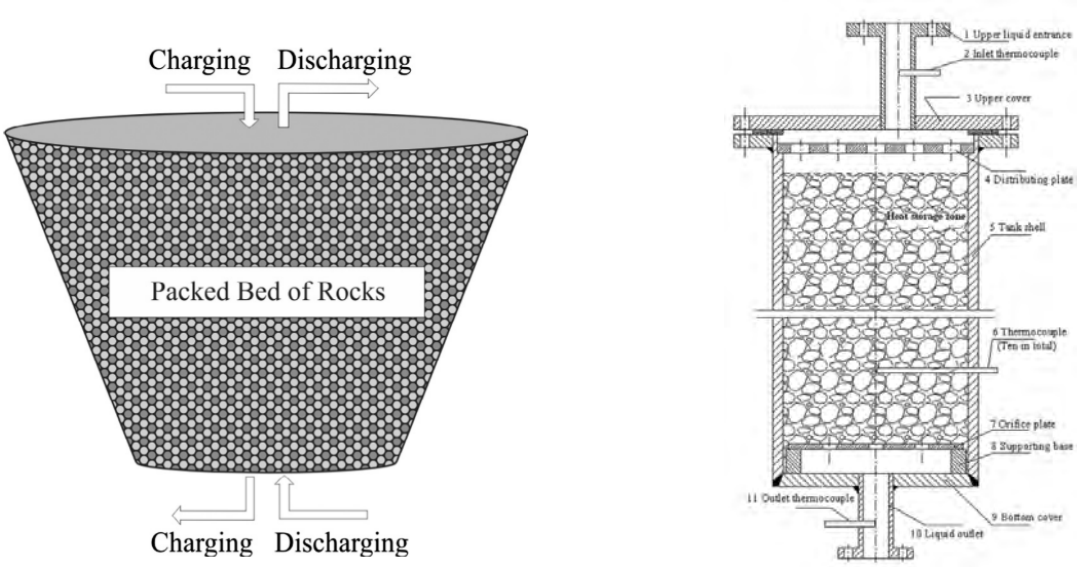

(a) (b)

Figure 2.12: (a) Scheme of 7.2 GWh_{th} single-layered truncated cone shape tank with 25 m tank height [87]. (b) The mixed-filler thermocline system with SiC foam and zirconium ball [117].

2.4.1.2. Multi-layered sensible-heat thermocline

For the multi-layered particle bed, it actually aims to the improvement on the thermal energy storage capacity and the stratification through filling materials into different layers. Relatively few studies have been devoted to multi-layered SHTPB tanks [118]. Some inspiring works still exist.

Crandall and Thacher [119] filled three layers of tank by the cast iron, copper, and rock to provide highest outlet temperature in discharging and the lowest outlet temperature in charging through the good stratification. The study showed that the cast iron with highest volumetric heat capacity at the inlet side in charging can maintain its temperature at low levels for an extended period. Li et al. [120] also put five sensible-heat storage materials in TES tank (**Figure 2.13**). Authors proposed a concept of the interface effect on thermocline, which refers to the enlarging or shortening effect at the interface between two types of filler on thermocline thickness. Once

HTF flows from one layer with slow thermocline expanding velocity to another one with fast expanding velocity, the thermocline thickness increases. Thus, the thermocline thickness can be controlled by filling different materials orderly with different volumetric heat capacities, vice versa.

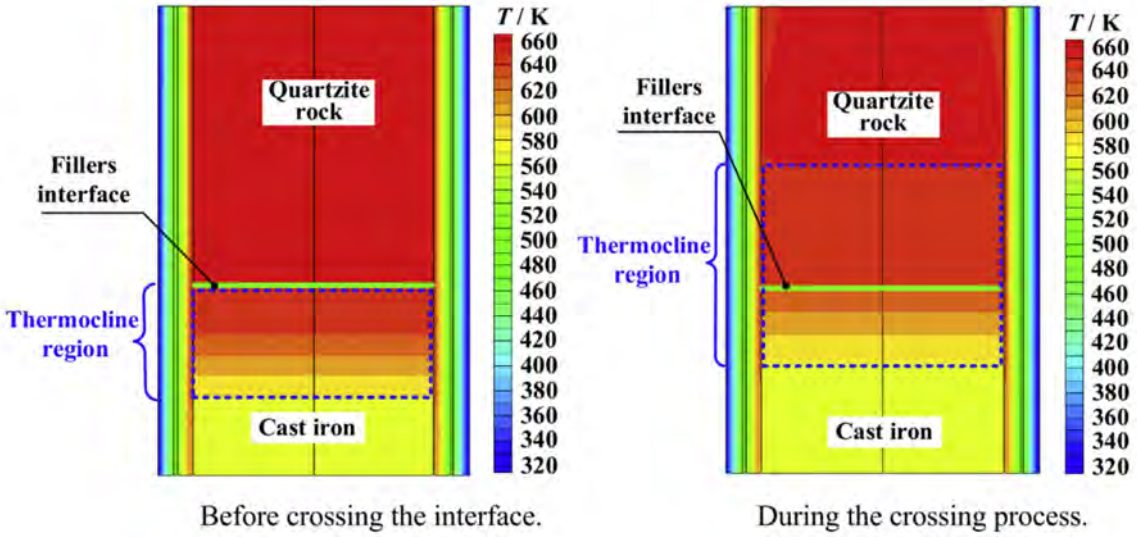

Figure 2.13: The multi-layered SHTPB system by filling quartzite cork at top layer and cast iron at the bottom layer: the expanding effect on HTF temperature distribution in charging process (5.9 m tank height, 3.0 m tank diameter, 0.04 m wall, 0.2 m insulation) [120].

2.4.2. Latent-heat thermocline packed bed (LHTPB)

Using PCM capsules as filler in TES system, the LHTPB can obtain much higher energy density than SHTPB and two-tank system [28]. In this sub-section, a summary of the "pure" TES verses "combined" TES in terms of material types, or single-layer thermocline versus multi-layer PCM thermocline system are presented. Various investigations carried out on LHTPB system for different temperature applications are listed in **Table 2.4**.

2.4.2.1. Single-layered latent-heat thermocline

There is a lot of works on basic thermal behavior investigation and efficiency enhancement for tank systems. Chen and Yue [121] developed a 1D model validated by experimental data to characterize the thermal performance of PCM capsules packed-bed system with air HTF. Their results presented that the lump model is a convenient and simple method to determine the thermal performance of cool storage systems. Another interesting attempt was conducted by

Rady [122] through the mixing of two or three kinds of PCMs and placing them in a packed bed to improve performance. Experiments on packed-bed column system were performed to obtain basic understanding of dynamic thermal behavior of the composite bed with different ratio of mixing materials. Authors found through determining the proper mixing ratio, the overall unit performance with multiple granular phase change composites could be enhanced by about 15% compared to the single material unit. An optimization strategy of the mixing ratio was determined according to the overall charging and discharging times and the exergy efficiency.

Many studies integrated this system into applications in different temperature ranges.

For low-temperature ranges, a single-layered LHTPB system has been applied and shown advantages of high security and easy operation for hot water or air condition system. Arkar et al. [74] interagrated the low-temperature LHTPB system in a ventilation system of a building, which is able to cut down the volume of the mechanical ventilation system with a better thermal comfort. Li et al. [123] demonstrated the optimal design of PCM storage tank for the outdoor open-air swimming pool during daytime operation in the City University of Hong Kong. This case can meet the enviroment temperautre comfort demand and achieve the economic operation (**Figure 2.14**).

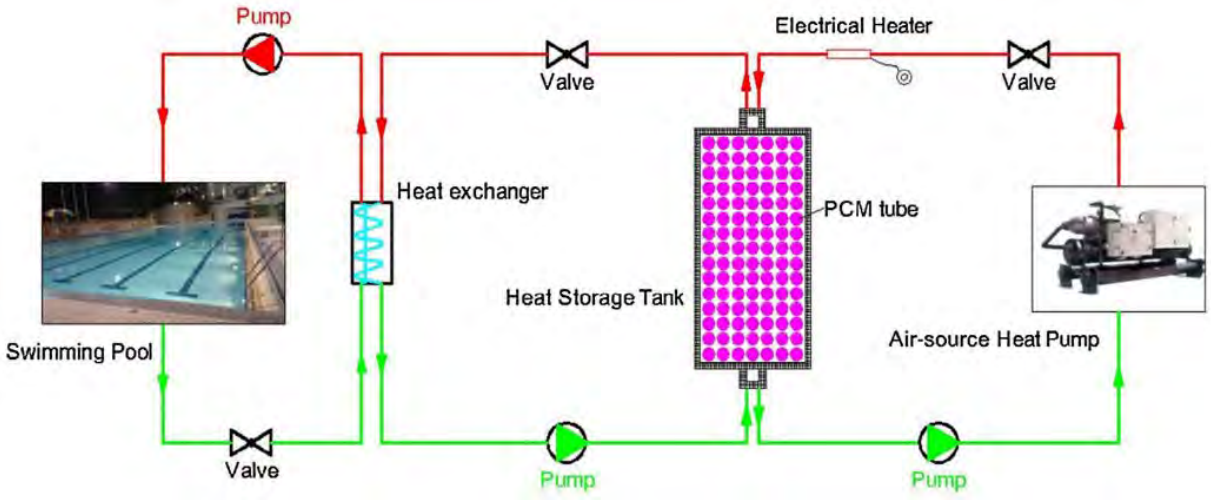

Figure 2.14: Schematic of the outdoor open-air swimming pooling system with PCM packed bed system in City University of Hong Kong [123].

Obtained copyright permission of Elsevier [License No. 5207680984690, Dec 14, 2021]

For high-temperature ranges, Flueckiger and Garimella [36] replaced the single-layered LHTPB system the conventional rock filler inside the tank in CSP. It found that the annual storage yield or plant output of the thermocline system could not be increased compared to a conventional rock-filled tank of equal size. A multiple filler structure consisting of cascaded PCMs with adjusted melting temperatures along the tank height should be designed, which will be introduced later.

In another study, the cost of this tank type was investigated. Li et al. [124] compared the two-tank, sensible-, and latent-heat packed-bed systems coupled with a supercritical carbon dioxide (S-CO_2) Brayton cycle. It was found that the sensible packed-bed tank had the smallest stored thermal energy due to the influence of the expanded thermocline thickness. The latent heat storage system showed the highest stored energy and effective discharging time. Moreover, the power cycle performance by integrating the latent packed-bed had the largest total work output with the lowest capital cost (37 US$ kWh_{th}^{-1}) compared to two tank (54 US$ kWh_{th}^{-1}) and sensible filler (52 US$ kWh_{th}^{-1}) concepts. That is because the vessel cost of tank were reduced a lot accoding to the definition of capital cost including thermal storage materials cost, vessel cost, and other costs.

2.4.2.2. Multi-layered latent-heat thermocline

The intention of multi-layered (or cascaded) LHTPB system is cascading PCMs in sequence of increasing phase change temperature in axial direction from bottom to top of packed bed, to harvest more heat by taking advantage of the temperature difference under the same flow velocity condition. In more detail, in single-layered system (charging for example), the hot HTF flows from the top to the packed-bed bottom and with decrease temperature due to the extracted heat from PCM storage media. The heat transfer rate near the bottom region of the tank would therefore be low since it is directly proportional to the temperature gap between HTF and PCM media, conversely in discharging.

To further enhance the heat transfer, it is a possible way to pack the tank by selecting the PCMs with different phase change temperature according to the HTF temperature distribution along the tank in axial direction [125]. More importantly, the PCM phase change process should be constrained within the require temperature of charging/discharging to stablize the outlet temperature. Commonly, the PCM with high melting temperature should be placed at the top of the tank, while the PCM with low melting temperature can be at the bottom to form a temperature gradient along tank height. Felix et al. [58] proposed that the complete melting time for the PCM bed system with a phase change temperature range, is faster than the system with a fixed phase change temperature.

Better thermal performance of this multi-stage concept has been proved in some packed-bed systems [126], no packed-bed systems with PCM modules [127][128][129], or multi-layered shell-tube filled systems [10][130]. **Table 2.5** lists the studied multi-layered LHTPB systems in the literature and their corresponding design parameters.

Yang et al. [60] developed a multi-stage LHTPB system evenly filled by three layers of PCMs. In contrast to the conventional single-layered PCM packed bed, the multi-layered system shows

higher energy and exergy efficiencies. Elfeky et al. [59] analyzed a three-stage LHTPB system (**Figure 2.15 a**) for CSP plant by using concentric-dispersion model (cf. Chapter 3 or 4 for detailed description of models). Their results proved that the three-stage PCMs unit with different phase change temperatures could achieve higher energy and exergy efficiencies in the cycling process than the single-stage system. This concept can also enhance the heat transfer rate and reduce the required heat storage time significantly. The influence of the phase change temperature on thermal performance of the storage tank was further evaluated. Results showed that an optimal three-layer cascaded thermocline tank should be constituted when the dimensionless phase change temperature is equal to 0.8 for the top, 0.5 for the middle, and 0.35 for the bottom PCM layer, respectively [131][132]. That dimensionless phase change temperature is based on the inlet temperature during charging/discharging.

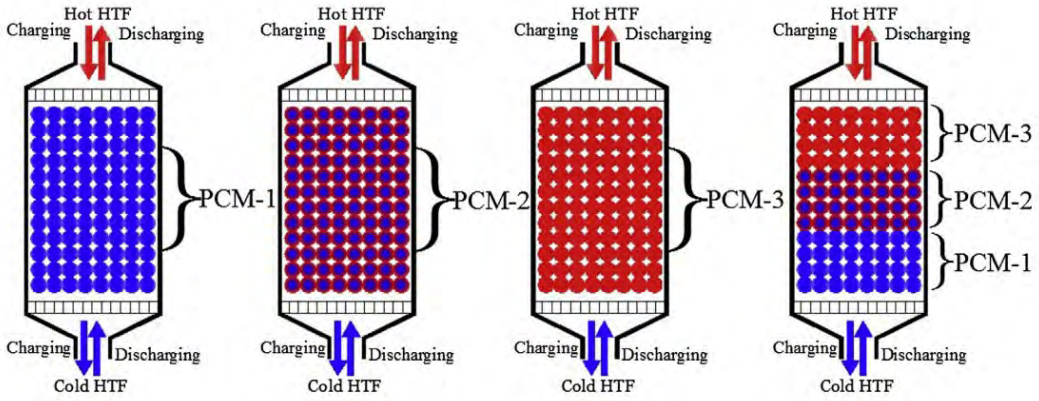

(a)

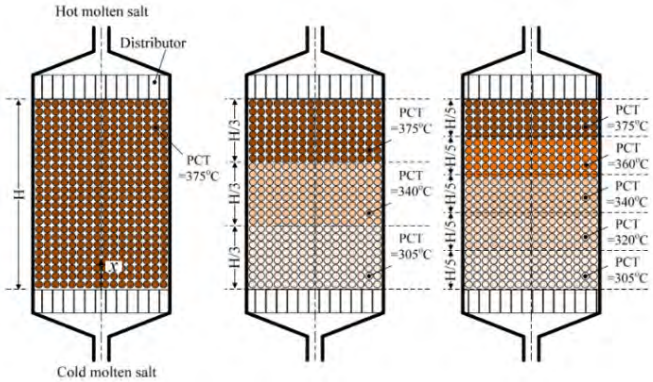

(b)

Figure 2.15: Multi-layered concept of LHTPB system: (a) 1-3 cascaded systems [59]; (b) 1-5 cascaded PCM systems (PCT: phase change temperature) [133].

Obtained copyright permission of Elsevier [License No. 5207681128925, No. 5207681314417, Dec 14, 2021]

Chirino et al. [133] conducted parametric study and sensitivity analysis under different operational parameters on a three-stage LHTPB system for a 60 MWe CSP. It is obtained under the same tank volume condition, the sensitivity as a function of the thermal energy storage efficiency by changing tank diameter alone is double than that from changing tank height. Their results also revealed that the thermocline thickness could be increased and the efficiency decreased due to the natural convection in the tank.

The number of PCM layers is also a parameter of optimization analyzed in some investigations. For example, Wu et al. [134] investigated the influence of cascaded number (3 or 5 layers of PCM) on this type of system (**Figure 2.15 b**). Their results showed that a higher cascade number could result in faster charging and discharging rates. The actual store capacity of this type of system relays deeply on the threshold (or cutoff) temperatures for charging or discharging process.

2.4.3. Heterogeneous-heat thermocline packed bed (HHTPB)

The features and limitations of SHTPB and LHTPB systems have been comprehensively compared in the literature [135][30][21]. SHTPB is commercially available by using cheap raw materials and well-studied by researchers. The main shortcomings are the low volumetric storage capacity and the temperature degradation at the end of dis-/charging cycles [136][137]. LHTPB is regarded as more promising owning to its high energy storage density and the unique characteristic of PCM, such as the relatively constant phase change temperature, but with a much higher cost [138][135].

The concept of HHTPB is proposed in order to reduce the amount of PCM fillers as well as to achieve the stable thermal behavior. This type of system, also called “combined” or “hybrid” sensible-latent TES system, can incorporate the advantages and cope with the techno-economic issues experienced by the LHTPB and SHTPB systems [139][140][141][142]. **Table 2.6** lists the present multi-layered HHTPB systems and their corresponding design parameters.

There are several works focusing on stabilizing the outlet HTF temperature. Galione et al. [143][57][142] conducted a series works and designed the multi-layer solid-PCM thermocline tanks for CSP plants. Two PCM layers acted as thermal buffers were respectively put at the top and bottom of the tank, whose phase change temperature were selected to control the outlet temperature within an admissible interval. Compared to other concepts introduced above, the novel multi-layered solid-PCM system can achieve high overall energy storage capacity as well as excellent thermal efficiency. Such strategies for different given cases are shown in **Figure 2.16**.

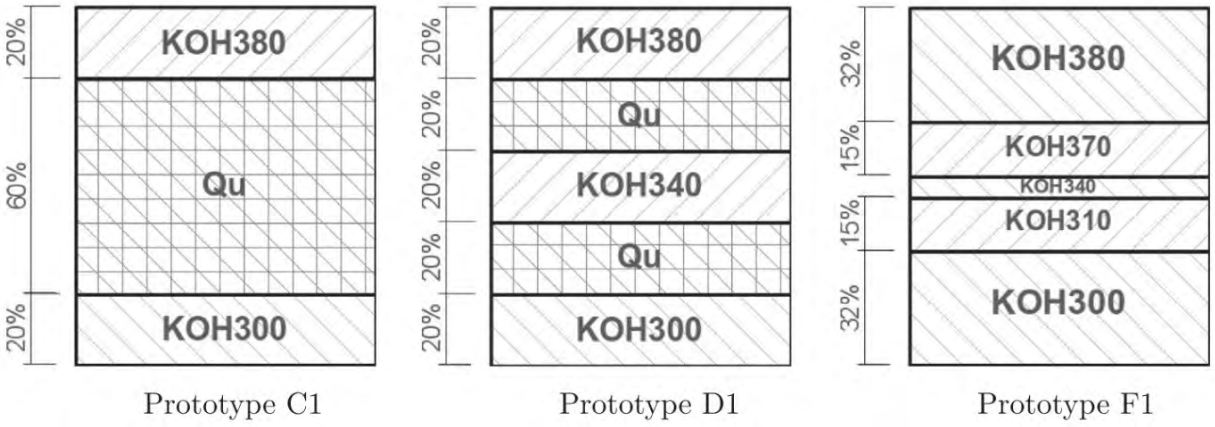

Figure 2.16: Scheme of the multi-layered solid-PCM of three configuration cases, C1: KOH380-Quartzite and rock (Qu)-KOH300 (20-60-20 v%), D1: KOH380-Qu-KOH340-Qu-KOH300 (20-20-20-20-20 v%), F1: KOH380-KOH370-KOH340-KOH310-KOH300 (32-15-6-15-32 v%) [142].

For example, Zanganeh et al. [63] designed and developed a 42 kWh_{th} pilot-scale TES for CSP application by placing the PCM section on top of the rocks. $AlSi_{12}$ with a phase change temperature of 575 °C was encapsulated in stainless steel tubes. Experimental and numerical analysis proved this "rocks+PCM" system could stabilize the outflow air temperature around the melting temperature of the PCM [144].

Zhao et al. [28][145][140] had performed a series of works on the designed thermocline TES system for CSP plants. Two different PCMs (high- and low- phase change temperature) were installed at the top and bottom position of the tank, respectively, cheaper solid being put in the middle. Their results highlighted the advantage of this concept, in term of cost, to meet various cyclic operating time durations than other systems, especially with a smaller packing thickness of PCM layer [28]. The corresponding performance has been optimized by selecting less lower cutoff temperatures to enhance the utilization rate from economic and operational aspects [83]. Its application has also been extended to a 200 MWe hybrid nuclear-solar power system for on-demand power supply [141] .

Abdulla and Reddy [146] compared the multi-layered HHTPB (PCM-rock-PCM) system with the single-layered rock media system. The improved HHTPB concept with PCM on the top and bottom 10% height of the tank showed longer discharge time for storing more energy. When the PCM width increases from 0 to 50%, the tank height decreases by around 50%. Thus, the cost associated with tank material, installation, maintenance, and operating could be significantly saved. However, the study of Liao et al. [84] showed that with extra PCM capsule layer, the

capacity ratio and the charging/ discharging time of the storage tank could be increased only when a special cutoff temperatures for the cycling processes were chosen.

In addition, Ahmed et al. [139] developed and compared three concepts of thermocline packed-bed storage tanks for mixing configuration: sensible rod structure (**Figure 2.17 a**), and spherical PCM capsules (**Figure 2.17 b**) and combined sensible-latent in radial direction (**Figure 2.17 c**). The effective discharging efficiency and capacity costs were estimated to be 95%, 87%, 76% and 42, 37, 35 US$ kWh^{-1}, respectively. The HHTPB concept showing optimized performance, comparatively cheaper cost, and a relatively constant HTF outlet temperature seem to be a more viable option among others.

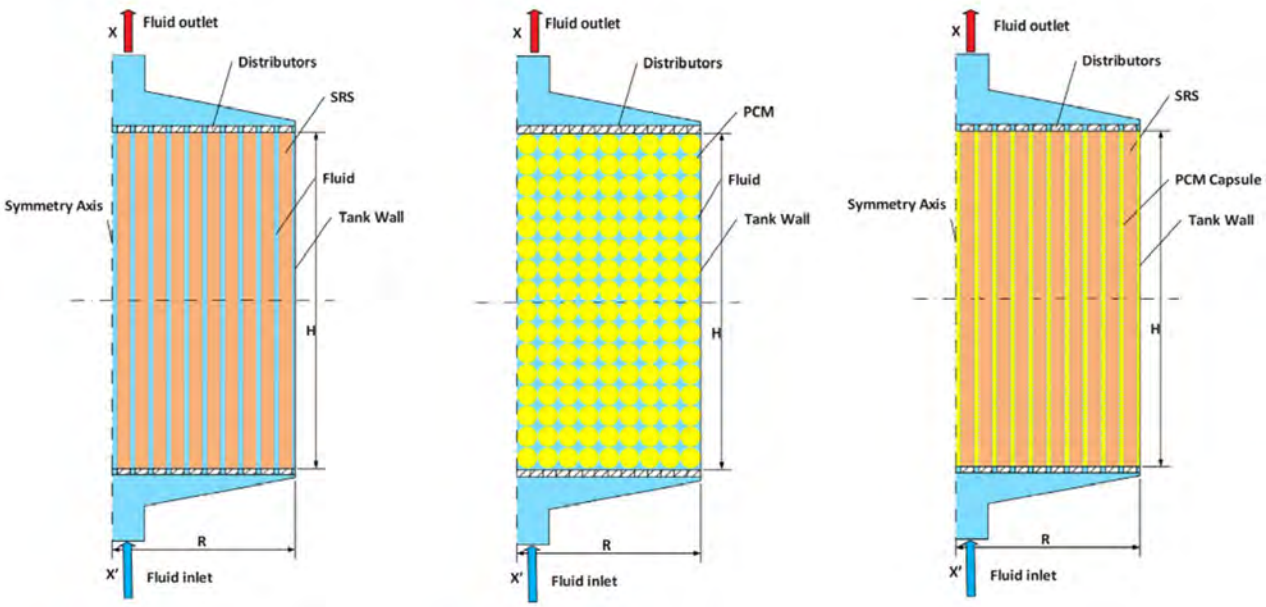

(a) (b) (c)

Figure 2.17: Scheme of three kinds of TES packing configurations: (a) sensible rod structure configuration, SRS; (b) encapsulated PCM configuration; (c) hybrid sensible rod structure and encapsulated PCM configuration [139].

2.4.4. The interests of packing configuration

Low economic investment and high system efficiency are two goals for system. Given those, the interest in designing configuration is to achieve higher system efficiency despite using the same amount of fillers and HTF. It should be noted that, the optimal configuration does not always get the highest thermal performance when operational changes.

Thus, this thesis is intended to design or optimize the packing configuration of thermocline packed system by using sensible heat or latent heat filler in layer structure.

2.5. Chapter conclusion

This chapter summarizes the development of the thermocline packed-bed tank for TES system. The storage material types, the influencing factors, and the state-of-art of tank concepts are overviewed. **Main conclusions** could be listed as follows.

- Good quality of thermocline reflects good thermal performance of packed-bed TES system. The objective is to maintain a stable and sharp stratification zone for high energy capacity ratio, thermodynamic efficiency, and proper operational time. High thermal performance of thermocline packed-bed tank with stable thermal stratification can be achieved by careful selection and determination of geometrical (packing), operational and thermophysical parameters.
- Based on storage materials, there are generally three types of thermocline packed-bed tanks, sensible-heat, latent-heat, heterogeneous-heat, with different packing structure and operating parameters. Sensible-heat system is cost-effective and commercial mature but has the problem of outlet temperature "decay" in cycling. Latent-heat system shows high energy density and stabilize outflow temperature but the PCM cost is also relatively higher than sensible fillers. The heterogeneous-heat system can combine characterizations and advantages of the former types, thus will have a bright foreground.
- Influence factors of operational, geometrical, and thermophysical parameters shows positive or negative on thermocline packed-bed system due to the complicated heat diffusion, heat convection, and hear transfer in charging/discharging cycling process. The useful/harmful impacts are need to be accounted and clarified and the trade-off between parameters still needs to be optimized.
- Packing configuration is a solution for efficiency improvement the thermal performance. Multi-layered structure (single-layered, multi-layered) and storage media are designed elements for configuration. Among them, packing PCMs in a multiple layer manner with different melting temperature along the axial direction of the tank can cause a large temperature gap between solid and fluid in charging/discharging process.

Some scientific and technological barriers remain to be overcome for the widespread industrial application of thermocline packed-bed storage systems, which are also the key issues and challenges of the current research and development.

1) improving stratification quality and stability of thermocline for high thermal performance in the operational process.

2) achieving benefits maximization of thermal efficiency, loading capacity, and economic cost of system under various parameters.

3) splitting the technology as a commercial one into wide applications like the low-temperature built environment.

Table 2.4 Single-layered PCM packed bed TES systems.

Literatures	Years	$H/D/W$ (m)	T_C/T_H (°C)	D_p (mm)	ε	PCMs	Filler shapes	Packings	HTFs	Flow rates	Exp./ Num.	Validation cases
Chen and Yue [121]	1991	0.260/0.100/0.005	0/25	34	0.36-0.61	Water	Sphere	Horizontal	Air	2-5 L min^{-1}	Exp./ Num.	Designed setup
Arkar et al. [74]	2007	1.52/0.34/--	<36	50	0.388	Paraffin	Sphere	Rhombic	Air	--	Exp./ Num.	Designed setup
Rady [122]	2009	0.200/0.045/0.0025	15/50	1.0-3.0 (~89.5%)	0.42	Rubitherm GR27 (21-29 °C); Rubitherm GR41 (31-45 °C)	Granule	Random	Air	0-130 L h^{-1}	Exp./ Num.	Designed setup
Flueckiger and Garimella [36]	2014	18/21/--	300/600	--	--	--	--	--	Molten salt	0.436 mm s^{-1}	Num.	[104]

Table 2.5 Multi-layered PCM packed bed TES systems.

Literatures	Years	$H/D/W$ (m)	T_C/T_H (°C)	D_p (mm)	ε	Layers	PCMs & T_m	Packings	HTFs	Filler shapes	Flow rates	Exp./ Num.	Validation cases
Yang et al. [60]	2014	0.69/0.36/--	32/70	55	0.84	1-3	Paraffin wax: (60-62 °C) (50-52 °C) (42-44 °C)	PCM1-PCM2-PCM3	Water	Sphere	2 L min^{-1}	Num.	[147]
Wu et al. [134]	2016	14/4.9/--	290/390	40	0.25	1-5	Molten salt: C1(375 °C) C2(360 °C) C3(340 °C) C4(320 °C) C5(305 °C)	PCM1-PCM2-PCM3-PCM4-PCM5-	Molten salt (60 wt% $NaNO_3$-40 wt % KNO_3)	Sphere	--	Num.	[65]
Elfeky et al. [59]	2018	7.3/10.6/--	288/565	26.53	0.22	1-3	Molten salt: (382.1 °C) (439.8 °C) (505 °C)	PCM1-PCM2-PCM3	Molten salt (60 wt% $NaNO_3$-40 wt% KNO_3)	Sphere	84.5175 kg s^{-1}	Num.	[148]
Chirino et al. [133]	2019	30/10/--	350/550	40	0.3	1-3	PCM: (380 °C) (435 °C) (496 °C)	PCM1-PCM2-PCM3	Molten salt (7.5 wt% NaCl-24 wt% KCl-69 wt% $ZnCl_2$)	Sphere	1058.2 kg s^{-1}	Num.	--

Table 2.6 Multi-layered sensible-PCM packed bed TES systems.

Literatures	Years	*H/D/W* (m)	T_C/T_H (°C)	PCM fillers				Sensible fillers			Packing	HTFs	Flow rates	Packing	Exp./Num.	Validation cases	Storage capacity
				Materials	D_p (mm)	ε	Filler Shapes	Materials	D_p (mm)	ε							
Galione et al. [143]	2014	6.1/3.0/--	290/390	KOH	15	0.22	Shpere	Quarzite rock-sand		0.22	PCM-S-PCM*2	Molten salt	5.54 kg s^{-1}	Random	Num.	[104]	--
Zanganeh et al. [63]	2015	0.168/0.400/0.003	25/700	AISI 316 stainless steel tubes & $AlSi_{12}$ for PCM	18	0.55	Tubes	Rock	32	0.4	PCM-S	Air	~0.015 kg s^{-1}	PCM arranged in 4 rows	Exp./Num.	Designed setup	42 kWh_{th}
Zhao et al. [28]	2016	14/32-44/--	288/570	Top layer: 20 v% Li_2CO_3-60 v% Na_2CO_3-20 v% K_2CO_3, Bottom layer: 60 v% $NaNO_3$-40 v% KNO_3	10	0.34	Shpere	Quarzite rock-sand	19.05	0.22	PCM1-S-PCM2	Molten salt (60 wt% $NaNO_3$-40 wt %KNO_3)	--	Uniform	Num.	[104] [147]	250 MW_t
Abdulla and Reddy [146]	2017	12/14.38/--	290/390	Top layer: PCM380*1 Bottom layer: PCM300*1	35	0.35	Shpere	Rock	33	0.22	PCM1-S-PCM2	Molten salt (60 wt% $NaNO_3$-40 wt %KNO_3)	0.000574 m s^{-1}	--	Num.	[147]	100 MWh
Liao et al. [84]	2018	10/6.5/--	20/650	$AlSi_{12}$	200	0.40	Shpere	Rock	0.2	0.4	PCM-S-PCM	--	30 kg s^{-1}	--	Num.	[48]	>100 MWh (only rocks)

Chapter 3

Thermocline packed-bed thermal energy storage system under wall impact

Abstract

As introduced in last chapter, tank wall and the insulation layer may affect the thermal stratification and cause thereby the thermocline degradation, which issue has not yet been fully addressed in the literature. **This chapter tried to** fill this research gap by exploring the effect of wall thermal properties and heat loss on thermocline thermodynamic behavior of packed-bed tanks with the aim of their efficiency improvement. Meanwhile, this is the premise of accurate optimization simulation for next work. The contents of this chapter contains:

- Develop and fully exploit a transient numerical model considering wall impact.
- Compare two tank configurations: a high-temperature pilot-scale tank with a steel wall and a low-temperature lab-scale tank with a polycarbonate wall, to find the wall impact applicability.
- Quantify the stored energy in wall and insulation at steady condition, and evaluate wall impact on thermocline evolution and system efficiency under dynamic condition.
- Propose an optimal wall design guideline for different industrial applications.

Keywords: wall impact, thermocline thickness, heat loss, lab-scale tank, pilot-scale tank, 1D-3P model

This chapter is published as:

Xie B, Baudin N, Soto J, Fan Y, Luo L. Wall impact on efficiency of packed-bed thermocline thermal energy storage system. Energy 2022;247:123503.

Chapter content

3.1. Introduction

Wall heat impact is a heat transfer phenomenon that the heat transfer fluid (HTF) in near-wall region appears to be overheated/overcooled than that in central tank region due to various factors, including the heat loss from storage tank to ambient, the stored/released wall energy in charging/discharging and the different void fraction in near-wall region compared to the center. It is regarded to be responsible, to some extent, for the thermocline decay or instability and thus the reduced efficiency of the thermal energy storage (TES) system.

3.1.1. Wall impact on thermocline packed bed: the state-of-art

Various studies have been done to investigate the wall impact or boundary conditions in packed-bed TES tanks [149]. Argo and Smith [150] conducted fundamental research on the effect of convective boundary layer in wall region on the temperature distribution of packed beds. By testing and comparing the temperature profiles in core region and near-wall region of a packed-bed tank with gas flow, their results showed that a temperature drop in near-wall region occurred. Chang et al. [114] further investigated the effect of physical boundary conditions including insert liner and sloped wall on the thermal performance of thermocline storage system by analyzing the entropy generation. It was observed that the thermocline thickness was larger and much more fluctuated in the near-wall region along the tank height than that in the center of the tank under the insert liner boundary condition. De Beer et al. [151] studied the influence of wall effects on the effective thermal conductivity in the near-wall region at different temperature levels and with different packing structures. A notable reduction of the thermal effective conductivity of the bed that separated into the inner and outer regions was found and the influence was more significant at high temperature. In summary, such wall effects are mainly caused by unevenly distributed fluid flow in the near-wall region, which can though be ignored/alleviated at low Reynolds numbers (Re) or using the effective bed thermal conductivity [152].

Another class of studies in the literature has focused on the heat loss and the stored/released heat in tank wall as well as in the insulation layer. Commonly three boundary types with increasing complexity have been used: (1) adiabatic boundary; (2) non-adiabatic boundary with heat loss and (3) non-adiabatic boundary with heat loss and with stored heat. The adiabatic/non-adiabatic

boundary condition was usually adopted to simplify the model when heat loss to ambient was negligible or could be calculated using an overall wall heat transfer coefficient. For example, Yang and Garimella [112] compared the adiabatic and non-adiabatic boundary on the thermocline performance. It was found that the heat loss under non-adiabatic boundary distorted the flow temperature distributions, but such influence became insignificant at large flow *Re*. The discharge efficiency of the thermocline tank was found to increase with the increasing *Re*, opposite to the trend under adiabatic condition. Mira-Hernández et al. [153] reported that the heat loss under non-adiabatic condition could cause inhomogeneous internal flow for the whole tank due to the cooling of molten salt near the tank wall. But the total heat lost during charge/discharge the cycle was estimated to be negligible compared to the heat storage capacity.

Nevertheless, when the wall volume (or mass) constitutes a large proportion of the whole storage system, the heat capacity of tank walls (including the insulation) has to be taken into account by adding the energy equation. In this regard, Beasley and Clark [154] have developed a 2D transient response model of both solid and fluid phases that includes the effects of longitudinal conduction, the stored heat in walls and the heat loss, with air as the working fluid. But the solid internal heat conduction term was neglected in this model. Xu et al. [41] developed a 2 dimension-2 phase (2D-2P) model with energy equations for the insulations and tank steel wall, and studied the effect of insulation on the thermocline behavior in a hypothetical high temperature utility-scale tank (14 m in height). Their results showed that the increased insulation thickness could form a uniform temperature in the cross-section even through the temperature of HTF (molten salt) near the wall could be slightly influenced by the wall temperature. Hoffmann et al. [155] further proposed a model with three governing equations considering the wall as a third component in addition to solid and fluid phases. Their model, validated in different size tanks with liquid HTF, showed that the tank walls and the heat loss had a direct influence on the HTF outlet temperature for a pilot-scale tank. However, the radiative loss from the outer tank surface and the thermal resistance of the wall was not considered in their modeling. **Table 3.1** summarizes main features of previous studies on the issues of wall impacts in thermocline packed-bed TES systems.

Table 3.1 Studies of walls impacts on thermocline packed-bed system.

Studies	Year	Dimensions (Fluid/Solid/ Wall)	Exp. /Num.	Wall impacts			Main findings
				Heat loss from wall to ambient (Yes/No)	Wall energy storage (Yes/No)	Near wall void fraction singularity (Yes/No)	
Beasley and Clark [154]	1984	2D/1D/1D	Exp./ Num.	Yes	Yes	Yes	● Effects of void fraction near the wall, wall heat capacity, and wall energy losses on dynamic response are identified.
Yang and Garimella [112]	2010	2D/2D/--	Num.	Yes	No	No	● Heat loss for non-adiabatic boundary distorts the flow temperature distributions, but such influence becomes insignificant at large flow rate (Re>250).
Xu et al. [41]	2012	2D/2D/2D	Num.	Yes	Yes	No	● Insulation tends to reduce temperature difference in the cross-section of tank.
Bellan et al. [108]	2014	2D/2D/--	Num.	Yes	No	No	● Heat loss through the wall increases with the decreasing insulation layer thickness, which is less than 1% of the inlet energy at a steady state.
Opitz and Treffinger [156]	2014	(1D,1D)/(1D, 1D)/--	Num.	Yes	No	Yes	● A general heterogeneous model with two zones mean void fraction is from in the cross-section is developed and validated.
Mira-Hernández et al. [153]	2015	2D/2D/--	Num.	Yes	No	No	● Heat loss under non-adiabatic conditions causes thermal-buoyancy-induced flow non-uniformities. ● Total heat loss during the cycle is negligible compared to the heat storage capacity.
Chang et al. [114]	2016	2D/2D/--	Num.	Yes	No	No	● Thermocline thickness is much more fluctuated in the near-wall region along the tank height than that in the center of the tank.
Cascetta et al. [157][148]	2016	2D/2D/--	Exp./ Num.	Yes	Yes	Yes	● Wall influences the radial temperature profile and the amount of the stored energy.
Hoffmann et al. [155]	2016	1D; 1D/1D/1D (No wall heat radiation)	Num.	Yes	Yes	No	● 1D-1P model is faster but another model integrated different phases of fluid, solid, and wall is more accurate. ● Over 5% of the energy storage capacity, the wall needs to be considered.
Fernández-Torrijos et al. [158]	2017	1D/1D/2D	Num.	Yes	Yes	No	● With a wall Nusselt number (Nu) of about 102, an optimum value of fluid flow rate can maximize the overall energy efficiency and minimize the steel shell stress.
ELSihy et al. [159]	2021	2D/2D/2D	Num.	Yes	Yes	No	● Employing heat loss boundary condition causes a faster temperature drop of the HTF near the tank wall, forming a temperature gradient.
This study	2022	1D/1D/--; 1D/1D/2D; 1D/1D/1D;	Num.	Yes	Yes	No	● Wall impact comparison on two different scale tanks. ● Wall impact on thermocline behavior. ● Wall parametric studies to provide wall design guideline.

3.1.2. Aim and scope

The above literature survey indicates that even though previous works investigated the influence of non-adiabatic boundary on the thermal performance of thermocline packed-bed tank, the research gap still exists in the following points. **Firstly**, the effects of wall thermal properties on the dynamic thermocline behavior are not fully addressed. The total amount of stored heat in the wall (and insulation) phase and its influence on the efficiency of the storage tank need to be further evaluated as well. **Secondly**, besides the large-scale thermocline tanks applied to concentrated solar power (CSP) plants at high temperature, thermocline tanks are also frequently used for waste heat recovery at medium temperature or for buildings at low temperature. For these applications, the size of the storage tanks is relatively small thus the tank wall and the insulation could occupy a relatively large volume ratio compared to the packed-bed region. It is thereby essential and necessary to explore wall impact on different size tanks to acquire a better understanding of system operation, especially the wall parameters. **Thirdly**, the trade-off between conflicting requirements that models correspond to different levels of detail and different calculation times has been rarely reported in the literature. Choosing a proper model to do such wall parametric study is equally important towards an optimal wall design for packed-bed TES tank.

In order to fill the above-mentioned research gap, the present study aims at developing adapted transient model(s) with balanced complex physical phenomena description and computation time to systematically explore the wall impact on the dynamic thermocline behavior of the packed-bed storage tanks. Main objectives of this study are as follows:

-- to comprehend the impact of the wall thermal properties on the heat loss and on the thermal performance of thermocline packed-bed storage tank with different sizes and under different working temperatures;

-- to identify the most influencing factors through the parametric and sensitivity analyses in order to provide design guidelines for thermocline packed-bed tank.

3.2. Methodology

3.2.1. Geometrical model

- **Storage tank structure**

A typical structure of thermocline packed-bed TES tank and the computational domain are illustrated in **Figure 3.1**. It is a vertical cylindrical tank with solid particles as heat storage medium to form the packed-bed thermal storage region. The HTF flows in void space of the region, the void fraction or porosity ($\varepsilon = \frac{V_b - V_s}{V_b}$) of packed-bed [65]. The packed-bed cylindrical tank has an inner wall to form the tank and an outer insulation to prevent heat loss. These two layers constitute a composite wall called 'tank walls' in the following text. Furthermore, the inlet and outlet ports are openings at the top and bottom of the tank, allowing HTF to flow in and out the tank.

- **Charging/discharging operation**

In charging or thermal storage stage, the hot HTF at T_H flows into the TES tank from the top port to transfer heat to low-temperature solid medium, and then flows out from the bottom port. Conversely, in discharging or energy on loading, the cold HTF with T_C enters from the tank bottom to absorb heat from high-temperature solid media and flows out of tank from the top port.

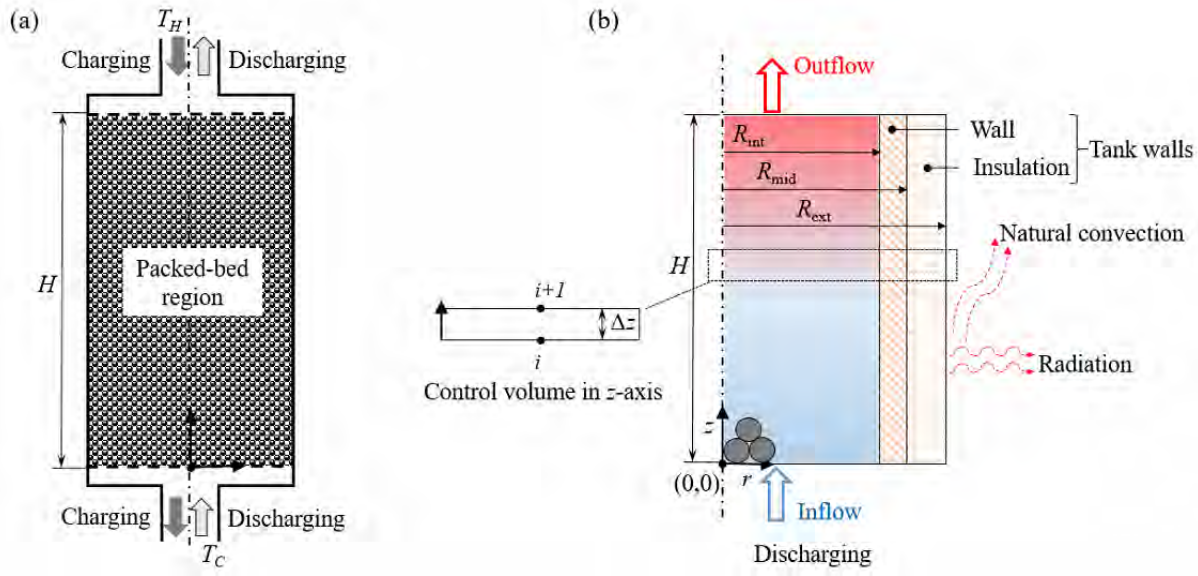

Figure 3.1: Thermocline packed-bed TES tank: (a) schematic illustration; (b) computational domain in discharging process.

where — H, the tank height in packed bed region.

— ε, the porosity of packed bed.

— R_{int}, R_{mid}, R_{ext}, the internal bed, middle wall, external insulation radius of tank, respectively.

— V_s, the total volume of solid particles.

— V_b, the whole tank volume based on R_{int} and H.

— T_H, the hottest operational temperature.

— T_C, the coldest operational temperature.

— z, r, the axial and radial coordinate of tank, respectively.

3.2.2. Three numerical models

In this chapter, three transient numerical models with different dimensions and phases, fluid, solid fillers, wall, or insulation phase, are studied: a *z*-axis 1D-2P model (fluid-solid), a *z*-axis 1D-3P model (fluid-solid-wall), and a 1.5D-4P model (1D *z*-axis for fluid-solid, 2D *z*-axis and *r*-axis for wall-insulation) that 1.5D refers to the average of 1D and 2D. **Figure 3.2** shows the research process and the relationship between models. At first, models were compared and validated by experimental data sets. Further, the wall thermal behavior for two different scale tanks was investigated by using a numerical reduced CPU resource model (1.5D-4P). After that, an appropriate model (1D-3P) is selected to conduct parametric sensitivity analysis and wall parametric study.

To simplify the model formulation and analysis, following assumptions have been employed:

(1) Inlet temperature and inlet/outlet mass flow rate of HTF are constant in charging and discharging.

(2) Bottom and top surfaces of the tank are adiabatic and there is no internal heat generation in the bed. The contact thermal resistance between wall and insulation is neglected.

(3) Thermal conduction and radiation between solid fillers are neglected as well as the heat transfer between solid particles and wall, due to the point contact.

(4) The thermo-physical properties of HTF and solid fillers are considered as constant and

determined by an average operating temperature: $T_{ave} = \left(\frac{T_H + T_C}{2}\right)$.

(5) HTF is assumed as incompressible fluid and plug flow (in z-axis direction). Solid fillers are identical and isotropic spherical particles with homogeneous temperature.

When the temperature inside a particle varies significantly in space coordinate, the internal heat conduction resistance cannot be ignored. This assumption is named as a lumped capacitance that is valid when the value of the solid Biot number ($Bi_s = \frac{h_{sf} \cdot D_p}{6 \cdot \lambda_s}$) is smaller than 0.1 [160,161]. Even the Bi_s in this work ranges between 0.2 and 0.28, the temperature gradient inside particle is neglected by introducing an effective heat transfer coefficient (HTC) between solid and fluid [162,163].

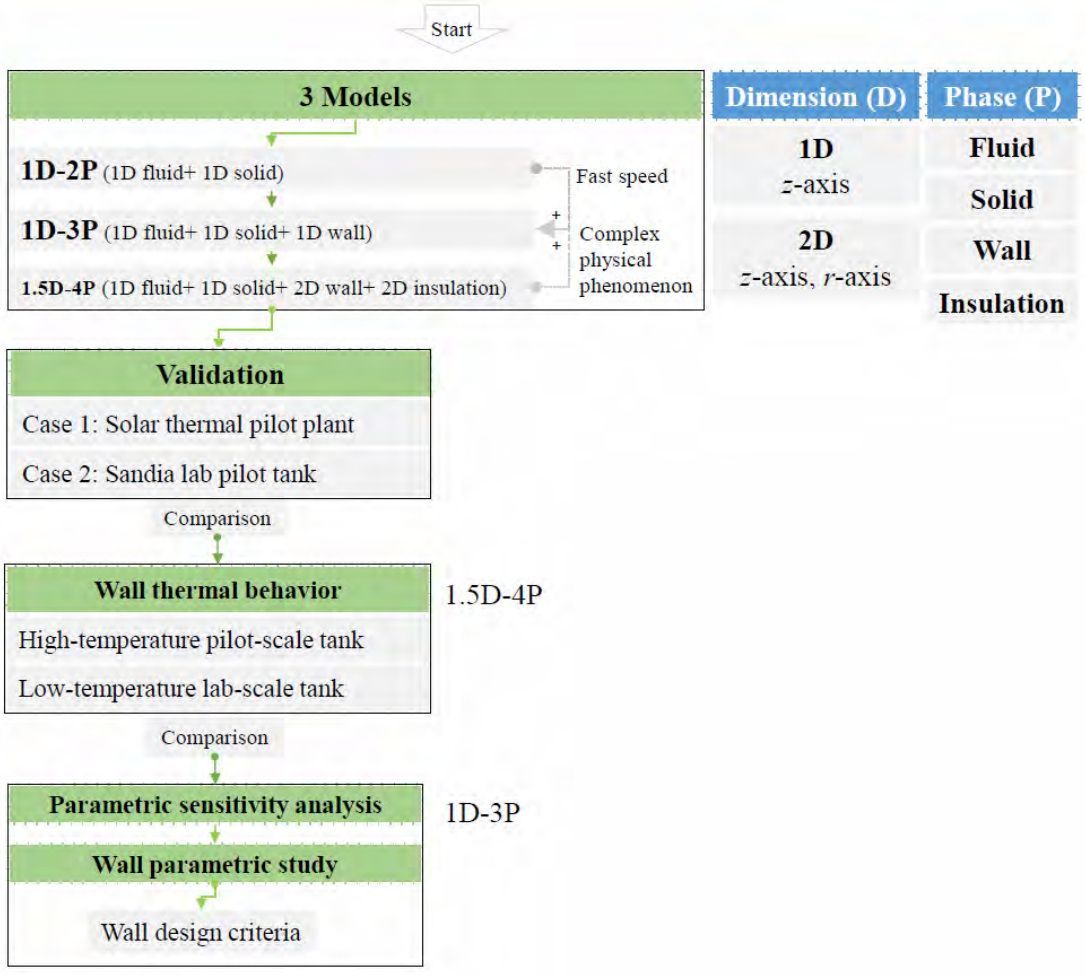

Figure 3.2: Diagram of the research process in this study.

3.2.2.1. One-dimensional two-phase model (1D-2P)

A 1D-2P model, or Schumann's model, is introduced to perform fast simulation. In this model, only fluid and solid filler material are modeled using an averaged porous model while the walls are not included. Governing equations of the control volume for two phases and corresponding correlations can be written as follows.

● Governing equations

Fluid (1D):

$$\varepsilon \cdot \rho_f \cdot C_{p,f} \cdot \left(\frac{\partial T_f}{\partial t} + u_f \cdot \frac{\partial T_f}{\partial z}\right) = \frac{\partial}{\partial z} \cdot \left(\lambda_{f,eff} \cdot \frac{\partial T_f}{\partial z}\right) + h_{sf,eff} \cdot \frac{A_s}{V_s} \cdot \left(T_s - T_f\right) + h_o \cdot \frac{A_b}{V_b} \cdot \left(T_{amb} - T_f\right) \quad (3.1)$$

Solid (1D):

$$(1-\varepsilon) \cdot \rho_s \cdot C_{p,s} \cdot \frac{\partial T_s}{\partial t} = \frac{\partial}{\partial z} \cdot \left(\lambda_{s,eff} \cdot \frac{\partial T_s}{\partial z}\right) + h_{sf,eff} \cdot \frac{A_s}{V_s} \cdot \left(T_f - T_s\right) \quad (3.2)$$

where — t, the time.

— D_p, the particle diameter.

— h, the heat transfer coefficient.

— *f*, *s*, *w*, o, *eff*, *amb* (subscripts), the fluid, solid, wall, overall value, effective value, and ambient, respectively.

— u_f, the interstitial fluid velocity, calculated by the mass flow rate $\dot{m}_f = u_f \cdot \rho_f \cdot \varepsilon \cdot \pi \cdot R_{int}^2$.

— $\frac{A_s}{V_s} = \frac{6 \cdot (1-\varepsilon)}{D_p}$, the shape ratio for solid particles diameter.

— $\frac{A_b}{V_b} = \frac{2}{R_{int}}$, the shape ratio for cylindrical bed.

On the left side of **Eq. 3.1**, the first term is the accumulative term of heat transfer for fluid and second term represents the heat convection of fluid. **On the right side**, the first term is the axial heat conduction, the second term is the heat exchange between solid and fluid, and the third term refers to heat losses to the ambient.

For solid phase in **Eq. 3.2**, the difference is that there is no heat conduction between solid and

wall, thus only two terms are on the right side.

● Effective HTC between solid and fluid

The forced convection and natural convection contribute dissimilarly to the heat transfer between fluid and solid [164]. The solid-to-fluid HTC (h_{sf}) from Pfeffer is given as [165]:

$$h_{sf} = \left(\frac{\lambda_f}{D_p}\right) \cdot \left\{1.26 \cdot \left[\frac{1-(1-\varepsilon)^{\frac{5}{3}}}{2-3\cdot(1-\varepsilon)^{\frac{1}{3}}+3\cdot(1-\varepsilon)^{\frac{5}{3}}-2\cdot(1-\varepsilon)^2} \cdot Re \cdot Pr\right]^{\frac{1}{3}}\right\} \quad (Re<74) \tag{3.3}$$

Moreover, in order to approach the assumption of uniform temperature inside the solid particle, or to extend the applicability of lumped capacitance method when Bi_s>0.1, the solid-to-fluid effective HTC ($h_{sf,eff}$) through the method of weight average time (or the effective average time [166]) is used [161]:

$$h_{sf,eff} = \frac{1}{1/h_{sf}+3\cdot Bi_s/m} \tag{3.4}$$

where the value of m equal to 5, 4, and 3 for different shapes of sphere, cylinder and slab (cube), respectively. m=5 is used in this study.

● Overall HTC through tank walls

The overall HTC through tank walls (h_o) based on the inner surface area is calculated by:

$$\frac{1}{h_o} = \frac{1}{h_{int}} + \left[\frac{1}{\lambda_w} ln\left(\frac{R_{mid}}{R_{int}}\right) + \frac{1}{\lambda_{ins}} ln\left(\frac{R_{ext}}{R_{mid}}\right)\right] \cdot R_{int} + \frac{1}{h_{ext}+h_{rad}} \cdot \frac{R_{int}}{R_{ext}} \tag{3.5}$$

where fluid-to-wall convective HTC (h_{int}) on internal or inner wall surface according to the empirical correlation of Yagi and Wakao [152], the insulation-to-ambient air convective HTC (h_{ext}) on external or outer surface based on a correlation of natural convection on vertical standing wall given by VDI-Wärmeatlas [167], and the radiative HTC (h_{rad}) based on the Stefan–Boltzmann law can be written:

$$h_{int} = \left(\frac{\lambda_f}{H}\right) \cdot 0.6 \cdot Re^{1/2} \cdot Pr^{1/3} \quad (1<Re<40) \tag{3.6}$$

$$h_{ext} = \left(\frac{\lambda_{air}}{H}\right) \cdot \left\{0.825 + \frac{0.387\cdot Ra_{air}^{1/6}}{\left[1+(0.492/Pr_{air})^{9/16}\right]^{8/27}}\right\}^2 \quad (Ra_{air}<10^{12}) \tag{3.7}$$

$$h_{rad} = \frac{\epsilon\cdot\sigma\cdot(T^4-T_{amb}^4)}{T-T_{amb}} \tag{3.8}$$

where — Ra, the Rayleigh number ($Ra_{air} = Gr_{air} \cdot Pr_{air}$).

— Gr, the Grashof number ($Gr_{air} = \frac{g \cdot \beta \cdot H^3 \cdot \Delta T}{v^2}$).

— ΔT, the temperature difference between the outer surface and the ambient of the HTF (refers to air here).

— ϵ, the emissivity factor is taken to 0.95, and σ=5.67×10^{-8} W m^{-2} K^{-4} is the Stefan-Boltzmann constant.

— g, β, and v, the acceleration of gravity, the thermal expansion coefficient of air, and the kinematic viscosity of the HTF (refers to air here), respectively.

—T in **Eq. 3.8** is defined as the outer surface temperature of the insulation calculated at average operational temperature T_{ave}, using the iterative method in advance.

● **Effective thermal conductivity for fluid and solid**

The heat transfer of the fluid phase takes into account the thermal diffusion in stagnant fluid and the turbulent thermal contribution in fluid mixing. Thus, the effective thermal conductivities for each fluid ($\lambda_{f,eff}$) and solid phase ($\lambda_{s,eff}$) are given as:

$$\lambda_{f,eff} \cong (\varepsilon \cdot \lambda_f + c \cdot \lambda_f) + \lambda_{mix} \tag{3.9}$$

$$\lambda_{s,eff} \cong [(1-\varepsilon) \cdot \lambda_s - c \cdot \lambda_s] \tag{3.10}$$

where $\lambda_{mix} = 0.5 \cdot Re \cdot Pr \cdot \lambda_f$ is the fluid mixing turbulent contribution based on Wakao and Kaguei's empirical correlation for Re >0.8 [168,169]. Besides, a coefficient (c) covering the geometry tortuosity of the packed-bed with parallel packing condition is introduced [170,171].

$$c \cong \frac{\lambda^0_{eff} - \varepsilon \cdot \lambda_f - (1-\varepsilon) \cdot \lambda_s}{\lambda_f - \lambda_s} \tag{3.11}$$

$$\lambda^0_{eff} = \left[\frac{1 + 2 \cdot \alpha \cdot (1-\varepsilon) + (2 \cdot \alpha^3 - 0.1 \cdot \alpha) \cdot (1-\varepsilon)^2 + (1-\varepsilon)^3 \cdot 0.05 \cdot exp(4.5 \cdot x)}{1 - \alpha \cdot (1-\varepsilon)}\right] \cdot \lambda_f \tag{3.12}$$

$$x = (\lambda_s - \lambda_f)/(\lambda_s + 2 \cdot \lambda_f) \tag{3.13}$$

where λ^0_{eff} is the thermal conductivity contribution of both phase in stagnant condition with the valid range of 0.15<ε<0.85, and 10^{-3}<λ_s/λ_f<10^4 [171].

3.2.2.2. One-dimensional three-phase model (1D-3P)

A modified 1D-3P model was developed by considering the tank wall as a separate phase in addition to the fluid and solid phases. In this way, the energy balance and the heat capacity of the tank wall are considered in 1D (z-axis direction). The insulation is simplified by a thermal resistance while its heat capacity is neglected due to the small temperature variation.

● Governing equations

Fluid (1D):

$$\varepsilon \cdot \rho_f \cdot C_{p,f} \cdot \left(\frac{\partial T_f}{\partial t} + u_f \cdot \frac{\partial T_f}{\partial z}\right) = \frac{\partial}{\partial z} \cdot \left(\lambda_{f,eff} \cdot \frac{\partial T_f}{\partial z}\right) + h_{sf,eff} \cdot \frac{A_s}{V_s} \cdot \left(T_s - T_f\right) + h_{f-w} \cdot \frac{A_{f-w}}{V_b} \cdot \left(T_w - T_f\right) \tag{3.14}$$

Solid (1D):

$$(1-\varepsilon) \cdot \rho_s \cdot C_{p,s} \cdot \frac{\partial T_s}{\partial t} = \frac{\partial}{\partial z} \cdot \left(\lambda_{s,eff} \cdot \frac{\partial T_s}{\partial z}\right) + h_{sf,eff} \cdot \frac{A_s}{V_s} \cdot \left(T_f - T_s\right) \tag{3.15}$$

Wall (1D):

$$\rho_w \cdot C_{p,w} \cdot \frac{\partial T_w}{\partial t} = \frac{\partial}{\partial z} \cdot \left(\lambda_w \cdot \frac{\partial T_w}{\partial z}\right) + h_{f-w} \cdot \frac{A_{f-w}}{V_w} \cdot \left(T_f - T_w\right) + h_{w-amb} \cdot \frac{A_{f-w}}{V_w} \cdot \left(T_{amb} - T_w\right) \tag{3.16}$$

where $\frac{A_{f-w}}{V_b} = \frac{R_{int}+R_{mid}}{R_{int}^2}$ and $\frac{A_{f-w}}{V_w} = \frac{R_{int}+R_{mid}}{R_{mid}^2-R_{int}^2}$ are the shape ratio for fluid-wall surface to packed-bed volume and fluid-wall surface to wall volume, respectively. The wall temperature (T_w) is defined as the temperature at the average diameter $[(R_{int} + R_{mid})/2]$ of the tank wall.

● Equivalent HTC of fluid-to-wall center, wall center-to-ambient

The equivalent HTC of fluid-to-wall center (h_{f-w}) and the equivalent HTC of wall center-to-ambient (h_{w-amb}) can be formulated as:

$$\frac{1}{h_{f-w}} = \frac{1}{h_{int}} + \frac{1}{\lambda_w} \cdot ln\left(\frac{R_{int}+R_{mid}}{2 \cdot R_{int}}\right) \cdot R_{int} \tag{3.17}$$

$$\frac{1}{h_{w-amb}} = \left[\frac{1}{\lambda_w} \cdot ln\left(\frac{2 \cdot R_{mid}}{R_{int}+R_{mid}}\right) + \frac{1}{\lambda_{ins}} \cdot ln\left(\frac{R_{ext}}{R_{mid}}\right) + \frac{1}{h_{ext}+h_{rad}} \cdot \frac{1}{R_{ext}}\right] \cdot R_{int} \tag{3.18}$$

3.2.2.3. One and half-dimensional four-phase model (1.5D-4P)

A 1.5D-4P model was used to explore the thermal behavior inside of the whole tank walls. In this model, the heat transfer in z-axis and r-axis for the wall and insulation occurs, and the different HTCs and effective thermal conductivities are calculated as defined before. It bases on

full resolution and shows even more accuracy than the former two models.

● **Governing equations**

Fluid (1D):

$$\varepsilon \cdot \rho_f \cdot C_{p,f} \cdot \left(\frac{\partial T_f}{\partial t} + u_f \cdot \frac{\partial T_f}{\partial z}\right) = \frac{\partial}{\partial z} \cdot \left(\lambda_{f,eff} \cdot \frac{\partial T_f}{\partial z}\right) + h_{sf,eff} \cdot \frac{A_s}{V_s} \cdot \left(T_s - T_f\right) + h_{int} \cdot \frac{A_b}{V_b} \cdot \left(T_{w,int} - T_f\right) \quad (3.19)$$

Solid (1D):

$$(1-\varepsilon) \cdot \rho_s \cdot C_{p,s} \cdot \frac{\partial T_s}{\partial t} = \frac{\partial}{\partial z} \cdot \left(\lambda_{s,eff} \cdot \frac{\partial T_s}{\partial z}\right) + h_{sf,eff} \cdot \frac{A_s}{V_s} \cdot \left(T_f - T_s\right) \quad (3.20)$$

Wall (2D):

$$\rho_w \cdot C_{p,w} \cdot \frac{\partial T_w}{\partial t} = \frac{\partial}{\partial z} \cdot \left(\lambda_w \cdot \frac{\partial T_w}{\partial z}\right) + \frac{\lambda_w}{r} \cdot \frac{\partial}{\partial r} \cdot \left(r \cdot \frac{\partial T_w}{\partial r}\right) \quad (3.21)$$

Insulation (2D):

$$\rho_{ins} \cdot C_{p,ins} \cdot \frac{\partial T_{ins}}{\partial t} = \frac{\partial}{\partial z} \cdot \left(\lambda_{ins} \cdot \frac{\partial T_{ins}}{\partial z}\right) + \frac{\lambda_{ins}}{r} \cdot \frac{\partial}{\partial r} \cdot \left(r \cdot \frac{\partial T_{ins}}{\partial r}\right) \quad (3.22)$$

where the subscript "*ins*" represents the insulation phase.

3.2.2.4. Initial and boundary conditions

In this chapter, only the discharging process was simulated and discussed. The initial conditions are given as:

$$T_s(t=0) = T_f(t=0) = T_H \quad (3.23)$$

$$T_{w,int}(t=0) = T_{w,int,ini};\ T_{w,mid}(t=0) = T_{w,mid,ini};\ T_{w,ext}(t=0) = T_{w,ext,ini} \quad (3.24)$$

The initial temperature of tank walls ($T_{w,int,ini}$; $T_{w,mid,ini}$; $T_{w,ext,ini}$) as shown in **Figure 3.3** before discharging is calculated by the fully charged tank temperature at the standby process using the iteration method as explained in **Figure 3.4.** The initial wall temperature ($T_{w,ini}$) in 1D-3P model is the average value of inner and middle surface temperature of wall.

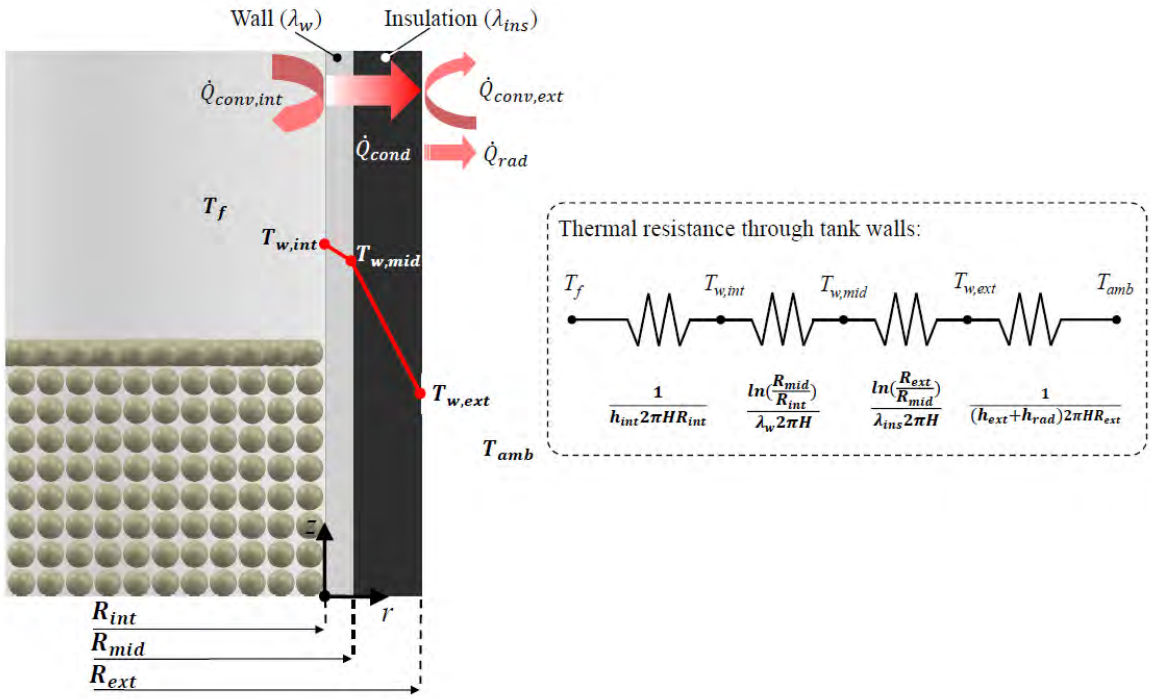

Figure 3.3: Initial and boundary conditions for the modeling of discharging operation: heat transfer through the wall and insulation at steady standby state ($T_{w,int}$, $T_{w,mid}$, and $T_{w,ext}$ is the temperature on inner, middle, and outer surface of tank, respectively).

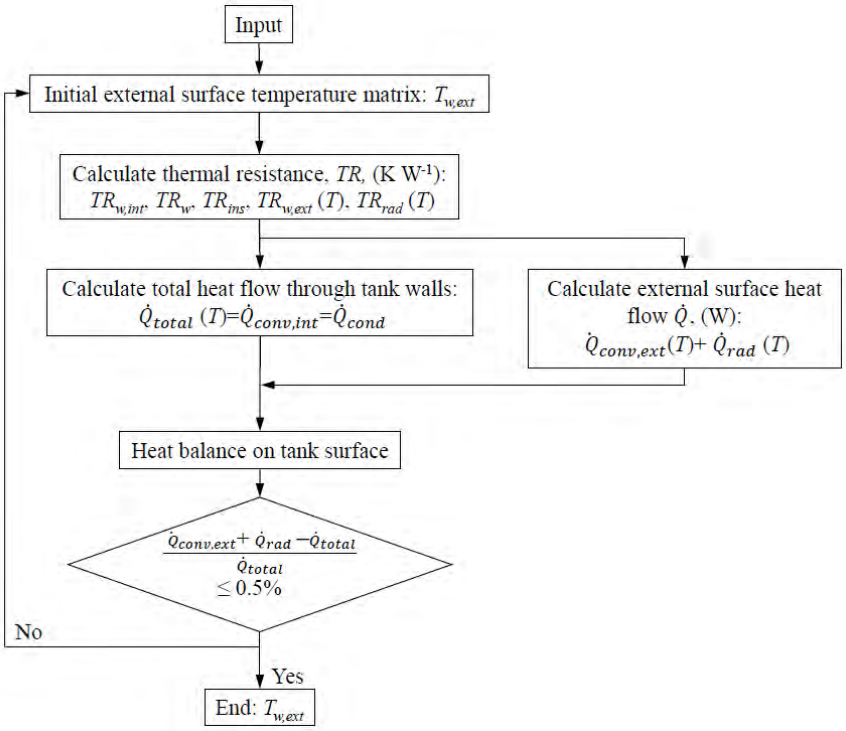

Figure 3.4: Iterative calculation to determine the initial outer surface temperature of fully charged tank before discharging.

The top and bottom boundary conditions for the computational domain shown in **Figure 3.1 b** are adiabatic. The HTF flows into the tank at T_C:

BC1: at the bottom inlet,

$$T_f(z=0) = T_C, \left.\frac{\partial T_s}{\partial z}\right|_{z=0} = \left.\frac{\partial T_w}{\partial z}\right|_{z=0} = \left.\frac{\partial T_{ins}}{\partial z}\right|_{z=0} = 0 \tag{3.25}$$

BC2: at the top outlet,

$$\left.\frac{\partial T_f}{\partial z}\right|_{z=H} = \left.\frac{\partial T_s}{\partial z}\right|_{z=H} = \left.\frac{\partial T_w}{\partial z}\right|_{z=H} = \left.\frac{\partial T_{ins}}{\partial z}\right|_{z=H} = 0 \tag{3.26}$$

In 1.5D-4P model, the boundary conditions at interfaces are added as:

BC3 for 1D-2P model: at the inner surface between wall and fluid,

$$h_{int} \cdot \left(T_{w,int} - T_f\right) = \lambda_w \cdot \left.\frac{\partial T_w}{\partial r}\right|_{r=R_{int}} \tag{3.27}$$

BC4 for 1D-3P model: at the middle surface between wall and insulation,

$$\lambda_w \cdot \left.\frac{\partial T_w}{\partial r}\right|_{r=R_{mid}} = \lambda_{ins} \cdot \left.\frac{\partial T_{ins}}{\partial r}\right|_{r=R_{mid}} \tag{3.28}$$

BC5 for 1.5D-4P model: at the outer surface between insulation and ambient,

$$\lambda_{ins} \cdot \left.\frac{\partial T_{ins}}{\partial r}\right|_{r=R_{ext}} = (h_{ext} + h_{rad}) \cdot \left(T_{amb} - T_{w,ext}\right) \tag{3.29}$$

3.2.3. Performance indicators

In this chapter, several performance indicators for evaluating walls impact are presented, other definitions will be introduced in Chapter 4 and Chapter 5.

● Discharging energy efficiency considering walls

For a given time, the discharging energy efficiency considering walls (η'_{dis}), is expressed as the ratio of the output energy by HTF in discharging (ΔE_{out}) (or cumulatively released energy) to the stored energy considering walls ($\Delta E'_{stored}$):

$$\eta'_{dis} = \frac{\Delta E_{out}}{\Delta E'_{stored}} = \frac{\int_0^{t_{dis}} [\dot{m}_f \cdot C_{p,f} \cdot (T_{out} - T_0)] dt}{\Delta E'_{f,stored} + \Delta E'_{s,stored} + \Delta E'_{w,stored} + \Delta E'_{ins,stored}} \tag{3.30}$$

where the $\Delta E'_{stored}$ is calculated by the energy at the initial state (that is $T_f = T_s = T_H, T_w(r) = T_{w,ini}$, $T_{ins}(r) = T_{ins,ini}$) to the fully discharged state (that is $T_{out} = T_C$, $T_f = T_s = T_C$, $T_w(r) = T_{w,end}$,

$T_{ins}(r) = T_{ins,end}$).

● Discharging exergy efficiency considering walls

For a given time, the discharging exergy efficiency considering walls ($\eta'_{x,dis}$) (or second law efficiency) is the ratio of the exergy of outlet fluid released from the bed ($\Delta E_{x,out}$) at a certain time to the exergy difference of all phases in packed bed before discharging ($\Delta E'_{x,stored}$):

$$\eta'_{x,dis} = \frac{\Delta E_{x,out}}{\Delta E'_{x,stored}} = \frac{\int_0^{t_{dis}} \dot{m}_f \cdot C_{p,f} \cdot \left[(T_{out} - T_C) - T_0 \cdot \ln\left(\frac{T_{out}}{T_C}\right)\right] dt}{\Delta E'_{x,f,stored} + \Delta E'_{x,s,stored} + \Delta E'_{x,w,stored} + \Delta E'_{x,ins,stored}} \tag{3.31}$$

where the reference temperature T_0 is selected as the coldest operational temperature (T_C) in this chapter.

● Pumping energy

The consumed pumping energy (ΔE_{pump}) for a given time is expressed as:

$$\Delta E_{pump} = \int_0^t \left(\frac{\dot{m}_f}{\rho_f} \cdot \Delta P\right) dt \tag{3.32}$$

where ΔP of the packed-bed tank is calculated using the superficial fluid velocity (u_{sup}) by Ergun equation [172] that the values of A and B depend on the variation of porosity ε [173]:

$$\frac{\Delta P}{H} = A \cdot \frac{(1-\varepsilon)^2}{\varepsilon^3} \cdot \frac{\mu_f \cdot u_{sup}}{D_p^2} + B \cdot \frac{(1-\varepsilon)}{\varepsilon^3} \cdot \frac{\rho_f \cdot u_{sup}^2}{D_p} \tag{3.33}$$

● Thermocline thickness

The dimensionless thermocline thickness ($L^*_{thermocline}$) is determined by the length of stratification region in bed [174], according to the physical boundary within a certain temperature range before reaching the top or bottom of the tank.

$$L^*_{thermocline} = \frac{z\{T = T_C + n\% \cdot (T_H - T_C)\} - z\{T = T_H - n\% \cdot (T_H - T_C)\}}{H} \tag{3.34}$$

— In charging, $z\{T = T_C + n\% \cdot (T_H - T_C)\} > 0$;

— In discharging, $z\{T = T_H - n\% \cdot (T_H - T_C)\} < H$;

where n is a threshold value that is defined as the hottest/coldest temperature differs n % to the operational temperature range ($T_H - T_C$), setting as 5% in this study. In experiment, the thermocline thickness is calculated by the fluid temperature variation at the axial centerline of the storage tank.

● **Threshold temperature**

In a cycling process, it assumes the initial condition of changing is fully discharged and with a homogenous coldest operating temperature, while the end of charging at the cutoff temperature is the beginning of discharging. In this study, the cutoff threshold temperature for charging/discharging changed by 20% of operational temperature [83][84][85]:

$$T_{cutoff,ch} = T_{0.2} = T_H - 20\% \cdot (T_H - T_C) \tag{3.35}$$

$$T_{cutoff,dis} = T_{0.8} = T_C + 20\% \cdot (T_H - T_C) \tag{3.36}$$

● **Dimensionless parameters**

Normalized parameters are defined for better comparison under different operational conditions. The dimensionless temperature (T^*), time based on flow velocity (t^*), time based on energy (t_E^*), height (z^*), radius (r^*), wall thickness (L_w^*), and wall thermal conductivity (λ_w^*) are introduced:

$$T^* = \frac{T - T_C}{T_H - T_C} \tag{3.37}$$

$$t^* = t \cdot \frac{u_f}{H} \tag{3.38}$$

$$t_E^* = t \cdot \frac{\dot{m}_f \cdot C_p \cdot (T_H - T_C)}{\Delta E'_{x,stored,max}} \tag{3.39}$$

$$z^* = \frac{z}{H} \tag{3.40}$$

$$r^* = \frac{r}{R_{in}} \tag{3.41}$$

$$L_w^* = \frac{L_w}{R_{int}} \tag{3.42}$$

$$\lambda_w^* = \frac{\lambda_w}{\lambda_f} \tag{3.43}$$

3.2.4. Model validation and comparison

The models were solved with the MATLAB function ode45 for the time derivatives. The explicit Runge Kutta (4.5) method was used with an adaptive time step. The advection term was discretized with a first order upwind finite difference, and the diffusion term was discretized with a second order central finite difference. The computational domain of numerical simulation was

discretized into non-overlapping control volumes as illustrated in **Figure 3.1.** To obtain accurate simulation results and reduce the consumption of time, the height node number (N) in z-axis and the time node number (M) were determined by using the cutoff time as an indicator of stable solution. When the cutoff time is in stable with increasing node numbers.

3.2.3.1. Cases description

Three cases with different scales, including two real tanks and a hypothetical lab-scale tank, are introduced. **Table 3.2** shows the characteristics and parameters of those three packed-bed TES tanks. **Table 3.3** summarizes the thermo-physical properties for HTF, solid fillers, and tank body materials**.** The first case widely used for model validation [49,155,175] is a 10 MW_e packed-bed TES tank for a solar thermal power plant in which Caloria HT 43 is used as HTF under the operating temperature range of 179.2-295.5 °C [176,177]. The second case is a 2.3 MWh_t packed-bed pilot-scale molten salt TES tank from Sandia lab provided by Pacheco et al. [104], with an operating temperature range of 290-390 °C. The molten salt used is a mixture of 60 wt% $NaNO_3$ and 40 wt% KNO_3. At last, a hypothetical lab-scale TES water tank with a smaller size and lower temperature range of 20-75 °C is introduced to simulate the thermal performance under different operations. The ambient temperature of 20 °C was set as a reference for all cases.

Table 3.2 Operational and geometric parameters of packed-bed TES tanks.

Parameters	**Units**	**Solar thermal pilot plant tank** [155,176,177]	**Sandia laboratory pilot-scale tank** [104]	**Hypothetical lab-scale tank**
HTF	--	Caloria Ht-43	Molten salt	Water
Solid filler	--	Granite rock and sand	Quartzite rock and sand	Quartzite rock and sand
Tank height (H)	m	12.0	6.0	0.4
Tank middle radius (R_{mid})	m	9.10	1.50	0.11
Wall thickness (L_w)	m	0.10	0.04	0.01
Insulation thickness (L_{ins})	m	0.20	0.20	0.04
Porosity (ε)	--	0.22	0.22	0.22
Packed bed volume (V_b)	m^3	3053.60	40.20	12.56×10^{-3}
Particle diameter (D_p)	m	4.61×10^{-3}	19.05×10^{-3}	5.00×10^{-3}
HTF mass flow rate ($\dot{m}_f$)	kg s^{-1}	23.00	5.46	8.30×10^{-3}
T_H/T_C	°C	295.2/179.2	390/290	75/20
Wall materials	--	Steel wall(ASTM 537 class 2)	Steel wall	Polycarbonate wall
Insulation	--	Mineral wool	Mineral wool	Mineral wool
Discharging time	h	8.0	3.0	0.5
Spatial node in height	--	200	200	200

Table 3.3 Thermophysical properties of HTF, solid fillers and tank body materials.

Solid fillers	**ρ_s (kg m^{-3})**	**$C_{p,s}$ (J kg^{-1} K^{-1})**	**λ_s (W m^{-1} K^{-1})**	**$\rho_s \cdot C_{p,s}$ (kJ m^{-3} K^{-1})**	**Ref.**
Granite rock and sand	2643	1020	2.20	2696	[49]
Quartzite rock and sand	2500	830	5.69	2075	[41]
Soda-lime glass	2400	760	1.00	1824	[42]
Tank body materials	**ρ_w (kg m^{-3})**	**$C_{p,w}$ (J kg^{-1} K^{-1})**	**λ_w (W m^{-1} K^{-1})**	**$\rho_w \cdot C_{p,w}$ (kJ m^{-3} K^{-1})**	
Steel wall(ASTM 537 class 2)	7850	475	47.00	3728	[175]
Steel wall	7800	470	35.00	3666	[41]
Polycarbonate wall	1200	1170	0.20	1404	--
Insulation of mineral wool	70*	960	0.036	67.2	[137]
Fluids	**ρ_f (kg m^{-3})**	**$C_{p,f}$ (J kg^{-1} K^{-1})**	**λ_f (W m^{-1} K^{-1})**	**μ (Pa s)**	
Caloria HT-43 (237.2 °C)	701	2700	0.16	7.6×10^{-4}	[155]
60 wt% $NaNO_3$ and 40 wt% KNO_3 (340 °C)	1874	1502	0.51	2.5×10^{-3}	[41,83]
Water (47.5 °C)	990	4187	0.634	5.8×10^{-4}	[30,178]

* It means the bulk density.

3.2.3.2. Validation results

Figure 3.5 shows the comparisons between numerical results and experimental data for axial temperature evolution curves of packed bed TES tanks in discharging. The measured experimental temperature profile at 0 h was used as the initial temperature profile in the modeling to have the same beginning. The standard deviation (SD) and root mean square (RMS) of temperature difference between experiment and simulation results were calculated to evaluate the agreement degree.

Figure 3.5 a shows the validation results of 1D-2P model using the measured data from the solar thermal power plant tank (Bi_s=0.1). It is found that the simulated temperature profiles at 4h to 8h are generally consistent with the experimental data considering that the experimental temperatures are taken at one radial position in the tank while the computed data are average temperatures on a cross section. Only slight deviations exist at some time intervals, indicating that the basic 1D-2P model has enough accuracy in modeling large-scale thermocline packed-bed tanks. **Figure 3.5 b** is the comparison on the results of 1D-2P, 1D-3P, and 1.5D-4P models with Sandia pilot-scale packed-bed tank. These simulation curves are not far away from experimental values, but the predicted temperature of 1D-3P and 1.5P-4P models are higher than that of 1D-2P model at a certain height, which may be due to the release of the stored heat in the walls. The phenomenon will be discussed in detail in the following section. By examining the mean difference

of different models shown in **Table 3.4**, it is found that three models show similar standard deviation of around 3 K and two detailed models which can characterize the physical phenomenon in walls show similar root mean square difference of about 5 K, close to that of 1D-2P simple model (4 K). All three models reflect good agreement with the experimental data with an acceptable average difference.

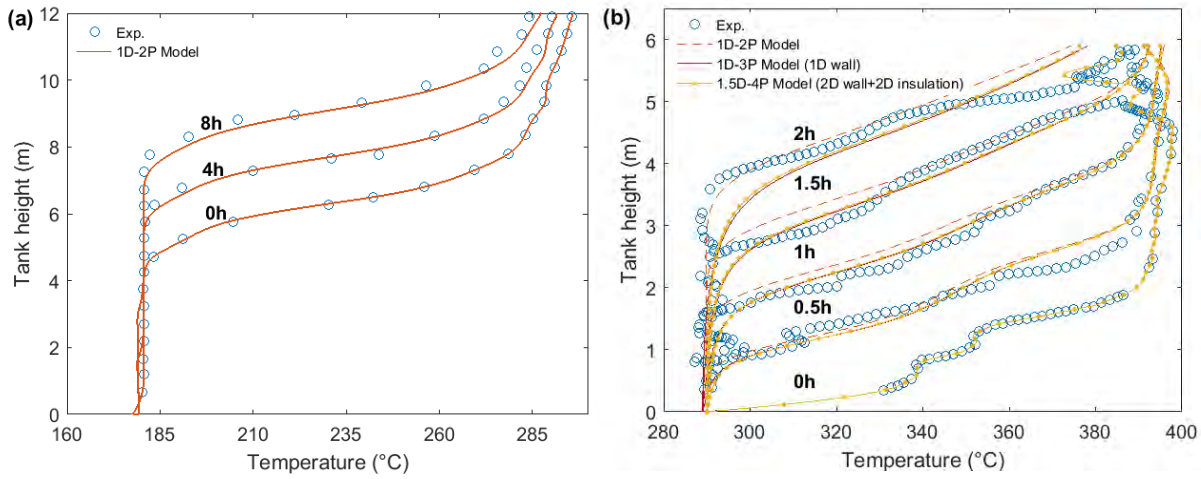

Figure 3.5: Comparison of axial temperature evolution curves in discharging process between numerical results and experimental data: (a) solar power plant [176,177]; (b) Sandia pilot-scale tank [104].

Table 3.4 Difference between experimental and numerical results of the Sandia pilot-scale tank [104] for different models: mean difference for different times 0, 0.5, 1, 1.5, and 2h.

Models	Average difference ($\overline{\Delta T}$, K)	Maximum difference (ΔT_{max}, K)	Standard Deviation (SD, K)	Root Mean Square difference (RMS, K)
1D-2P	2.91	12.7	2.80	4.06
1D-3P	3.63	12.5	3.44	5.02
1.5D-4P	3.56	12.3	3.40	4.93

3.2.3.3. Unification of different scale tanks

Two tanks listed in **Table 3.2**, the pilot-scale tank (Sandia's Lab) and the hypothetical lab-scale one, will then be fully studied to investigate the wall impact. Despite different sizes and operational temperatures, the influence levels of governing terms should be set similar for better

comparison and exploitation. For this purpose, the dimensionless numbers (Π_i) (in **Eq.s A 3.4-A 3.11**) are used to unify two tanks. The dimensionless governing equations of the 1D-3P model (in **Eq.s A 3.1-A 3.3**) and corresponding analysis are provided in **FigureA 3.1** of the *Appendix*.

3.3. Wall thermal behavior discussion

3.3.1. General temperature profiles

The 1.5D-4P model was first used to analyze detailed thermal behaviors of fluid and tank walls in discharging. **Figure 3.6** shows the fluid temperature profiles of two tanks along *z*-axis height at different times. Recall that t_E^* is the dimensionless time based on energy flow through the tank, the thermocline zone is defined within the fluid temperature range of $0.05<T^*<0.95$, and the center position of thermocline refers to the height where $T^*=0.5$. At half discharging time ($t_E^*=0.5$), the thermocline center position of large pilot-scale tank is at around $z^*=0.54$, slightly lower than that of the small lab-scale tank at $z^*=0.57$. At the same time, in both cases, the thermocline zone is found to be nearly symmetrical. The thermocline thickness $L^*_{thermocline}$ of pilot-scale tank (0.33) is smaller than that of the lab-scale tank (0.54). All these differences indicate that the pilot-scale tank may have a higher discharging (release) efficiency.

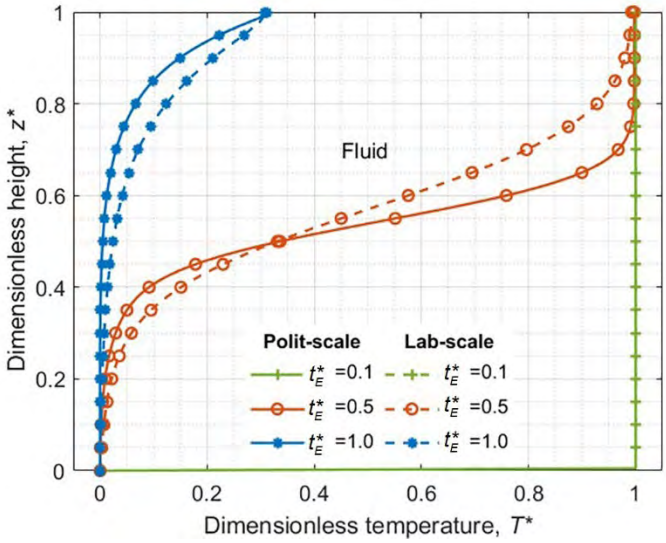

Figure 3.6: Evolution of temperature profiles of two tanks for the discharging process using 1.5D-4P model: fluid temperature along *z*-axial height.

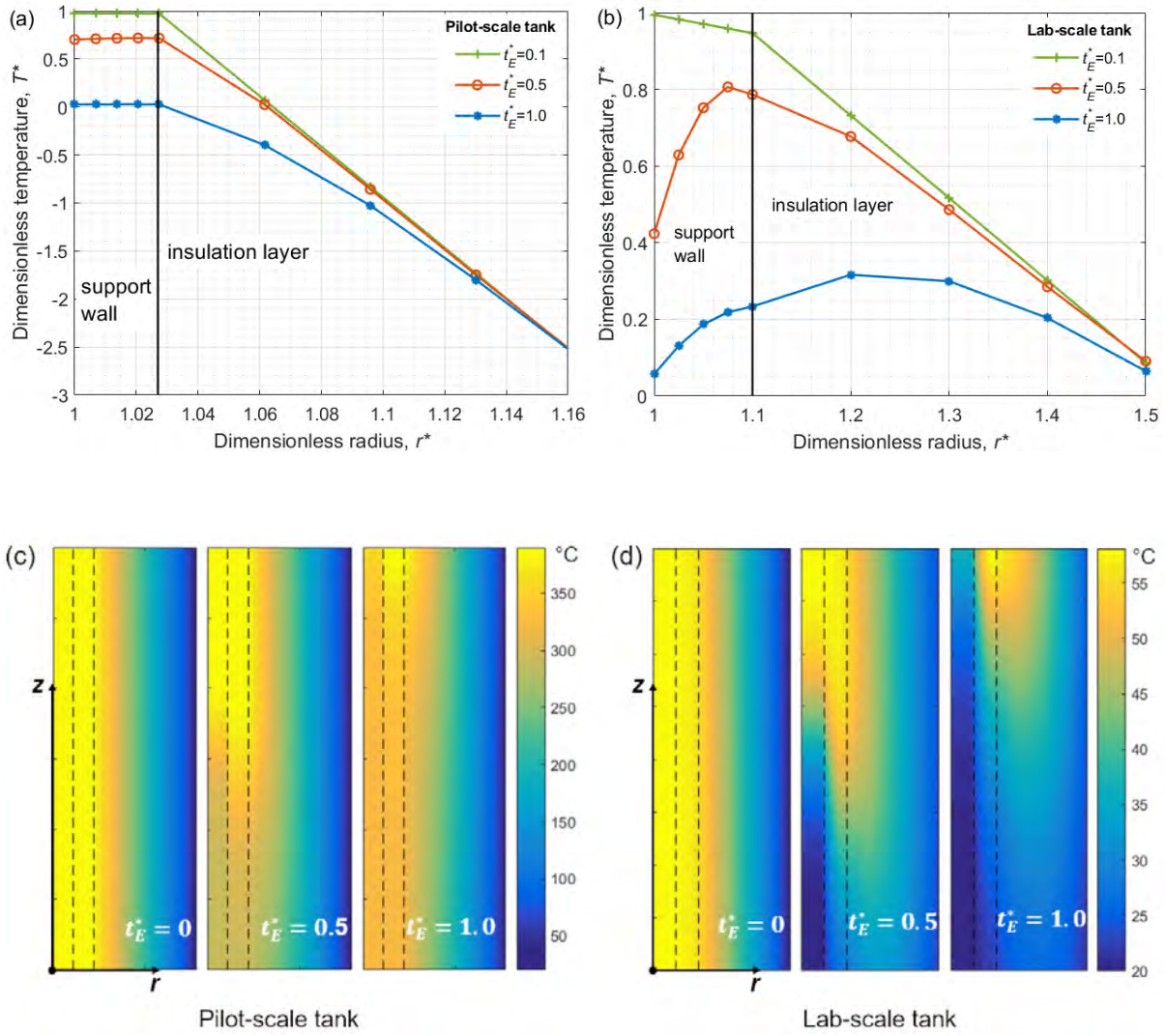

Figure 3.7: Wall and insulation temperature along *r*-direction at the middle tank height (z^*=0.5); (c)(d) temperature color map of fluid, wall, and insulation at t_E^*=0, 0.5 and 1.

Figure 3.7 a b show temperature distribution of tank walls along the radial direction at the middle tank height (z^* =0.5). **Figure 3.7 c d** show the cross-sectional temperature color map of three phases. When discharging proceeds, the wall and insulation are cooled down from bottom to top as the cold fluid flows. Note that the insulation temperature T_{ins}^* near the outer surface of the pilot-scale tank shows a negative value due to the far greater cold fluid temperature than the ambient ($T_C \gg T_{amb}$). The variation of T_w^* and T_{ins}^* as a function of t_E^* in the pilot-scale tank shows the same tendency, while for lab-scale tank, the T_w^* shows sharper decrease over the discharging time and there is a heat delay for T_{ins}^*. That is because the fluid-wall Biot number Bi_w ($Bi_w = \frac{h_{int} \cdot L_w}{\lambda_w}$) is calculated to be 0.1 for pilot-scale tank and be 9 for lab-scale tank. Smaller Bi_w for the

pilot-scale tank means that heat transfer is mainly governed by convection between the wall and the fluid. For the lab-scale tank, the insulation can be hotter than the small temperature gradient within the wall, the conduction thermal resistance can thereby be ignored. A heat transfer from the insulation layer to the wall is then occupying, which may lead to instability. Furthermore, the dimensionless thermal diffusivity time t^*_{diff} ($t^*_{diff} = \frac{L^2}{\alpha} \cdot \frac{t^*_E}{t}$) is around 0.01 and 2.2 for wall and insulation in the pilot-scale tank, respectively, and is 0.65 and 2.8 in the lab-scale tank. Lower t^*_{diff} shows fast heat transfer speed from wall to fluid. For this reason, T^*_w is almost horizontal at different discharging times in pilot-scale tank.

3.3.2. Wall heat flux

Figure 3.8 exhibits the heat flux through the wall surfaces based on Fourier's law. At inner (fluid-wall) surface, the negative value of heat flux represents the radial heat transfer from wall to fluid. At outer (insulation-ambient) surface, the positive value indicates the heat flux (heat loss) from the storage tank to the ambient and it reduces with upward fluid flowing. At the beginning of discharging (t^*_E=0.1), the inner surface at the top portion of both tanks has a small positive heat flux while the bottom has a larger negative. This is due to the heat loss from the storage tank to the ambient through the top part of tank walls as long as the cold HTF does not reach it. After the arrival of cold fluid, the walls are cooled down and a large proportion of heat initially stored in the tank walls is released back to the fluid, indicated by the negative values of heat flux curves. A small proportion of heat stored in the walls is still dissipated to the ambient, indicated by the always positive values of heat flux through the outer surface of both tanks.

Furthermore, in curves of the inner surface, the peak point of heat flux with the maximum temperature difference between wall and fluid is near the thermocline center, slightly higher than the height of the sharper inflection point of outer surface curve. This height difference (Δz^*) of thermocline on inner and outer surface reflecting the time delay (Δt^*_E) is caused by the thermal resistance of wall and insulation. At the same time, the height difference of lab-scale tank ($\Delta z^* \approx 0.04$) is lower than that of pilot-scale one ($\Delta z^* \approx 0.1$), demonstrating less time to move thermocline on both surfaces due to the lower thermal diffusivity time. Note that the time delay and the height difference are calculated as follows:

Time delay: $\Delta t_E^* = t_E^*\{z^* = 0.5, \text{peak point of inner surface}\} - t_E^*\{z^* = 0.5, \text{sharper inflection point of outer surface}\}$

Height difference: $\Delta z^* = z^*\{t^* = 0.5, \text{peak point of inner surface}\} - z^*\{t^* = 0.5, \text{sharper inflection point of outer surface}\}$

Moreover, the increase of peak span along the z-direction reflects an increment of thermocline thickness over discharging time. The peak height in radial direction decreases over time, due to the smaller wall-fluid temperature difference caused by the continuous heat release from wall to fluid. Diffusivity in z-axis within the wall is significantly smaller in lab-scale tank, but it's not clear how it impacts the heat flux.

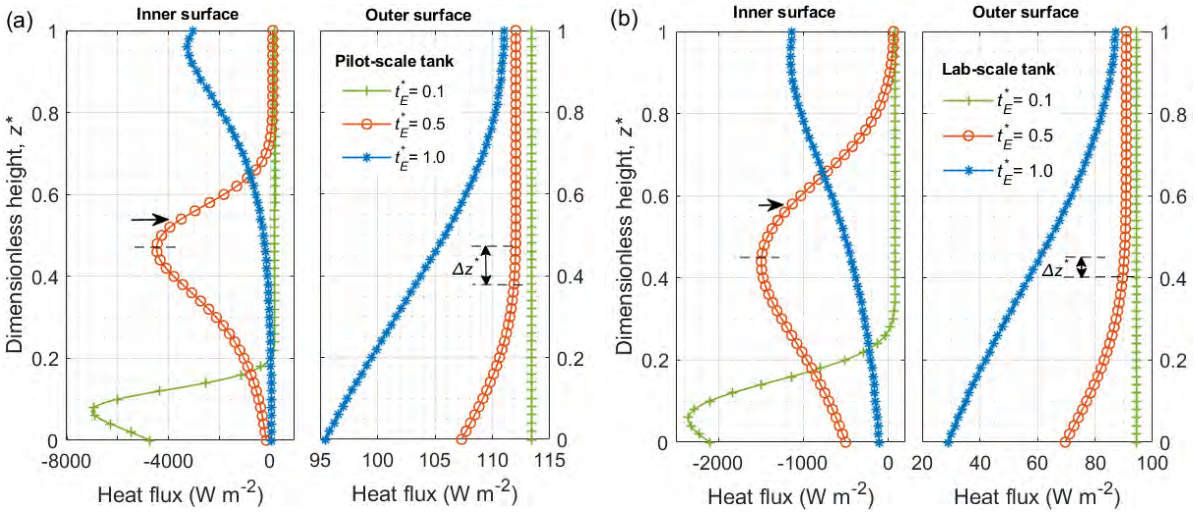

Figure 3.8: Heat flux at the inner (fluid-wall) and outer (insulation-ambient) surface during the discharging process: (a) pilot-scale tank; (b) lab-scale tank.

3.3.3. Wall heat transfer rate analysis

Heat transfer rate ($\dot{Q}$) analysis of tank walls was conducted to investigate the rate of energy transfer in discharging process. **Figure 3.9** is the schematic of heat transfer rate balance through tank walls, including inner surface convection ($\dot{Q}_{int}$), wall axial diffusion ($\dot{Q}_{w,diff}$), insulation axial diffusion ($\dot{Q}_{ins,diff}$), inside increment ($\dot{Q}_{w,increment} + \dot{Q}_{ins,increment}$), and outer surface convection and radiation ($\dot{Q}_{ext}$).

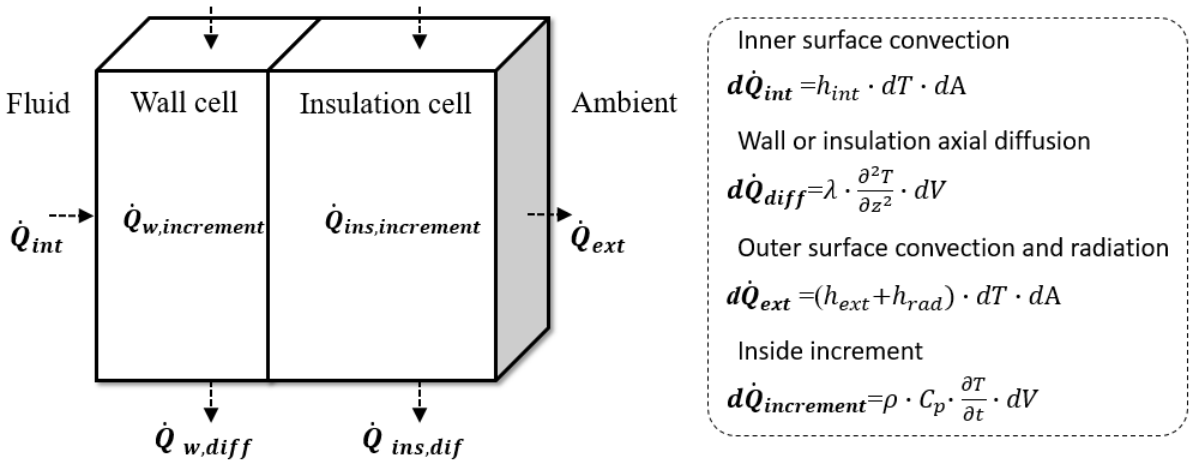

Figure 3.9: Schematic of heat transfer rate balance in wall and insulation.

Figure 3.10 shows the heat transfer ratio at the middle height of tank at different discharging times. In this chapter, each contribution was compared with inner surface input heat transfer rate ($\dot{Q}_{int}$). The $\frac{dT_f}{dt}$ represents the rate of fluid temperature variation at the middle position. At the beginning ($t_E^* = 0.1$), cold flow enters from tank bottom showing a small value of $\frac{dT_f}{dt}$. With time increases to $t_E^* = 0.5$, the thermocline with temperature gradient zone moves to the middle height of tank showing a large $\frac{dT_f}{dt}$. The cutoff time, $t_E^* = cutoff$ referring to the ending time, is a little longer than $t_E^* = 1$. Near the ending time ($t_E^* = 1$), cold fluid fills the tank up showing again a small $\frac{dT_f}{dt}$. A similar tendency can be found for the wall temperature variation rate $\frac{dT_w}{dt}$. Through the results of heat transfer ratio, it can be found that the $\dot{Q}_{int}$ is close to the $\dot{Q}_{ext}$ at the beginning. But with the increase of discharging time, $\dot{Q}_{int}$ becomes dominant over other parts. It should be specially noted that the wall and insulation axial diffusion ($\dot{Q}_{w,diff}$ and $\dot{Q}_{ins,diff}$) are all near 0, indicating that the influence of heat diffusion in axial direction of walls can even be ignored compared to the inner or outer surface heat transfer.

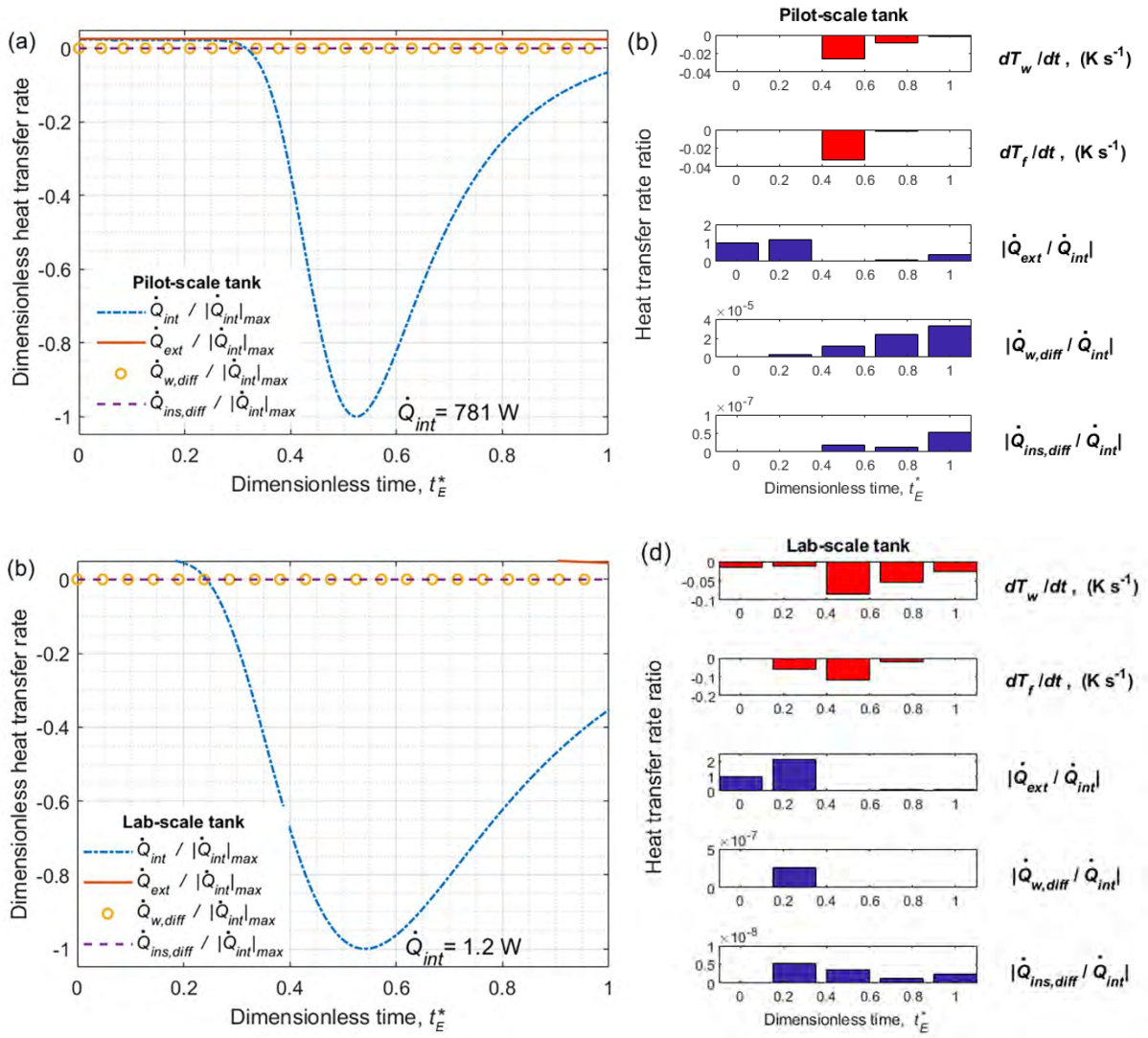

Figure 3.10: The variation of heat transfer rate over discharging time at middle tank height (z^*=0.5). (a), (b) pilot-scale tank; (c), (d) lab-scale tank.

3.3.4. Stored heat in wall

Figure 3.11 a shows the percentage of stored energy in each phase at the beginning and of discharging. Before discharging (fully charged state), the solid phase has a dominant energy storage percentage of 65% for lab-scale tank and 55% for pilot-scale tank. The proportion of energy stored in the tank wall is also as high as 8% and 10%, respectively. This non-negligible part of energy remains no valorized. Nevertheless, the stored energy in the insulation can hardly be captured, implying that the insulation phase may be simplified in the modeling without affecting much the energy efficiency calculation of the packed-bed TES tank. The stored energy ($\Delta E'_{stored}$) of pilot-scale tank at initial time is larger than that of lab-scale tank. At $t_E^* = 1$, it decreases from

1×10^{10} to 4×10^{8} J (-96%) for the pilot-scale tank, and from 2×10^{6} to 1×10^{5} J (-95%) for the lab-scale tank. At the cutoff time, energy of each part still decreases and the pump energy due to packed bed pressure drop at cutoff time is 7.3 $\times10^{3}$ J and 0.24 J, respectively, which can be neglected safely ($\leqslant$1%).

Figure 3.11 b shows the contribution of each factor to the total thermal resistance of each tank. The biggest proportion of the total thermal resistance is from the insulation layer. Nevertheless, the heat loss due to the radiation should be considered, accounting for about 5% of the total heat loss (lab-scale tank). **Table 3.5** shows that the lab-scale tank presents higher HTC h_o (1.0 W m^{-2} K^{-1}) through the tank walls than that of the pilot-scale tank (0.2 W m^{-2} K^{-1}), exhibiting a higher possibility to lose heat to ambient despite a lower value of total heat loss. In summary, the impacts of wall stored energy and radiation heat loss must be considered in the performance evaluation while the insulation heat capacity and pump energy consumption can be neglected in Chapter 4 and Chapter 5.

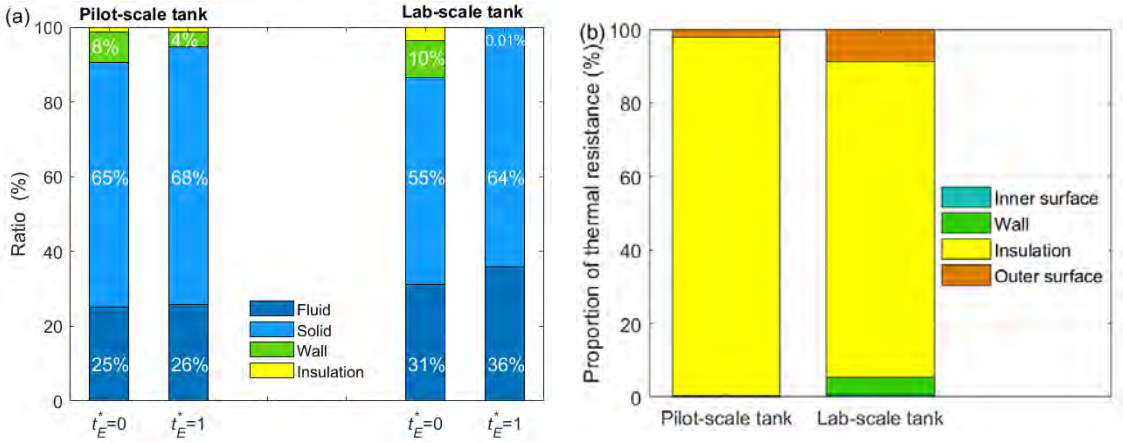

Figure 3.11: (a) Proportion of stored energy in different phases of packed-bed TES tank at the beginning $t_E^* = 0$ and at the ending $t_E^* = 1$ of discharging; (b) proportion of different thermal resistances at stable heat flux state.

Table 3.5 Values of different HTC* for two tanks at average temperature (T_{ave}).

Types	h_{int} (W m^{-2} K^{-1})	h_{ext} (W m^{-2} K^{-1})	h_{rad} (W m^{-2} K^{-1})	h_o (W m^{-2} K^{-1})
Pilot-scale tank	78	2.5	5.6	0.2
Lab-scale tank	179	2.2	5.5	1.0

* HTCs are defined in Section 3.2.2 in numerical model.

3.3.5. Energy and exergy efficiency

Energy and exergy efficiency variation during discharging and comparison between models based on two indicators are presented in **Figure 3.12.** Exergy, as the work potential of energy, is defined as the maximum useful work that can be obtained from system before reaching the equilibrium state [179]. The 100% exergy efficiency refers to completely reversible process and the higher efficiency can be achieved by forming a stable and thinner thermocline or enhanced thermal stratification [180]. It can be observed that energy and exergy efficiencies are time-dependent and show the same increasing tendency for discharging. The energy efficiency at the $t_E^* = 1$ for lab-scale tank (86% using 1D-2P model) is lower than that of the pilot-scale tank (90%), as well as the exergy efficiency. This is because of the higher heat loss to ambient due to the higher h_o and the more extended thermocline as discussed above. Moreover, it is observed that the difference on exergy efficiency between 1D-3P (1D wall domain) and 1.5D-4P (2D wall and 2D insulation domain) models is below 5% and both energies higher than 1D-2P (no wall, no insulation domain) model due to the extra heat from wall. Because of complex physical phenomenon description than 1D-2P model and decreased computational time by a factor of 100 than 1.5D-4P model (cf. **TableA 3.1)**, the 1D-3P model can be selected to conduct the wall parameter study. Therefore, taking into the wall has an impact on the energy and exergy efficiency close to 5%.

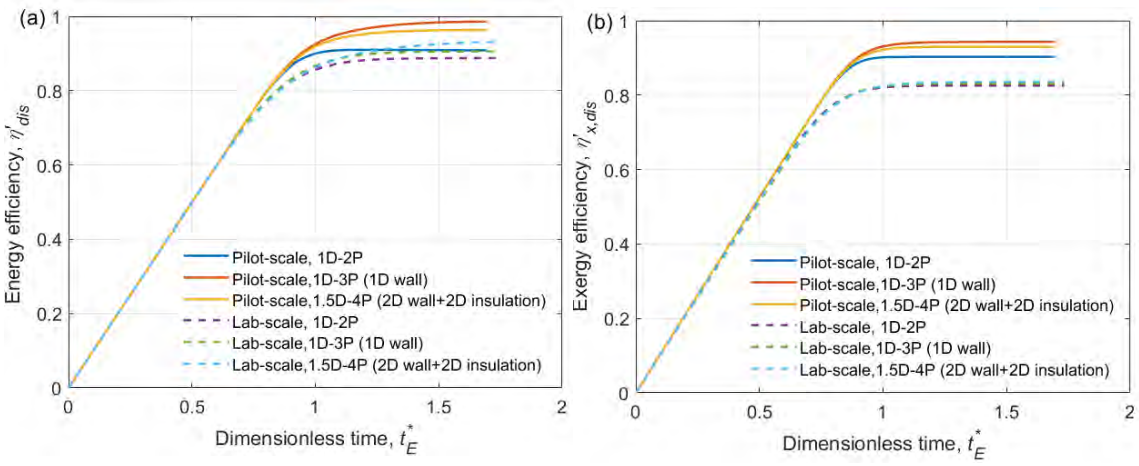

Figure 3.12: Comparison of (a) energy efficiency and (b) exergy efficiency between 1D-2P, 1P-3P, and 1.5P-4P models for pilot-scale tank and lab-scale tank.

3.4. Wall parametric study

3.4.1. The effect of convection and radiation of external surface

Figure 3.13 a b show the influence of emissivity variation on the tank outer surface temperature, energy and exergy efficiencies. When emissivity changes from a low value of 0.65 to a high value of 0.95, the radiative HTC (h_{rad}) increases from 3.8 to 5.6 W m^{-2} K^{-1}, causing outer surface temperature to decline and more radiative heat loss to ambient. However, the energy and exergy efficiencies at cutoff time are almost the same, indicating that the tiny influence of emissivity on the overall efficiency of the storage system efficiency when the insulation thickness is "sufficient".

Figure 3.13 b is the comparison of natural convection and forced convection on the outer surfaces for two tanks, which were calculated by **Eq. 3.8**. When the effective outdoor HTC (including both convection and radiation) ranges from 17 to 50 W m^{-2} K^{-1} [181], the external HTC (h_{ext}) varies from 2 to 17 W m^{-2} K^{-1}. This value range considers the heat exchange between the outer surface and the ambient air in real practice [182][183]. The simulation results show the noticeable influence of the external heat transfer coefficient on the evolution of outer surface temperature. Nevertheless, the energy and exergy efficiencies of the storage tank at cutoff time vary slightly by about 0.01% and little influence on the thermocline thickness can be observed.

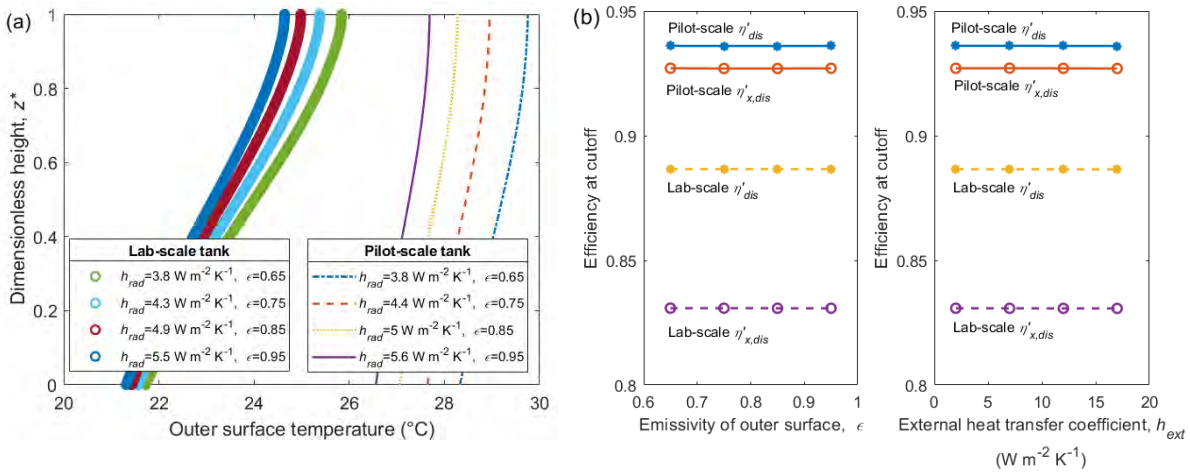

Figure 3.13: (a) Outer surface temperature at cutoff with emissivity variation; (b) energy and exergy efficiency at cutoff with external heat transfer coefficient variation.

3.4.2. The effect of heat stored in wall and heat loss

In order to evaluate the influence of the wall thermal properties and the heat loss on the efficiency of different size tanks, the thermocline thickness over discharging time under different boundary conditions are investigated, including (1) adiabatic or non-adiabatic and (2) with or without wall and insulation. The ending time was set as when thermocline region reaches the tank top in discharging. **Figure 3.14** shows that the thermocline thickness of other three conditions in discharging is always larger than the ideal condition (no wall, no insulation, and adiabatic state), proving that both the stored heat in walls and the heat loss would enlarge the thermocline thickness. Comparing adiabatic conditions of with/without wall and insulation, the degradation of thermocline in the lab-scale tank is more obvious than pilot-scale tank, due to more stored heat of wall returning to fluid in discharging as explained in earlier sub-sections. Without considering the stored heat in walls and the heat loss, the thermocline thickness might be underestimated by 10% and 15% for pilot-scale tank and for lab-scale tank, respectively.

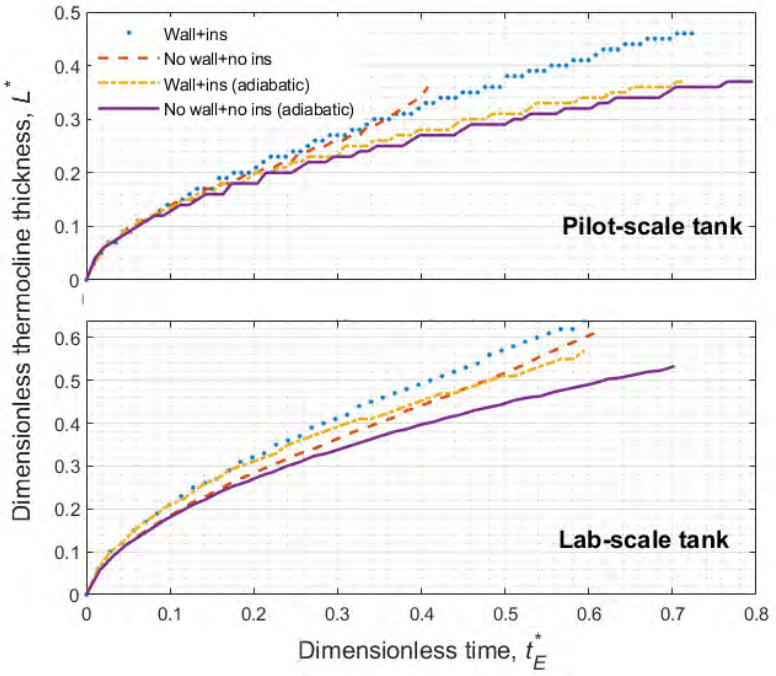

Figure 3.14: Thermocline thickness variation over discharging time under different boundary conditions of two tanks.

3.4.3. The effect of wall thickness and thermal conductivity

The walls parametric study was performed on the wall thermal conductivity and thickness by using the 1D-3P model according to sensitivity analysis in **FigureA 3.2** of the *Appendix*. Three indicators, including the energy efficiency (η), the exergy efficiency (η_x) and the discharging cutoff time, were examined in **Figure 3.15**. Recall that $\lambda_w^* = \frac{\lambda_w}{\lambda_f}$ means the ratio of wall thermal conductivity to fluid thermal conductivity (λ_f), and $L_w^* = \frac{L_w}{R_{int}}$ reflects the ratio of wall thickness to inner radius of fluid region (R_{int}).

At first, the reliable range of the model shows when λ_w^*>5. Because the Bi_w is low enough in this range the wall can be considered as a 1D, as discussed in detail in **FigureA 3.3** of the *Appendix*. Then, for both tanks, minimizing the wall thickness can maximize energy and exergy efficiencies (see yellow region) and decrease discharging cutoff time, because a thinner wall means less the initially stored heat of wall according to **Eq. 3.30**. In addition, for pilot-scale tank, the energy and exergy efficiencies decrease with the wall thermal conductivity increases, because the heat exchange rate from wall to fluid improves and the released heat of outlet improves. However, for lab-scale tank, efficiencies decrease with the wall thermal conductivity increase, because the cutoff time is decreased a lot. The stored heat in wall increases fluid temperature less for lab-scale tank than the pilot-scale tank. Thus, it was obtained that a thinner wall thickness causes a smaller impact on energy and exergy efficiency at the cutoff time.

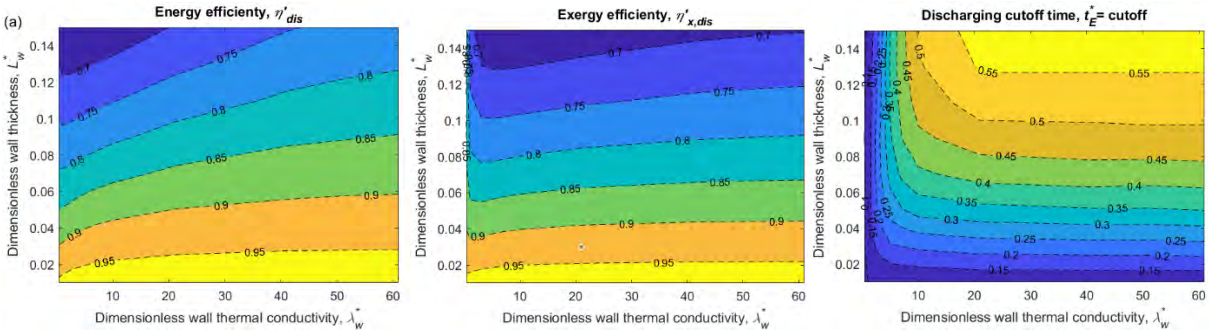

Pilot-scale tank

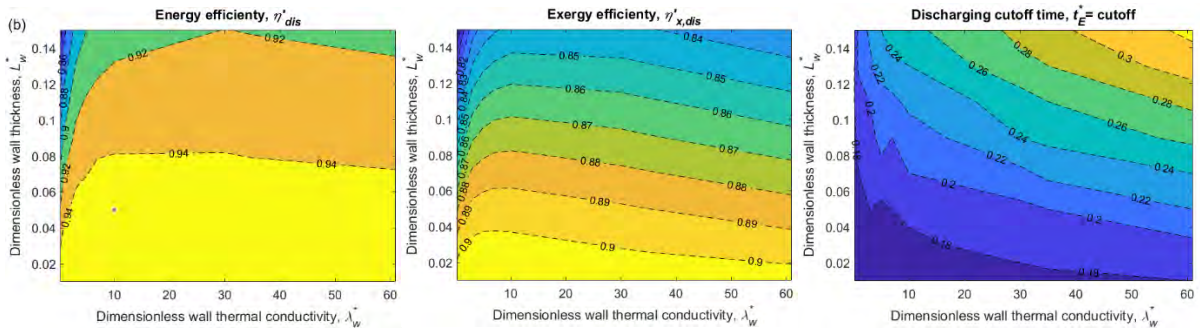

Lab-scale tank

Figure 3.15: The effect of wall thickness and thermal conductivity on energy efficiency, exergy efficiency and discharging time. (a) pilot-scale tank; (b) lab-scale tank.

3.5. Chapter conclusion

In this chapter, three models (1D-2P, 1D-3P, and 1.5D-4P) of thermocline packed-bed tank were first developed. After model validation by experimental data, the wall dynamic thermal behavior was fully investigated and the wall impact on the performance of packed-bed TES tanks has been evaluated. Finally, sensitivity and parametric analyses have been performed using the appropriate 1D-3P model to evaluate the influence of wall parameters. Main findings of this study may be summarized as follows.

(1) Before discharging, the maximum energy stored in wall at fully charged state can be up to 10% of the total stored energy. During discharging, the stored heat in wall can be released back to the fluid, increasing thereby the fluid temperature in contact as well as the thermocline thickness by up to 15%.

(2) The convective heat transfer between fluid and inner wall is dominant while the heat loss from the outer wall to the ambient is time-dependent and non-negligible. In contrast, the axial heat conduction in the walls and the pump power consumption can be ignored for these configurations.

(3) The stored energy in the insulation is small. As a result, the insulation phase may be simplified as a thermal resistance in the modeling. In this regard, the 1D-3P model could be a balanced choice between the complex physical phenomenon description and required computational time.

(4) The wall thermal conductivity and thickness have a great impact on wall energy balance, as well as a great interaction degree with other parameters. The optimal wall parameters for packed-bed TES tank are that a thinner wall has a smaller impact on the energy and exergy efficiencies at the discharging cutoff time.

The next chapter is focused on the thermocline packed-bed TES systems under influence factors in radial and axial direction including inlet configuration, insulation, flow rate, and inlet temperature, by comparing experimental and numerical results.

Appendix 3.I

Definition of dimensionless numbers

In order to solve the model with different parameters, the governing equations of 1D-3P model are nondimensionalized into:

$$\left(\frac{\partial T_f^*}{\partial t^*}+\frac{\partial T_f^*}{\partial z^*}\right)=\Pi_1\cdot\frac{\partial}{\partial z}\cdot\left(\frac{\partial T_f^*}{\partial z^*}\right)+\Pi_2\cdot\left(T_s^*-T_f^*\right)+\Pi_3\cdot\left(T_w^*-T_f^*\right) \quad \text{(A 3.1)}$$

$$\frac{\partial T_s^*}{\partial t^*}=\Pi_4\cdot\frac{\partial}{\partial z^*}\cdot\left(\frac{\partial T_s^*}{\partial z^*}\right)+\Pi_5\cdot\left(T_f^*-T_s^*\right) \quad \text{(A 3.2)}$$

$$\frac{\partial T_w^*}{\partial t^*}=\Pi_6\cdot\frac{\partial}{\partial z^*}\cdot\left(\frac{\partial T_w^*}{\partial z^*}\right)+\Pi_7\cdot\left(T_f^*-T_w^*\right)+\Pi_8\cdot\left(T_{amb}^*-T_w^*\right) \quad \text{(A 3.3)}$$

$$\Pi_1=\frac{1}{Pe}\cdot\frac{\lambda_{f,eff}}{\lambda_f}\cdot\frac{D_p}{H} \quad \text{(A 3.4)}$$

$$\Pi_2=St_{sf,eff}\cdot a_s\cdot H \quad \text{(A 3.5)}$$

$$\Pi_3=St_{f-w}\cdot a_f\cdot H \quad \text{(A 3.6)}$$

$$\Pi_4=\frac{1}{Pe}\cdot\frac{\varepsilon}{(1-\varepsilon)}\cdot\frac{\alpha_{s,eff}}{\alpha_f}\cdot\frac{D_p}{H} \quad \text{(A 3.7)}$$

$$\Pi_5=St_{sf,eff}\cdot a_s\cdot H\frac{\rho_f\cdot C_{p,f}}{\rho_s\cdot C_{p,s}}\cdot\frac{\varepsilon}{(1-\varepsilon)} \quad \text{(A 3.8)}$$

$$\Pi_6=\frac{1}{Pe}\cdot\varepsilon\cdot\frac{\alpha_w}{\alpha_f}\cdot\frac{D_p}{H} \quad \text{(A 3.9)}$$

$$\Pi_7=St_{sf,eff}\cdot a_w\cdot H\cdot\frac{\rho_f\cdot C_{p,f}\cdot\varepsilon}{\rho_w\cdot C_{p,w}} \quad \text{(A 3.10)}$$

$$\Pi_8=St_{w-amb}\cdot a_w\cdot H\cdot\frac{\rho_f C_{p,f}\varepsilon}{\rho_w\cdot C_{p,w}} \quad \text{(A 3.11)}$$

where,

Péclet number: $Pe=Re\cdot Pr=\frac{D_p\cdot u_{sup}}{\alpha_f}$ (A 3.12)

Stanton number: $St=\frac{Nu}{Re\cdot Pr}=\frac{Nu}{Pe}$ (A 3.13)

Heat diffusivity: $\alpha=\frac{\lambda}{\rho\cdot C_p}$ (A 3.14)

In definition, Π_i reflect the energy contribution to each phase. For example, Π_1, Π_4, and Π_6

represent the influence of the ratio of heat diffusion to increment term on energy, while Π_2, Π_3, Π_5, Π_7, and Π_8 represent the influence of ratio of the heat convection plus radiation to increment term on energy.

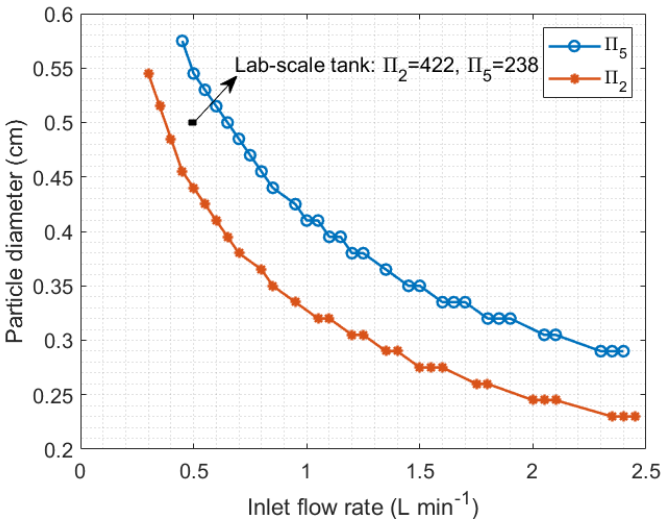

FigureA 3.1 The dominant dimensionless number of Π_2 and Π_5 of the lab-scale tank at the certain fluid interfacial velocity and particle diameter is near to the pilot-scale tank (Π_2=525, Π_5=201).

In order to set two tanks at a similar resolution condition, the Π_i were calculated and compared. Here, for the pilot-scale tank with a certain packing configuration, the Π_2 and Π_5 are dominant. Therefore, a comparison of both tanks can thus be conducted under the condition that the value of dominant Π_i of two tanks is determined to be close to each other in **FigureA 3.1**.

Appendix 3.II

Computational time needed for different models

TableA 3.1 Computational time of 1D-2P, 1D-3P, and 1.5D-4P model at cutoff time*.

Models	**Computation time (s)**		
	1D-2P model	**1D-3P model (1D wall+1D insulation)**	**1.5D-4P model (2D wall+2D insulation)**
Pilot-scale tank	5	8	833
Lab-scale tank	9	10	606

*The processor of the modeling computer is: Intel Processor Xeon CPU E5-2609 @2.40GHz.

Appendix 3.III

Parametric sensitivity analysis

To better understand the effect of different parameters on the performance of the storage tank, especially the wall impact, global sensitivity analysis (GSA) was conducted by using the 1D-3P model. An adaptation algorithm named the Morris method, or Elementary Effect (EE) method, which gives rough quantitative estimations with a limited number of calculations, was used based on a MATLAB toolbox provided by Pianos [184]. It computes two sensitivity indices for each input: one is the mean of EEs, measuring the effect of an input over output, and another is the standard deviation of EEs, representing the interaction degree with other factors. In this study, the main parameters ($\varepsilon, u_{v,f}, D_p,\ \lambda_s, L_w, \rho_s \cdot C_{p_s},\ \lambda_w, \rho_w \cdot C_{p_w}$) were served as input after considering the determined tank geometry size and HTF type. The Π_i in dimensionless energy equation were taken as outputs, which reflect the contribution of the heat convection, the convection, or the radiation on fluid, solid, and wall energy. The definition has been introduced in **Eq.s A 3.4-A 3.11**.

TableA 3.2 Value range of parameters for sensitivity analysis.

Parameters	**Symbols**	**Units**	**Ranges**	
			Pilot-scale tank	**Lab-scale tank**
Particle diameter	D_p	cm	0.2-1.0	0.2-1.0
Porosity	ε	--	0.2-0.4	0.2-0.4
Mass flow rate*1	$\dot{m}_f$	kg s^{-1}	3-10	8.3×10^{-3}-24.8×10^{-3}
Wall thickness*2	L_w	cm	4-15	0.3-1.0
Wall thermal conductivity	λ_w	W m^{-1} K^{-1}	0.2-60	0.2-60
Wall volumetric heat capacity*3	$\rho_w \cdot C_{p,w}$	J m^{-3} K^{-1} ($\times10^5$)	15-66	15-66
Solid thermal conductivity	λ_s	W m^{-1} K^{-1}	0.1-35	0.1-35
Solid volumetric heat capacity*3	$\rho_s \cdot C_{p,s}$	J m^{-3} K^{-1} ($\times10^5$)	15-66	15-66

*1 Mass flow rate for both tanks is determined according to the similar interfacial velocity range.

*2 Wall thickness for both tanks is determined according to the similar ratio range (wall thickness/tank height).

*3 Volumetric heat capacity for solid and wall are in range between the low (like glass or plastic) and high value (like metals).

TableA 3.3 Dimensionless number (Π_i) variation within the value range of parameters.

Dimensionless number	Pilot-scale tank	Uncertainty	Lab-scale tank	Uncertainty
Π_1	5×10^{-4}	$\pm 4\times10^{-4}$	8×10^{-3}	$\pm 5\times10^{-3}$
Π_2	4000	$\pm 3\times10^{4}$	243	± 1790
Π_3	1	± 1	1	± 1
Π_4	2×10^{-4}	$\pm 10\times10^{-4}$	4×10^{-3}	$\pm 10\times10^{-3}$
Π_5	14000	± 35000	120	± 1380
Π_6	10×10^{-4}	$\pm 8\times10^{-4}$	14×10^{-3}	$\pm 80\times10^{-3}$
Π_7	2	± 14	3	± 15
Π_8	22×10^{-4}	± 0.2	14×10^{-3}	$\pm 70\times10^{-3}$

For different operational conditions or packing configurations, the parametric sensitivity analysis within the variable ranges of parameters was studied. The value range of parameters is indicated in **TableA 3.2** and the corresponding dimensionless number variation is reported in **TableA 3.3**. For both tanks, the influence of heat convection (Π_2, Π_5) on the performance of storage tank is larger than heat loss (Π_3, Π_7, Π_8), while the influence of axial conduction (Π_1, Π_4, Π_6) can be largely ignored. This is in line with our findings reported above. Samples number is defined as 4000 according to the convergence result shown in **FigureA 3.2 a b.**

The dominant Π_i (Π_2, Π_5, Π_7, and Π_8) for each phase all own to heat convection. Π_7 have dominant influence on wall energy balance due to the wall impact on heat loss of lab-scale tank. Thus, **FigureA 3.2 c d** displays the means and standard deviation of EEs of main parameters for Π_7 of two tanks. It was demonstrated that wall volumetric heat capacity, wall thickness, and wall thermal conductivity have a great impact on wall energy balance, as well as a great interaction degree with other parameters. Considering the wall volumetric heat capacity is the inherent property of material, the wall parameters only containing wall thickness and wall thermal conductivity be studied in this study.

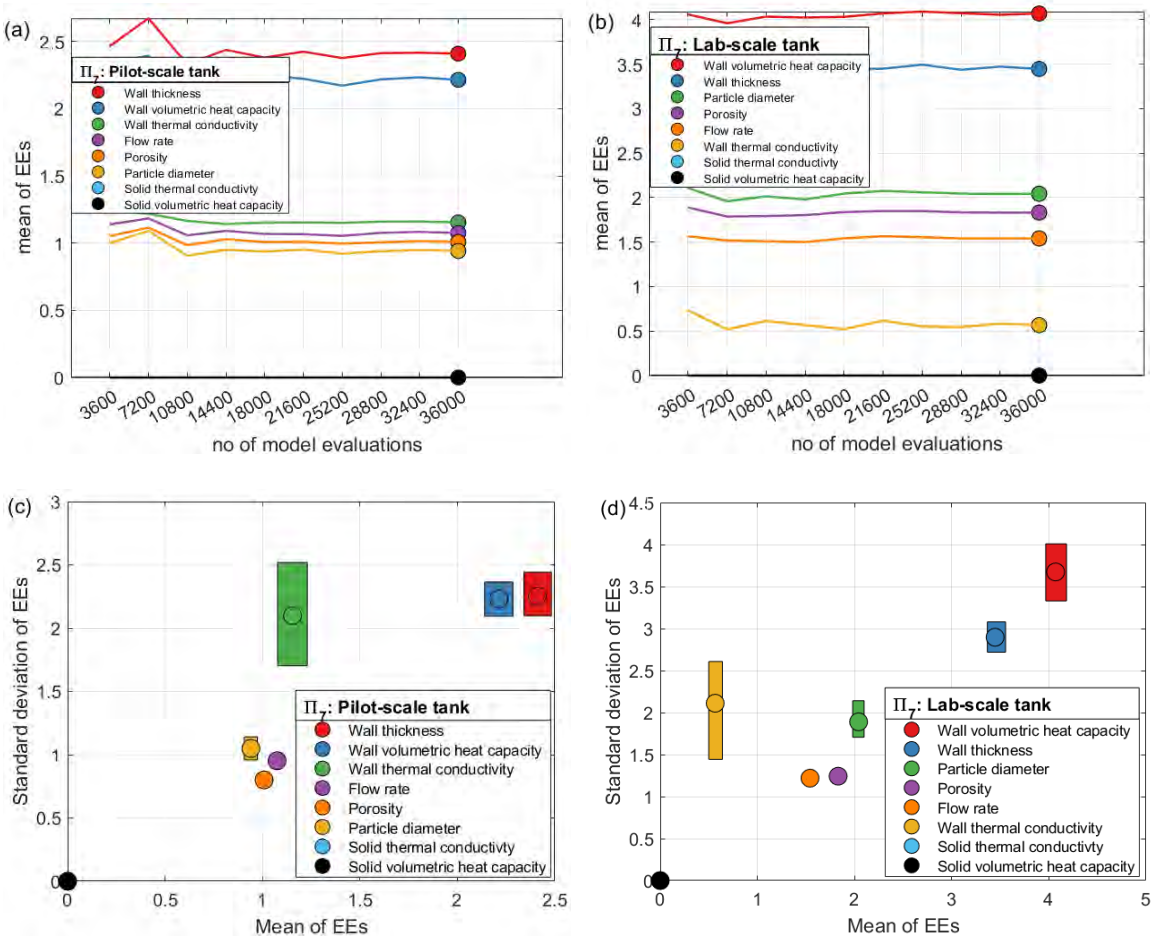

FigureA 3.2: Sensitivity analysis: convergence results of dominant dimensionless number Π_7 (a), (b); elementary effect method of Π_7 (c), (d).

Appendix 3.IV

Variation of wall-to-fluid Biot number

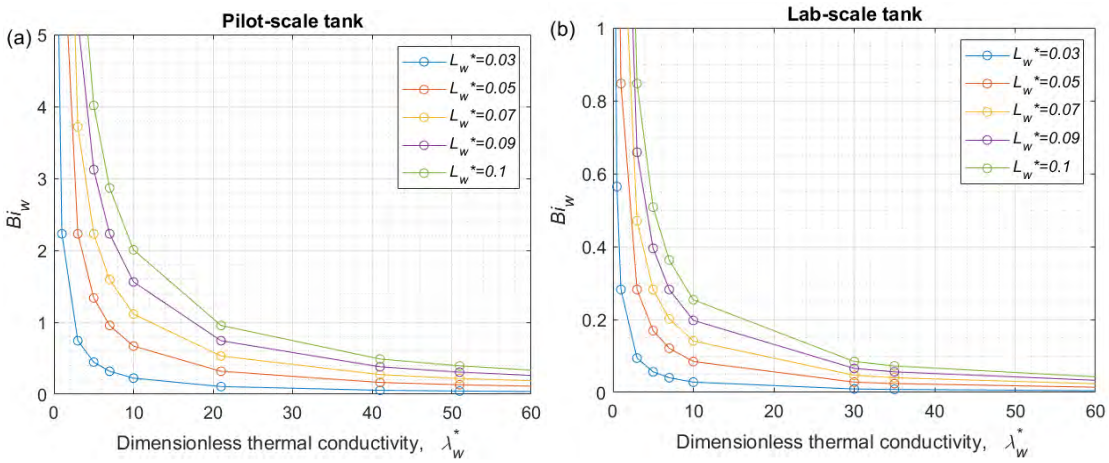

FigureA 3.3: Wall-to-fluid Biot number (Bi_w) variation with the change of wall thermal conductivity and dimensionless wall thickness: (a) pilot-scale; (b) lab-scale tank.

FigureA 3.3 shows the variation of Bi_w with the change of two variables: the wall thermal conductivity and the dimensionless wall thickness. The Bi_w, a ratio of thermal resistance of the inside wall and inner surface of wall, can reflect the reliability of the model at relatively low value (especially Bi_w<0.1). As it shows, the Bi_w increases sharply when λ_w^*<5. Thus, the inflection point near λ_w^*=5 can be used as a threshold value that the model results is validated.

Chapter 4
Thermocline in packed-bed storage tank with sensible fillers under impacts in radial and axial direction

Abstract

After exploring the wall impact in the last chapter, **this chapter is trying to** investigate the impacts including the inlet configuration, insulation, mass flow rate, inlet temperature, and etc., in both radial and axial direction, on thermocline behavior and overall performances. The investigation is based on a sensible packed-bed thermal storage system (SHTPB) of a low-temperature lab-scale tank. The goal of this chapter is to provide useful design and operational guidelines for SHTPB tanks in practical.

The objective of this chapter includes:

- Improve the model of wall heat capacity for large size particles and determine the applicable ranges.
- Validate the thermal gradient inside sensible particle.
- Assess the influences of radial temperature non-uniformity due to the injecting flow and heat loss with experiments.
- Clarify the impact of solid and fluid heat transfer and the axial diffusion based on parametric study through comparison of numerical and experimental results.
- Propose an application of this configuration and model for latent heat packing.

Keywords: sensible fillers, flow diffuser, insulation, mass flow rate, experiment, DC-3P model

This chapter is under review by Renewable Energy.

Chapter content

4.1. Introduction

In theory, the thermocline quality evaluated by its stability and thickness reflects the SHTPB system's performance: higher level of thermal stratification in the thinner thermocline zone means higher energy and exergy efficiencies [32][33]. Nevertheless, the thermal stratification tends to become unstable and expanded over dynamic and cycling operations. This thermocline degradation (or decay) can be due to many factors [34][35]. On one hand, the low heat transfer rate between heat transfer fluid (HTF) and solid fillers or the strong heat diffusion inside HTF, solid media, or wall phases, would result in the expanded thermocline thickness in the axial direction [185]. On the other hand, the flow injection, the heat loss to the environment, and the wall impacts would cause the non-uniform radial temperature distribution inside the tank, lowering thereby the thermocline stability and increasing the thermocline thickness [148][186].

4.1.1 Effect on radial temperature gradient

Uniform radial flow velocity and temperature profiles are usually assumed in one-dimensional (1D) models (e.g., Schumann model) for modeling SHTPB systems due to the flow homogenizing effect of the porous fillers [187]. The necessity of additional flow diffuser instead of inlet port in packed bed storage tanks to guarantee the good and stable thermal stratification is controversy in early stages. There is study focusing on installing special types of flow diffuser in SHTPB tanks to effectively utilize the bed domain [188]. Later, Bruch et al. [90] experimentally observed that there was no significant inhomogeneity of radial temperature in a SHTPB tank without diffuser (tank height to diameter aspect ratio $\frac{H}{D_{tank}}$=3) and proposed that the 1D heat transfer model was adequate. Yin et al. [117][189] also experimentally tested in a near-tube tank ($\frac{H}{D_{tank}}$=5) and showed that the porous fillers could help to maintain the HTF as an ideal plug flow pattern. However, up to different inside configurations and various heat transfer behavior, the real impact of the injecting flow on the thermal performance is different. For example, Reddy and Pradeep [190] numerically observed that the radial non-uniform temperature distribution of their SHTPB tank ($\frac{H}{D_{tank}}$=4) is negligible in laminar flow owing to the porous packed bed working as flow distributor, but not in turbulent condition. Wang et al. [191] simulated a flow annul diffuser (80% annular area) at the inlet of a SHTPB tank ($\frac{H}{D_{tank}}$=1/3) and found that the non-uniformly radial flow has a limited influence on output energy but it affects the interstitial heat transfer thus improving thermal performance. Recently, there is an interesting and systematic work conducted by Vannerem et al. [4] to analyze these problems by comparing three types of baffle-type flow diffusers, as well as considering different flow rates. They found that the solid filler acts as a natural distributor and fluid distribution at the inlet does not impact the global storage

performance due to the flow being restricted to a small fraction of the packed bed in their SHTPB tank ($\frac{H}{D_{tank}}$=2). Low flow rate keeps this homogeneity. In brief, more investigations are still needed to show from what height (distance to the inlet) such radial temperature gradient can be eliminated by the porous bed with different packing properties (e.g., particle size, Biot number, etc.), and to further clarify the relation between the thermocline expansion due to the injecting flow and the global thermal performance reduction of the SHTPB tank.

The wall impact and associated heat losses are another influencing factor on the radial temperature distribution of SHTPB tank. Early studies [186][192] reported the existence of radial temperature gradient for about 30-40% of the tank radius due to the heat loss, leading to the higher centerline temperature than that in near-wall region. This radial temperature gradient cannot be reflected in the 1D model and will cause the smaller amount of energy stored in the SHTPB tank than predicted [193][148]. Hoffmann et al. [34][155] reported that the heat losses would lead to the unstable thermocline, reduced output power, and decreased outlet temperature. Xie et al. [88] have developed adapted transient models to systematically explore the wall impact on the dynamic thermocline behavior of the SHTPB tanks by including the wall and insulation heat capacity in the governing equations. The most influencing factors have also been identified to provide useful design guidelines. Nevertheless, systematic experimental investigation of a SHTPB tank under two extreme conditions (with or without insulation) is still needed in order to validate the developed numerical model. This topic will be discussed in detail in the current work.

4.1.2 Effect on axial heat diffusion and heat transfer

The thermal stratification in the axial direction of SHTPB tank is mainly determined by the heat transfer rate between the HTF and solid fillers as well as the thermal diffusion of the liquid and solid phases. One of the key operating parameters is the charging/discharging flow rate (or the superficial fluid velocity) which has been subjected to many parametric studies with the purpose of improving the overall efficiency of the storage tank [25]. On the one hand, the increasing flow rate would enhance the solid-fluid heat transfer, decrease the thermal diffusion [4][194], and reduce the heat loss to environment owing to the lower charging/discharging time (or residence time) [195]. These effects contribute to the increased overall efficiency of the SHTPB tank. In this regard, Al-Azawii et al. [195] experimentally tested a SHTPB tank with small particles size (Sphere Biot number, Bi_s<0.1, $\frac{H}{D_{tank}}$=8) under 21.5-150 °C and found that the overall exergy efficiency could be increased from 35.7% to 55.4% by increasing the air flow rate from 120 to 366 L min^{-1}. On the other hand, the incoming flow at a high flow rate can penetrate deeper along the centerline of the SHTPB tank (radial temperature non-uniformity as mentioned above), leading consequently to the thermocline expansion and lowered efficiency. Kocak and Paksoy (2019) [196]

numerically proved that when the Reynolds numbers (Re) increased from 22 to 135 the charging efficiency reduced by about 30% because of the local flow turbulences. As a result, efforts have been devoted to find the optimal operating flow rate (or velocity) that leads to the best performance of SHTPB tanks. For example, Hoffmann et al. (2017) [34][155] and Vannerem et al (2021) [4] both numerically proved the existance of an optimal HTF flow rate for a SHTPB tank (Bi_s<0.1) operated under medium or high temperature (100-300 °C). Kocak and Paksoy (2020) [71] experimentally obtained a maximum system energy efficiency of 67% at charging temperature of 150 °C under the optimum charging superficial fluid velocity of 1.9 mm s^{-1} (Re<10, Bi_s<0.1). Nevertheless, all the tested cases are with small particle fillers and a low Bi_s number, the combined impact of HTF flow rate and heat loss on the thermocline expansion of SHTPB tanks with larger particle size (Bi_s>0.1) is still not enough clear thus should be further investigated experimentally.

4.1.3 Aim and scope

Numerical modeling and simulation tools have the advantage of testing the influences of various variables so to predict the thermal performance of the SHTPB tanks under different operational and geometrical conditions. Nevertheless, each numerical model for SHTPB tanks has its own accuracy due to different assumptions made, and at first, its applicable range needs to be tested and validated by experimental results. **Table 4.1** lists main experimental investigations using sensible fillers reported in the open literature. Systematic investigations on the impacts of various influencing factors on the thermocline expansion are still needed, especially for SHTPB tanks operated under low temperature range (<100 °C).

For all these reasons, a lab-scale SHTPB tank has been fabricated, instrumented and experimentally tested under controlled conditions. The dynamic thermocline behaviors under charging and discharging operations have been systematically characterized by both the numerical and experimental approaches so as to evaluate the impacts of various influencing factors (inlet configuration, insulation, HTF flow rate, filler particle size, etc.) on the axial and radial thermocline expansion and on the overall performances of the SHTPB tank. The obtained experimental data-sets, especially under small flow rate (Re<15), relatively large particle size (Bi_s>0.1) and low temperature (<100 °C) operational conditions, could also be used to determine the applicable range of different numerical models in view of model validation. It is also expected that this work can provide useful design and operating guidelines for alleviating thermocline expansion in SHTPB tanks in practical applications.

Table 4.1 Summary of experimental investigations on SHTPB TES systems.

Studies	Years	Solid fillers	HTFs	T_C/T_H (°C)	ε	H/D_{tank} (m)	Number of thermocouples & arrangement	Diffuser	Insulation	Num./ Exp.	Tested parameters in Exp.	Main findings
Faas et al. [176][177]	1986	Granite Rock and sand	Caloria ® HT 43	179.2/ 295.5	0.22	12/1 8.2	--	--	Yes	Exp.	--	● Low Rankine-cycle efficiency of 21% due to limited upper temperature of TES tank.
Meier et al. [48]	1991	Rock	Air	150/55 0	0.36	1.2/0 .15	-- (axial)	--	Yes	Exp.	--	● Considerable heat losses through the wall. ● Smaller measured pressure drop than predicted due to low flow resistance near wall.
Pacheco et al. [104]	2002	Quartzite rock & sand	Molten salt	290/39 0	0.22	6/3	-- (axial and radial)	Yes	Yes	Num./ Exp.	--	● Thermocline thickness well predicted by the model. ● higher heat loss than predicted due to the lack of insulation on the top cover of the tank.
Yang et al. [197]	2012	Rock	Molten salt	300/50 0	0.2	2/1	12 (axial)	No	Yes	Num./ Exp.	--	● Higher thermal storage capacity and efficiency by using fillers with higher density and specific heat, but also higher entropy generation (Num.).
Yin et al. [117][189]	2014/ 2017	Zirconium & silicon carbide	Molten salt	290/39 0	--	0.6/0 .12	6 (axial)	Yes	Yes (heating strap)	Exp.	● Inlet HTF temperature ● Flow rate ● Mixed fillers	● Heat storage efficiency is smaller than 80% due to the thermocline expansion. ● Thermocline evolution influenced by HTF velocity. ● Piston flow pattern achieved by buffering effect of porous fillers.
Anderson et al. [198]	2014	Alumina	Air	20/120	0.4	10/9. 56	-- (5 for axial outer tank surface)	No	Yes	Num./ Exp.	--	● Vessel heat loss is acceptable due to only loss 12% of supplied energy.
Bruch et al. [90]	2014	Silica gravel & silica sand	Oil	⩽ 300	0.27	3/1	250 (for fillers and HTF, axial and radial circle)	Yes	Yes	Num./ Exp.	● Cycling number	● No significant inhomogeneity of radial temperature distribution. ● Differed thermocline behavior between multiple cycle and single cycle operation. ● Impact of metal tank wall on the thermocline moving in charging.
Cascetta et al. [148][193]	2015/ 2016	Alumina	Air	25/300	0.385 - 0.395	1.8/0 .58	19 (axial equally spaced), 5 (radial, decreasing distance), 10 (axial outer surface) 5 (circumferential outer surface)	Yes	Yes	Num./ Exp.	● Cycling number	● 40% radial temperature profile affected by metal wall heat, which cannot be predicted by 1D model. ● 60% reduction of stored energy after 4 cycles.
Hoffmann et al. [155][34]	2016/ 2017	Quartzite rock	Rapeseed oil	160/21 0	0.4	1.8/0 .4	32 (axial and radial equally spaced)	No	Yes	Num./ Exp.	● Flow rate ● Particle size	● Higher heat losses and heat diffusion due to low HTF flow rate. ● Stronger forced convection due to high HTF flow rate. ● Maximum discharging efficiency of 75% at an optimal flow rate of 0.3 kg s^{-1}.

Al-Azawii et al. [195][199]	2018/ 2019	Alumina	Air	21.5/150	0.375	1/0.1247	--	Yes (10 cm distance)	Yes	Num./ Exp.	● Flow rate	● Higher heat losses due to low HTF flow rate. ● Increased exergy efficiency from 35.7% to 55.4% with increasing flow rate from 0.002 to 0.006 $m^3 s^{-1}$.
Tuttle et al. [72]	2020	Limestone and stone	Air	25/587	0.3	0.9/0.3	8 (axial equally spaced)	--	Yes	Num./ Exp.	--	● Relative error on the temperature between particle surface and center larger than 55% at particle Bi_s = 3 (Num.).
Kocak and Paksoy [71]	2020	Demolition wastes	Therminol 66	120/180	0.39	0.9/0.3	9 (axial and radial)	No	Yes	Num./ Exp.	● Inlet HTF temperature ● Flow rate	● Reduced energy efficiency with the increasing charging temperature. ● Thermocline expansion at higher flow rate due to the stratification disturbance. ● Thermocline expansion at lower flow rate due to heat loss.
Keilany et al. [200]	2020	Alumina/ Cofalit® rock	Jarysol® oil	100/300	0.417	2.64/1.2	22 (axial and radial)	Yes	Yes	Num./ Exp.	● Solid filler	● Good thermal performance of Cofalit® filler than alumina.
Vannerem et al. [4]	2021	Alumina	Jarysol® oil	100/300	0.485	2.64/1.2	22 (axial and radial)	Yes	Yes	Num./ Exp.	● Flow rate	● Maximized storage utilization rate (80.6%) at an optimal velocity (Num.). ● Robust performance of storage tank under the experimental testing range (100 - 130 °C) and (0.2 - 0.9 kg s^{-1})
Vannerem et al. [5]	2022	Alumina	Jarysol® oil	100/300	0.485	2.64/1.2	63 (axial and radial)	Yes	Yes	Exp.	● Flow distributor	● Solid filler acts as a natural distributor. ● Distributor does not influence storage behavior. ● Radial homogeneity is then improved at low fluid velocity.
Gautam and Saini [201]	2021	--	Air	<100	--	1.25/0.6	50 (for fillers and HTF, axial and radial)	No (but plenum achieve uniform flow)	Yes	Exp.	● Flow rate ● Sizes for particles with pore	● Correlations proposed to predict the Nusselt number.
Bruch et al. [202]	2021	Rock	Water	20/70	--	4/2	5 (axial equal and radial circle)	Yes	No	Exp.	● Flow rate ● Inlet HTF temperature	● Cold energy storage system is able to successful store cold at night and compensate performance loss of cooler in daytime.
Alonso and Rojas [203]	2022	Silica/ Soft stone	Air	25/700	0.31/0.37	0.72/0.5	28 (axial and radial, for HTF and outer surface)	--	Yes	Num./ Exp.	● Solid filler	● Important role of heat capacity of solid fillers. ● Very low heat loss owing to the well-insulated tank walls.
Xu et al. [204]	2022	Aluminum silicate	Water	<60	--	3/1	164 (axial and radial, for HTF and outer surface)	Yes	Yes	Num./ Exp.	● Flow rate	● Thermocline stability disturbed by the radial plate-type diffuser. ● Model developed based on thermal diffusion to predict the thermocline evolution in axial direction, with an average error of about 13.9%.
This study	2022	Glass	Water	20/70	0.38/0.39	0.4/0.2	32 (axial and radial, for HTF and solid fillers)	Yes	Yes	Num./ Exp.	● Diffuser ● Insulation ● Particle size ● Flow rate ● Inlet temperature	--

4.2. Experimental setup and improved model

4.2.1. Test-rig description

This experimental set-up is first designed by Lou et al. [8] in LTEN laboratory of a one-tank system for flow diffuser optimization. It was then modified for the packed-bed one tank system in this thesis.

The laboratory-scale SHTPB tank tested has a cylindrical shape with a height of 398 mm and an inner diameter of 194 mm (**Figure 4.1 a**), the total useful volume being 11.8 L. It has a transparent polycarbonate wall (3 mm in thickness) enclosed by an insulation layer made of black nitrile rubber (25 mm thickness). Glass spheres as the sensible fillers are randomly filled inside the tank. Water is used as the HTF. During charging process, the hot water flows the top port and cold water flows out from the bottom port of the tank, and vice-versa for the discharging process. Note that top and bottom ports are simple tubes (Φ= 11.6 mm) located at the center of the top and bottom cover of the tank.

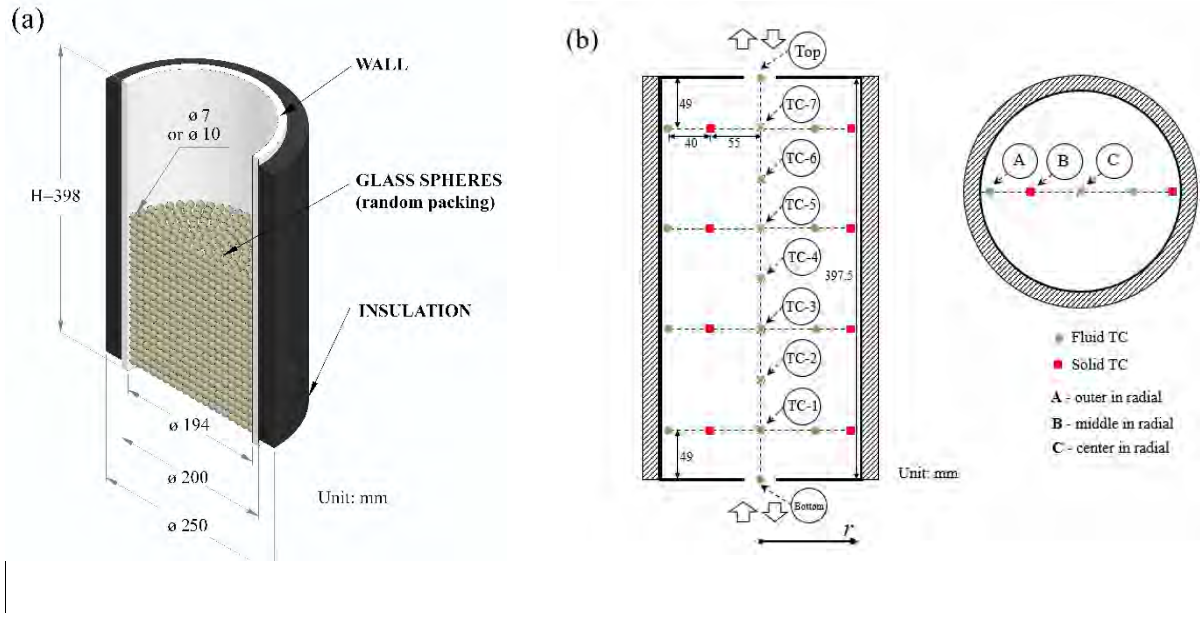

Figure 4.1: Laboratory-scale SHTPB tank tested: (a) Geometry and dimensions; (b) axial and radial thermocouples locations inside the tank.

In total, 32 k-type thermocouples have been used to measure the local temperatures at different locations in the storage tank, including 17 for the fluid phase and 15 for the solid phase. They are all attached to a plastic tree which has been carefully installed inside the tank, as schematically shown in **Figure 4.1 b**. In axial direction, both fluid and solid temperatures were measured with 7 thermocouples located on heights of the centerline (C in **Figure 4.1 b**). They are at 49 mm distance one from another and notated as TC-1 to TC-7 from the bottom to the top of the

tank. In order to investigate the radial temperature distribution, the fluid and solid temperatures at the middle (B in **Figure 4.1 b**; tank diameter coordinate r=0.55) and outer (A in **Figure 4.1 b**; r=0.95) positions were measured in four radial arms (TC-1; 3; 5; 7). In addition, the inlet and outlet fluid temperatures were also measured at the top and bottom port, respectively. Note that the thermocouples for glass sphere were installed in the center of sphere and sealed by glue with similar thermal conductivity as glass (cf. **Figure 4.3**).

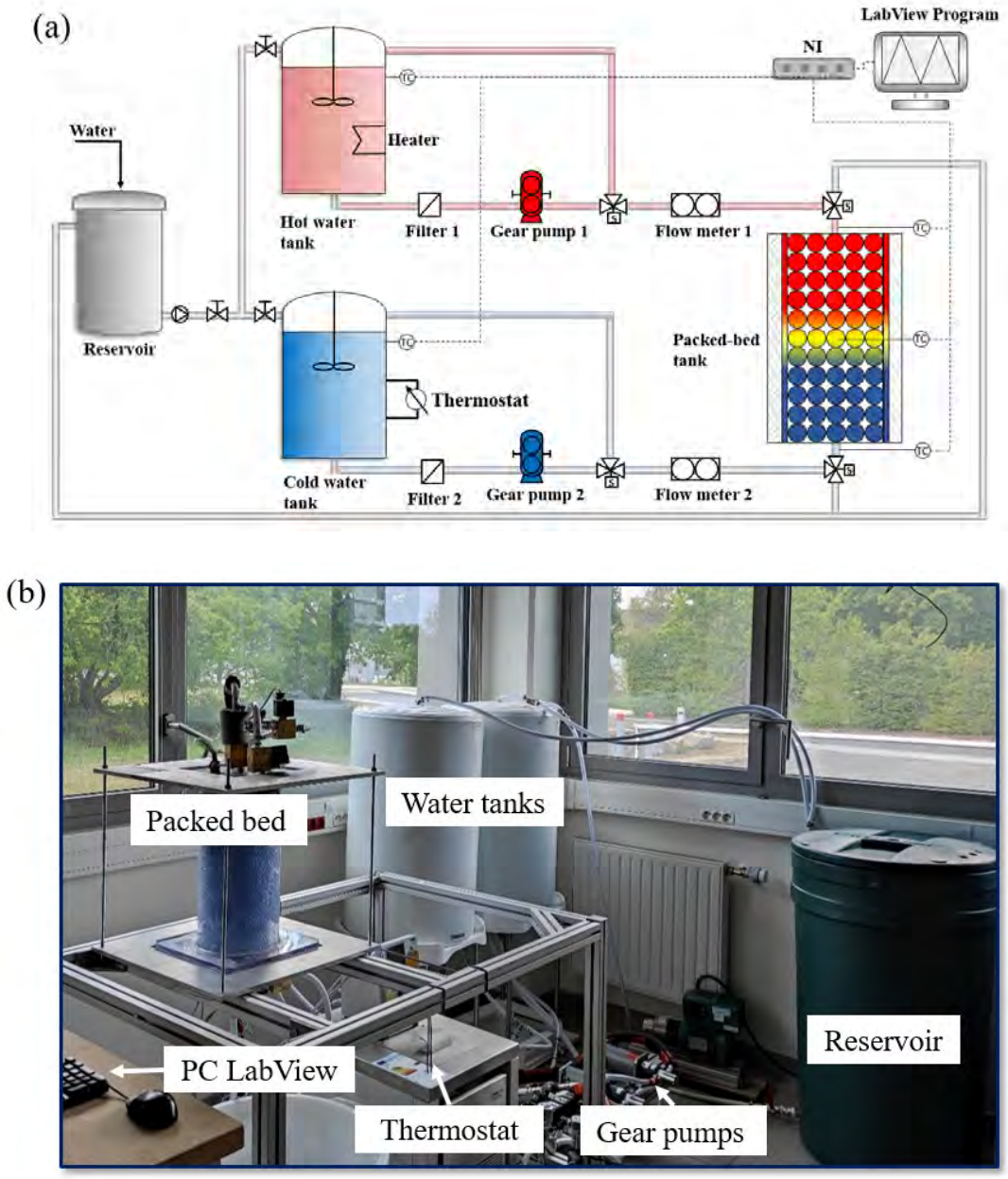

Figure 4.2: Schematic view (a) of the experimental test loop and photographic view and (b) for the laboratory-scale SHTPB tank (without insulation).

Figure 4.2 shows the schematic and the photo view of the experimental setup used to study the SHTPB TES system. A hot and a cold water tank was used as hot and cold source for testing the SHTPB tank in charging or discharging, respectively. A PID-controlled electrical heater installed inside the hot water tank and a low-temperature thermostat with smart cool system (Lauda, RP 855) connected to the cold water tank were used to stabilize the water temperature in each tank. Stirring devices were installed in both water tanks, ensuring the homogenous water temperature inside. Two magnetic coupled external gear pumps (Tuthill D-series, 0.07 to 7.63 L min^{-1}) with filters were used to deliver the HTF from the water tank to the top/bottom port of the storage tank. The flow rate of the HTF was controlled and measured by a flow meter (Kobold DPM-1550, 0.05 to 50 L min^{-1}) A reservoir was used to collect the water flowing out from the SHTPB tank for recycling.

The electronic signals, including the valves, thermocouples, and the gear pump and the flow meters, were controlled and recorded by corresponding modules. In particular, the temperature measurements of K-type thermocouples (-75 to 260 °C.) were recorded by a temperature input module (NI 9214 and NI 9213) with up to 0.02 K uncertainty. The recorded signals were monitored at an interval of 0.25 s by using a LabView program developed by the LTEN laboratory. The pressure drop was estimated to be very small (ΔP<50 Pa) due to the small tank volume and relatively low flow rate, thereby it could be neglected. A detailed estimation of the measurement uncertainties is presented in Section 4.2.5.

Both the charging and discharging operations were tested. In charging, hot water first entered from tank top port and transfers heat to solid fillers inside to store heat. In discharging, cold water entered from tank bottom port to drive the stored hot water from tank top to release heat. The charging or discharging stopped when each outlet temperature reached the corresponding set point according to the designed requirement.

4.2.2. Tested cases

To evaluate the various impacting factors (inlet configurations, mass flow rate, insulation, inlet temperature, etc.) on the thermocline, six SHTPB configurations were experimentally investigated in this work, including two sizes of glass fillers, three inlet diffuser configurations, and with/without insulation. Details of these configurations and the main operating parameters are listed in **Table 4.2**.

In order to verify the temperature gradient inside the glass sphere and to explore the influence of particle size on the thermocline behavior, two sizes of glass spheres (7 mm and 10 mm) with the same thermophysical properties (cf. **FigureA 4.1 a** of the *Appendix*) were used as packing in **Figure 4.3**.

Table 4.2 Tested SHTPB configurations.

Configurations	**Diameter of the glass sphere D_p (mm)**	**Diffuser position z_1 (mm)**	**Insulation thickness (mm)**	**ε**	**Flow rate (L min^{-1})**	**T_C/T_H (°C)**
Case 1	7	--	25	0.38	0.3-1.5	20/(50, 60, 70)
Case 2	7	--	--	0.38	0.3	20/70
Case 3	10	--	25	0.39	0.3-1.5	20/(50, 60, 70)
Case 4	10	--	--	0.39	0.3	20/70
Case 5	10	10	25	0.39	1.5	20/(50, 60, 70)
Case 6	10	35	25	0.39 (bed region)	1.5	20/(50, 60, 70)

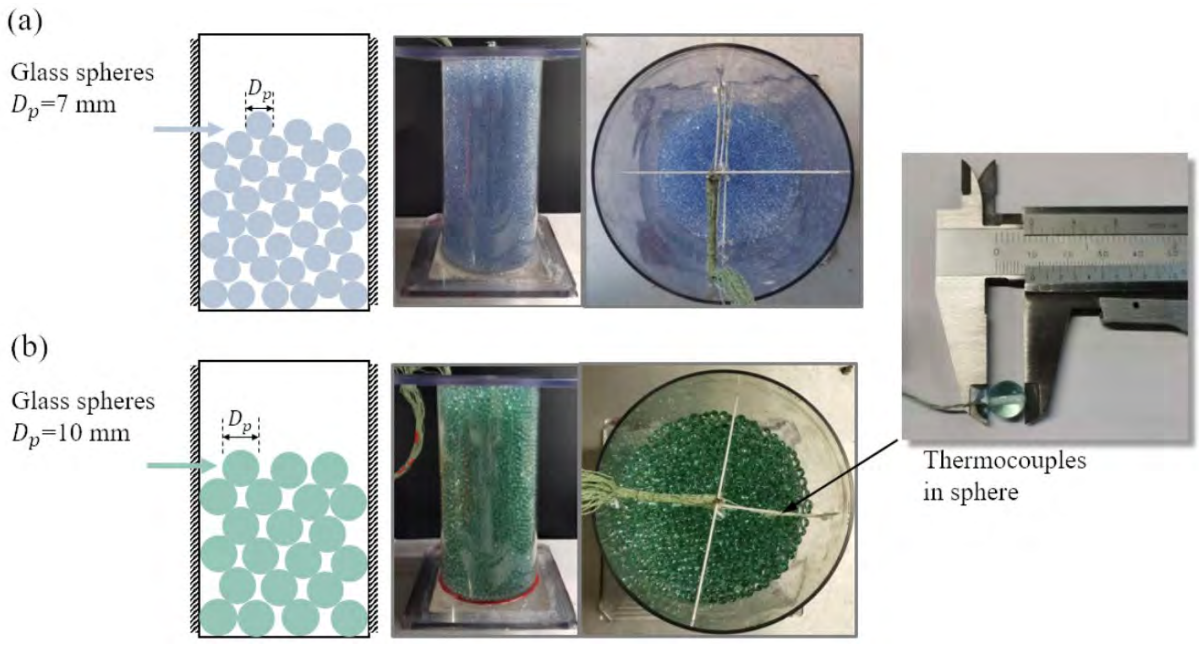

Figure 4.3: Photograph of SHTPB tank configurations without insulation: (a) case 2, 7 mm glass ball (b) case 4, 10 mm glass ball.

In order to analyze the buffering effect of porous bed to alleviate the impact of inflowing HTF jet on the thermocline stability, 3 inlet configurations were tested for comparison as shown in **Figure 4.4**. Case 3 is the fully packed tank without diffuser while top and bottom diffusers are introduced in Cases 5 and 6. The plate-type diffuser (6 mm in thickness) having three ring-shaped grooves has been optimized and tested for a single-media thermocline TES tank in our previous works [8]. In Case 5, the gap between the diffuser at z_1=10 mm and the tank top/bottom cover was filled with one layer of glass spheres to make full use of the tank volume, both the porous bed and the plate diffuser acting as the inlet configuration. In comparative Case 6, no solid fillers were

packed in this gap to eliminate the effect of porous fillers, and the height was set to be larger (z_1=35 mm) to amplify the impact of inflowing jet and mitigating effect of the plate-type diffuser. Moreover, in order to explore the impact of heat loss on thermocline expansion, both Case 2 and Case 4 without insulation layer were tested and compared with others.

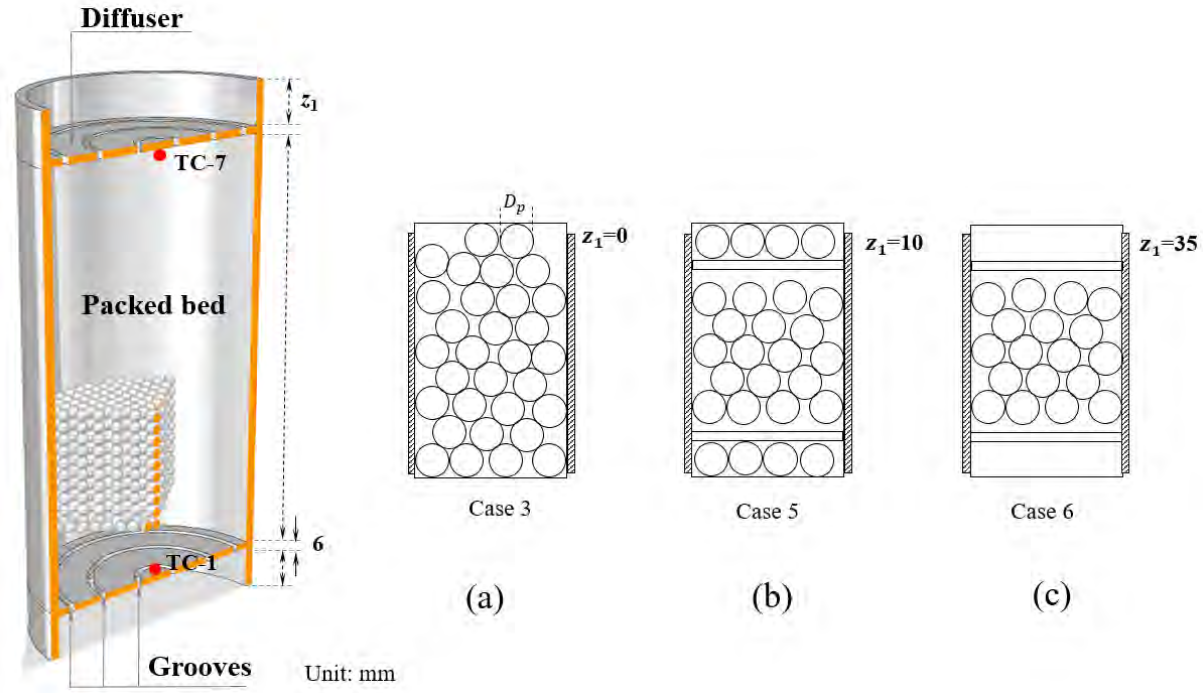

Figure 4.4: Different inlet diffuser configurations experimentally tested in this study: (a) only porous bed; (b) porous bed & plate diffuser; (c) only plate-type diffuser.

4.2.3. Improved dispersion-concentric three-phase model

In order to consider the thermal gradient inside the ball (Bi_s>>0.1), a dispersion-concentric three-phase (DC-3P) numerical model (**Figure 4.5**) is developed based on the 1D-3P model in Chapter 3. Assumptions and equations are follows:

(1) Solid sphere is modeled as dispersion concentric because of the possible non-ignorable temperature gradient inside (Bi_s>0.1).

(2) Wall is modeled as a separate phase in 1D (axial direction).

(3) Insulation layer is simplified and represented by a thermal resistance in Chapter 3.

(4) Thermophysical properties of fluid and solid materials (**Table 4.3**) are set as constant due to relatively small operational temperature range.

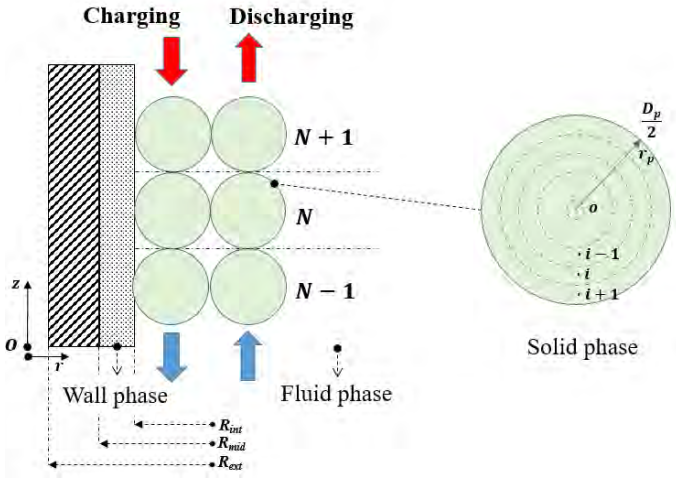

Figure 4.5: Schematic of numerical resolution domain for the developed DC-3P model.

Table 4.3 Thermophysical properties of different materials used in this study.

	Material	Density ρ (kg m^{-3})	Heat capacity C_p (J kg^{-1} K^{-1})	Thermal conductivity λ (W m^{-1} K^{-1})	Kinematic viscosity μ (Pa s)
Fluid (47.5 °C) [178][30]	Water	990	4187	0.634	5.8×10^{-4}
Ambient (20 °C, 100 kPa)	Air	1.17	1004	2.63×10^{-2}	1.8×10^{-5}
Solid media (20 °C)	Soda lime glass	2463	840	1.129	--
Wall (20 °C)	Transparent polycarbonate	1200	1170	0.200	--
Insulation (20 °C)	Black nitrile rubber	160	1350	0.0412	--

● Governing equations

Fluid (1D):

$$\varepsilon \cdot \rho_f \cdot C_{p,f} \cdot \left[\frac{\partial T_f(z)}{\partial t} + u_f \cdot \frac{\partial T_f(z)}{\partial z}\right] = \frac{\partial}{\partial z} \cdot \left[\lambda_{f,eff} \cdot \frac{\partial T_f(z)}{\partial z}\right] + h_{sf} \cdot \frac{A_s}{V_s} \cdot \left[T_s'(z, r_p = \frac{D_p}{2}) - T_f(z)\right] + h_{f-w} \cdot \frac{A_{f-w}}{V_b} \cdot \left[T_w(z) - T_f(z)\right] \quad (4.1)$$

Solid (2D spherical radius coordinate):

$$\rho_s \cdot C_{p,s} \cdot \frac{\partial T_s(z,r_p)}{\partial t} = \frac{1}{r_p^2} \cdot \frac{\partial}{\partial r_p} \cdot \left[r_p^2 \cdot \lambda_s \cdot \frac{\partial T_s(z,r_p)}{\partial r_p}\right] \quad (4.2)$$

Wall (1D):

$$\rho_w \cdot C_{p,w} \cdot \frac{\partial T_w(z)}{\partial t} = \frac{\partial}{\partial z} \cdot \left[\lambda_w \cdot \frac{\partial T_w(z)}{\partial z}\right] + h_{f-w} \cdot \frac{A_{f-w}}{V_w} \cdot \left[T_f(z) - T_w(z)\right] + h_{w-amb} \cdot \frac{A_{f-w}}{V_w} \cdot \left[T_{amb} - T_w(z)\right] \quad (4.3)$$

where r_p-axis is the spherical coordinate in the schematic used for the fillers, differ to the r-axis radial coordinate of tank. T_s' is the solid surface temperature.

● Boundary and initial conditions

In a charging/discharging cycling process, the boundary and initial condition are described in **Table 4.4**. It assumes the initial condition of changing is fully discharged and with a homogenous coldest operating temperature, while the cutoff temperature after charging is the beginning of discharging.

● Solving and steps

The solving of the model is the same to that one designed in Chapter 3. **Figure 4.6** shows the results of height mesh size and time step sensibility test with a variation of the particle mesh size. It calculated that the cutoff temperature variation is smaller than 1% when the height node number ($N = \frac{H}{\Delta z}$) and time node number ($M = \frac{t}{\Delta t}$) is larger than 1000, with an increase of particle radius node number ($F = \frac{D_p}{\Delta r_p}$) from 5 to 20. The particle nodes have a minor influence on the convergence of cutoff temperature. Thus, *N*=1000 and *M*=1000 are used for height and time node differential mesh, respectively, and *F*=20 is chosen to better capture the temperature gradient inside the particle.

Table 4.4 Initial and boundary condition in axial z-direction and spherical radius r_p-direction.

Initial condition (t=0)			
All domains	$T_s = T_f = T_w = T_{ini}$, where $T_{ini} = T_C$, (Ch) $T_{ini} = T_{cutoff,ch}$, (Dis)	$z \in [0, H]$	$r_p \in [0, \frac{D_p}{2}]$
Boundary condition ($t \geq 0$)			
Surface of solid particle	$-\lambda_s \cdot \frac{\partial T_s(z,t)}{\partial r} = h_{sf} \cdot (T_s' - T_f)$	$z \in [0, H]$	$r_p = \frac{D_p}{2}$
Center of solid particle	$\frac{\partial T_s(z,t)}{\partial r} = 0$	$z \in [0, H]$	$r_p = 0$
Tank top & bottom	$\frac{\partial T_s(z,t)}{\partial z} = \frac{\partial T_w(z,t)}{\partial z} = 0$	$z = 0, \& z = H$	$r_p \in \left[0, \frac{D_p}{2}\right]$
Inlet HTF	$T_f(z = H, t) = T_H$, (Ch) $T_f(z = 0, t) = T_C$, (Dis)	--	--
Outlet HTF	$\frac{\partial T_f(z=0,t)}{\partial z} = 0$, (Ch) $\frac{\partial T_f(z=H,t)}{\partial z} = 0$, (Dis)	--	--

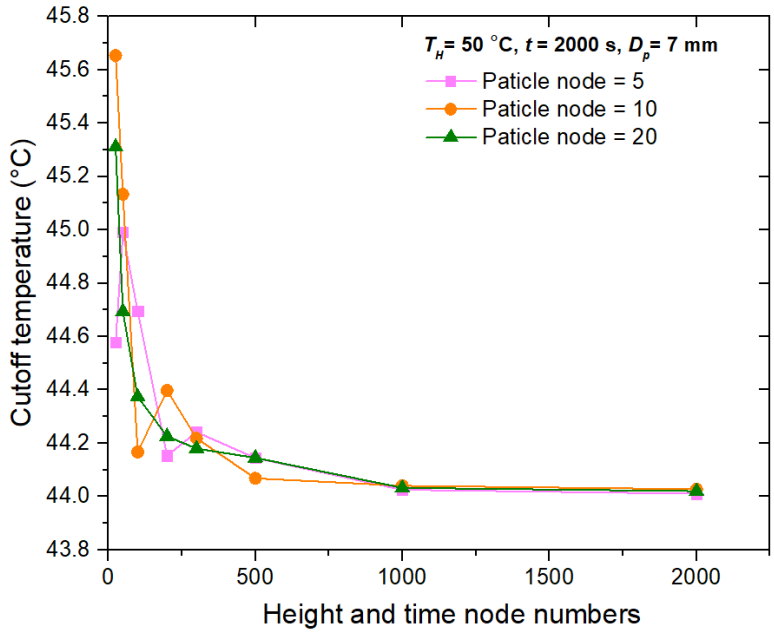

Figure 4.6: Height, time, and particle radius node number independence tests in differential mesh.

4.2.4. Key performance indicators

In this chapter, the energy efficiency indicators chosen are different compared to Chapter 3. Still, they are uniform to Chapter 4 because it's not only focused on tank walls but more on the cycling process. Additional energy efficiency indicators are used in this Chapter.

● Energy efficiency (1st law)

Charging energy efficiency (η_{ch}) is defined as the ratio of the stored energy (ΔE_{stored}) to the input energy by HTF (ΔE_{in}). The stored energy of ΔE_{stored} is the amount of thermal energy stored in solid and fluid phases from beginning (t=0) to ending (t=t_{ch}) in charging. Discharging energy efficiency (η_{dis}) is the ratio of the output energy by HTF (ΔE_{out}) in discharging to the stored energy of ΔE_{stored} at the beginning of discharging. The heat loss ratio of charging ($\eta_{ch,loss}$) is defined as the ratio of the heat loss (ΔE_{loss}) to the total input energy of ΔE_{in} in charging.

$$\eta_{ch} = \frac{\Delta E_{stored}}{\Delta E_{in}} = \frac{\Delta E_{stored}(t=t_{ch}) - \Delta E_{stored}(t=0)}{\int_0^{t_{ch}} [\dot{m}_f \cdot C_{p,f} \cdot (T_{in} - T_0)] dt} \tag{4.4}$$

$$\eta_{ch,loss} = \frac{\Delta E_{loss}}{\Delta E_{in}} = \frac{\int_0^{t_{ch}} [\dot{m}_f \cdot C_{p,f} \cdot (T_{in} - T_{out})] dt - \Delta E_{stored}(t=t_{ch})}{\int_0^{t_{ch}} [\dot{m}_f \cdot C_{p,f} \cdot (T_{in} - T_0)] dt} \tag{4.5}$$

$$\eta_{dis} = \frac{\Delta E_{out}}{\Delta E_{stored}} = \frac{\int_0^{t_{dis}} [\dot{m}_f \cdot C_{p,f} \cdot (T_{out} - T_0)] dt}{\Delta E_{stored}(t=t_{ch})} \tag{4.6}$$

where — T_{in} is the inlet temperature of HTF.

— T_{out} is the outlet temperature of the HTF.

— T_0 is the reference coldest operational temperature T_C (20 °C).

In addition, the stored energy in the tank at a certain time for fluid and solid is calculated:

$$\Delta E_{stored}\,(t) = \pi \cdot R_{int}^2 \cdot \int_0^H \left[\rho_f \cdot C_{p,f} \cdot \varepsilon \cdot (T_f - T_0) + \rho_s \cdot C_{p,s} \cdot (1-\varepsilon) \cdot (\bar{T}_s - T_0)\right] dz \tag{4.7}$$

where $\bar{T}_s$ is the average temperature of single solid spheres at the same height. In experiment, the stored energy is calculated using the average temperatures of solid and fluid for a number of small unit volumes. More precisely, the tank volume is firstly divided into small cells by thermocouple points and the temperature of such single unit volume is considered as homogenous.

● Storage/utilization ability

Capacity ratio (C_{ratio}) [43] [7] [32] in charging is the comparison of the actual stored energy and the theoretical maximum stored energy. Theoretically, $C_{ratio} = 1$ refers to fully and $C_{ratio} < 1$ represents partially utilized tank region in charging/discharging, so that better energy utilization ratio means smaller tank volume.

$$C_{ratio} = \frac{\Delta E_{stored}}{\Delta E_{stored,max}} = \frac{\Delta E_{stored,s} + \Delta E_{stored,f}}{\Delta E_{stored,max,s} + \Delta E_{stored,max,f}} \tag{4.8}$$

Utilization ratio (U_{ratio}) [205] [206] in discharging process.

$$U_{ratio} = \frac{\Delta E_{out} - \Delta E_{in}}{\Delta E_{stored,max}} = \frac{\int_0^{t_{dis}} [\dot{m}_f \cdot C_{p,f} \cdot (T_{out} - T_{in})]\, dt}{\Delta E_{stored,max,s} + \Delta E_{stored,max,f}} \tag{4.9}$$

4.2.5. Uncertainty analysis

The uncertainties of experimentally measured parameters and calculated parameters are listed in **Table 4.5**.

The measurement uncertainties were obtained by evaluating the standard deviation in repeated testing [207]. The thermocouples were calibrated with an oil FLUKE 6102 MICRO-BATH calibration device in the validation range of 35-200 °C and by the low-temperature thermostat below 35 °C. The specific heat capacity of glass sphere was measured by Differential Scanning Calorimetry (DSC Q200) with a heating/cooling rate of 5 K min^{-1} showing in **FigureA 4.1 a** of *Appendix*. The inlet flow rate was calibrated by the gravimetric method with testing curves shown in **FigureA 4.1 b**. The thermal conductivity of insulation was measured by Thermal Constants Analyser (Hot-Disk TPS1500) at different temperatures, with a small variation rate of 2.7×10^{-3} W m^{-1} K^{-1} per 1 K shown in **FigureA 4.1 c**.

The analytical uncertainties for indirect parameters, such as energy efficiency, are determined by the components uncertainties, ϑ, that are contributed by the measurement uncertainties based on error propagation [208]. In experiment, the average temperature of small unit volume is used

to calculate energy. Both measurement uncertainty and analytic interpolation integral uncertainty of the average temperature can influence the energy calculation (average temperature is actually a type of middle point integration method). Firstly, the temperature error (systematic error) is estimated to be ±0.37 K, the measurement uncertainty on average temperature is calculated to be ±0.15 K, and the numerical integration uncertainty is below that, as calculated in **FigureA 4.2 a**. Especially due to the different radial thermocouples number, the uncertainty is different for radial thermocouples. Thus, among those, system error of ±0.37 K is used to calculate the in-direct parameters uncertainty. The corresponding uncertainty of stored energy, input energy, and efficiency of the validation case are exhibited in **FigureA 4.2 b-d**.

Table 4.5 The uncertainties of measured and calculated parameters.

Measured parameters		**Uncertainties**
Temperature	T	± 0.37 K
Volumetric flow rate	$\dot{V}_f$	± 1%
Particle diameter*1	D_P	± 0.1 mm
Solid density*1	ρ	± 1.6% (40 kg m^{-3})
Thermal conductivity*1	λ	± 0.001 W m^{-1} K^{-1}
Specific heat capacity*1	C_p	± 8 J kg^{-1} K^{-1}
Calculated parameters*2		
Porosity	ε	± 0.004
Energy efficiency	η_{ch}	± 5%
Capacity ratio	C_{ratio}	± 2%
Thermocline thickness	$L^*_{thermocline}$	± 5% (20 mm)

Assess measurement error:

*1 The standard uncertainty is defined by standard deviation: $SD = \sqrt{\frac{1}{n}\sum_{i=1}^{n}(x_i - \bar{x})^2}$, where x is measured parameter and n is the repeated measurement times [207].

Assess calculation error:

*2 The components uncertainty is defined as :$\vartheta = \sqrt{\sum_{j=1}^{m-1}\left(\frac{\partial y}{\partial x_j} SD_{x_j}\right)^2}$, where $y = f(x_1, x_2 \ldots . . x_m)$ is the in-directly parameter, and m is the number of components [209].

4.3. Experimental study on the influence of diffuser and insulation

This work experimentally investigated the thermocline expansion of SHTPB TES system due to various factors, including the inlet diffuser configuration, the insulation, the filler diameter, the HTF flow rate and the working temperatures. The developed DC-3P was firstly validated by comparison with the experimental data and then was used to conduct numerical parametric study.

4.3.1. Model validation

The experimental data of Case 1 (Péclet number Pe=12, Particle Reynolds number Re=3, Bi_s=0.76, charging process) have firstly been used for the numerical model validation. **Figure 4.7 a** shows the comparison of fluid temperature evolution at TC1-7 axial positions (cf. C in **Figure 4.4 b**; r=0). A good agreement between numerical and experimental results can be found at first sight. **Figure 4.7 b** further shows the variation of temperature difference (ΔT) vs. charging time and the corresponding standard deviation (SD). For most of thermocouples in the axial centerline of the tank, ΔT< ±2.5 K and SD< 0.7 K can be observed, indicating that the temperature evolution at these positions can be well predicated by the developed DC-3P model. However, for TC-7 near the top inlet, the discrepancy (ΔT ≈10 K and SD ≈2 K) is still noticeable, implying that the assumption of plug flow used in this 1D model at this position is not validated. This is mainly due to the impact of inflowing HTF jet from the inlet port on the radial velocity distribution and consequently on the thermocline expansion and evolution, which will be further investigated in detail and discussed in later sub-sections.

During the charging process, the energy efficiency difference at the cutoff time between numerical and experimental results is around 2%, which is within the experimental uncertainty of 5% (cf. **FigureA 4.2 d**). At the final cutoff fluid outlet temperature of 43.8 °C (θ=0.2), the energy efficiency is calculated to be η_{ch}=83.3% by modeling and is η_{ch}=85.5% in experiment, showing a good agreement. In conclusion, the DC-3P model shows good accuracy in simulating the large size sphere (Bi_s>0.1) and tank with large wall volume of SHTPB.

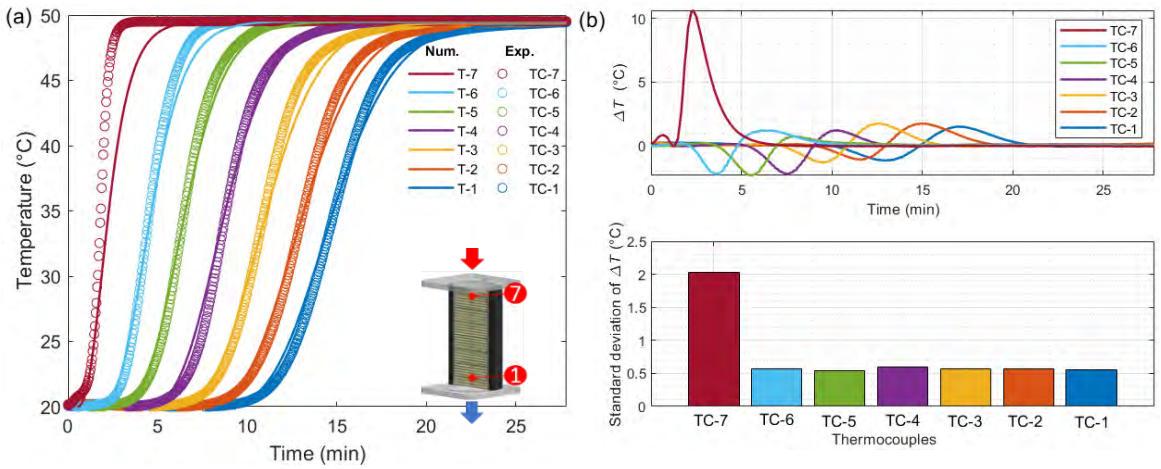

Figure 4.7: Comparison between numerical results and experimental data: (a) Evolution of fluid temperature at different locations of axial centerline; (b) fluid temperature differences and corresponding standard deviations (Case 1: T_C/T_H=20/50 °C, D_p=7 mm, $\dot{V}_f$ =0.5 L min^{-1}, Pe=12, Re=3, Bi_s=0.76, charging operation).

4.3.2. Validity range of the DC-3P model

Numerical and experimental results are compared for the investigated Case 1 (7 mm glass ball) and Case 3 (10 mm glass ball) in order to determine the precision or applicable range of the developed DC-3P model. **Figure 4.8** reports the values of temperature standard deviation (SD) and the energy efficiency difference ($\Delta\eta_{ch}$) obtained under various operating conditions. It is found that, within the tested condition of Re <15 and Bi_s<1.3, the SD and $\Delta\eta_{ch}$ can be kept below 2.5 K and 3%, respectively. The developed DC-3P model could thereby be safely used with good precision under this applicable range even though the inlet HTF penetration has a non-negligible effect on the thermocline expansion.

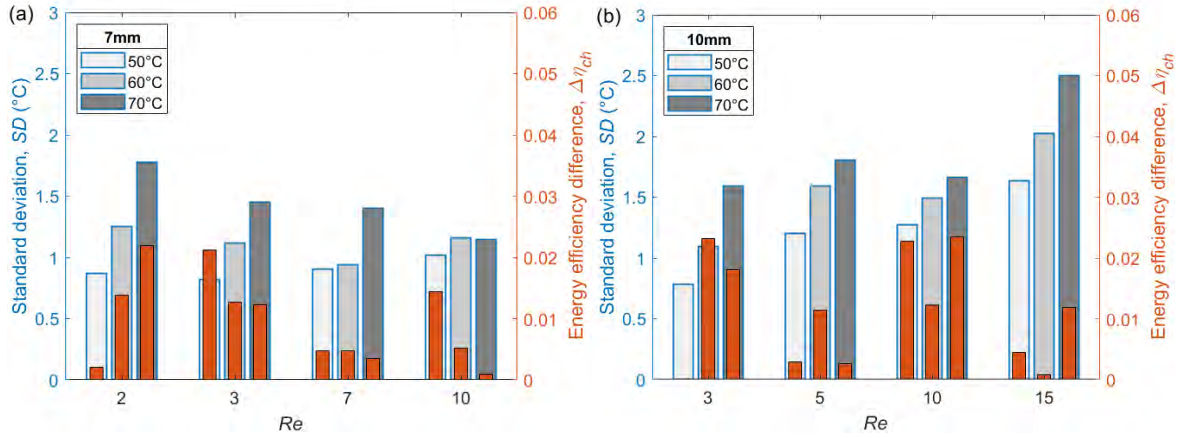

Figure 4.8: Comparison of numerical and experimental results on temperature standard deviation (SD) and energy efficiency difference ($\Delta\eta_{ch}$) in charging process: (a) Case 1 (D_p=7 mm); (b) Case 3 (D_p=10 mm).

4.3.3. Evolution of temperature field

Figure 4.9 shows the evolution of the fluid temperature cartography inside the SHTPB tank experimentally measured for one fully charging and discharging cycle. Case 3 with porous bed inlet (D_p=10 mm) has been tested at two flow rates, i.e., $\dot{V}_f$=0.3 (Re=5) and 1.5 L min^{-1} (Re=15), to highlight the impact of inflowing jet on the thermocline expansion in SHTPB. The colormap is constructed from data interpolation of 17 thermocouples measurements (linear interpolation in axial direction). The dimensionless time equaling to t^*=1 (cf. in Chapter 3) means that the theoretical plug flow reaches the tank top or bottom. It can be observed that at the beginning of charging (t^*=0), the tank has a quasi-homogeneous temperature of T_C (blue color). But for the beginning of discharging, the temperature distribution inside tank is a bit less homogeneous since the ending of fully charging (θ=0.01, for better observation) has been used as the initial condition for discharging.

By examining the temperature color maps, it can be observed that the thermocline region grows thicker over charging or discharging time. Moreover, the shape of thermocline region is not flat, indicating that temperature gradient exists in radial direction. The impact of penetrating flow inject on the thermocline expansion can be clearly seen, especially under high flow rate ($\dot{V}_f$=1.5 L min^{-1}) with more important inertial force. It seems that the solid fillers alone are not totally capable of buffering the momentum-dominated injecting flow under this tested condition, resulting in the non-uniform fluid distribution which destabilizes much the temperature stratification. Note that the shape of thermocline is a little bit different in charging and discharging due the influence of gravity and the lowered temperature at near-wall region due to the heat loss.

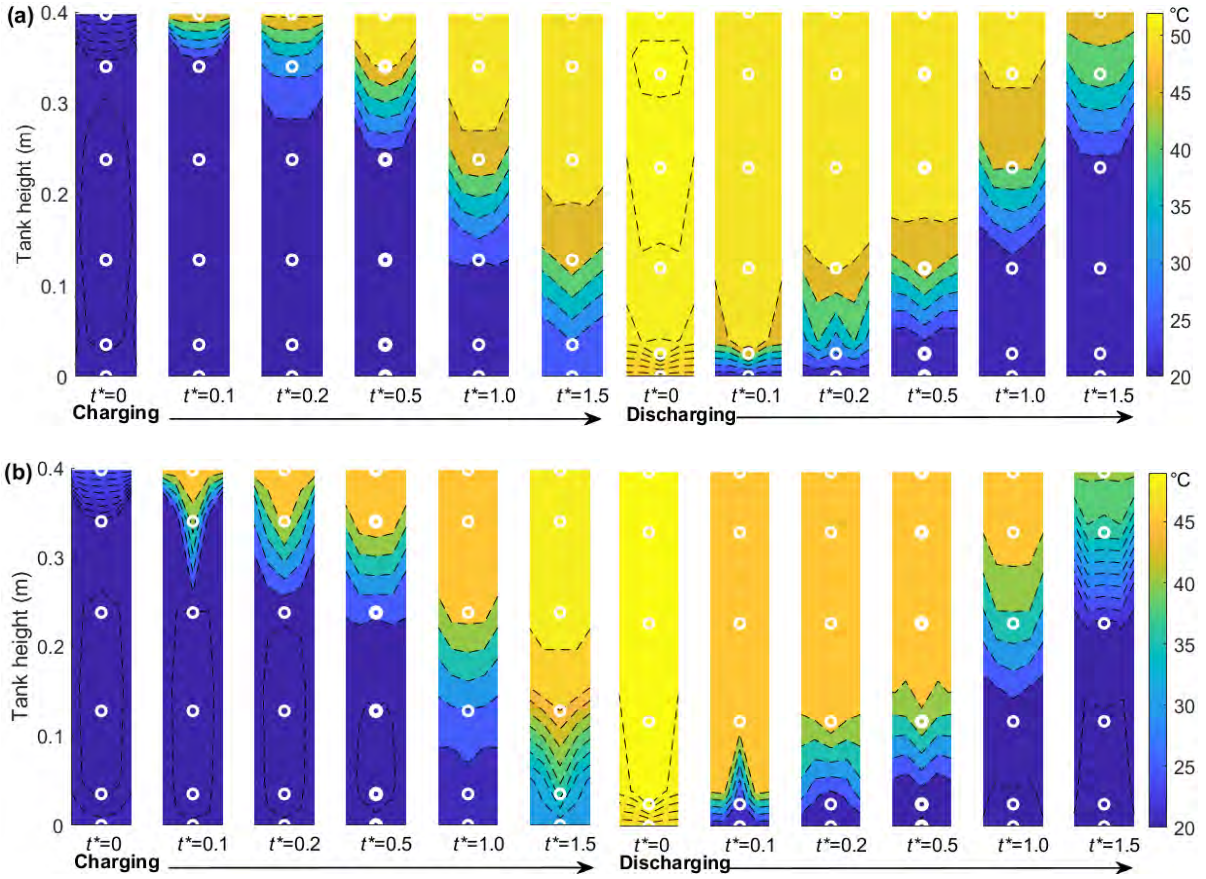

Figure 4.9: Evolution of fluid temperature distribution experimentally measured for one charging-discharging cycle (Case 3: T_C/T_H=20/50 °C, D_p=10 mm): (a) $\dot{V}_f$=0.3 L min^{-1}; (b) $\dot{V}_f$=1.5 L min^{-1}.

4.3.4. Impact of inlet configuration

The testing results of Case 3 (packed bed), Case 5 (packed bed + diffuser) and Case 6 (diffuser) in **Figure 4.4** are compared to assess the performance of different inlet configurations to mitigate the impact of penetrating flow inject. **Figure 4.10** shows the evolution of radial fluid temperature differences over charging time for the center to outer (T^C-T^A) and for the center to middle (T^C-

T^B) positions at TC-7 (near the top inlet, under the diffuser; z^*=0.875) and TC-5 (near middle tank height; z^*=0.625) levels. A non-uniformity factor (f_r) defined as the max temperature difference in radial direction to the operating temperature range (**Eq. 4.10**) is introduced to indicate the (non)-uniformity of radial temperature distribution, as presented at the upper-right corner of **Figure 4.10**. When the value of f_r approaches 0, there is almost no radial temperature gradient, indicating that the shape of thermocline is flattened as assumed in 1D numerical model. From **Figure 4.10 a**, the radial temperature difference (ΔT) at TC-7 level decreases after adding the plate-type diffuser. The corresponding value of f_r is 0.83 for basic case 3 (z_1=0, only the packed bed), 0.66 for case 6 (z_1=35 mm, only the diffuser), and 0.30 for case 5 (z_1=10 mm, the combined diffuser and packed bed), respectively. As expected, the combined effect of diffuser and packed bed largely alleviates the influence of penetrating HTF jet on the thermocline stability in the entrance, better than that with only the diffuser or only the packed bed.

At TC-5 level near the middle tank height, the impact of penetrating HTF jet on the radial temperature distribution uniformity is shown to be rather limited even at high flow rate, reflected by the small radial temperature differences and low f_r values (<0.2) for all tested inlet configurations (**Figure 4.10 b**). The outer radial temperature of Case 6 (no packed bed in entrance region) is a little higher than the center temperature because of the double-hump shape of thermocline caused by higher velocity in near-wall region [7]. Without packed bed in the entrance, the double-hump phenomena being more obvious that the f_r value for case 6 is higher than other configurations.

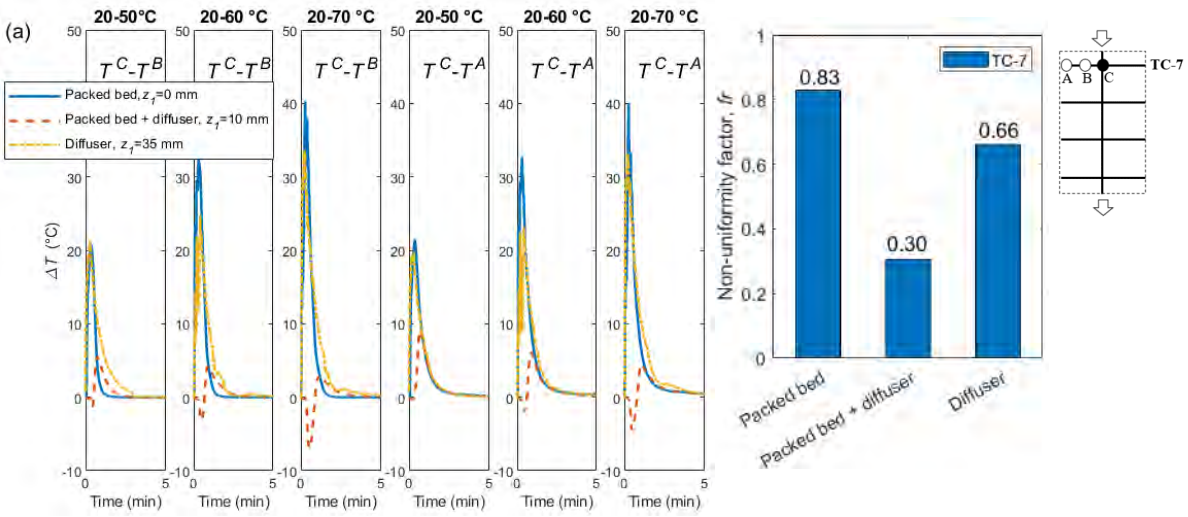

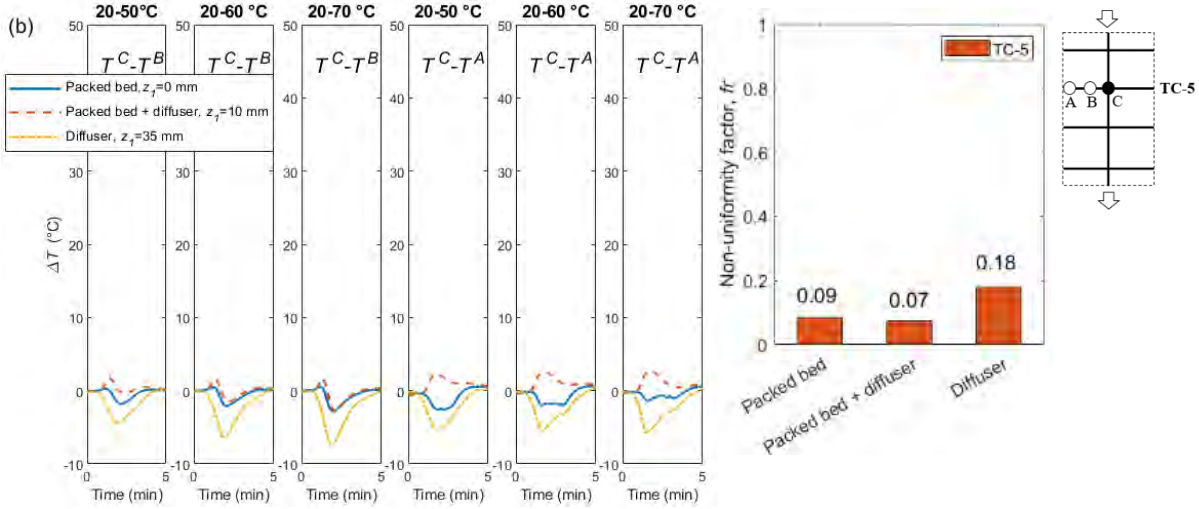

Figure 4.10: Radial temperature difference inside the SHTPB tank with different tested inlet configurations: (a) TC-7 position; (b) TC-5 position (Case 3, 5 & 6: D_p=10 mm; $\dot{V}_f$=1.5 L min^{-1}; charging).

$$f_r = \max\left[\left|\frac{\Delta T(t)}{T_H - T_C}\right|\right] = \max\left[\left|\frac{T^C(r,z,t) - \{T^B(r,z,t)\,,\, T^A(r,z,t)\}}{T_H - T_C}\right|\right] \quad (4.10)$$

The influence of radial thermocline expansion or instability due to the penetrating jet on the global performance of the SHTPB tank needs further discussion. To this end, **Figure 4.11 a** shows the energy efficiency (η_{ch}) and capacity ratio (C_{ratio}) or utilization at the cutoff time for different inlet configurations. For all studied inlet configurations, when T_H increases, the energy efficiency slightly decreases mainly due to the higher heat loss, while the capacity ratio slightly increases because of the higher heat transfer rate by larger temperature difference, which will be discussed in detail in the next sub-section.

Case 5 with the most uniform radial temperature distribution at the inlet region has the largest capacity ratio and the longest charging time. The near plug flow pattern and the flattened thermocline shape renders the better utilization of the storage capacity (around 3%) of the SHTPB tank. However, it presents the lowest energy efficiency (**Figure 4.11 a**) mainly due to the longest charging time before reaching the cutoff fluid outlet temperature thus additional amount of heat loss as shown in **Figure 4.11 b**. In reality, the η_{ch} curves for Case 3 with serious radial thermocline expansion and Case 5 are very close (<2%) during the charging operation (**Figure 4.11 b**). This implies that the radial temperature non-uniformity and the thermocline expansion near inlet region caused by the penetrating HTF inject may have negligible influence on the energy efficiency of the SHTPB tank. It actually depends largely on the cutoff temperature and the corresponding cutoff time. The energy efficiency and capacity ratio of Case 6 with full water HTF in entrance (thereby larger volumetric heat capacity than that of glass) are very close to those for Case 3. The

near-entrance region of the tank is less utilized due to the strong mixing of hot and cold fluids, such like in single-medium thermocline tanks [7].

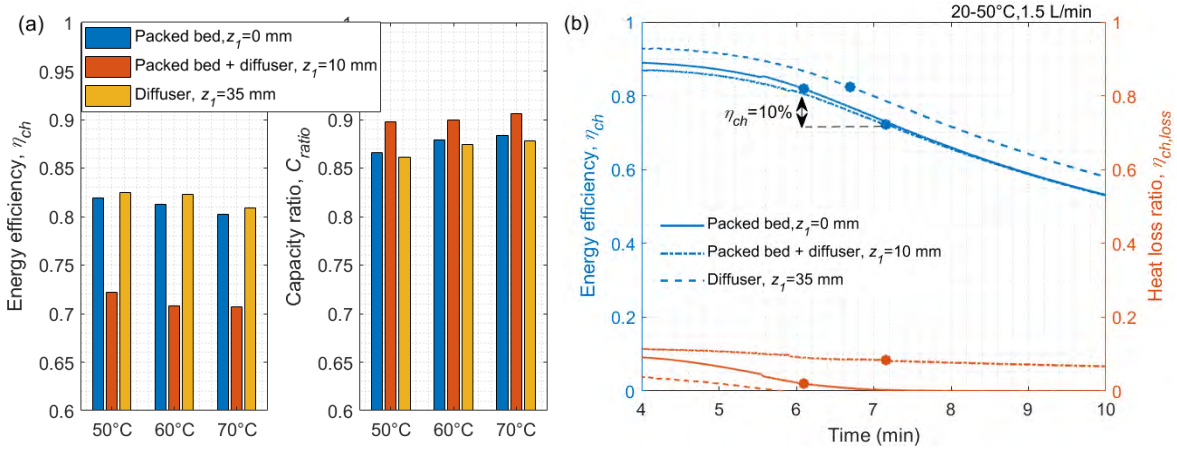

Figure 4.11: Effect of inlet configuration on the global performance of the SHTPB tank: (a) energy efficiency and capacity ratio at cutoff time; (b) energy efficiency and heat loss ratio vs. charging time (Case 3, 5 & 6: D_p=10 mm, $\dot{V}_f$=1.5 L min^{-1}, charging).

Moreover, thermal infrared imaging is used to observe the qualitative trend of thermocline behavior on the outer surface of the tank. The wall emissivity is 0.90, the acquisition frequency is 10 s by using the Fluke thermal image camera TiS75 with a verification range of -20 to 80°C. **Figure 4.12** shows the captured images for Case 5 but without insulation layer in charging and discharging operations. The thermocline region on the images is marked by dash line, showing that its thickness increases by 13 % from 2 min to 5 min in charging and discharging process. The flat shape of the thermocline region captured by infrared imager, though at the outer surface of the tank, may imply the good flow distribution behavior by the combined effect of porous bed and flow diffuser (Case 5).

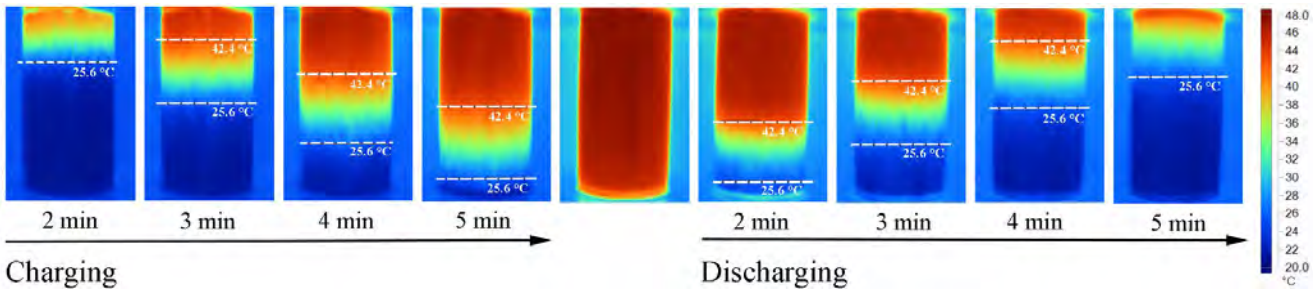

Figure 4.12: Experimental thermal infrared images of charging and discharging process (T_C/T_H=20/50 °C, D_p=10 mm, 1.5 L min^{-1}, diffuser z_1=10 mm, no insulation, ϵ=0.90, T_{amb}=20.7 °C).

4.3.5. Impact of insulation

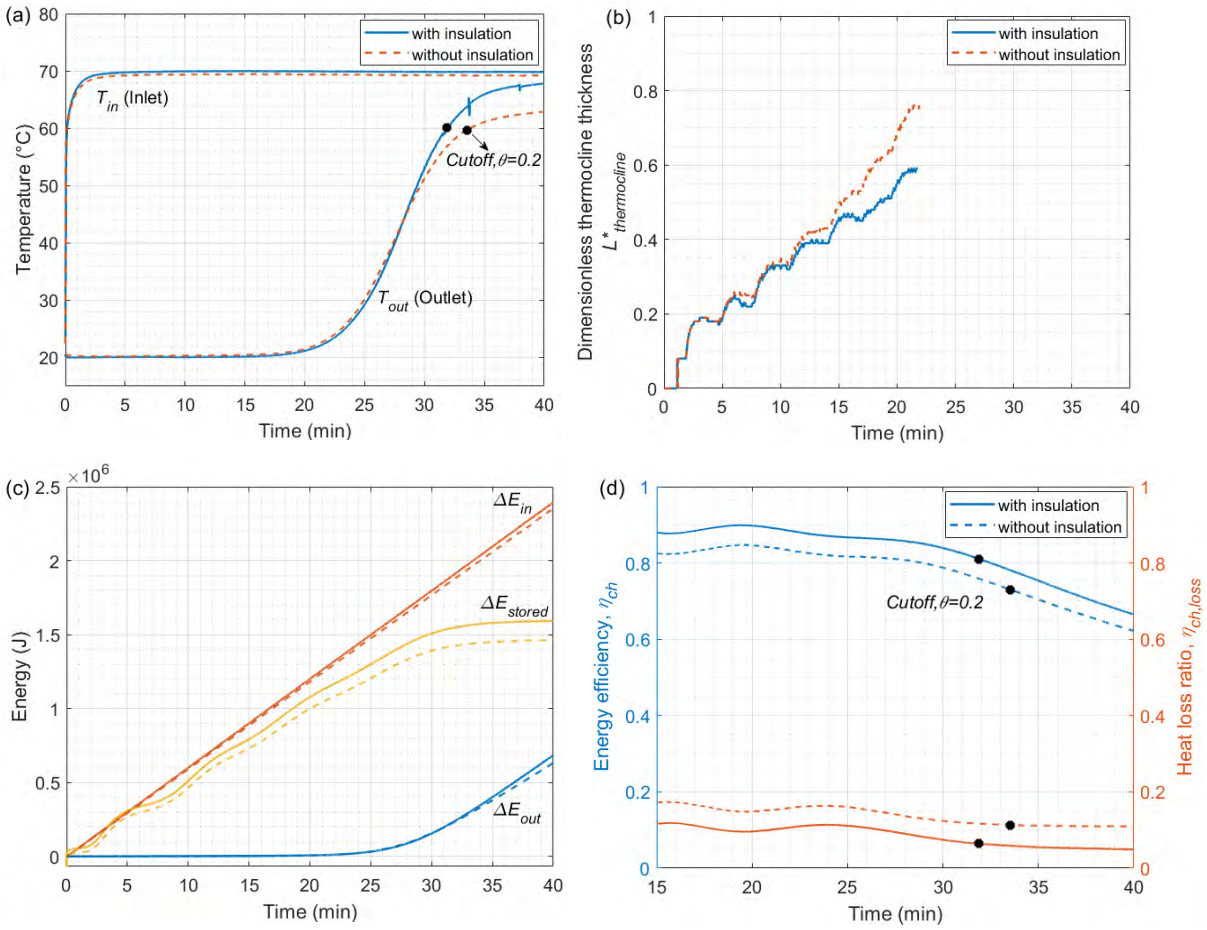

Figure 4.13: Experimental results comparing the performance of SHTPB tank with/without insulation. (a) inlet and outlet temperature; (b) dimensionless thermocline thickness $L^*_{thermocline}$; (c) inlet/outlet and stored energy; (d) energy efficiency and heat loss ratio (Case 3 & 4: T_C/T_H=20/70 °C, D_p=10 mm, $\dot{V}_f$=0.3 L min^{-1}, θ=0.2).

The impact of heat loss on the performance of the SHTPB tank has been evaluated by comparing the experimental results of Case 3 (with insulation) and Case 4 (without insulation) for the same testing condition. From **Figure 4.13 a**, it is found that due to the heat loss, the outlet fluid temperature of no-insulation tank is 5 K lower than that of the tank with insulation at the ending moment of charging (40 min, t^*=2.5). Longer charging time by around 5% is also needed to reach the cutoff temperature (θ=0.2) when the tank is not insulated due to the serious tailing effect. **Figure 4.13 b** shows the variation of the normalized thermocline thickness over charging time for the two cases. It may be observed that the $L^*_{thermocline}$ values are almost the same before t^*=0.34 (11 minute) for the two cases. This is because at the beginning of charging, the thermocline expansion at axial centerline is mainly caused by the fluid mixing and diffusion. The near-wall region of the SHTPB tank is still occupied by low-temperature HTF (cf. **Figure 4.9 a**) thus the

influence of heat loss on the thermocline expansion is negligible. But at the second half of the charging, there is an obvious discrepancy between the two $L^*_{thermocline}$ curves, implying the noticeable influence of heat loss on the thermocline expansion. Comparing the insulation tank and no-insulation tank, the $L^*_{thermocline}$ is calculated to be 0.59 and 0.76 at t^*=1.38 (thermocline zone reaching the tank bottom).

Figure 4.13 c shows the variation of input energy (ΔE_{in}), stored energy (ΔE_{stored}), and outlet energy (ΔE_{out}) as a function of charging time for the SHTPB tank with/without the insulation. It is observed that both E_{stored} curves increase almost linearly until reaching a plateau. At the cutoff moment of charging, the E_{stored} value of no-insulation tank is 4-7% lower than that of the tank with insulation, mainly due to the heat loss. **Figure 4.13 c** shows the energy efficiency (η_{ch}) curve and heat loss ratio ($\eta_{ch,loss}$) curve, not surprisingly both indicating that the SHTPB tank performs better when well-insulated. At the cutoff temperature set as θ=0.2, the SHTPB tank with an insulation can improve the energy efficiency by about 5-7%, increase total stored energy for 4-7%, and augment the capacity ratio by about 3-5%.

4.3.6. Impact of flow rates and inlet HTF temperature

The influence of HTF flow rate and inlet temperature on the thermocline evolution in axial direction is further investigated experimentally and reported in this sub-section. **Figure 4.14** shows the fluid temperature profile along the tank height (centerline) for various flow rates, particles size, and operating temperatures at charging time of t^*_E=0.5 (input energy by HTF is equal to the half of ideal maximum stored energy of tank). When HTF flow rate increases from 0.3 to 1.5 L min^{-1} and the theoretical input energy by HTF is the same, the fluid temperature at the same z^* becomes higher. That's because the shorter residence time at high flow rate causes insufficient heat exchange between solid and HTF.

Figure 4.15 is the fluid temperature profiles for various inlet temperatures at a charging time of t^*_E=0.75. The time is chosen in order to get the more obvious comparison results. When the inlet temperature increase from 50 to 70 °C, the fluid temperature at the same height under the same flow rate decreases. That's because the higher operational temperature causes more heat loss to decrease fluid temperature.

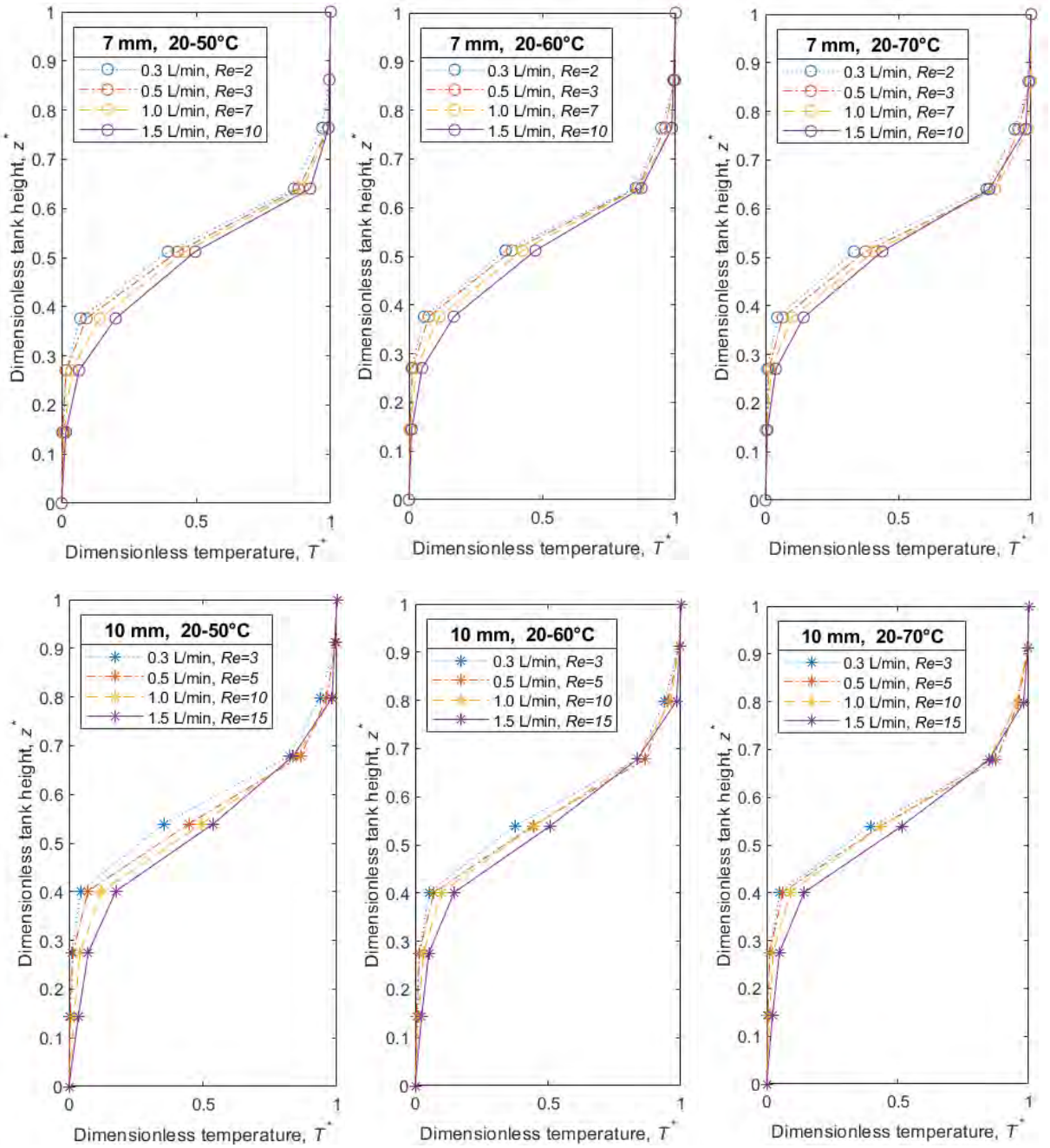

Figure 4.14: Experimental fluid temperature profile at the axial centerline of the SHTPB tank for various flow rates, particles sizes, and working temperatures at charging time of t_E^*=0.5.

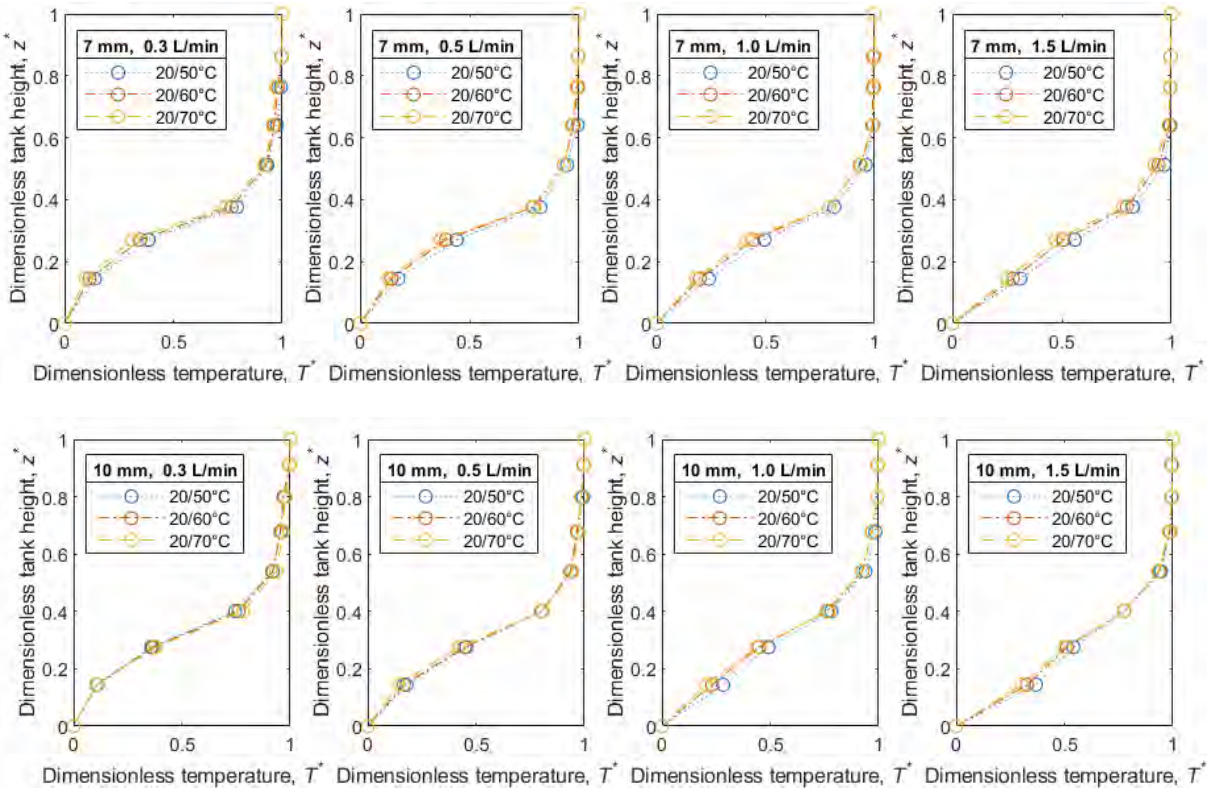

Figure 4.15: Experimental fluid temperature profile of different inlet temperature at charging time of t_E^*=0.75.

Figure 4.16 shows the variation of normalized thermocline thickness as a function of t_E^* in charging. Curves are fitted linearly for a better comparison using the direct proportion formula, $L^*_{thermocline} = k \cdot t_E^*$, and the slope value k for each curve is indicated aside. The thermocline expands over time due to various factors discussed before and its thickness can go up to 70% of the total tank height. From **Figure 4.16,** it can be observed that the thermocline thickness increases faster at high low rate (high Re). Whether there is an optimum flow rate value at very low Re condition will be discussed later. In addition, the slope value becomes a bit smaller with increasing T_H under the same flow rate. This is because the higher inlet fluid temperature augments the fluid-solid heat transfer rate, thereby slowing the thermocline expansion.

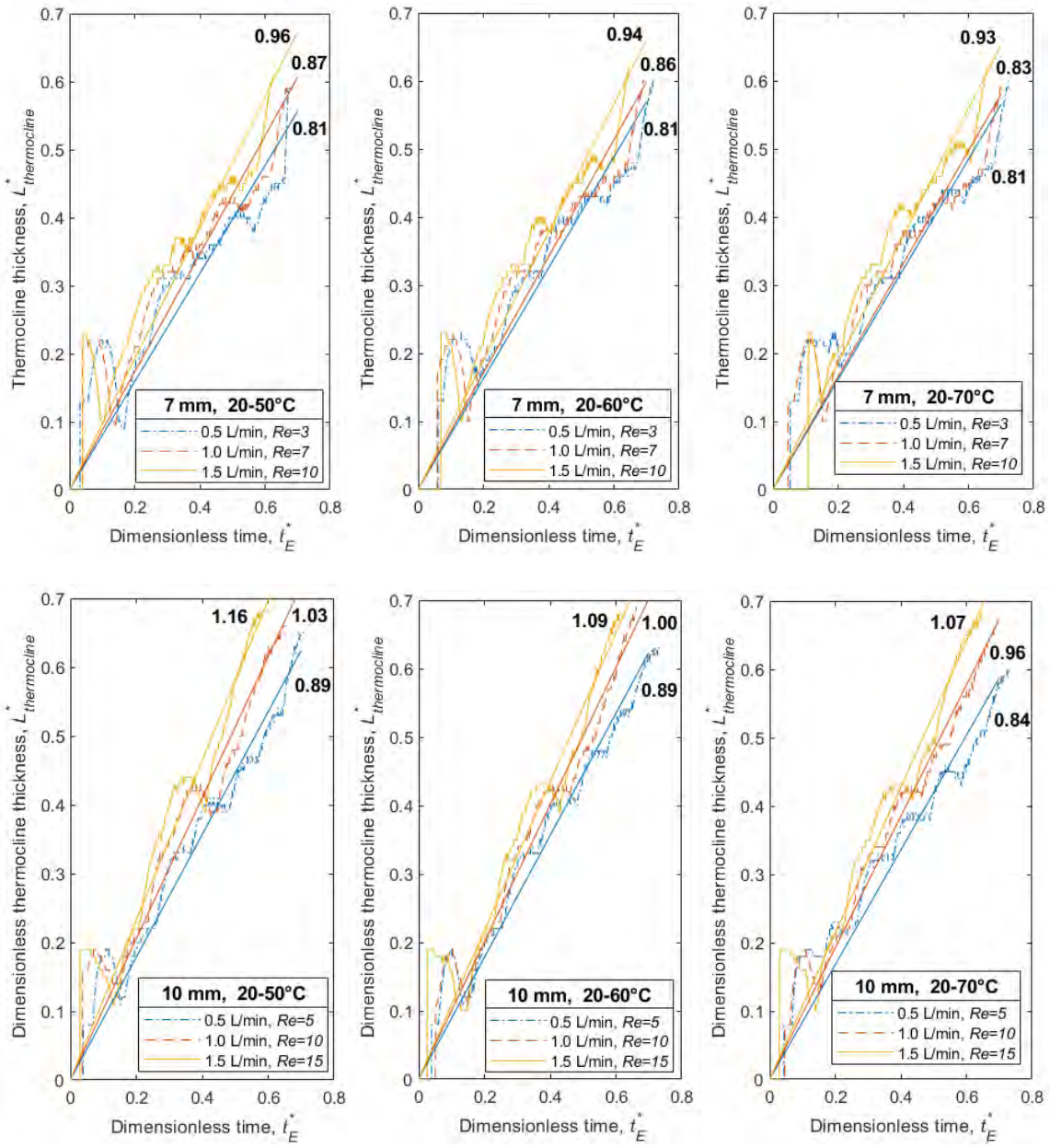

Figure 4.16: Evolution of thermocline thickness for various flow rates, particles sizes, and working temperatures in charging process.

4.4. Further comparison between numerical and experimental results

Further interpretation and comparison between numerical (DC-3P) and experimental results are performed with the intention of addressing some interesting issues such as the temperature gradient inside the solid particles, the existence of optimum flow rate for SHTPB and the applicable range of the DC-3P model.

4.4.1. Temperature gradient inside sphere particles

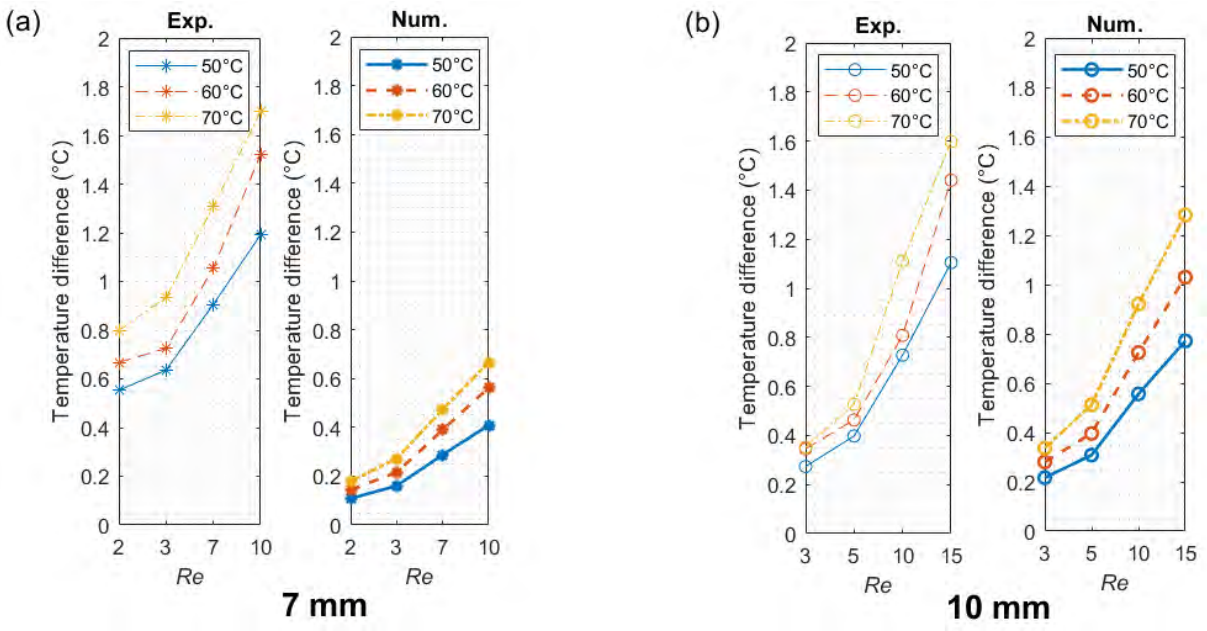

Figure 4.17: Average temperature difference between sphere center and fluid in charging process: comparison between experimental and numerical results: (a) D_p=7 mm; (b) D_p=10 mm

$$\Delta\bar{T}_{sf}\ (K) = \frac{\int_0^H \int_0^{t_{cutoff}} [T_f - T_s(r_p=0)]dtdz}{H \cdot t_{cutoff}} \tag{4.11}$$

The temperature gradient inside sensible fillers, reflected by the existence of a temperature difference between the solid sphere center and the surrounding HTF, has been reported by numerical modeling but inadequately investigated nor validated in experiments. To addressee this question, **Figure 4.17** presents the time and volume-averaged temperature gap between solid sphere center and fluid as defined in **Eq. 4.11**, obtained both by experimental measurements of all thermocouples and by DC-3P modeling. The solid Biot number Bi_s ranges from 0.6-1.1 for 7 mm sphere fillers (Case 1) and from 0.7-1.2 for 10 mm sphere fillers (Case 3) with the tested flow rates, implying that the dispersion-concentric model is necessary to be used [210]. Both numerical and experimental results show that the $\Delta\bar{T}_{sf}$ increases with the increasing flow rate and inlet fluid temperature (T_H). Comparing two sphere sizes, the difference between the numerical and experimental results is smaller than 0.3 K for 10 mm fillers and about 1 K for 7 mm fillers, respectively, showing good agreement. Contrary to theory, the temperature gap in experiments is larger for small size particles, may be due to heat transfer surface difference of the flow thermal front [34] as well as the measurement uncertainties and difficulties. But in general, the $\Delta\bar{T}_{sf}$ value up to 1.7 K can be detected in experiments, confirming the existence of noticeable temperature gradient inside sphere under certain circumstances which is rarely reported in the open literature.

4.4.2. Optimal flow velocity

Additional simulations using the DC-3P model have been performed and compared with the experimental data in order to exhibit the existence (or not) of an optimal HTF flow rate (Re) for SHTPB TES tanks. **Figure 4.18** shows the numerical results of the energy efficiency and remained thermocline thickness at cutoff time with HTF flow rate ranging from 0.12 to 2.5 L min^{-1} (Re=0.8-25). The inlet fluid temperature has negligible effect on the energy efficiency and the remained thermocline thickness. Numerically, the smaller filler particle size is more advantageous and an optimal inlet flow rate (about Re=3) in charging can be identified for this SHTPB under low temperature operation. This finding is in line with other researches for high- or middle-temperature applications [71][34][4]. Unfortunately, this optimum is not significant enough to be detected in experiments. One reason is may due to the stability of operations and measuring uncertainties. Another reason is may be caused by the regime in the change of flow behind obstacles or particles, which cannot be simulated in the 1D fluid model in Matlab. When the HTF flow distance in the packed bed increases and when the mass flow rate increases, the heat transfer efficiency of the regime behind the particle thereby decrease.

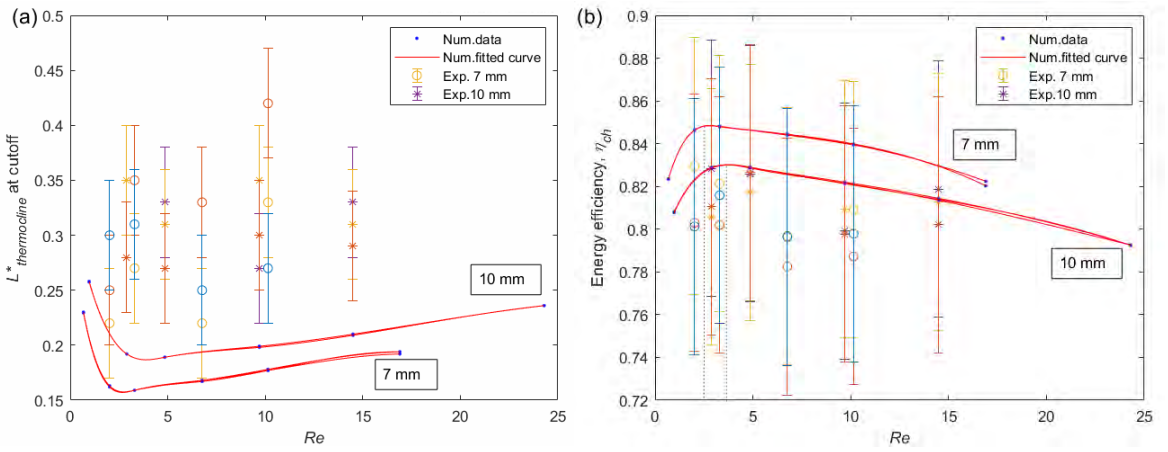

Figure 4.18: Influences of flow velocity (Re) on energy efficiency and thermocline thickness: comparison between experiment and numerical results (T_H: 50-70 °C, $\dot{V}_f$=0.12-2.5 L min^{-1}).

4.5. Chapter conclusion

In this work, a laboratory-scale SHTPB has been systematically evaluated by experimentally measuring the temperature evolution of both the fluid phase and the solid phase at different axial and radial positions inside the tank. In parallel, a dispersion-concentric 3-phase (DC-3P) numerical model has been developed and simulations have been performed with various operating conditions to be compared with the experimental data for model validation. In particular, the impacts of penetrating inlet flow and heat loss on the thermocline expansion and on the global

performances of the TES tank have been investigated and analyzed in detail. Other issues such as the temperature gradient inside the solid particles, the influences of flow rate and working temperature and the applicable range of the DC-3P model have also been discussed. Main conclusions of this study are summarized as follows.

(1) The developed DC-3P model considering the wall heat capacity and heat loss is proved to be capable of precisely predicting the global performance of the SHTPB TES tank. Compared to the experimental data, the temperature standard deviation and energy efficiency difference can be kept below 2.5 K and within 3%, respectively, under the applicable range of Re <15 and Bi_s<1.3.

(2) The inlet HTF penetration into the packed-bed will cause the non-uniform radial temperature distribution and thermocline expansion near the inlet region of the SHTPB tank, especially with higher flow rate (higher *Re*) condition. Nevertheless, the middle height of the tank is less affected due to the buffering effect of porous fillers. The combined effect of diffuser and packed bed as inlet configuration could better maintain the radial temperature uniformity as well as the thermocline stability, increasing the capacity ratio of the storage tank by about 3% at the cutoff time. Nevertheless, slightly decreased energy efficiency could be registered for this inlet configuration due to the delayed cutoff time and the resulted higher amount of total heat loss.

(3) The heat loss without no insulation condition lead to a noticeable thermocline expansion (>20%), lowered charging energy efficiency (5-7%), increasing cutoff time (4-5%), and decreased capacity ratio (3-5%), even for low-temperature applications of the SHTPB TES tank.

(4) There is a temperature gradient inside sensible sphere particle due to the convection resistance between the solid and fluid and the conduction resistance of the solid particles. A temperature difference up to 1.7 K between the sphere particle center and surrounding fluid has been observed both by modeling and experimental measurement for our tested conditions.

(5) An optimal flow velocity corresponding to Reynolds number of Re=3 has been determined in simulation for this tank geometry ($\frac{H}{D_{tank}}$=2, inlet port width/tank diameter=0.06) and tested temperature range (20/70°C). But this optimum is not enough significant to be confirmed in experiments.

This chapter contributes to exploring the influencing factors based on a packing configuration by sensible fillers, enabling the inclusion of thermocline expansion into the design and optimization of low-temperature thermocline packed-bed system. It used the optimized diffuser by Lou et al. [7]

in the thermocline one-tank system and served as an improvement of the thermocline packed-bed system.

Next chapter will focus on optimization of multi-layered packing configuration, using diverse PCMs or mixtures of PCM-sensible material as fillers for different applications.

Appendix 4.I

Calibrating experiment measurement

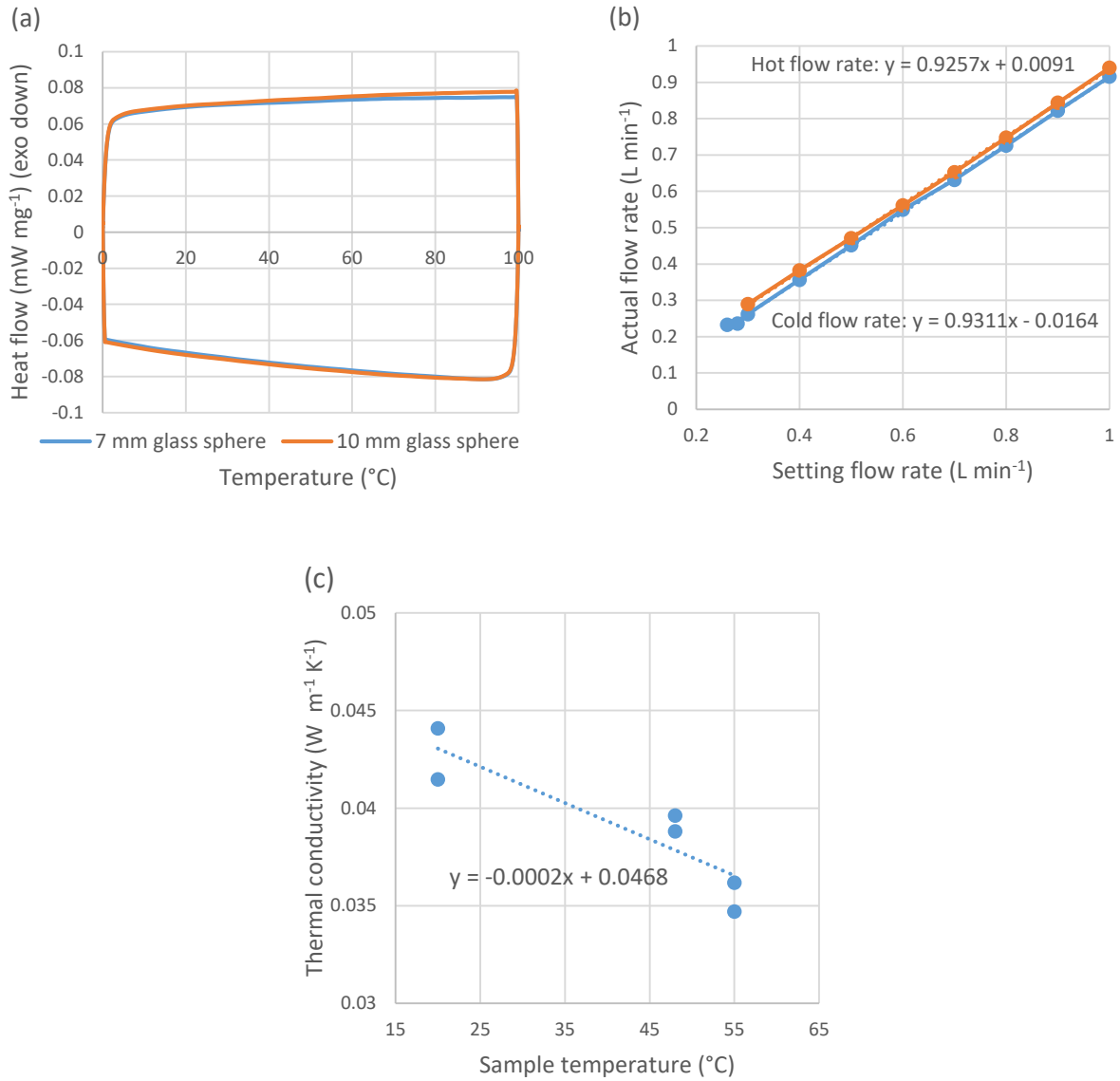

FigureA 4.1: (a) Differential scanning calorimetry curves of glass sphere in range of 0-100 °C; (b) Calibrated flow rates of hot and cold water; (c) Measured thermal conductivity of insulation with temperature increase.

The hot flow rate (L min^{-1}) is calibrated into:

$$\dot{V}_f(Actual) = \dot{V}_f(setting) \cdot 0.9257 + 0.0091$$

The cold flow rate (L min^{-1}) is calibrated into:

$$\dot{V}_f(Actual) = \dot{V}_f(setting) \cdot 0.9311 - 0.0164$$

Appendix 4.II

Uncertainty analysis

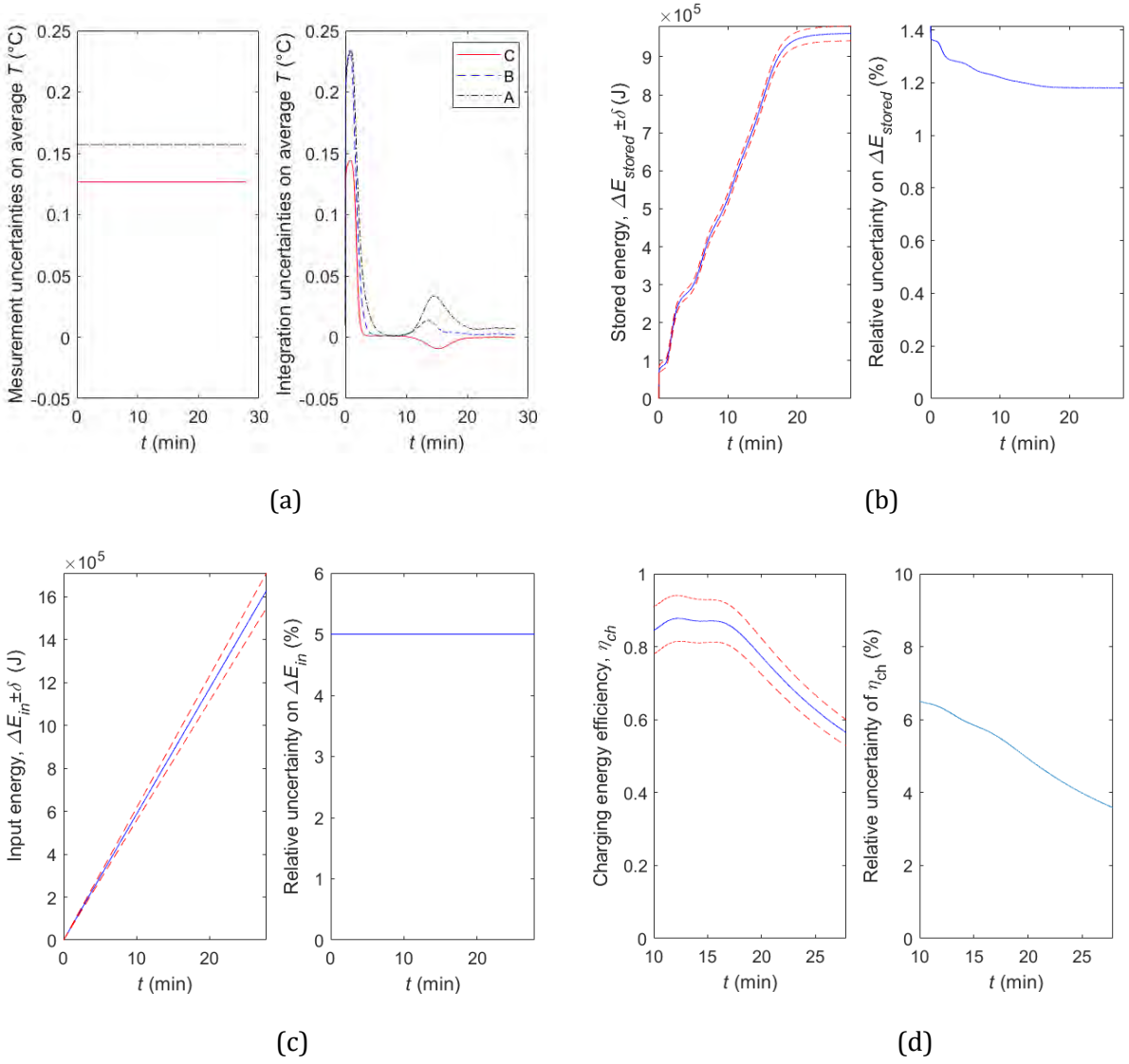

FigureA 4.2: Uncertainty of the validation case: (a) bed average temperature; (b) stored energy (E_{stored}) based on bed average temperature; (c) input energy (E_{in}) based on bed average temperature; (d) charging energy efficiency (η_{ch}) based on bed average temperature.

The measurement uncertainty of average temperature is around 0.15 K and integration uncertainty is below than that. From the uncertainties of center (C), middle (B), and outer (A) position, the middle and outer position thermocouples has higher error than the center position due to the less thermocouples numbers. In the beginning, the relative uncertainty of stored energy is larger because less hot water enters the tank. When it becomes stable, the relative uncertainty is around 1%.

Appendix 4.III

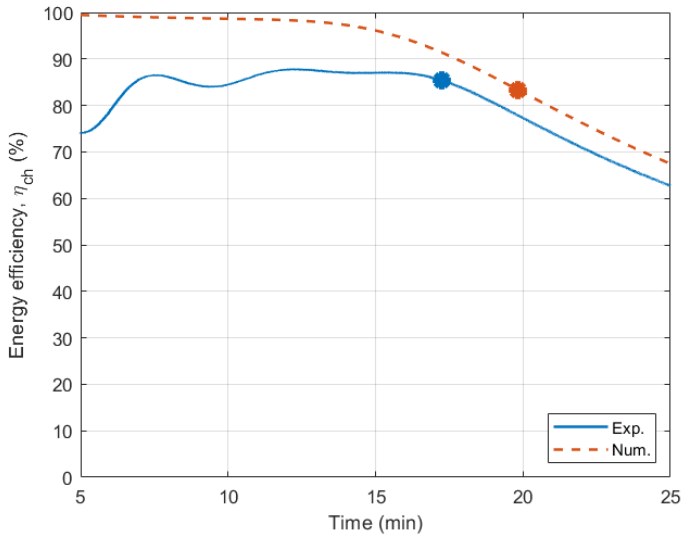

FigureA 4.3: Energy efficiency comparison for numerical and experimental in charging process (T_C/T_H=20/50 °C, D_p=7 mm, $\dot{V}_f$ =0.5 L min^{-1}).

Chapter 5
Optimization of thermocline packed-bed system with PCM fillers for greenhouse application

Abstract

This chapter aims the optimization of a thermocline packed-bed storage tank for a given greenhouse application through a multi-layer and multi-material configuration. This system is able to solve the problems of the low utilization and lower efficiency of conventional uniform layer packing tank. Phase change material (PCM) is used to improve efficiency of storage.

The objective of this chapter are as below:

- Validate the model for PCM through a lab-scale multi-layered latent-sensible heat storage tank experimental data.
- Design an initial TES tank on the meteorology and heating consumption data of a greenhouse in Carquefou, France.
- Propose a methodology for designing a given tank through multi-objective genetic algorithm (MOGA) optimization in multiple cycles.
- Propose a solution to stabilize inlet temperature and low utilization of system in multiple cycles.
- Compare steady and seasonal operation in the application for the greenhouse in different utilization scenario to find shortcomings for improving future work.

Keywords: Multi-objective optimization, phase change material, layer configuration; multiple cycles; greenhouse.

Chapter content

5.1. Introduction

5.1.1. Greenhouse energy consumption issues

A roadmap for the global energy sector by International Energy Agency (IEA)'s Net Zero by 2050 reported that, achieving transformation of the global energy system is critical to reaching carbon dioxide (CO_2) emissions to net zero by 2050 [211]. Rapidly boost clean or renewable energy technologies like solar energy is one solution to net zero emission. To sustain agriculture, greenhouse (GH) needs considerable energy consumption for heat, cool, light, and etc. to maintain the desired climate for plant growing. In north European region, the annual energy demand of greenhouse agriculture is up to 3,600 MJ m^{-2} [212][13]. Conventionally, GH integrates extra heater systems to supply heat, such as gas heater or steam from power plant, causing CO_2 emission [213].

5.1.2. Net-zero greenhouse

Agricultural net-zero energy greenhouse (net-zero GH) is a solution, that employ renewable energy-conservation techniques like solar photo-voltaic or solar thermal to address energy consumption or provide electric power. In terms of energy-saving strategies and overcoming global hunger and poverty, net-zero GH shows advantages [13]. Integrating thermal energy storage (TES) in net-zero energy GH is one good way on solving the issues like overheating in daytime and excessive cold at night through providing stable energy supplies.

Employing latent heat material or PCM in TES is more useful for improvement of energy loading capacity and efficiency over sensible heat material due to the high energy density. Latent heat thermocline packed-bed (LHPTB) system is applied in reduction of investment comparing to conventional two tanks. Filling one type of PCM in the one tank is a common configuration strategy, but under the limitation of utilization ratio. Designing packing configuration is a method to enhance storage ability [135].

5.1.3. Multi-layered PCM thermocline system

Multi-layered (or cascaded) PCM in thermocline storage tank is good at enhance thermal performance by filling different layer PCMs comparing to uniform filled PCM. Packing PCMs from top to bottom with a declining melting temperature configuration also improve charging/discharging rate due to the larger temperature difference along the flow direction. Moreover, thermal buffering in cycling on PCM layer causes minor degradation of thermocline [2].

In early stages, the multi-layered PCM system using cylindrical PCM capsules were analyzed on longitudinal heat transfer fluid (HTF) [214] and transverse HTF [215]. Later, in thermocline system, researchers [60][216][217][59] proposed the two or three-staged tank configuration shows higher exergy and energy efficiency than single-stage tank. For example, Wu et al. [134]

investigated the PCM packed-bed system with 1, 3, and 5 cascaded phase change temperatures with high-temperature molten salt HTF in cycles. It proved more number of PCM layers have a faster charging/discharging rate, higher accumulated efficiency, and even can reach a repeatable state after some cycling in the adiabatic boundary. Meanwhile, increasing threshold outlet temperature is good to enlarge storage capacity in the cascaded system.

However, uniform or proportional layer thickness is often adopted and the selection of cascaded phase change temperature configuration is hard to be determined according to cutoff temperature threshold [218]. Parametric studies or optimization were carried out to explain the influence of those variables (including, layer thickness, phase change temperature) and give instruction of designing multi-layered PCM strategies. Cascetta et al. [2] compared a two-tank system with one-tank systems, including a packed-bed one-tank system filled with rock and another tank filled with PCM in 10% top layer to avoid substantial thermocline degradation. Results show that the one-tank system increases annual thermal energy output than the two-tank direct system by 5% higher. Li et al. [205] studied the influence of melting temperature on the effective utilization rate of non-cascaded and cascaded PCM system. It was found that in two- and three- cascaded system, the top and bottom melting temperature can be chosen as slightly lower/higher than threshold temperature in charging/discharging, the maximum effective utilization rate reaches 84% which is higher than the non-cascaded system only about 40%.

5.1.4. Aim and scope

The optimization performed in literatures is almost on the basis of particular or few amount of configurations [219][96][205]. In addition, PCM suffering from low thermal conductivity but can be improved by adding high thermal conductivity material like graphite [220]. As an influence factor, thermal conductivity is less considered in literatures for thermocline TES tank. This point has to be investigated more clearly.

Therefore, **the goal of this chapter** is to propose two-layered PCM configuration optimization method to improve the overall energy efficiency and the storage/utilization ability in multiple cycles. Design factors of PCM (phase change temperature, thermal conductivity, and layer thickness) are chosen as constraints for multi-objective optimization. The optimization is used for greenhouse application.

At first, built a multi-layered PCM system in a Lab-scale experimental set-up to validate the model. Then, an initial tank is designed according to the meteorology data and requirement of a greenhouse application. Later, a multi-objective optimization is used to optimize the layer packing and results were compared with real greenhouse to find the potential improvement work.

5.2. Model and experiment

In this chapter, the mathematical model of dispersion-concentric three-phase (DC-3P) used in Chapter 4 is validated by lab-scale experimental tank with multi-layered PCM-sensible packing configuration. This model is for optimization.

5.2.1. Numerical model: PCM capsule properties

Differently, this model taken into account the PCM capsule parameters, including the thermophysical properties of PCM in phase change process, the characteristic length of capsule, and capsule-fluid heat transfer coefficient.

● Equivalent thermophysical properties of PCM capsule

The apparent parameter method is used to define the thermophysical parameters of PCM, assuming the phase changes from solid to liquid in a narrow temperature ranges [58][77][65][95][59][180]:

$$C_{p,PCM}(T) = \begin{cases} C_{p,PCM,s} & , \quad (T < T_{m1}) \\ C_{p,PCM.sl} = \frac{C_{p,PCM.s}+C_{p,PCM.l}}{2} + \frac{H_m}{T_{m2}-T_{m1}}, & (T_{m1} < T < T_{m2}) \\ C_{p,PCM,l} & , \quad (T_{m2} < T) \end{cases} \tag{5.1}$$

$$\rho_{PCM}(T) = \begin{cases} \rho_{PCM,s} & , \quad (T < T_{m1}) \\ \rho_{PCM,sl} = \frac{\rho_{PCM,s}+\rho_{PCM,l}}{2}, & (T_{m1} < T < T_{m2}) \\ \rho_{PCM,l} & , \quad (T_{m2} < T) \end{cases} \tag{5.2}$$

$$\lambda_{PCM}(T) = \begin{cases} \lambda_{PCM,s} & , \quad (T < T_{m1}) \\ \lambda_{PCM,sl} = \frac{\lambda_{PCM,s}+\lambda_{PCM,l}}{2}, & (T_{m1} < T < T_{m2}) \\ \lambda_{PCM,l} & , \quad (T_{m2} < T) \end{cases} \tag{5.3}$$

$$H_{m,PCM}(T) = C_{p,PCM}(T) \cdot T \tag{5.4}$$

where – $C_{p,PCM}$, the equivalent specific heat capacity of PCM.

– ρ_{PCM} , the equivalent density.

– λ_{PCM}, the equivalent thermal conductivity.

– T_{m1}, T_{m2}, the initial and ending phase change temperature.

– H_m (J kg^{-1}), the enthalpy.

– Subscript of *'s, l'* represents the solid and liquid phases of PCM.

Once the volumetric heat capacity of shell is significantly higher than PCM ($\rho_{PCM} \cdot C_{p,PCM} \ll \rho_{shell} \cdot C_{p,shell}$) or the volume difference for both is large ($V_{PCM} \gg V_{shell}$), the stored heat in shell

cannot be ignored. For example, metal shell or shell with considerable thickness. For simplification, the thermophysical properties of C_p, and ρ for capsule shell should be equivalently considered.

$$C_p = w_1 \cdot C_{p,shell} + (1 - w_1) \cdot C_{p,PCM} \tag{5.5}$$

$$\rho = 1/\left[\frac{w_1}{\rho_{shell}} + \frac{1-w_1}{\rho_{PCM}}\right] \tag{5.6}$$

where w_1 is the mass fraction of capsule shell to PCM capsule.

• Stored energy of PCM capsule

The stored energy in PCM capsule ($\Delta E_{stored,PCM}$) depends on temperature that is calculated based on liquid fraction [107] [206].

$$\Delta E_{stored,PCM}(T) = V_{PCM} \cdot \begin{cases} \rho_{PCM,s} \cdot C_{p,PCM,s} \cdot (T - T_C), & (T < T_{m1}) \\ \rho_{PCM,s} \cdot C_{p,PCM,s} \cdot (T_{m1} - T_C) + \rho_{PCM,sl} \cdot C_{p,PCM,sl} \cdot (T - T_{m1}), & (T_{m1} < T < T_{m2}) \\ \rho_{PCM,s} \cdot C_{p,PCM,s} \cdot (T_{m1} - T_C) + \rho_{PCM,sl} \cdot C_{p,PCM,sl} \cdot (T_{m2} - T_{m1}) + \rho_{PCM,s} \cdot C_{p,PCM,l} \cdot (T - T_{m2}), & (T_{m2} < T) \end{cases} \tag{5.7}$$

• Characteristic length of PCM capsule (L_c)

When the capsule is cylinder or cubic shapes, the L_c or equivalent diameter (D_p) of capsule is defined according the ratio of the volume ($V_{capsule}$, m³) to outer surface area ($A_{capsule}$, m²) [73]:

$$D_p = L_c = \frac{V_{capsule}}{A_{capsule}} \tag{5.8}$$

• Equivalent heat transfer coefficient between HTF and PCM capsule (h_{fPCM})

When the capsule shell has high thermal conductivity and the Bi_{shell} is less than 0.1, the temperature inside shell assumed spatially uniform based on the lump capacitance method. The total thermal resistance of shell and convection HTC between HTF and capsule surface (h_{sf}) are both taken account into equivalent HTC (h_{fPCM}) [73].

$$\frac{1}{h_{fPCM}} = \left[\frac{1}{h_{sf} \cdot A_{capsule}} + \frac{r_{p,2} - r_{p,1}}{4\pi \cdot r_{p,2} \cdot r_{p,1} \cdot \lambda_{shell}}\right] \cdot A_{capsule} \tag{5.9}$$

$$h_{sf} = \frac{Nu_{sf} \cdot \lambda_f}{L_c} \tag{5.10}$$

where $-\ Nu_{sf}$, the Nusselt number between solid phase and HTF, from the correlation [165].

$-\ \lambda_{shell}$,the capsule shell thermal conductivity.

$-\ r_{p,1}$, the capsule internal radius.

$-\ r_{p,2} = \frac{L_c}{2}$, the capsule external radius or shell radius.

5.2.2. Experimental validation: PCM capsule configuration

Two experimental cases were used to validate the model. The first is a single-layer latent-heat thermocline packed-bed (LHTPB) tank integrated with solar water heating system in literature [81]. Another is the LTEN-designed experimental system in the lab in Chapter 4 with a heterogeneous thermocline packed-bed (HHTPB) tank.

The HHTPB tank is with good insulation and there are two layers. The upper layer is filled by PCM capsules with 1/3 volume ratio, while the remained bottom layer is filled by 7 mm glass sphere used in **Figure 5.1**. These PCM capsules are the same of the one used in SOTO et al. [76]. The capsules are a cylindrical aluminum shells where the paraffin-compressed expanded natural graphite composite is encapsulated. All capsules were samples after the cycling test. **Table 5.1** lists the main parameters of the two packed-bed experimental cases.

Table 5.1 Main parameters for validation of PCM packed-bed TES system.

Terms	**Symbols**	**Units**	**Nallusamy's experiment** [147] [60][221][81] [146]	**Validation cases in LTeN lab** [76]	
Tank type	**--**	**--**	**Stainless-steel cylinder tank**	**Polycarbonate cylinder tank**	
Height of tank	H	m	0.46	0.398	
Internal bed radius	R_{int}	m	0.18	0.097	
Outer wall radius	R_{mid}	m	0.185	0.1	
External insulation radius	R_{ext}	m	0.235	0.125	
Volume of tank (*R_{int})	--	L	47	11.8	
Fillers	--	--	Paraffin capsule	**Upper layer** (1/3, v%): Paraffin expanded graphite capsule	**Lower layer** (2/3, v%): Glass sphere
Porosity	$\boldsymbol{\varepsilon}$	--	0.49	0.59	0.38
Shape	--	--	Sphere	Cylinder	Sphere
Capsule characteristic length, or capsule diameter	L_c, or D_p	mm	55	20*	7
Capsule shell thickness	--	mm	0.8	0.5	--
PCM melting temperature	T_m	°C	60±0.1	69±0.5	--
PCM phase change enthalpy	ΔH_m	J g^{-1}	213	230	--
Capsule shell material	**--**	**--**	High-density polyethylene (HDPE)	Aluminium	--
Insulation layer	--	--	Glass wool	Bitrile rubber	
HTF	--	--	Water	Water	
Operational temperatures	T_C/T_H	°C	32/70	20/75	
Flow rate	$\dot{V}_f$	L min^{-1}	2	0.5	

* The capsule has a volume of 2.5 ml and surface area of 1.25 mm^2 [76].

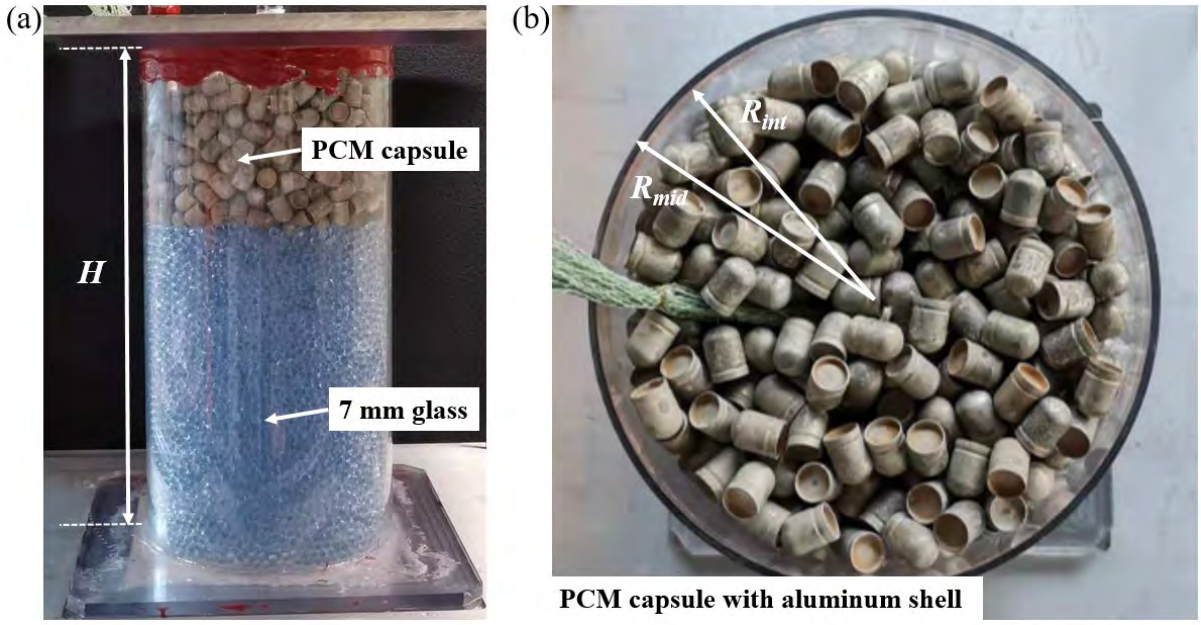

Figure 5.1: Photograph of multi-layered HHTPB system with latent and sensible heat fillers: (a) lateral view; (b) sectional view.

The comparison of fluid temperature profiles with time variation in different height positions is illustrated in **Figure 5.2**. For both cases, dot line is the experimental results and solid line is the numerical results of the PCM model. In **Figure 5.2 a**, no obvious temperature difference is observed at the tank top because two flow distributors on the top of the tank to make uniform flow of HTF. While in **Figure 5.2 b**, the temperature curve at top (TC-7) shows an obvious jump because of the flow jet at the inlet. This point has been proved in Chapter 4 that the packed bed region can alleviated the flow jet influence near the middle tank. Overall, the model is in good agreement with two reference cases, showing a temperature standard deviation (*SD*) below 1 K as calculated. In all, this model can be used for further optimization studies.

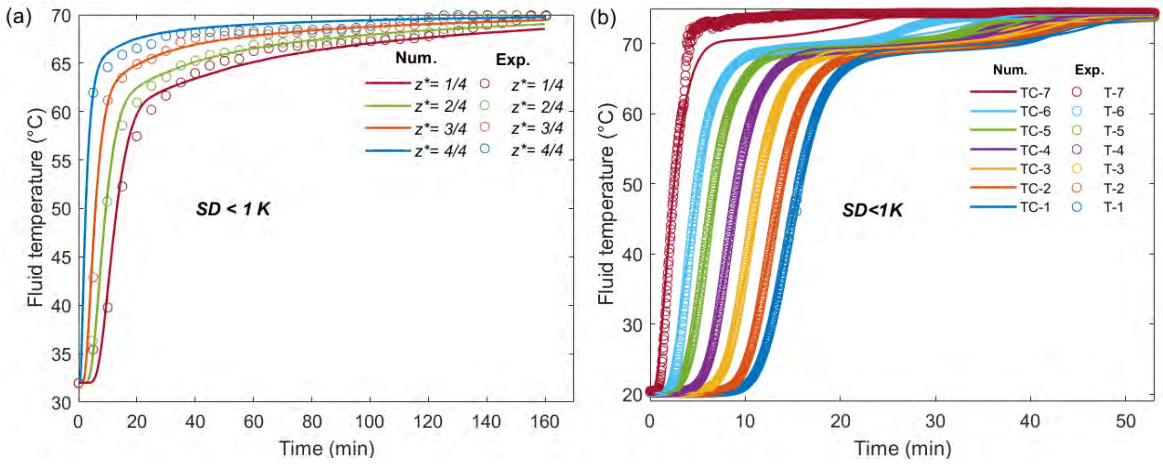

Figure 5.2: Validation of numerical model with [147] (*Re*=30) experimental works and multi-layered experimental study in LTEN lab (*Re*=7).

5.3. Multi-layered optimization methodology

In this chapter, a methodology for the design of multi-layered PCM packed-bed TES tank through the multi-objective optimization is proposed.

Step 1: Propose a single-layered packed-bed PCM tank.

Step 2: Design an initial tank based on the practical application of greenhouse (*@Project SERRES+*)[222]: first, to determine the initial tank volume according to the input (radiation intensity) and output (greenhouse consumption); then considering different charging/discharging time, to determine two mass flow rates for charging/discharging process; at last, taking into account the unstable weather, to obtain the dynamic inlet temperature input based on meteorological data.

Step 3: Evaluate the thermodynamic behavior of the initial tank: first, to explore the difference between steady and dynamic operation through the comparison the thermal performance of steady and dynamic inlet temperature; then to conduct sensitivity analysis of different phase change temperature to define key performance indicators' (KPI) influence; at last, through consecutive thermal cycling test, to discuss the cycling numbers influence.

Step 4: Conduct the multi-objective optimization: first, to define the best option between one or two layer packing filling; and then, to identify the parameter variables for a simplified irradiation boundary steady condition; at last, analyze results to a real greenhouse application from the optimized configuration defined in steady state, assess the stability of performance indicators of the TES to solar irradiation change: on steady case.

5.3.1. Initial tank design

The objective of this section is to design an initial tank size and define the initial operational condition for multi-objective optimization of the multi-layered PCM packed-bed tank based on a practical greenhouse application.

(1) It was first calculated the maximum energy demand of greenhouse to design a baseline tank storage capacity.

(2) Then, it was evaluated the energy need during a daily cycling process based on the meteorological data to determine a heat transfer rate. A mass flow rate-time profile for the charging/discharging was then calculated as a constant variable considering outlet temperature.

(3) Finally, considering the seasonal differences, it was defined two types of inlet temperature (steady and dynamic conditions) in charging process. Four typical seasonal days were selected to present the difference.

(4) Other parameters at a steady condition were finally decided and optimization was then performed for the steady condition.

5.3.1.1. System operation

The greenhouse internal temperature needs to be kept constant for plant growing. However, temperature drops sharp especially at night that needs to be avoided through the extra gas heating source.

The thermocline PCM packed-bed as alternative is designed to supply heat to keep the greenhouse night temperature at relatively constant level, while charge itself by absorbing free natural solar energy provided by solar panel in daytime. Moreover, comparing to the traditional single-media water or dual-media sensible thermocline storage system, PCM packed-bed TES system have more stable outlet temperature and significant higher energy density. In this chapter, a PCM thermocline packed-bed is thereby designed for daily greenhouse operation. **Figure 5.3** is the designed greenhouse integrating the thermocline TES system: the solar collector input, the greenhouse output, the TES tank, and the heat exchange system.

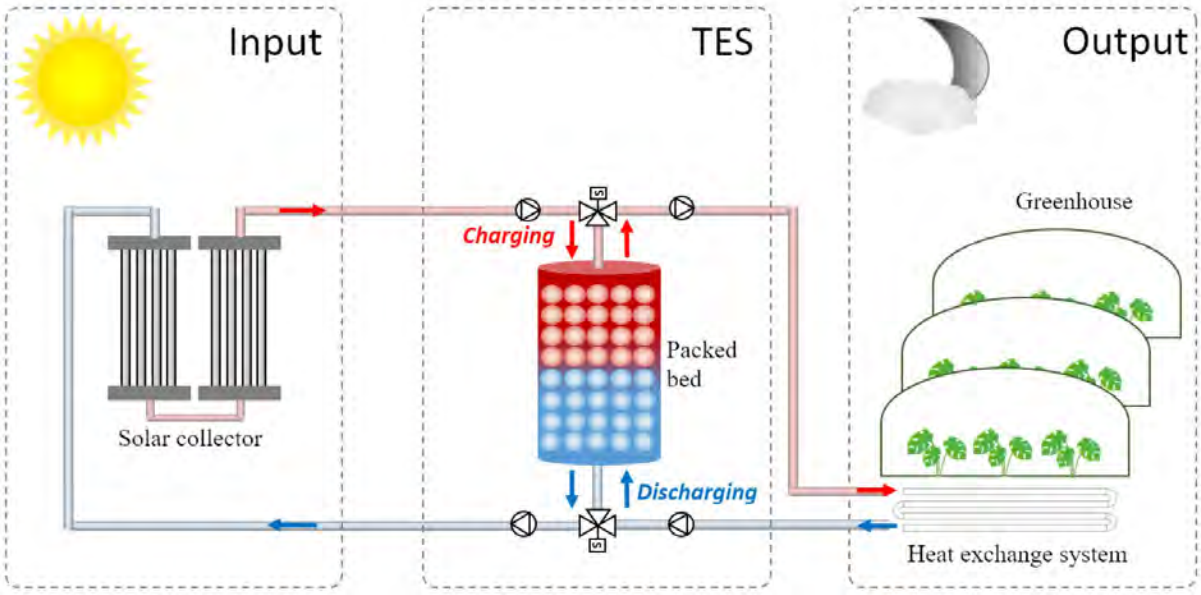

Figure 5.3: Schematic of thermocline system in greenhouse.

The input solar energy is used to heat the water HTF with collectors, and then directly flows into the thermocline packed-bed tank to minimize the thermal losses to the environment. The output energy from TES is an indirect system that HTF flows out from top of thermocline tank and then transfers heat in heat exchanger unit to feed greenhouse. In real application, both output and

input energy are dynamic in function of varying independently under the influence of changeable weather and climate. In this work, an assumption that the dynamic output for greenhouse heating can be achieved by controlling the operational condition of the exchanger was proposed for simplification. Thus, only the dynamic input is investigated under the fluctuation of solar radiation.

5.3.1.2. Defining tank volume

The preliminary tank volume (V_{DES}) is estimated based on the maximum daily consumption of greenhouse in one year with a steady initial condition.

$$V_{DES} = \frac{E_{GH,max}}{[(1-\varepsilon)\cdot\rho_{PCM}\cdot C_{p,PCM}+\varepsilon\cdot\rho_f\cdot C_{p,f}]\cdot\Delta T_{DES}\cdot\eta_{dis,DES}} \quad (5.11)$$

► E_{GH} [J] is the daily greenhouse consumption, calculated by integrating the required thermal power (P_{output}, W) within the designed daily discharging time ($t_{dis,DES}$, s). Here**,** the maximum daily value, $E_{GH,max}$, is selected to amplify the operational flexibility for extreme weather when designing a tank.

► $\eta_{dis,DES}$ is the designed discharging efficiency of TES system, accounting heat loss and outlet temperature drop in discharging, which can be set as 0.85 based on different studies [223][43][63].

► ΔT_{DES} [K] is the designed maximum temperature difference on the tank, $T_H - T_C$.

5.3.1.3. Defining mass flow rates

Constant operational condition (mass flow rate or inlet temperature) is necessary for an ideal steady operational condition for thermocline packed-bed optimization. However, the output and input of greenhouse are changeable with the fluctuant solar radiation intensity and unstable heating requirement, respectively. In this system, in discharging process, the greenhouse consumption is assumed to be stable in steady condition.

A constant mass flow rate but changeable inlet temperature for real application was defined to simulate the dynamic process. Once the difference between steady and dynamic conditions are larger, the dynamic influence then need to be considered in optimization.

Designed mass flow rates in charging and discharging processes ($\dot{m}_{f,ch,DES}$, $\dot{m}_{f,dis,DES}$) are assumed to be constant value.

$$\dot{m}_{f,dis,DES} = \frac{E_{GH,max}}{C_p\cdot\Delta T_{DES}\cdot t_{dis,DES}\cdot\eta_{dis,DES}} \quad (5.12)$$

$$\dot{m}_{f,ch,DES} = \frac{E_{GH,max}}{C_p\cdot\Delta T_{DES}\cdot t_{ch,DES}\cdot\eta_{o,DES}} \quad (5.13)$$

►$\eta_{o,DES}$ is the designed overall efficiency, accounting for the charging efficiency, standby heat loss, as well as charging efficiency. The designed mass flow rate allows to the keep the

outlet temperature be higher than the hottest cutoff temperature in charging and lower than the coldest cutoff temperature in discharging to make full use of the tank.

5.3.1.4. Defining inlet temperature

Steady working temperature range is first designed into 20-70 °C depending on the water properties and practical condition, which is the maximum temperature difference ($\Delta T_{DES,max}$).

$$\Delta T_{DES,max} = T_H - T_C = 50 \text{ K} \tag{5.14}$$

Dynamic working temperature range ($\Delta T_{DES}(t)$) is calculated based on the real time-solar radiation intensity.

$$\Delta T_{DES}(t) = T_{in}(t) - T_C = \frac{I(t) \cdot \eta_{collector} \cdot S_{collector}}{\dot{m}_{f,ch,DES} \cdot C_{p,f}} \tag{5.15}$$

In order to set dynamic working temperature close to the steady working temperature range and without designing (proposing) a detailed surface area of solar collector. The $\Delta T_{DES}(t)$ is evaluated according to the maximum steady temperature.

$$\Delta T_{DES}(t) = \Delta T_{DES,max} \cdot \frac{I(t)}{I_{max}} \tag{5.16}$$

► I [W/m^2] is the solar radiation intensity or direct normal irradiation obtained from actual measurement data.

► $\eta_{collector}$ is the overall efficiency of thermal solar panel which is assumed as a constant value. Only solar thermal is taken into account. An efficiency of 50% is taken for solar collector system [224].

► $S_{collector}$ [m^2] is the effective surface area of solar collector, which is designed as the lowest value under the highest radiation day.

5.3.1.5. Meteorological data

Figure 5.4 is the meteorological data of four seasonal days for the first day in January, April, July, and October. It shows gas heating consumption happens mostly in the 24 h per day, but solar supply only in daytime.

On the one hand, for a whole year, the average daily heating consumption ($E_{GH,night}$) from night to morning (**22:00-10:00**) accounts for about 50% of the total daily heating energy ($E_{GH,total}$), including in winter (Dec.-Feb., 50%), in spring (Mar.-May, 53%), in summer (Jun.-Aug., 45%), and in autumn (Sep.-Nov., 53%).

On another hand, the average daily radiation is different during the year but is nearly located at **10:00-18:00** which accounts for around 83% of total daily radiation, including in winter (Dec.-

Feb., 94%), in spring (Mar.-May, 82%), in summer (Jun.-Aug., 78%), and in autumn (Sep.-Nov., 87%).

Therefore, two different times for charging and discharging process are designed as $t_{dis,DES}$=**12 h** (22:00-10:00), $t_{ch,DES}$=**8 h** (10:00-18:00) finally. In daytime, solar collector absorbs thermal energy and then transfer to greenhouse for daily heating, as well as to the thermocline system for charging. At night, thermocline discharges thermal to greenhouse for heating. Thus, during the night, thermocline tank releases energy that drop into the minimum storage condition. During the daytime, it stores excess energy that reaches the maximum condition.

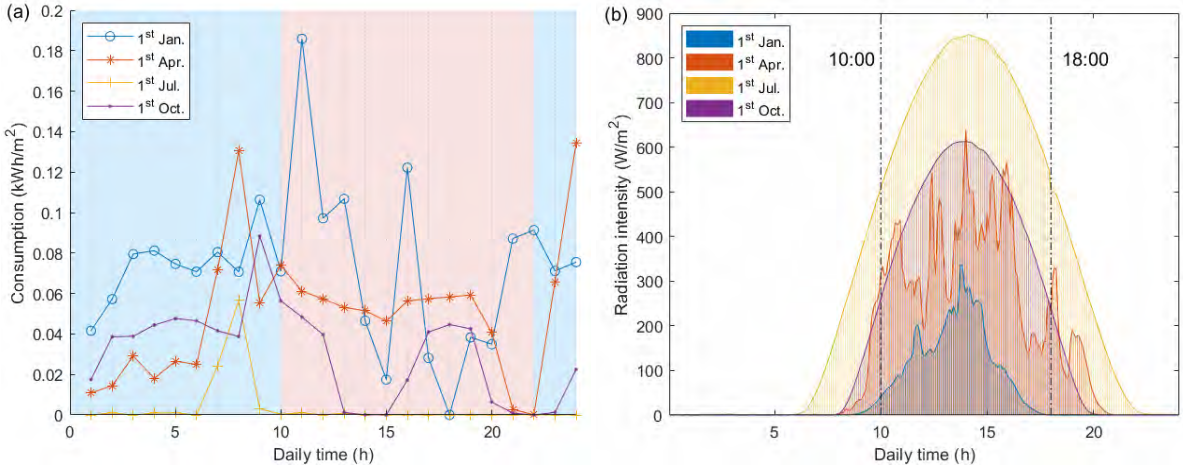

Figure 5.4: Meteorological data in the 1st day of typical seasonal month (Jan., Apr., Jul., Oct.): (a) gas heating consumption; (b) daily radiation intensity.

Table 5.2 is the annual energy consumption and solar energy supply of the greenhouse. The maximum energy demand of greenhouse of $E_{GH,max}$ =1 kWh m^{-2}/day in *Appendix* **FigureA 5.1** is used to determine the tank volume. The maximum solar thermal radiation of I_{max}=6 kWh m^{-2}/an in **FigureA 5.2** is selected to calculate the dynamic inlet temperature in charging. This choice might be utilized as the maximum of energy demand is in winter and the maximum energy supply is in summer. We choose anyway to start with these conditions.

The output energy to greenhouse and input energy from solar are daily different, as well as seasonal changeable in *Appendix* **FigureA 5.1**-**FigureA 5.2**. To simplify the optimization process, the steady initial condition is set and the total daily consumption is assumed to be the same in different seasons. The assessment of the life cycle assessment and economic cost optimization will not be considered in this chapter. The pump energy is not considered.

Table 5.2 Greenhouse application data: the semi-fermée CTIFL-Carquefou system*1 [222].

	Output (energy consumption) *2	**Input (energy supply)** *3
	Required gas heating energy, E_{GH} *2 **(**22:00-10:00**)***6	**Solar radiation *I*** (10:00-18:00)*6
Total*5	136 KWh/m^2/an (334 days)	967 kWh/m^2/an (334 days)
Maximum*4	1 KWh/m^2/day (12 h)	6 kWh/m^2/day (10 h)

*1 Data collected from 3rd December 0:00 in 2014 to 1st November 23:00 in 2015 (334 days).

*2 The energy consumption contains the gas heating to keep constant temperature and the extra electrical energy for ventilation which is not discussed here.

*3 The data is collected from outside of greenhouse.

*4 The selection of maximum data eliminating the abnormal data.

*5 Three unit greenhouse units have total surface area around S_{GH}=900 m^2.

*6 The discharging is designed for the time (22:00-10:00), and charging is within the time of 10:00-18:00.

5.3.1.6. Final design results

Preliminary tank parameters and final designing results for greenhouse are listed in **Table 5.3**. The steady and dynamic inlet temperature in charging in **Figure 5.5**.

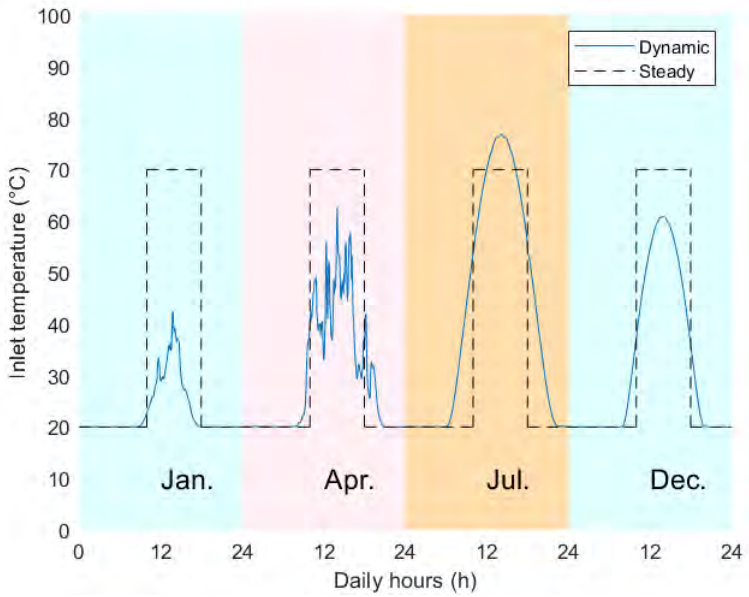

Figure 5.5: Steady and dynamic inlet temperature of thermocline packed-bed tank for four seasonal days.

Table 5.3 Initial tank parameters and design results for greenhouse application.

Tank parameters	**Symbols**	**Value**
PCM:paraffin [147]	T_m	60±0.5 °C
	ΔH_m	213 J g^{-1}
	$\rho_{PCM,s} \cdot C_{p,PCM,s}$	1.6 × 10^6 J m^{-3} K^{-1}
	$\rho_{PCM,l} \cdot C_{p,PCM,l}$	1.8 × 10^6 J m^{-3} K^{-1}]
HTF: water	$\rho_f \cdot C_{p,f}$	4.13 × 10^6 J m^{-3} K^{-1}
Porosity	ε	0.5
Tank aspect ratio	H/D_{tank}	2
Particle diameter	D_p	50 mm
Steady working temperature	T_C/T_H	20/70 °C
Cutoff	--	20%
Assumed discharging energy efficiency	$\eta_{dis,DES}$	0.85
Assumed overall efficiency	$\eta_{o,DES}$	0.8
Solar system efficiency	$\eta_{collector}$	0.5
Designed parameter	**Symbols**	**Value**
Tank volume	V_{DES}	16.45 m^3
Diameter	D_{tank}	2.19 m
Charging time	t_{ch}	8 h
Discharging time	t_{dis}	12 h
Charging mass flow rate	$\dot{m}_{f,ch}$	0.673 kg s^{-1} (40.78 L min^{-1}, *Re*=15)
Discharging mass flow rate	$\dot{m}_{f,dis}$	0.422 kg s^{-1} (25.59 L min^{-1}, *Re*=10)

Paraffin is a phase change material for thermal energy storage that was used because it has features of the wide commercial application, cost-economy, non-corrosion, low phase separation, chemical and thermal stability [68][225]. Most importantly, it shows various phase change temperatures below 100 °C and large with unreasonably high enthalpy around 150-250 J g^{-1} due to the different length of alkane chain [226][227]. The thermal conductivity of PCM can be improved by additive like graphite [228].

5.3.2. Multi-objective optimization

The multi-objective genetic algorithm (MOGA) optimization based on the non-dominated sorted genetic algorithm-II (NSGA-II) that controls elitism selection strategy, is applied as tool.

The optimization of this work is to find the optimal layer thickness of PCM, phase change temperature, and thermal conductivity based one or several similar PCM materials through a multi-layered packing strategy for a given greenhouse application. The nonlinear optimization problem with bound constraints is studied.

5.3.2.1. Optimization process

A flow chart of designing tank and optimization process is shown in **Figure 5.6**. Based on the initial design of the single tank, optimizing the thermal performance of packed-bed tank by multi-layered PCM packing.

Step 1: Determining the two layer numbers.

Step 2: Designing four configurations as optimization target to conduct MOGA in turns.

Step 3: MOGA optimization process:

S1: determining the cycling times, cutoff temperature operational conditions of TES system for model simulation.

S2: defining the variables and objectives, initial and final condition for MOGA optimization.

S3: initializing and run DC-3P model in cycling.

S4: generation, selection, mutation, until to final condition to obtain the Pareto front.

Step 4: Defining a better configuration as the optimization result.

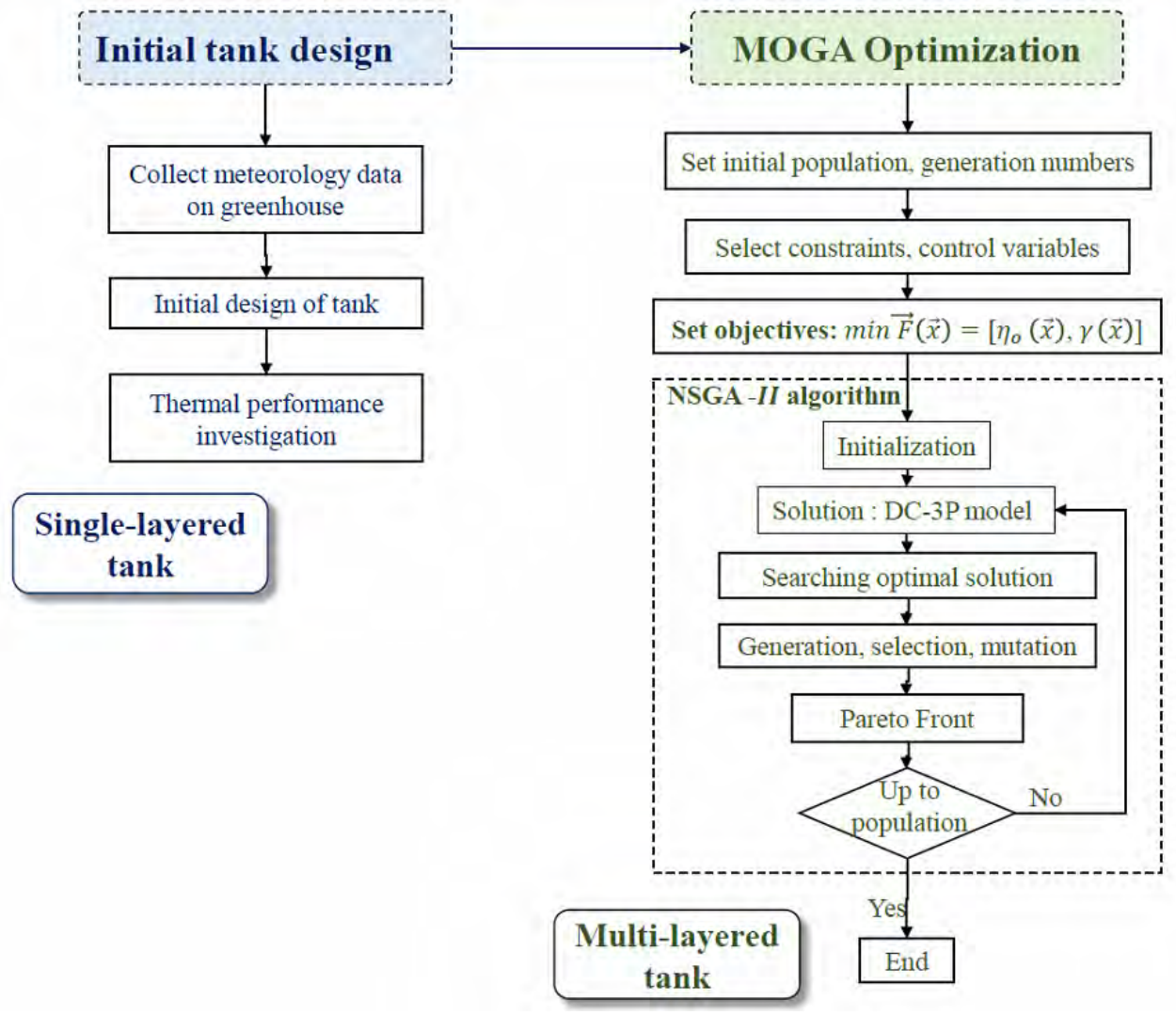

Figure 5.6: Flowchart of design methodology and multi-layered optimization process of the PCM thermocline packed-bed TES system.

5.3.2.2. Variables and objectives

Variables constraints and objectives functions of MOGA optimization are in **Table 5.4**.

(1) Control variables (x): All design variables were normalized. The layer thickness (L_i^*) is selected because it is the basic layer variable of the multi-layered packing strategy. The phase change temperature ($T_{m,i}^*$) and thermal conductivity ($\lambda_{PCM,i}^*$) are used since those are inherent properties of PCM and have relevant influence on thermal performance. Moreover, the maximum constraint of the mass flow rate in charging ($\dot{m}_{f,ch}^*$) and mass flow rate in discharging ($\dot{m}_{f,dis}^*$) are determined to use the full tank volume based on the model validation ranges. The minimum constraint of the mass flow rate is equal to the initial design value because the tank cannot be full used.

(2) Two KPIs are considered as objective functions or fitness functions (F_i) to access the thermodynamic behavior in **Eq.s 5.17- 5.18**: the overall energy efficiency (η_o), and the overall storage/utilization ratio (γ_o), considering the capacity ratio in charging (C_{ratio}) and the utilization ratio in discharging (U_{ratio}).

(3) The optimization algorithm is the elitist genetic algorithm by using the global optimization Toolbox in Matlab 2021a® [229], which is the variant of the non-dominant sorting genetic algorithm (NSGA-II) [230]. This genetic algorithm is good at the continuity and differentiability of fitness function [231] and is able to create a set of points on the Pareto front to minimize the objective functions [232]. The algorithm is completed when the average change in the spread of Pareto solutions is below a determined threshold or to the max setted generations.

Two KPIs in the objective functions are as follows:

Overall energy efficiency (η_o) physically means the comparison of the total energy released from the tank by HTF in discharging process and the total energy supplied to the tank by HTF in charging process. [43]

$$\eta_o = \eta_{ch} \cdot \eta_{disch} = \frac{\int_0^{t_{dis}} [\dot{m}_f \cdot C_{p,f} \cdot (T_{out} - T_0)] dt}{\int_0^{t_{ch}} [\dot{m}_f \cdot C_{p,f} \cdot (T_{in} - T_0)] dt} \tag{5.17}$$

where T_{in} is the inlet temperature of HTF and T_0 is the reference coldest operational temperature T_C (20 °C), respectively, T_{out} is the outlet temperature of the HTF.

Overall storage/utilization ratio (Υ_o) is used to evaluate the both effect of capacity ratio (C_{ratio}) in charging and the utilization ratio (U_{ratio}) in cycles, accessing by the weight-mass method [233] in Chapter 4 in Section 4.2.4.

$$\Upsilon_o = \frac{C_{ratio} + U_{ratio}}{2} \tag{5.18}$$

Table 5.4 Variables and objective functions definition of the multi-objective genetic algorithm (MOGA) optimization.

Design variables	**Symbols**	**Contraints**	**Actual value**
PCM layer thickness *1	$L_i^*=\frac{L_i}{H}$, $\sum L_i^* = 1$	[0.1 0.9]	--
PCM phase change temperature	$T_{m,i}^*=\frac{T_{m,i}-T_c}{T_H-T_c}$	[0.2 0.8]	$T_{m,i} \in [T_{20\%}\ T_{80\%}]$ *5
PCM thermal conductivity*2	$\lambda_{PCM,i}^* = \frac{\lambda_{PCM,i}-\lambda_{PCM}(min)}{\lambda_{PCM}(max)-\lambda_{PCM}(min)}$	[0 1]	$\lambda_{PCM} \in$ [0.2 20]
Mass flow rate in charging*3	$\dot{m}_{f,ch}^* = \frac{\dot{m}_f-\dot{m}_{f,ch}(min)}{\dot{m}_{f,ch}(max)-\dot{m}_{f,ch}(min)}$	[0 1]	$\dot{m}_{f,ch} \in$ [0.673 1.65]
Mass flow rate in discharging*3	$\dot{m}_{f,dis}^* = \frac{\dot{m}_f-\dot{m}_{f,dis}(min)}{\dot{m}_{f,dis}(max)-\dot{m}_{f,dis}(min)}$	[0 1]	$\dot{m}_{f,dis}^* \in$[0.422 1.65]
Indicators	**Objective functions***4	--	--
Overall energy efficiency	F_1=max $[\eta_o = \eta_{ch} \cdot \eta_{dis}]$	--	--
Overall storage/utilization ratio	F_2= max $[\gamma_o=(U_{ratio}+C_{ratio})/2]$	--	--

*1 i is the packing layer number.

*2 Liquid and solid phase thermal conductivity are assumed as the same for PCM.

*3 The *Re* of mass flow rate in charging/discharging are all within validation ranges of [15 40].

*4 Performance indictors has been defined in Chapter 4 of Section 4.2.

*5 x% =20% or 80% means the phase change temperature T_m is equal to x%·(T_H-T_C).

In optimization process, four configurations presented in **Figure 5.7** and listed in **Table 5.5** were optimized. Design A and Design A+ are LHTPB tank, whereas Design B and design B+ are HHTPB tank that the lower layer is sensible filler. For Design A, where 5 variables is set the phase change temperature of upper/lower layer equal to the charging/discharging cutoff temperature, respectively. For Design A+ with 7 variables, the phase change temperature imposed. Other parameters for four cases are the same.

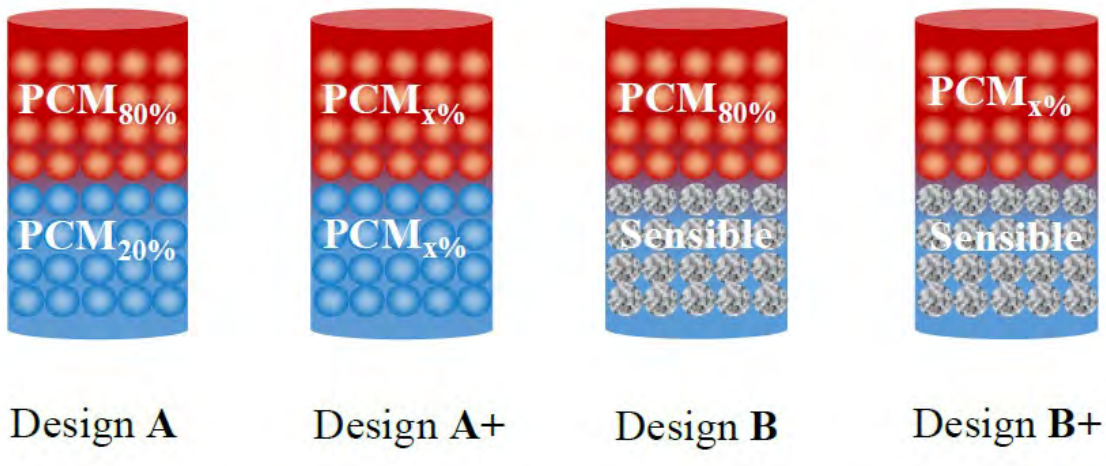

Figure 5.7: Multi-layered packing configurations for optimization: two-layer optimization.

Table 5.5 Evaluation index of thermal performance.

Configurations	Layers		Tank types	Variable numbers	Variables						
	Upper*2	lower*2			L^*_{up}	$T^*_{m,up}$	$T^*_{m,low}$	$\lambda^*_{PCM,up}$	$\lambda^*_{PCM,low}$	$\dot{m}^*_{f,ch}$	$\dot{m}^*_{f,dis}$
Design A+	$PCM_{x\%}$	$PCM_{x\%}$	LLTPB	7	√	√	√	√	√	√	√
Design A	$PCM_{80\%}$	$PCM_{20\%}$	LHTPB	5	√	--	--	√	√	√	√
Design B+	$PCM_{x\%}$	Sensible	HLTPB	5	√	√	--	√	--	√	√
Design B	$PCM_{80\%}$	Sensible	HHTPB	4	√	--	--	√	--	√	√

*1 i is the layer number, '*up*'=upper layer, '*low*'=lower layer.

*2 x% means the PCM phase change temperature T_m is equal to x%·(T_H-T_C).

5.3.2.3. Grid and time step convergence study

Time step and grid independence are tested based on the designed PCM thermocline packed-bed tank in **Figure 5.8** in charging process for greenhouse. It obtained the standard deviation of charging efficiency and outlet temperature stay below below 1% when the nodes of height ($N = \frac{H}{\Delta z}$) × time ($M = \frac{t}{\Delta t}$) × particle radius ($F = \frac{D_p}{\Delta r_p}$) is 300×300×10. Therefore, they are adopted in the following simulation and optimization algorithm.

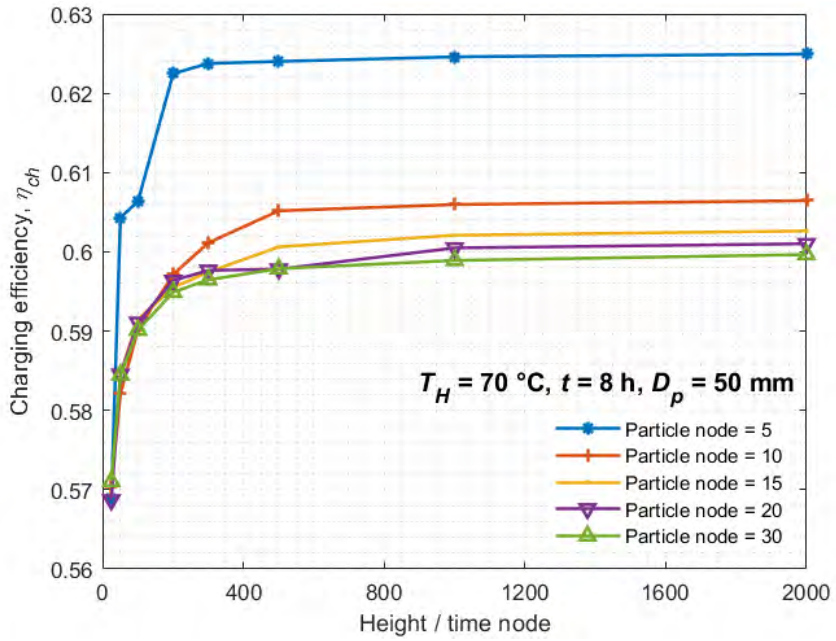

Figure 5.8: Height node, time node, and particle radius node independence tests.

5.4. One-layer TES tank design

Once defining an initial tank with single PCM, the second step of this study is to evaluate the thermal performance of this tank.

(1) Considering the real fluctuated weather, it is necessary to compare the dynamic operation of real greenhouse and the steady operation of simulation to explore the influence degree at first.

(2) Then, as the dominant factor, the phase change temperature cause influence on performance is meant to be discussed by sensitivity analysis.

(3) Later, the cycling performance should be evaluated to determine the cycling number to obtain stable condition.

5.4.1. Performance at steady and dynamic operational conditions

In real greenhouse, the input to TES tank is dynamic due to the fluctuated radiation of weather. PCM is characterized by absorbing energy during the phase transition and keep the phase change temperature at a constant value. It thus interesting to use PCM as a temperature buffer to alleviate the influence of fluctuated inlet temperature on thermocline and to achieve stable output.

Based on this premise, we selected two paraffin PCMs (PCM60 and PCM30 that phase change temperatures is T_m=30 °C and T_m=60 °C, respectively) and compare to both with the sensible rock fillers in packed-bed tank based on a representative day of 1st January and 1st July. **Figure 5.9** presents the steady and dynamic comparison results.

As shown in **Figure 5.9 a**, the PCM filler has the advantage of stabilizing the outlet temperature at around its phase change temperature than sensible fillers. But, the initial design tank of PCM60 has not shown a complete daytime storage loading after 8h, as well as the PCM30 filler tank. That is one of the reasons why the capacity ratio in charging of PCM fillers tank is lower than the rock fillers tank in **Figure 5.9 b**. This results suggest that it's possible to improve thermal performance by designing phase change temperatures in different layers, based on one PCM with the similar volumetric heat capacity and enthalpy but different phase change temperature, like paraffin.

The dynamic results of a sunny day in July are not so different from the steady results in the aspect of outlet temperature and capacity ratio. Therefore, in this study, the steady input will be used in optimization simulation and the realistic variable input will be evaluated based on the optimization result at the end.

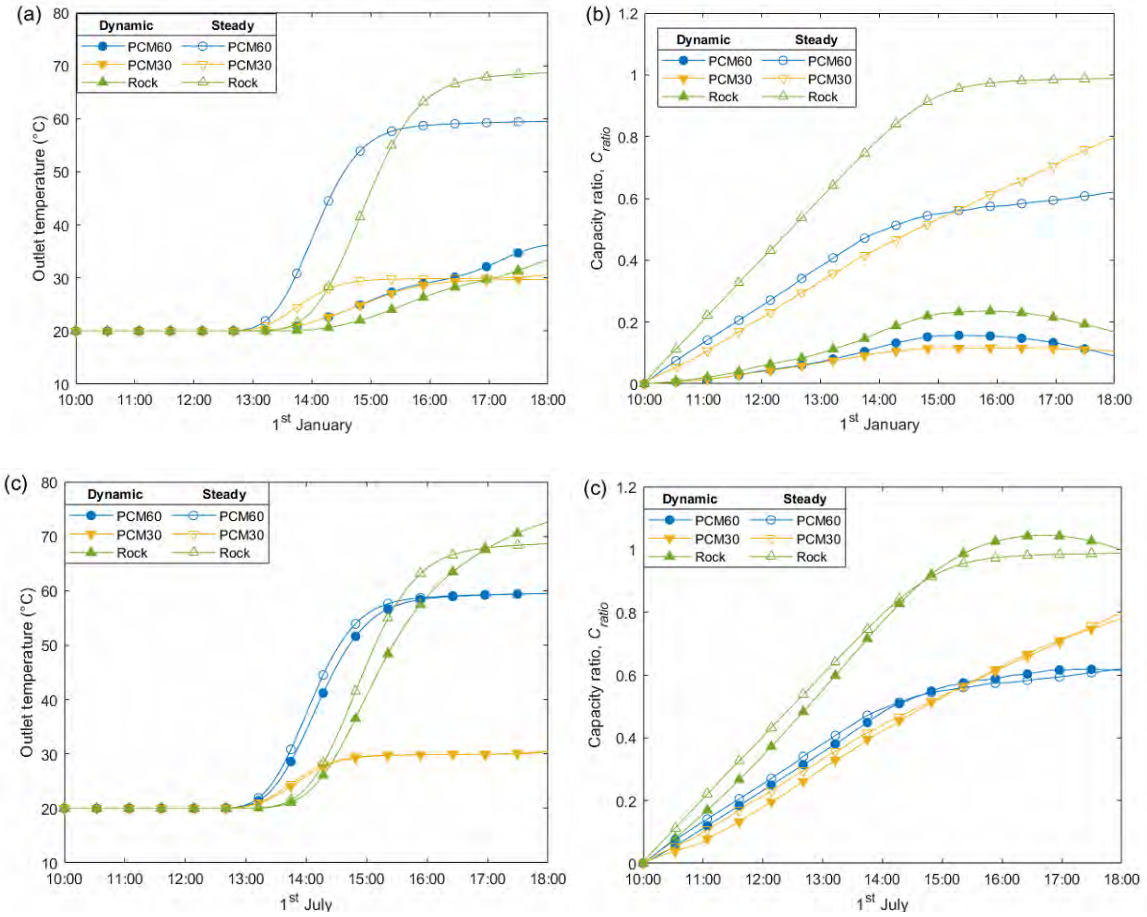

Figure 5.9: Evaluation of steady and dynamic inlet temperature for one representative day in charging (1st January, 1st July): (a)(c) outlet temperature profile; (b)(d) capacity ratio. (N=300, M=300, F=10).

5.4.2. Sensitivity of efficiency of the phase change temperature

Figure 5.10 is the evaluation results of the phase change temperature in the first charging and discharging cycling with a constant cutoff threshold temperature. $T_{20\%}$ is cutoff for discharging and $T_{80\%}$ is for charging. With the phase change temperature from 20 °C to 70 °C, the KPIs, including overall energy efficiency (η_o), capacity ratio (C_{ratio}), utilization ratio (U_{ratio}), and dimensionless cycling time (the average time for charging and discharging process), vary and exhibits obvious stages: below $T_{20\%}$, between $T_{20\%}$~$T_{80\%}$, above $T_{80\%}$. Sensitivity analysis shows the selection of phase change temperature is influenced by cutoff threshold temperature.

In addition, in **Figure 5.10 a**, when the phase change temperature is between two cutoff temperature ranges ($T_{20\%} < T_m < T_{80\%}$), the overall efficiency is only around 60% and dimensionless time is all equal to 1. That means that PCM cannot be fully utilized within this designed time. This result suggested that the mass flow rate should be designed higher than the present value to fully store energy for design, and later optimization on the thermal conductivity increase to enhance the heat transfer with the PCM capacity ratio increase.

The result in **Figure 5.10 b** shows the influence of phase change temperature on capacity and utilization ratio are converse, which suggests that filling different phase change temperature PCM in layers of tank maybe a good solution to contradiction.

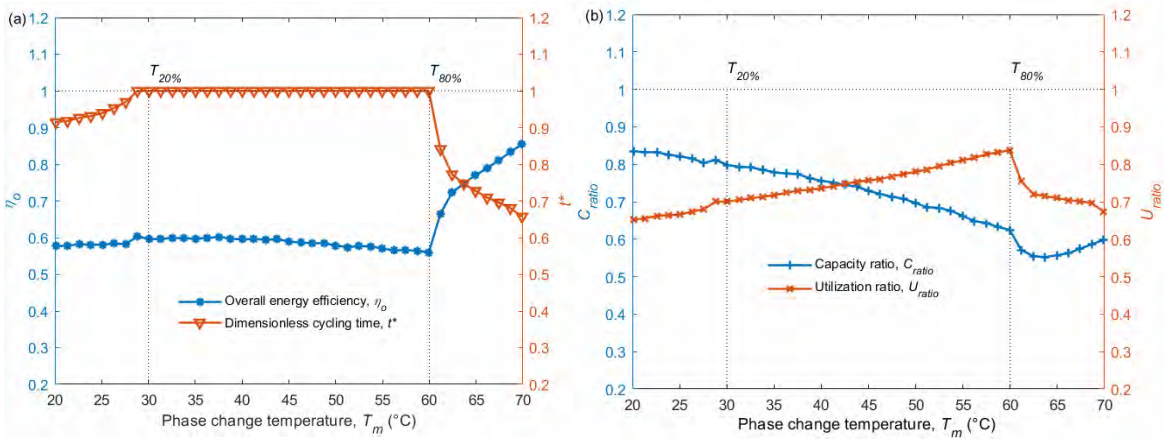

Figure 5.10: Variation of phase change temperature ($T_m \pm 0.1$ °C).

5.4.3. Cycling performance

Performance indicators in a stable condition are the principle of system evaluation. Stable thermocline behavior in cycling means a constant outlet temperature at the ending of each discharging and means with cycling numbers increase there is no degradation increase. **Figure 5.11** is cycling test during 10 cycles based on the overall energy efficiency of the initial designed PCM tank. In cycling, each ending condition is the initial condition of next charging/discharging process. It was observed that the overall energy efficiency at the third cycles is relatively constant (0.4≲%) which indicates the system becomes stable. Thus, KPIs at the 3rd cycling can be set as performance indicator in cycling for optimization.

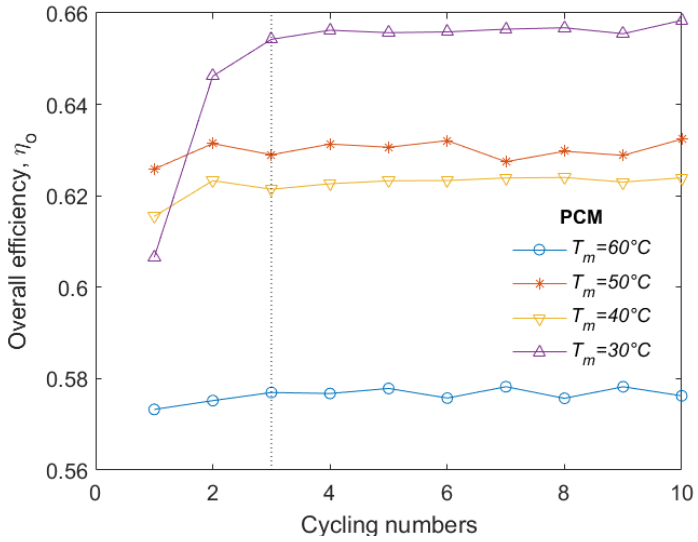

Figure 5.11: Evaluation of cycling numbers.

5.5. Two-layer optimized TES tank design

As mentioned in Section 5.3, the optimization process is designed to obtain an optimal PCM packed tank of two layers, that is subjected to the maximum 7 constraints. All parameters were calculated at the third cycle of steady conditions. But before that, to better understand why this case is optimal, it should begin from a basic case of Design A & B with fewer constraints, and then to the advanced Design A+ & B+.

The method is the following:

(1) Calculate and observe on the Pareto front of design cases to compare the difference of basic and advanced configuration.

(2) Select the optimal special case from Pareto front and comparing with the reference case. An optimized design is determined.

(3) Based on the optimized design results, explain the influence of variables on MOGA result.

(4) Extend the analysis to a more general case in order to define a design guideline.

5.5.1. Optimization results

Pareto front is a set of optimal results that designer can select compromised results according to requirement of packed-bed system. **Figure 5.12**. is the Pareto front based on two objectives, the overall energy efficiency (η_o) and the combined capacity-utilization ratio (Υ_o), for MOGA optimization of two-layer arrangement. As exhibited, the Pareto front clearly shows the trade-off between maximizing η_o and Υ_o. Among design cases, the Design A+ (PCM-PCM) with two layer PCMs has the highest η_o and Υ_o, showing an optimal result, while the Design B ($PCM_{80\%}$-Sensible) with upper/lower layer of PCM/sensible rock filler shows the lowest η_o and Υ_o.

The Design A ($PCM_{80\%}$-$PCM_{20\%}$) fixing the upper/bottom layer PCM temperature equal to the charging/discharging cutoff temperature is investigated. Contrast to Design A+, the Υ_o of Design A+ is less changed and maintained at around 0.98, while Design A+ has a Υ_o about 0.95. This difference demonstrates Design A+ is better than Design A, optimizing upper layer PCM is beneficial to enhancement of the storage and utilization ability by about 3% in LHTPB tank.

The Design B that fixing the phase change temperature of the upper layer PCM that is equal to the cutoff temperature. Comparing to Design B+ (PCM-Sensible) that optimizing the upper layer PCM, it can improve the overall storage and utilization ratio of Υ_o of tank in cycling by around 4% in HHTPB tank.

It is proposed that once fixing the upper/lower layer phase change temperature according to the cutoff temperature, the storage and the utility of tank are not as high as enough within the

designed variable ranges. Thus, Design A+ is a better case which is determined to be the optimization subject in this study and will be introduced later.

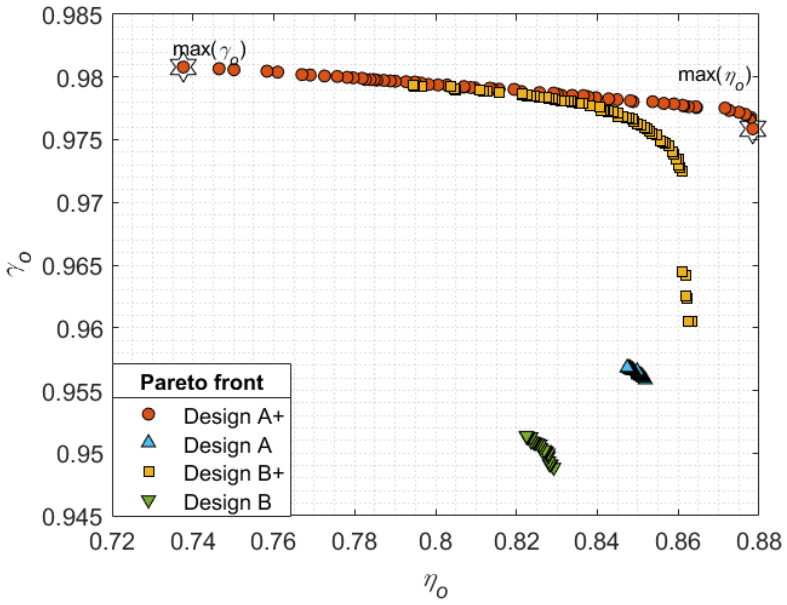

Figure 5.12: Pareto front of Design A+ ($PCM_{x\%}$-$PCM_{x\%}$), A ($PCM_{80\%}$-$PCM_{20\%}$), B+ ($PCM_{x\%}$-Sensible), and B ($PCM_{80\%}$-Sensible).

5.5.2. Advantages of optimal result

● Energy storage density

In order to illustrate the advantages of the optimized tank of Design A+, as a reference, the single sensible ROCK tank is first compared. **Table 5.6** and **Table 5.7** lists three special results and corresponding variables of Design A+ and B+ in Pareto front (**Figure 5.12**): the maximum η_o, maximum Υ_o, and the tradeoff both objectives. Among those, a selected point at maximum η_o is used to compare with the reference tank considering the Υ_o is almost not changed.

Figure 5.13 is the comparison results under the same initial condition for Design A+ and ROCK tank. As depicted, Design A+ shows higher value of Υ_o, η_o and, near 2 times (30-55%) stored/released energy than single ROCK tank in this study, which means the one advantage of PCM tank is the high energy storage capacity.

Noted that if filling sensible fillers with higher volumetric heat capacity material (like direct using water, $\rho \cdot C_p = 4138$ kJ m^{-3} K^{-1} is 2 times higher than rock $\rho \cdot C_p = 2075$ kJ m^{-3} K^{-1}). The advantage of store energy of PCM is not so obvious. In the low-temperature application with adequate water, the cheaper rock cannot present great advantage in the improvement of heat storage capacity in industrial. Another important advantage of PCM is to keep stable temperature that will be discussed following.

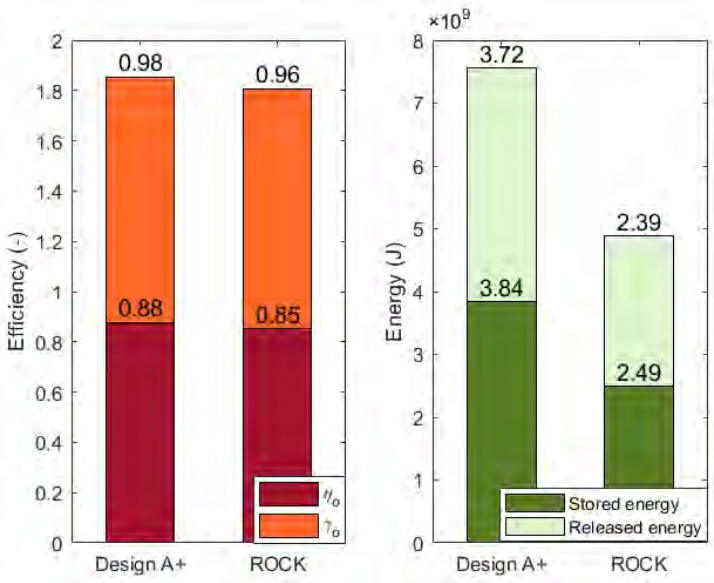

Figure 5.13: Comparison of Design A+ and single ROCK tank based on a particular case of maximum energy efficiency in Pareto front.

Table 5.6 Selected special optimal results and designed variables from Pareto front of Design A+.

Optimization	**Overall**		**Charging**		**Discharging**		**Operational parameters**		**Geometrical parameters**				
	Unit (-)	η_o	γ_o	η_{ch}	C_{ratio}	η_{dis}	U_{ratio}	$\dot{m}^*_{f,ch}$	$\dot{m}^*_{f,dis}$	$L^*_{m,up}$	$T^*_{m,up}$	$T^*_{m,low}$	$\lambda^*_{PCM,up}$	$\lambda^*_{PCM,low}$
Design A+	Max η_o	0.88	0.98	0.91	0.99	0.97	0.96	0.19	0.34	0.50	0.35	0.20	0.73	0.64
	Max γ_o	0.74	0.98	0.76	0.99	0.97	0.97	0.19	0.26	0.53	0.39	0.49	0.69	0.83
	Tradeoff	0.82	0.98	0.84	0.99	0.97	0.97	0.18	0.27	0.56	0.38	0.32	0.73	0.79

Table 5.7 Selected special optimal results and designed variables from Pareto front of Design B+.

	Optimization	**Overall**		**Charging**		**Discharging**		**Operational parameters**		**Geometrical parameters**		
	Unit (-)	η_o	γ_o	η_{ch}	C_{ratio}	η_{dis}	U_{ratio}	$\dot{m}^*_{f,ch}$	$\dot{m}^*_{f,dis}$	$L^*_{m,up}$	$T^*_{m,up}$	$\lambda^*_{PCM,up}$
Design B+	Max η_o	0.86	0.96	0.88	0.97	0.97	0.95	0.25	0.13	0.15	0.26	0.47
	Maxi γ_o	0.79	0.98	0.81	0.99	0.98	0.97	0.15	0.29	0.90	0.38	0.73
	Tradeoff	0.84	0.98	0.87	0.99	0.97	0.97	0.16	0.30	0.90	0.28	0.72

● Evolution of outlet temperature

In order to exhibits the advantages on stabilizing outlet temperature, the outlet temperature of optimal Design cases is presented in **Figure 5.14**. **Table 5.8** shows optimal cases with maximum η_o in Pareto front. The higher outlet temperature in charging process means less energy is stored, the more stable outlet temperature in longer time refers to released more energy.

In **Figure 5.14 a** of the LHTPB, three cases have the same maximum stored energy for different application requirements. It shows Design A+ has the highest stored/released energy ratio ($E^* = \frac{E_{stored,max}}{E_{released,max}}$) but constant low outlet temperature, a reference non-optimized case (half $PCM_{80\%}$ and half $PCM_{20\%}$) has lowest E^* but high outlet temperature. For HHTPB tank in **Figure 5.14 b,** Design B+ also shows larger E^* but constant lower outlet temperature.

An upper layer phase change temperature close to cutoff temperature is necessary for application like CSP, however, unsolidification PCM after discharging or utilized problem is serious in this types of cases. Therefore, if one wants to have a constant high outlet temperature (close to cutoff temperature) the Design A or Design B are good selections with fixed phase change temperature at the top. If only need constant outlet temperature, the Design A+ or B+ are the optimal case.

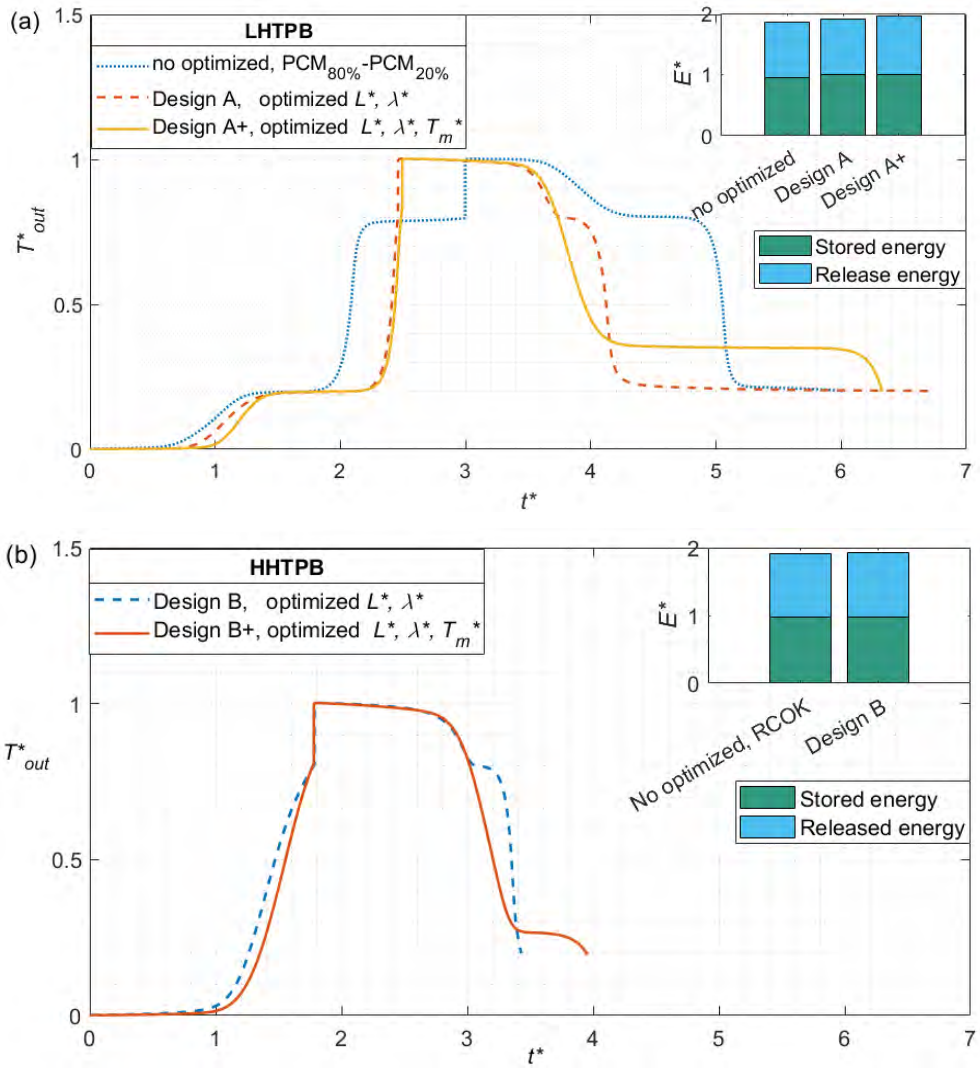

Figure 5.14: Outlet temperature and stored/released energy at the third cycles.

Table 5.8 Maximizing overall energy efficiency optimal variables of four design cases and a reference case.

Configuration	L^*_{up}	L^*_{low}	$T^*_{m,up}$	$T^*_{m,low}$	$\lambda^*_{PCM,up}$	$\lambda^*_{PCM,low}$
Ref. $PCM_{80\%}$-$PCM_{20\%}$	0.50	0.5	0.80	0.20	<0.1	<0.1
Design A	0.15	0.75	0.80	0.20	0.45	0.72
Design A+	0.50	0.5	0.35	0.20	0.73	0.63
Design B	0.1	0.9	0.8	--	0.24	--
Design B+	0.15	0.75	0.26	--	0.47	--

● Evolution of fluid temperature profile

The thermocline behavior of optimal result is compared with sensible filler tank to show the advantage of PCM in keeping inside temperature stratification. **Figure 5.15** is the fluid temperature profiles of the third cycle for Design A+ and Design B in charging. In cycling, the initial condition of third charging is the cutoff time of the second discharging, while the initial condition of discharging is the end of charging. As shown, the HTF (solid line) and PCM (dot line) temperature and thermocline (white dash line) are observed.

- In Design B of charging, there is a thin $PCM_{80\%}$ in the upper layer with a thickness L^*_{up}=0.1 (in **Table 5.8**). The thermocline increase and reaches 30% tank height at t^*=1.
- In Design A+ (L^*_{up} =0.5, in **Table 5.8**) of charging, albeit the thermocline zone or thermocline thickness accounts for 32% of the tank height with a range of 20% to 80% of operational temperature ranges at t^*=1, there is an "extreme" plateau temperature region in Design A+.
- Comparing both cases, the thermocline of Design A+ expanded higher than Design B. One reason is the thermal conductivity for Design A is larger, the thermocline expansion is avoidable. Another is that the heat capacity is higher the temperature of material is increased slower when heating. However, the thermocline thickness is interesting compressed when reaching to the second layer of Design A in charging, and stretched to keep longer outlet temperature constant in discharging.

Therefore, it should be necessary to take into account the thermocline using another definition in multi-layer configuration and considering the exergy efficiency optimization in future work.

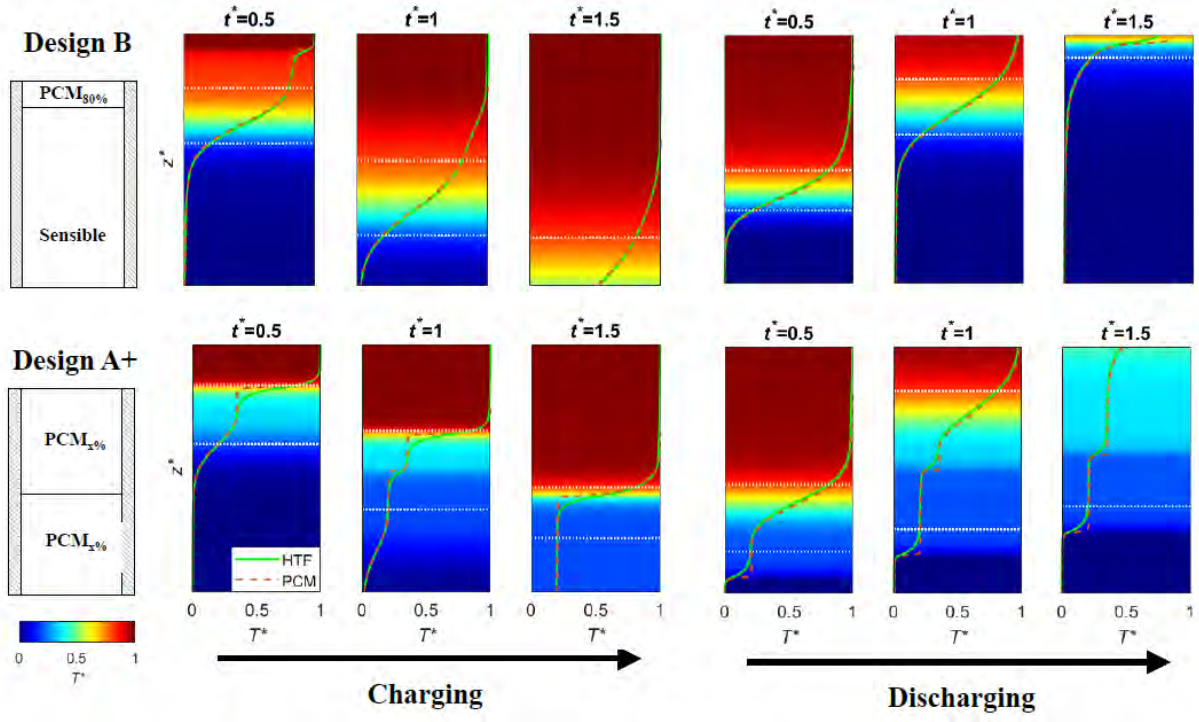

Figure 5.15: HTF temperature profile in charging/discharging at steady inlet condition of the third cycles.

5.5.3. Effect of designed variables

To clarify the influence trends of parameters, the MOGA results should be compared with designed variables, including the operational parameters (mass flow rate, $\dot{m}^*_{f,ch}$, $\dot{m}^*_{f,dis}$) and geometric configuration parameters (upper layer thickness L^*_{up}, phase change temperature $T^*_{m,up}$, $T^*_{m,low}$, thermal conductivity, $\lambda^*_{PCM,up}$, $\lambda^*_{PCM,low}$). The obtained Pareto front results is also better to understand the relationship of different variables and designed objectives. All variables were normalized to obtain generic optimization strategy. **Figure 5.16** presents objectives verse variables in the last genetic iteration.

In this study, the volumetric heat capacity and phase change enthalpy are the same for all PCM. The inlet configuration of charging and discharging process is conversed, the influence of packing configuration parameters on objectives may opposite.

- A higher phase change temperature enables to improve the Y_o but decrease η_o, as shown in **Figure 5.16 a b**. In charging process, larger phase change temperature means smaller temperature gap with inlet temperature of T_H, leading to smaller heat transfer rate between solid PCM and HTF and longer charging time **(Figure 5.17)**. In discharging, the phenomenon is inverse, the improved the heat transfer rate and the decreased discharging time. According to the definition of overall energy efficiency, the overall efficiency η_o is thus decreased. Whereas the Y_o means the combined effect of the total stored energy in

charging and released energy in discharging, which is unclarified which one is dominant or both are positive in increasing Υ_o.

- **Figure 5.16 c d** depicts MOGA results with thermal conductivity variation. It is found when increasing the thermal conductivity of upper layer PCM and decreasing its value of the lower layer PCM, the η_o becomes higher. In fact, heat transfer rate is still the main reason and heat diffusion in HTF is negligible under the mass flow rate. Due to the higher thermal conductivity (higher heat transfer rate,) of upper layer, the upper layer temperature of HTF within same charging time will be higher and stable. When it comes to discharging process, this part of HTF in good quality will results in higher outlet temperature within same discharging time, which is beneficial to higher η_o.
- **Figure 5.16 e** presents the upper layer thickness variation. A smaller upper layer thickness is with higher η_o but it also has lower η_o simultaneously. It's unclear to explain the influence of upper layer thickness by physical phenomena. Because in this case, the optimized phase change temperature of upper layer is not always larger than upper layer temperature, as well as changeable thermal conductivity.

In general, to improve η_o, one could increase heat transfer rate or one could decrease phase change temperature of PCM fillers but is not beneficial to have a high outlet temperature. To improve the Υ_o, it is necessary to increase upper-layer temperature within designed variables range.

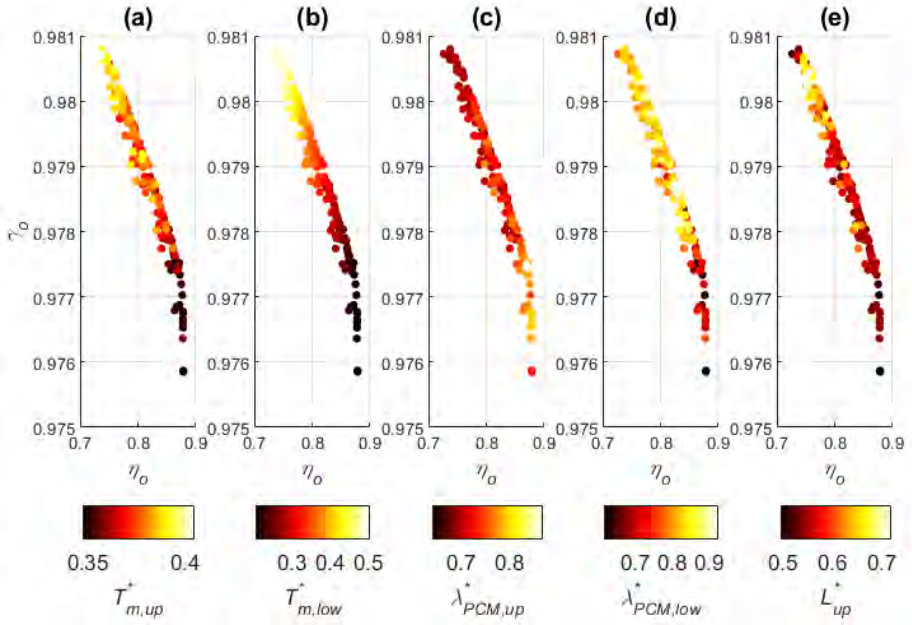

Figure 5.16: Multi-objective optimization results of objectives verse variables for Design A+.

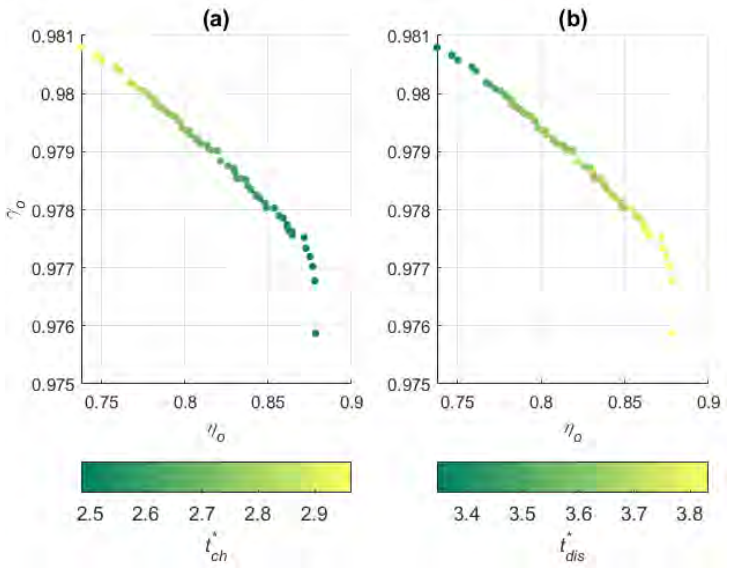

Figure 5.17: Charging and discharging time for MOGA results.

5.5.4. Variables ranges

Figure 5.18 is all optimal variable ranges in the Pareto front of Design A+. At first sight, all designed variables are in a specific range instead of a messy distribution, presenting a regular optimized result.

Firstly, it is observed that the flow rate is located in a range of 0.16-0.19 for charging, and 0.26-0.34 for discharging. In theory, the minimum boundary value of flow rate (m^*_f=0) is set according to the initial design of the single PCM pack-bed tank. While the maximum mass flow rate value (m^*_f =1) depends on the verification range of the equation empirical correlation of the model. In this range, the tank can be fully or near-fully charged/discharged within the designed cycling time (**Figure 5.17**). However, the optimal charging/discharging time is not total equal to the designed initial time and there is little bit higher for discharging time than that of charging process. In real case optimization, the designed time and the optimized time could be unified by using linear constraints of time in future work.

Secondly, it is interesting to find that the phase change temperature of upper and lower layers is in 0.35-0.39 and 0.20-0.49 respectively. Actually, if the outlet temperature is unnecessary to be equal to the cutoff temperature, the phase change temperature is suggested to set near to the average operational temperature (T_{ave}). It can achieve a high energy efficiency in cycling, as well as higher utilization-capacity ratio. Moreover, the upper layer value is lower than the lower layer considering the influence of packing is converse in charging and discharging, that's why the upper layer thickness is not extrude half height of tank (0.50-0.67). Upper and lower layer configuration effect on charging and discharging process are different and sometimes opposite

converse, causing the optimal PCM phase change temperature of two layer into average operational temperature in Design A+, instead of cut off temperature.

Thirdly, the λ^*_{PCM} of bottom is near the same, the thermal conductivity is in 0.6-0.8 for upper layers and 0.6-0.9 for lower layers. In actual definition, the PCM thermal conductivity should be selected many times higher than pure PCM.

These results are useful in selecting PCM with different thermal conductivities and proposes configuration strategies for filling 2-layer pure PCM packed-bed thermocline. Overall, the variable ranges can be determined and give a degree of optimization results that can be achieved.

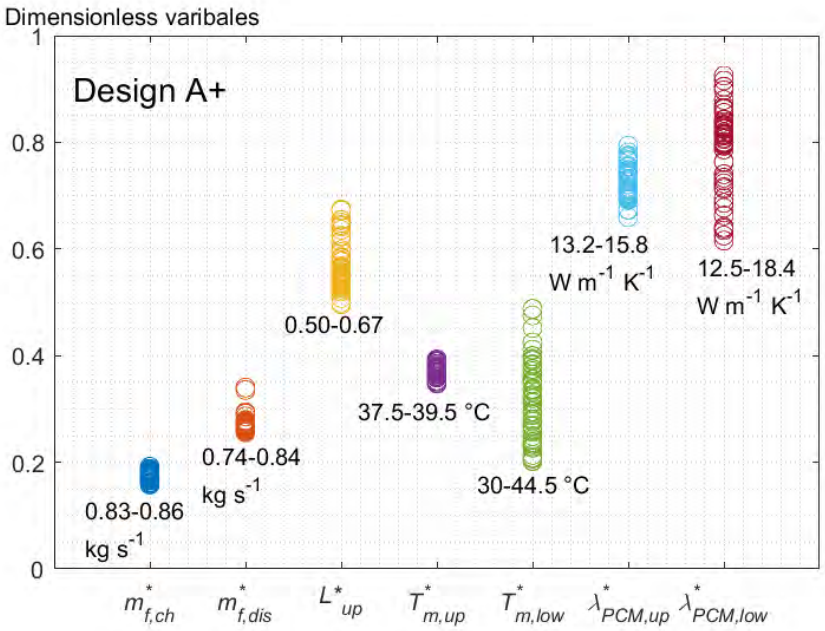

Figure 5.18: Multi-objective optimization results of Pareto front plotted by dot color: the optimal variable ranges of Design A+.

5.6. Evaluation of dynamic performance based on optimization results

This section is to apply the optimal Design A+ in real application and try to find the problem for future improvement. On 1st July, the inlet temperature during a day is smooth and looks like a Gaussian curve (**Figure 5.5**), increasing temperature in the morning and decreasing in the afternoon. Alleviating the fluctuated inlet to and achieving a stable outlet of thermocline tank is needed to better control the heat transfer process with greenhouse.

Figure 5.19 is the temperature profile under dynamic inlet of 1st July of optimal Design A+ and reference Rock tank. As shown in rock tank, the thermocline thickness is almost 100% from the begin to the end, while in Design A+, it can alleviate the influence of fluctuated inlet temperature and compressed the thermocline thickness at t*=1 by around 20%.

Table 5.9 is KPIs results for four seasonal days. One aspect, the dynamic seasonal inlet condition in charging causes the reduction of capacity ratio by up to larger than 80% in winter and 4% in summer for both cases, and leads to reduction of charging energy efficiency by 50% in winter and 1% in summer.

Another aspect, the design A+ improves charging energy efficiency of dynamic condition by 34% than rock tank, but utilization ratio is negligible because the tank is designed according to the maximum load.

In winter, the tank cannot be fully used because the tank volume is designed according to the maximum heat load within one year. It is thus necessary to design an ideal tank for seasonal storage but the inlet temperature can be maintained by filling PCM.

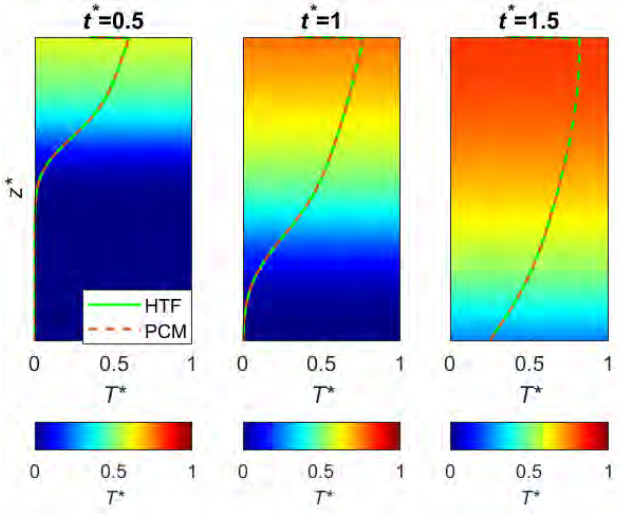

(a)

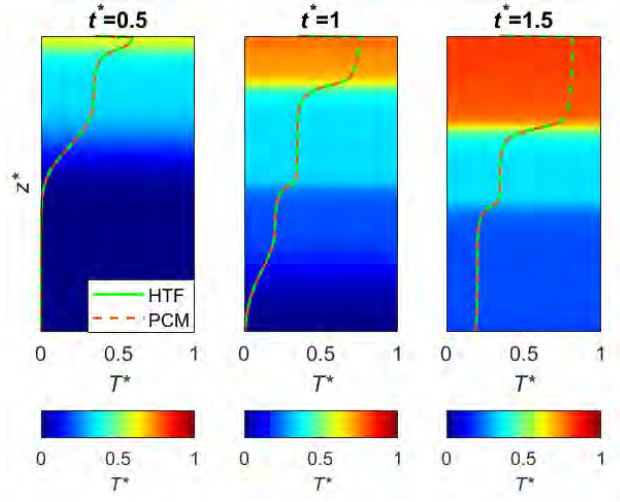

(b)

Figure 5.19: Temperature profiles at dynamic inlet condition in greenhouse in 1st July: (a) Rock tank; (b) Design A+.

Table 5.9 KPIs results for dynamic input of inlet temperature based on MOGA results.

Configuration	KPIs	Steady condition	Dynamic condition			
			Jan.	Apr.	Jul.	Dec.
ROCK tank	η_{ch}	0.89	0.38	0.48	0.80	0.49
	C_{ratio}	0.97	0.13	0.46	1.00*	0.63
Design A+	η_{ch}	0.91	0.48	0.76	0.90	0.87
	C_{ratio}	0.99	0.11	0.47	1.00*	0.71

* The calculated standard according to the T_H and T_C, in July, the hottest inlet temperature is larger than T_H in some times. That' why the efficiency is equal to 1.

5.7. Chapter conclusion

The multi-layered PCM packing configuration strategy of a thermocline PCM packed-bed TES tank for a 0.9 MWh agriculture greenhouse in Carquefou, France, was studied and optimized based on the multi-objective genetic algorithm using NSNA-II. The steady and dynamic input were compared in the final optimal multi-layered tank.

Main results are as follows:

- Optimizing upper and lower configuration using PCMs is good for optimal energy efficiency and utilization ratio in charging/discharging process in Pareto front. An optimal Design A case and corresponding variable ranges are obtained through optimizing the thermal conductivity, phase change temperature, and layer thickness.
- Layer configuration effects on charging and discharging process are different leading to optimized phase change temperature of the two layers close to the average operational temperature in optimization. But fixing the upper phase change temperature of PCM equaling to or close to the charging cutoff temperature leads to high outlet temperature but low utilization ability. According to requirements, selecting appreciated optimization goal.
- According to influence investigation of variables, decreasing two-layer PCMs phase change temperature leads to larger overall energy efficiency but smaller storage/utilization ability. Increasing upper layer thermal conductivity and decreasing the lower layer thermal conductivity simultaneously, facilitating improvement of overall energy efficiency.
- Variable inlet temperature in charging influences the thermal performance, resulting in a capacity ratio reduction of 80% in winter 5% in summer and efficiency decreasing of 50% in winter and 1% in summer based on the optimal tank Design A+. Comparing to filling sensible rock tank, the optimal tank can alleviate the influence of fluctuated inlet temperature and compress themocline thickness around 20% and charging energy efficiency by 34% in a summer day.

In further work, it should take the dynamic input into account for configuration optimization strategy of thermocline packed-bed TES tank to understand how the efficiency and cost can be tradeoff by using different fillers under seasonal weather condition. Moreover, it is meaningful to combine the exergy efficiency (or thermocline thickness) in optimizing objectives to get better and thinner stratification zone and useful energy. In addition, it would be good to test the optimal tank design in real experiment case and to apply the optimization produce for designing of different size tank and different temperature applications.

Appendix 5.I

Meteorological data

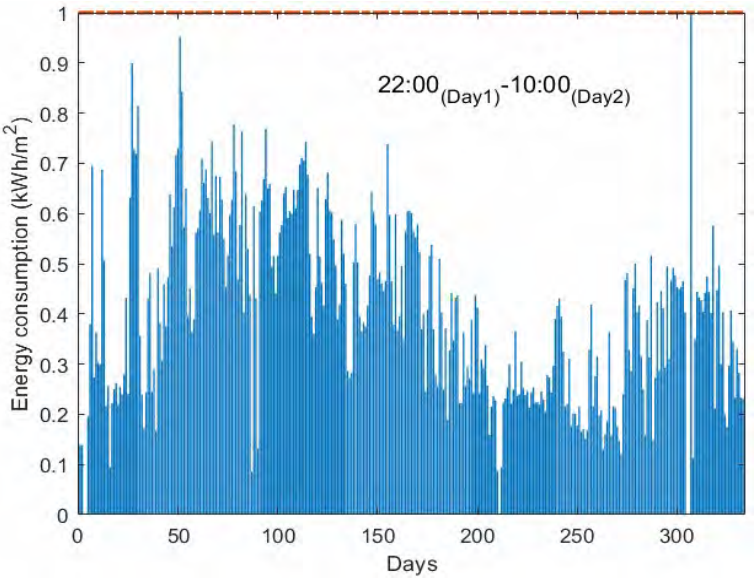

FigureA 5.1: Heating consumption of greenhouse from 22:00(day1)-10:00(day2). (The dot line is the maximum daily value in one year of around **1** kWh/m²)

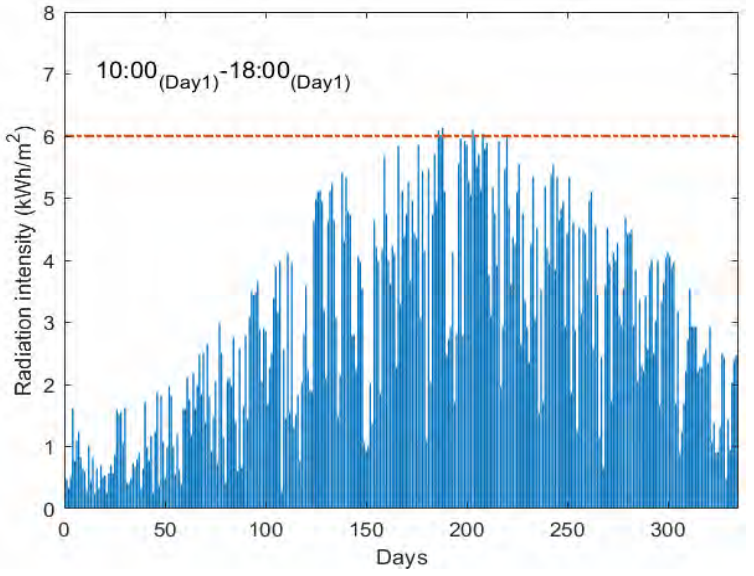

FigureA 5.2: Solar radiation intensity from 10:00(day1)-20:00(day1). (The dot line is the maximum daily value in one year of **6** kWh/m²)

Chapter 6

General conclusions and perspectives

6.1. Conclusions

This thesis focuses on the optimization of packing configuration strategies for the thermocline packed-bed TES system under different influence factors. The main conclusions of each chapter are concluded as below.

In **chapter 1**, the interests of the thermocline packed-bed TES system are presented. The objective and guideline are introduced.

In **chapter 2**, the literatures concluded that storage media is the core of the system. The influence factors of operational, geometrical, and thermophysical parameters showing positive or negative especially the impact degree on system is necessary to be considered in designing the system. The status of three types of systems including sensible-heat system, latent-heat system, heterogeneous-heat system, based on storage media presents the advantages of packing configuration on thermal performance improvment.

In **chapter 3**, the wall impact on the performance of packed-bed TES tanks was first evaluated by using three models through comparing two tank configurations: a high-temperature pilot-scale tank with a steel wall and a low-temperature lab-scale tank with a polycarbonate wall. The maximum energy stored in wall at fully charged state is up to 10% of the total, increasing the thermocline thickness by up to 15% during discharging, but negligible stored energy in the insulation. A transient model considering wall impact is thereby developed. At last, parametric studies show a thinner wall has a smaller impact on the energy and exergy efficiencies.

In **chapter 4**, various influencing factors including inlet configuration, insulation, mass flow rate, inlet temperature, etc., on thermocline behavior and on the overall performances of a lab-scale sensible-heat storage tank is then investigated through both experiment and modeling. The combined effect of diffuser and packed bed as inlet configuration maintains the radial temperature uniformity and the axial thermocline expansion, increasing the capacity ratio by about 3% but effect on the global performance is rather limited. Good insulation reduces the thermocline thickness by about 20%, and increase the energy efficiency by 5-7% and the capacity ratio by 3-5%. At last, validating a temperature difference up to 1.7 K between the fluid and the solid particle center, determining an optimal flow velocity of about Re=3.

In **chapter 5**, the multi-layered packing configuration strategy of a thermocline packed-bed TES tank for a 0.9 MWh agriculture greenhouse application in Carquefou, France, was studied and optimized. Optimizing upper and lower layer configuration for PCMs is good choice for optimal energy efficiency of 88% and storage/utilization ability of 98% in multiple cycles. On the optimal tank, variable inlet temperature results in a capacity ratio reduction of 80% in winter 5% in summer and efficiency decreasing of 50% in winter and 1% in summer. Comparing to filling sensible rock tank, the optimal tank compress thermocline around 20% and charging energy efficiency by 34% in a summer day.

6.2. Perspectives

In fact, this thesis is the basic work in the packing configuration optimization of the thermocline packed-bed TES system. They are still a lot of work to do before being integrated into a real greenhouse application. Based on the results that obtained in this thesis, several perspectives were proposed for future work.

- **Validation of the optimal tank**
  At first, it is looking forward to test the optimal tank design in real experiment case and to apply the optimization produce for designing of different size tank and different temperature applications.
- **Optimization for the economic cost and efficiency**
  Investment reduction and efficiency improvement are mutual and necessary for a commercial mature application. This thesis doesn't extend to it. In future work based on this thesis, it should be taken into account: 1) Make a trade-off between cheaper sensible fillers and higher storage capacity; 2)The investment of storage media should account for the cost of storage media themselves, the investment in preparation of PCM capsules to avoid phase change leakage, and the cost of graphite additives for thermal conductivity improvement of capsules; 3) The investment in solar collectors should be considered in the optimization of operational parameters (the mass flow rate and inlet temperature) because those parameters depend on the solar collective (heat source input power).
- **Topology optimization of packing configuration**
  The topology optimization is interesting to design the packing configuration according to the the fluid flow, or temperature distribution inside the tank.
- **Optimization based on dynamic seasonal application**
  In the whole year, the climate changes a lot that the optimal tank under steady input is not suitable for application in variable input conditions. It should take the dynamic input into account for configuration optimization strategy of thermocline packed-bed TES tank to

understand how the efficiency and cost can be tradeoff by using different fillers under seasonal weather condition.

- **Life cycling assessment (LCA) after integration**

  The environmental impacts or potential impacts of this thermocline packed-bed greenhouse system need to be estimated compared to conventional system with fossil sources or CO_2 emission sources, through a standardized, mature, systems-oriented analytical tool of LCA.

References

[1] Lou W, Luo L, Hua Y, Fan Y, Du Z. A review on the performance indicators and influencing factors for the thermocline thermal energy storage systems. Energies 2021;14:8384.

[2] Cascetta M, Petrollese M, Oyekale J, Cau G. Thermocline vs. two-tank direct thermal storage system for concentrating solar power plants: A comparative techno-economic assessment. Int J Energy Res 2021;45:17721–37.

[3] Xie B, Baudin N, Soto J, Fan Y, Luo L. Thermocline packed bed thermal energy storage system : a review. In: Jeguirim M, editor. Renew. Energy Prod. Distrib. 1st ed., Elsevier; 2022, p. 325–85.

[4] Vannerem S, Neveu P, Falcoz Q. Experimental and numerical investigation of the impact of operating conditions on thermocline storage performance. Renew Energy 2021;168:234–46.

[5] Vannerem S, Neveu P, Falcoz Q. Experimental investigation of the impact of fluid distribution on thermocline storage performance. J Energy Storage 2022;52:104864.

[6] Keilany MA, Vannerem S, Milh M, Falcoz Q. Experimental and numerical study of combining encapsulated phase change material to sensible heat storage material in one-tank pilot scale thermal energy storage. J Energy Storage 2022;51:104504.

[7] Lou W, Fan Y, Luo L. Single-tank thermal energy storage systems for concentrated solar power: Flow distribution optimization for thermocline evolution management. J Energy Storage 2020;32:101749.

[8] Lou W, Xie B, Aubril J, Fan Y, Luo L, Arrivé A. Optimized flow distributor for stabilized thermal stratification in a single-medium thermocline storage tank: A numerical and experimental study. Under Rev 2022.

[9] IEA, Renewable Power Tracking Report 2020. Int Energy Agency 2021. https://www.iea.org/reports/renewable-power.

[10] Prieto C, Cabeza LF. Thermal energy storage (TES) with phase change materials (PCM) in solar power plants (CSP). Concept and plant performance. Appl Energy 2019;254:113646.

[11] Pelay U, Azzaro-Pantel C, Fan Y, Luo L. Life cycle assessment of thermochemical energy storage integration concepts for a concentrating solar power plant. Environ Prog Sustain Energy 2020;39:e13388.

[12] Pelay U, Luo L, Fan Y, Stitou D. Dynamic modeling and simulation of a concentrating solar power plant integrated with a thermochemical energy storage system. J Energy Storage 2020;28:101164.

[13] Gorjian S, Ebadi H, Najafi G, Singh Chandel S, Yildizhan H. Recent advances in net-zero energy greenhouses and adapted thermal energy storage systems. Sustain Energy Technol Assessments 2021;43:100940.

[14] Pelay U, Luo L, Fan Y, Stitou D, Castelain C. Integration of a thermochemical energy storage system in a Rankine cycle driven by concentrating solar power: Energy and exergy analyses. Energy 2019;167:498–510.

[15] Alva G, Lin Y, Fang G. An overview of thermal energy storage systems. Energy 2018;144:341–78.

[16] Merlin K, Soto J, Delaunay D, Traonvouez L. Industrial waste heat recovery using an enhanced conductivity latent heat thermal energy storage. Appl Energy 2016;183:491–503.

[17] Guewouo T, Luo L, Tarlet D, Tazerout M. Identification of optimal parameters for a small-scale compressed-air energy storage system using real coded genetic algorithm. Energies 2019;12:1–32.

[18] Tatsidjodoung P, Le Pierrès N, Luo L. A review of potential materials for thermal energy storage in building applications. Renew Sustain Energy Rev 2013;18:327–49.

[19] Akeiber H, Nejat P, Majid MZA, Wahid MA, Jomehzadeh F, Zeynali Famileh I, et al. A review on phase change material (PCM) for sustainable passive cooling in building envelopes. Renew Sustain Energy

Rev 2016;60:1470–97.

[20] McKenna P, Turner WJN, Finn DP. Geocooling with integrated PCM thermal energy storage in a commercial building. Energy 2018;144:865–76.

[21] Gautam A, Saini RP. A review on technical, applications and economic aspect of packed bed solar thermal energy storage system. J Energy Storage 2020;27:101046.

[22] Wei G, Wang G, Xu C, Ju X, Xing L, Du X, et al. Selection principles and thermophysical properties of high temperature phase change materials for thermal energy storage: A review. Renew Sustain Energy Rev 2018;81:1771–86.

[23] Sarbu I, Sebarchievici C. A comprehensive review of thermal energy storage. Sustain 2018;10:191.

[24] Chen X, Zhang Z, Qi C, Ling X, Peng H. State of the art on the high-temperature thermochemical energy storage systems. Energy Convers Manag 2018;177:792–815.

[25] Chandra YP, Matuska T. Stratification analysis of domestic hot water storage tanks: A comprehensive review. Energy Build 2019;187:110–31.

[26] Herrmann U, Kearney DW. Survey of thermal energy storage for parabolic trough power plants. J Sol Energy Eng Trans ASME 2002;124:145–52.

[27] Niedermeier K, Flesch J, Marocco L, Wetzel T. Assessment of thermal energy storage options in a sodium-based CSP plant. Appl Therm Eng 2016;107:386–97.

[28] Zhao B, Cheng M, Liu C, Dai Z. Thermal performance and cost analysis of a multi-layered solid-PCM thermocline thermal energy storage for CSP tower plants. Appl Energy 2016;178:784–99.

[29] Brosseau D, Kelton JW, Ray D, Edgar M, Chisman K, Emms B. Testing of thermocline filler materials and molten-salt heat transfer fluids for thermal energy storage systems in parabolic trough power plants. J Sol Energy Eng Trans ASME 2005;127:109–16.

[30] Esence T, Bruch A, Molina S, Stutz B, Fourmigué JF. A review on experience feedback and numerical modeling of packed-bed thermal energy storage systems. Sol Energy 2017;153:628–54.

[31] Singh H, Saini RP, Saini JS. A review on packed bed solar energy storage systems. Renew Sustain Energy Rev 2010;14:1059–69.

[32] Le Roux D, Lalau Y, Rebouillat B, Neveu P, Olivès R. Thermocline thermal energy storage optimisation combining exergy and life cycle assessment. Energy Convers Manag 2021;248.

[33] Rosen MA. The exergy of stratified thermal energy storages. Sol Energy 2001;71:173–85.

[34] Hoffmann JF, Fasquelle T, Goetz V, Py X. Experimental and numerical investigation of a thermocline thermal energy storage tank. Appl Therm Eng 2017;114:896–904.

[35] Davenne TRG, Garvey SD, Cardenas B, Rouse JP. Stability of packed bed thermoclines. J Energy Storage 2018;19:192–200.

[36] Flueckiger SM, Garimella S V. Latent heat augmentation of thermocline energy storage for concentrating solar power - A system-level assessment. Appl Energy 2014;116:278–87.

[37] Mohamed SA, Al-Sulaiman FA, Ibrahim NI, Zahir MH, Al-Ahmed A, Saidur R, et al. A review on current status and challenges of inorganic phase change materials for thermal energy storage systems. Renew Sustain Energy Rev 2017;70:1072–89.

[38] Kuravi S, Trahan J, Goswami DY, Rahman MM, Stefanakos EK. Thermal energy storage technologies and systems for concentrating solar power plants. Prog Energy Combust Sci 2013;39:285–319.

[39] Stutz B, Le Pierres N, Kuznik F, Johannes K, Palomo Del Barrio E, Bédécarrats JP, et al. Storage of thermal solar energy. Comptes Rendus Phys 2017;18:401–14.

[40] Tiskatine R, Oaddi R, Ait El Cadi R, Bazgaou A, Bouirden L, Aharoune A, et al. Suitability and characteristics of rocks for sensible heat storage in CSP plants. Sol Energy Mater Sol Cells 2017;169:245–57.

[41] Xu C, Wang Z, He Y, Li X, Bai F. Sensitivity analysis of the numerical study on the thermal performance of a packed-bed molten salt thermocline thermal storage system. Appl Energy 2012;92:65–75.

[42] Molina S, Haillot D, Deydier A, Bedecarrats JP. Material screening and compatibility for thermocline storage systems using thermal oil. Appl Therm Eng 2019;146:252–9.

[43] Hänchen M, Brückner S, Steinfeld A. High-temperature thermal storage using a packed bed of rocks - Heat transfer analysis and experimental validation. Appl Therm Eng 2011;312:1798–806.

[44] Geyer MA. Thermal storage for solar power plants. Sol. Power Plants, Springer; 1991, p. 199–214.

[45] Fasquelle T, Falcoz Q, Neveu P, Walker J, Flamant G. Compatibility study between synthetic oil and vitrified wastes for direct thermal energy storage. Waste and Biomass Valorization 2017;8:621–31.

[46] Hoffmann JF, Fasquelle T, Vaitilingom G, Olives R, Py X, Goetz V. Compatibility of vegetable oils with solid filler materials for thermocline thermal energy storage systems. Sol Energy Mater Sol Cells 2019;200:109932.

[47] Xu C, Li X, Wang Z, He Y, Bai F. Effects of solid particle properties on the thermal performance of a packed-bed molten-salt thermocline thermal storage system. Appl Therm Eng 2013;57:69–80.

[48] Meier A, Winkler C, Wuillemin D. Experiment for modelling high temperature rock bed storage. Sol Energy Mater 1991;24:255–64.

[49] Bayón R, Rojas E. Simulation of thermocline storage for solar thermal power plants: From dimensionless results to prototypes and real-size tanks. Int J Heat Mass Transf 2013;60:713–21.

[50] Jian Y, Falcoz Q, Neveu P, Bai F, Wang Y, Wang Z. Design and optimization of solid thermal energy storage modules for solar thermal power plant applications. Appl Energy 2015;139:30–42.

[51] Calderón-Vásquez I, Segovia V, Cardemil JM, Barraza R. Assessing the use of copper slags as thermal energy storage material for packed-bed systems. Energy 2021;227:120370.

[52] Li C, Xie B, Chen J, He Z, Chen Z, Long Y. Emerging mineral-coupled composite phase change materials for thermal energy storage. Energy Convers Manag 2019;183:633–44.

[53] Xie B, Li C, Zhang B, Yang L, Xiao G, Chen J. Evaluation of stearic acid/coconut shell charcoal composite phase change thermal energy storage materials for tankless solar water heater. Energy Built Environ 2019:0–39.

[54] Li C, Xie B, He Z, Chen J, Long Y. 3D structure fungi-derived carbon stabilized stearic acid as a composite phase change material for thermal energy storage. Renew Energy 2019;140:862–73.

[55] Mehling H, Cabeza LF. Heat and cold storage with PCM. vol. 308. Springer; 2008.

[56] Reddy KS, Mudgal V, Mallick TK. Review of latent heat thermal energy storage for improved material stability and effective load management. J Energy Storage 2018;15:205–27.

[57] Galione P, Pérez-Segarra C, Rodríguez I, Torras S, Rigola J. Numerical evaluation of multi-layered solid-PCM thermocline-like tanks as thermal energy storage systems for CSP applications. Energy Procedia 2015;69:832–41.

[58] Felix Regin A, Solanki SC, Saini JS. An analysis of a packed bed latent heat thermal energy storage system using PCM capsules: Numerical investigation. Renew Energy 2009;34:1765–73.

[59] Elfeky KE, Ahmed N, Wang Q. Numerical comparison between single PCM and multi-stage PCM based high temperature thermal energy storage for CSP tower plants. Appl Therm Eng 2018;139:609–22.

[60] Yang L, Zhang X, Xu G. Thermal performance of a solar storage packed bed using spherical capsules filled with PCM having different melting points. Energy Build 2014:639–46.

[61] Bruno F, Belusko M, Liu M, Tay NHS. Using solid-liquid phase change materials (PCMs) in thermal energy storage systems. Adv. Therm. energy storage Syst., Elsevier; 2015, p. 201–46.

[62] Li Y, Li C, Lin N, Xie B, Zhang D, Chen J. Review on tailored phase change behavior of hydrated salt as

phase change materials for energy storage. Mater Today Energy 2021;22:100866.

[63] Zanganeh G, Khanna R, Walser C, Pedretti A, Haselbacher A, Steinfeld A. Experimental and numerical investigation of combined sensible-latent heat for thermal energy storage at 575°C and above. Sol Energy 2015;114:77–90.

[64] Ge H, Li H, Mei S, Liu J. Low melting point liquid metal as a new class of phase change material: An emerging frontier in energy area. Renew Sustain Energy Rev 2013;21:331–46.

[65] Wu M, Xu C, He YL. Dynamic thermal performance analysis of a molten-salt packed-bed thermal energy storage system using PCM capsules. Appl Energy 2014;121:184–95.

[66] Sharma A, Tyagi V V., Chen CR, Buddhi D. Review on thermal energy storage with phase change materials and applications. Renew Sustain Energy Rev 2009;13:318–45.

[67] Lee YT, Kim MH, Lee SS, Gim J, Chung JD. Numerical analysis in a full-scale thermal energy storage tank with dual PCM capsules. Energy Build 2019;204:109410.

[68] He B, Martin V, Setterwall F. Phase transition temperature ranges and storage density of paraffin wax phase change materials. Energy 2004;29:1785–804.

[69] Kenisarin MM. High-temperature phase change materials for thermal energy storage. Renew Sustain Energy Rev 2010;14:955–70.

[70] Mostafavi Tehrani SS, Taylor RA, Nithyanandam K, Shafiei Ghazani A. Annual comparative performance and cost analysis of high temperature, sensible thermal energy storage systems integrated with a concentrated solar power plant. Sol Energy 2017;153:153–72.

[71] Kocak B, Paksoy H. Performance of laboratory scale packed-bed thermal energy storage using new demolition waste based sensible heat materials for industrial solar applications. Sol Energy 2020;211:1335–46.

[72] Tuttle JF, White N, Mohammadi K, Powell K. A novel dynamic simulation methodology for high temperature packed-bed thermal energy storage with experimental validation. Sustain Energy Technol Assessments 2020;42:100888.

[73] Khor JO, Yang L, Akhmetov B, Leal AB, Romagnoli A. Application of granular materials for void space reduction within packed bed thermal energy storage system filled with macro-encapsulated phase change materials. Energy Convers Manag 2020;222:113118.

[74] Arkar C, Vidrih B, Medved S. Efficiency of free cooling using latent heat storage integrated into the ventilation system of a low energy building. Int J Refrig 2007;30:134–43.

[75] Arkar C, Medved S. Influence of accuracy of thermal property data of a phase change material on the result of a numerical model of a packed bed. Thermochim Acta 2005;438:192–201.

[76] Soto J, Jadal M, de Guyenro N, Delaunay D. Thermal cycling aging of encapsulated phase change material – Compressed expanded natural graphite composite. Therm Sci Eng Prog 2021;22:100836.

[77] Galione PA, Lehmkuhl O, Rigola J, Oliva A, Rodríguez I. Numerical simulations of thermal energy storage systems with phase change materials. 30th ISES Bienn Sol World Congr 2011, SWC 2011 2011;6:4785–96.

[78] Tan FL, Hosseinizadeh SF, Khodadadi JM, Fan L. Experimental and computational study of constrained melting of phase change materials (PCM) inside a spherical capsule. Int J Heat Mass Transf 2009;52:3464–72.

[79] Li G. Sensible heat thermal storage energy and exergy performance evaluations. Renew Sustain Energy Rev 2016;53:897–923.

[80] Li Q, Li C, Du Z, Jiang F, Ding Y. A review of performance investigation and enhancement of shell and tube thermal energy storage device containing molten salt based phase change materials for medium and high temperature applications. Appl Energy 2019;255:113806.

[81] Nallusamy N, Sampath S, Velraj R. Study on performance of a packed bed latent heat thermal energy

storage unit integrated with solar water heating system. J Zhejiang Univ Sci 2006;7:1422–30.

[82] Bruch A, Fourmigue JF, Couturier R, Molina S. Experimental and numerical investigation of stability of packed bed thermal energy storage for CSP power plant. Energy Procedia 2014;49:743–51.

[83] Zhao B, Cheng M, Liu C, Dai Z. System-level performance optimization of molten-salt packed-bed thermal energy storage for concentrating solar power. Appl Energy 2018;226:225–39.

[84] Liao Z, Zhao G, Xu C, Yang C, Jin Y, Ju X, et al. Efficiency analyses of high temperature thermal energy storage systems of rocks only and rock-PCM capsule combination. Sol Energy 2018;162:153–64.

[85] Fasquelle T, Falcoz Q, Neveu P, Hoffmann JF. A temperature threshold evaluation for thermocline energy storage in concentrated solar power plants. Appl Energy 2018;212:1153–64.

[86] Mahmood M, Traverso A, Traverso AN, Massardo AF, Marsano D, Cravero C. Thermal energy storage for CSP hybrid gas turbine systems: Dynamic modelling and experimental validation. Appl Energy 2018;212:1240–51.

[87] Zanganeh G, Pedretti A, Haselbacher A, Steinfeld A. Design of packed bed thermal energy storage systems for high-temperature industrial process heat. Appl Energy 2015;137:812–22.

[88] Xie B, Baudin N, Soto J, Fan Y, Luo L. Wall impact on efficiency of packed-bed thermocline thermal energy storage system. Energy 2022;247:123503.

[89] Zurigat YH, Liche PR, Ghajar AJ. Influence of inlet geometry on mixing in thermocline thermal energy storage. Int J Heat Mass Transf 1991;34:115–25.

[90] Bruch A, Fourmigué JF, Couturier R. Experimental and numerical investigation of a pilot-scale thermal oil packed bed thermal storage system for CSP power plant. Sol Energy 2014;105:116–25.

[91] Yang Z, Garimella S V. Thermal analysis of solar thermal energy storage in a molten-salt thermocline. Sol Energy 2010;81:974–85.

[92] Agalit H, Zari N, Maalmi M, Maaroufi M. Numerical investigations of high temperature packed bed TES systems used in hybrid solar tower power plants. Sol Energy 2015;122:603–16.

[93] Sorour MM. Performance of a small sensible heat energy storage unit. Energy Convers Manag 1988;28:211–7.

[94] Li MJ, Jin B, Ma Z, Yuan F. Experimental and numerical study on the performance of a new high-temperature packed-bed thermal energy storage system with macroencapsulation of molten salt phase change material. Appl Energy 2018;221:1–15.

[95] Regin AF, Solanki SC, Saini JS. Latent heat thermal energy storage using cylindrical capsule: Numerical and experimental investigations. Renew Energy 2006;31:2025–41.

[96] Gao L, Gegentana, Liu Z, Sun B, Che D, Li S. Multi-objective optimization of thermal performance of packed bed latent heat thermal storage system based on response surface method. Renew Energy 2020;153:669–80.

[97] Allen KG, von Backström TW, Kröger DG. Packed bed pressure drop dependence on particle shape, size distribution, packing arrangement and roughness. Powder Technol 2013;246:590–600.

[98] Salunkhe PB, Shembekar PS. A review on effect of phase change material encapsulation on the thermal performance of a system. Renew Sustain Energy Rev 2012;16:5603–16.

[99] Van Lew JT, Li P, Chan CL, Karaki W, Stephens J. Analysis of heat storage and delivery of a thermocline tank having solid filler material. J Sol Energy Eng Trans ASME 2011;133:021003.

[100] Li P, Van Lew J, Karaki W, Chan C, Stephens J, Wang Q. Generalized charts of energy storage effectiveness for thermocline heat storage tank design and calibration. Sol Energy 2011;85:2130–43.

[101] Anderson R, Bates L, Johnson E, Morris JF. Packed bed thermal energy storage: A simplified experimentally validated model. J Energy Storage 2015;4:14–23.

[102] Nellis G., Klein S. Heat Transfer. Cambridge; 2009.

[103] Faas SE, Thorne LR, Fuchs EA, Gilbertsen ND. 10 MWe Solar Thermal Central Receiver Pilot Plant: thermal storage subsystem evaluation. Final report. Sandia National Labs., Livermore, CA (USA); 1986.

[104] Pacheco J, Showalter S. Development of a molten-salt thermocline thermal storage system for parabolic trough plants. J Sol Energy Eng 2002;124:153–9.

[105] Cárdenas B, Davenne TR, Wang J, Ding Y, Jin Y, Chen H, et al. Techno-economic optimization of a packed-bed for utility-scale energy storage. Appl Therm Eng 2019;153:206–20.

[106] Thoenes D, Kramers H. Mass transfer from spheres in various regular packings to a flowing fluid. Chem Eng Sci 1958;8:271–83.

[107] Bellan S, Alam TE, González-Aguilar J, Romero M, Rahman MM, Goswami DY, et al. Numerical and experimental studies on heat transfer characteristics of thermal energy storage system packed with molten salt PCM capsules. Appl Therm Eng 2015;90:970–9.

[108] Bellan S, Gonzalez-Aguilar J, Romero M, Rahman MM, Goswami DY, Stefanakos EK, et al. Numerical analysis of charging and discharging performance of a thermal energy storage system with encapsulated phase change material. Appl Therm Eng 2014;71:481–500.

[109] Zhang H, Wang X. Synthesis and properties of microencapsulated n-octadecane with polyurea shells containing different soft segments for heat energy storage and thermal regulation. Sol Energy Mater Sol Cells 2009;93:1366–76.

[110] Mostafavi Tehrani SS, Shoraka Y, Nithyanandam K, Taylor RA. Shell-and-tube or packed bed thermal energy storage systems integrated with a concentrated solar power: A techno-economic comparison of sensible and latent heat systems. Appl Energy 2019;238:887–910.

[111] Strasser MN, Selvam RP. A cost and performance comparison of packed bed and structured thermocline thermal energy storage systems. Sol Energy 2014;108:390–402.

[112] Yang Z, Garimella S V. Molten-salt thermal energy storage in thermoclines under different environmental boundary conditions. Appl Energy 2010;87:3322–9.

[113] Zanganeh G, Pedretti A, Zavattoni S, Barbato M, Steinfeld A. Packed-bed thermal storage for concentrated solar power - Pilot-scale demonstration and industrial-scale design. Sol Energy 2012;86:3084–98.

[114] Chang Z, Li X, Xu C, Chang C, Wang Z, Zhang Q, et al. The effect of the physical boundary conditions on the thermal performance of molten salt thermocline tank. Renew Energy 2016;96:190–202.

[115] Singh S, Sørensen K, Condra T, Batz SS, Kristensen K. Investigation on transient performance of a large-scale packed-bed thermal energy storage. Appl Energy 2019;239:1114–29.

[116] Marti J, Geissbühler L, Becattini V, Haselbacher A, Steinfeld A. Constrained multi-objective optimization of thermocline packed-bed thermal-energy storage. Appl Energy 2018;216:694–708.

[117] Yin H, Ding J, Yang X. Experimental research on thermal characteristics of a hybrid thermocline heat storage system. Appl Therm Eng 2014;62:293–301.

[118] Türkakar G. Performance analysis and optimal charging time investigation of solar air heater with packed bed sensible heat storage device. Sol Energy 2021;224:718–29.

[119] Crandall DM, Thacher EF. Segmented thermal storage. Sol Energy 2004;77:435–40.

[120] Li MJ, Qiu Y, Li MJ. Cyclic thermal performance analysis of a traditional Single-Layered and of a novel Multi-Layered Packed-Bed molten salt Thermocline Tank. Renew Energy 2018;118:565–78.

[121] Chen SL, Yue JS. Thermal performance of cool storage in packed capsules for air conditioning. Heat Recover Syst CHP 1991;11:551–61.

[122] Rady M. Thermal performance of packed bed thermal energy storage units using multiple granular phase change composites. Appl Energy 2009;86:2704–20.

[123] Li Y, Huang G, Xu T, Liu X, Wu H. Optimal design of PCM thermal storage tank and its application for winter available open-air swimming pool. Appl Energy 2018;209:224–35.

[124] Li M, Li M, Ma Z, Yuan F. Comparisons of thermal performance and cost for three thermal energy storage systems utilized in supercritical CO_2 Brayton cycle. Energy Procedia 2019;158:4696–701.

[125] Aldoss TK, Rahman MM. Comparison between the single-PCM and multi-PCM thermal energy storage design. Energy Convers Manag 2014;83:79–87.

[126] Watanabe T, Kanzawa A. Second law optimization of a latent heat storage system with PCMS having different melting points. Heat Recover Syst CHP 1995;15:641–53.

[127] Domański R, Fellah G. Exergy analysis for the evaluation of a thermal storage system employing PCMS with different melting temperatures. Appl Therm Eng 1996;16:907–19.

[128] Mujumdar S. Thermodynamic of the Thermal Process in Energy Storage Using Multiple. Appl Therm Eng 1997;17:1067–83.

[129] Gong ZX, Mujumdar AS. Enhancement of energy charge-discharge rates in composite slabs of different phase change materials. Int J Heat Mass Transf 1996;39:725–33.

[130] Mostafavi Tehrani SS, Shoraka Y, Nithyanandam K, Taylor RA. Cyclic performance of cascaded and multi-layered solid-PCM shell-and-tube thermal energy storage systems: A case study of the 19.9 MW e Gemasolar CSP plant. Appl Energy 2018;228:240–53.

[131] Elfeky KE, Ahmed N, Naqvi SMA, Wang Q. Numerical investigation of the melting temperature effect on the performance of thermocline thermal energy storage tank for CSP. Energy Procedia 2019;158:4715–20.

[132] Elfeky KE, Li X, Ahmed N, Lu L, Wang Q. Optimization of thermal performance in thermocline tank thermal energy storage system with the multilayered PCM(s) for CSP tower plants. Appl Energy 2019;243:175–90.

[133] Chirino H, Xu B, Xu X. Parametric study of cascade latent heat thermal energy storage (CLHTES) system in Concentrated Solar Power (CSP) plants. J Energy Inst 2019;92:653–64.

[134] Wu M, Xu C, He Y. Cyclic behaviors of the molten-salt packed-bed thermal storage system filled with cascaded phase change material capsules. Appl Therm Eng 2016;93:1061–73.

[135] Nithyanandam K, Pitchumani R, Mathur A. Analysis of a latent thermocline storage system with encapsulated phase change materials for concentrating solar power. Appl Energy 2014;113:1446–60.

[136] Reddy KS, Jawahar V, Sivakumar S, Mallick TK. Performance investigation of single-tank thermocline storage systems for CSP plants. Sol Energy 2017;144:740–9.

[137] Cocco D, Serra F. Performance comparison of two-tank direct and thermocline thermal energy storage systems for 1MWe class concentrating solar power plants. Energy 2015;81:526–36.

[138] Dinker A, Agarwal M, Agarwal GD. Heat storage materials, geometry and applications: A review. J Energy Inst 2017;90:1–11.

[139] Ahmed N, Elfeky KE, Lu L, Wang QW. Thermal and economic evaluation of thermocline combined sensible-latent heat thermal energy storage system for medium temperature applications. Energy Convers Manag 2019;189:14–23.

[140] Zhao B, Cheng M, Liu C, Dai Z. An efficient tank size estimation strategy for packed-bed thermocline thermal energy storage systems for concentrated solar power. Sol Energy 2017;153:104–14.

[141] Zhao B chen, Cheng M song, Liu C, Dai Z min. Conceptual design and preliminary performance analysis of a hybrid nuclear-solar power system with molten-salt packed-bed thermal energy storage for on-demand power supply. Energy Convers Manag 2018;166:174–86.

[142] Galione PA, Pérez-Segarra CD, Rodríguez I, Oliva A, Rigola J. Multi-layered solid-PCM thermocline thermal storage concept for CSP plants. Numerical analysis and perspectives. Appl Energy

2015;142:337–51.

[143] Galione PA, Lehmkuhl O, Rigola J. A new thermocline-PCM thermal storage concept for CSP plants. Numerical analysis and perspectives. Energy Procedia 2014;49:790–9.

[144] Zavattoni SA, Geissbühler L, Barbato MC, Zanganeh G, Haselbacher A, Steinfeld A. High-temperature thermocline TES combining sensible and latent heat - CFD modeling and experimental validation. AIP Conf Proc 2017;1850:080028.

[145] Zhao B chen, Cheng M song, Liu C, Dai Z min. Cyclic thermal characterization of a molten-salt packed-bed thermal energy storage for concentrating solar power. Appl Energy 2017;195:761–73.

[146] Abdulla A, Reddy KS. Comparative study of single and multi-layered packed-bed thermal energy storage systems for CSP plants. Appl Sol Energy (English Transl Geliotekhnika) 2017;53:276–86.

[147] Nallusamy N, Sampath S, Velraj R. Experimental investigation on a combined sensible and latent heat storage system integrated with constant/varying (solar) heat sources. Renew Energy 2007;32:1206–27.

[148] Cascetta M, Serra F, Arena S, Casti E, Cau G, Puddu P. Experimental and numerical research activity on a packed bed TES system. Energies 2016;9:1–13.

[149] Díaz-Heras M, Belmonte JF, Almendros-Ibáñez JA. Effective thermal conductivities in packed beds: Review of correlations and its influence on system performance. Appl Therm Eng 2020;171:115048.

[150] Argo WB, Smith JM. Heat transfer in packed beds-prediction of radial rates in gas-solid beds. Chem Eng Prog 1953;49:443–51.

[151] De Beer M, Du Toit CG, Rousseau PG. Experimental study of the effective thermal conductivity in the near-wall region of a packed pebble bed. Nucl Eng Des 2018;339:253–68.

[152] Yagi S, Wakao N. Heat and mass transfer from wall to fluid in packed beds. AIChE J 1959;5:79–85.

[153] Mira-Hernández C, Flueckiger SM, Garimella S V. Comparative analysis of single- and dual-media thermocline tanks for thermal energy storage in concentrating solar power plants. J Sol Energy Eng Trans ASME 2015;137.

[154] Beasley DE, Clark JA. Transient response of a packed bed for thermal energy storage. Int J Heat Mass Transf 1984;27:1659–69.

[155] Hoffmann JF, Fasquelle T, Goetz V, Py X. A thermocline thermal energy storage system with filler materials for concentrated solar power plants: Experimental data and numerical model sensitivity to different experimental tank scales. Appl Therm Eng 2016;100:753–61.

[156] Opitz F, Treffinger P. Packed bed thermal energy storage model - Generalized approach and experimental validation. Appl Therm Eng 2014;73:245–52.

[157] Cascetta M, Cau G, Puddu P, Serra F. A comparison between CFD simulation and experimental investigation of a packed-bed thermal energy storage system. Appl Therm Eng 2016;98:1263–72.

[158] Fernández-Torrijos M, Sobrino C, Almendros-Ibáñez JA. Simplified model of a dual-media molten-salt thermocline tank with a multiple layer wall. Sol Energy 2017;151:146–61.

[159] ELSihy ElsS, Liao Z, Xu C, Du X. Dynamic characteristics of solid packed-bed thermocline tank using molten-salt as a heat transfer fluid. Int J Heat Mass Transf 2021;165:120677.

[160] Çengel YA, Ghajar AJ. Heat and mass transfer: fundamentals and applications. McGraw Hill Education; 2020.

[161] Ranmode V, Singh M, Bhattacharya J. Analytical formulation of effective heat transfer coefficient and extension of lumped capacitance method to simplify the analysis of packed bed storage systems. Sol Energy 2019;183:606–18.

[162] Bradshaw A V, Johnson A, McLachlan NH, Chiu YT. Heat transfer between air and nitrogen and packed beds of non-reacting solids. Trans Inst Chem Eng Chem Eng 1970;48:T77–84.

[163] Xu B, Li PW, Chan CL. Extending the validity of lumped capacitance method for large Biot number in thermal storage application. Sol Energy 2012;86:1709–24.

[164] Yang B, Bai F, Wang Y, Wang Z. Study on standby process of an air-based solid packed bed for flexible high-temperature heat storage: Experimental results and modelling. Appl Energy 2019;238:135–46.

[165] Pfeffer R. Heat and mass transport in multiparticle systems. Ind Eng Chem Fundam 1964;3:380–3.

[166] Stuke B. Berechnung des Wärmeaustausches in Regeneratoren mit zylindrischem und kugelförmigem Füllmaterial. Angew Chemie 1948;20:262–8.

[167] Staff V-GV und C. VDI-wärmeatlas. Springer Berlin Heidelberg; 2006.

[168] Wakao N, Kaguei S, Funazkri T. Effect of fluid dispersion coefficients on particle-to-fluid heat transfer coefficients in packed beds. Correlation of nusselt numbers. Chem Eng Sci 1979;34:325–36.

[169] Kaguei S, Shiozawa B, Wakao N. Dispersion-concentric packed bed heat. Chem Eng Sci 1976;32:507–13.

[170] Deissler RG, Boegli JS. An investigation of effective thermal conductivities of powders in various gases. Trans Am Soc Mech Engrs 1958;80:1417–23.

[171] Gonzo EE. Estimating correlations for the effective thermal conductivity of granular materials. Chem Eng J 2002;90:299–302.

[172] Ergun S. Fluid flow through packed columns. Chem Eng Prog 1952;48:89–94.

[173] Prieur du Plessis J, Woudberg S. Pore-scale derivation of the Ergun equation to enhance its adaptability and generalization. Chem Eng Sci 2008;63:2576–86.

[174] Chang Z, Li X, Xu C, Chang C, Wang Z. The design and numerical study of a 2 MWh molten salt thermocline tank. Energy Procedia 2015;69:779–89.

[175] Flueckiger SM, Yang Z, Garimella S V. Thermomechanical simulation of the solar one thermocline storage tank. J Sol Energy Eng Trans ASME 2012;134:041014.

[176] Fass SE. 10 MWe solar thermal central receiver pilot plant: thermal storage subsystem evaluation-final report. SAND86-8212, Sandia Natl Lab Albuquerque, New Mex 1986.

[177] Douglas M. 10 MWe solar thermal central receiver pilot plant mode 5 (test 1150) and mode 6 (test 1160) test report. Sandia Natl Lab SAND86-8175 1986.

[178] Shaikh W, Wadegaonkar A, Kedare SB, Bose M. Numerical simulation of single media thermocline based storage system. Sol Energy 2018;174:207–17.

[179] Bejan A, Tsatsaronis G, Moran MJ. Thermal design and optimization. John Wiley and Sons; 1995.

[180] Bindra H, Bueno P, Morris JF, Shinnar R. Thermal analysis and exergy evaluation of packed bed thermal storage systems. Appl Therm Eng 2013;52:255–63.

[181] Chartered Institution of Building Services Engineers(CIBSE). Thermal properties of building structures in: K.J. Butcher (Ed.), GuideA: Environmental Design, 7th ed., Norwich: 2006, p. 5–48.

[182] Howell JR, Menguc MP, Siegel. R, Siegel R. Thermal radiation heat transfer. Boca Raton, FL, USA: National Aeronautics and Space Administration; 1964.

[183] Incropera FP, Lavine AS, Bergman TL, Dewitt DP. Fundamentals of heat and mass transfer. New York: Wiley; 2007.

[184] Pianosi F, Sarrazin F, Wagener T. A Matlab toolbox for Global Sensitivity Analysis. Environ Model Softw 2015;70:80–5.

[185] Geissbühler L, Mathur A, Mularczyk A, Haselbacher A. An assessment of thermocline-control methods for packed-bed thermal-energy storage in CSP plants, Part 2: Assessment strategy and results. Sol Energy 2019;178:351–64.

[186] Cascetta M, Cau G, Puddu P, Serra F. Experimental investigation of a packed bed thermal energy

storage system. J. Phys. Conf. Ser., vol. 655, 2015, p. 012018.

[187] Nicolas LF, Falcoz Q, Pham Minh D, Hoffmann JF, Meffre A, Nzihou A, et al. Flexibility and robustness of a high-temperature air/ceramic thermocline heat storage pilot. J Energy Storage 2019;21:393–404.

[188] Sanderson TM, Cunningham GT. Performance and efficient design of packed bed thermal storage systems. Part 1. Appl Energy 1995;50:119–32.

[189] Yin H, Ding J, Jiang R, Yang X. Thermocline characteristics of molten-salt thermal energy storage in porous packed-bed tank. Appl Therm Eng 2017;110:855–63.

[190] Reddy KS, Pradeep N. Stability analysis of the thermocline thermal energy storage system during high flow rates for solar process heating applications. Sol Energy 2021;226:40–53.

[191] Wang L, Yang Z, Duan Y. Influence of flow distribution on the thermal performance of dual-media thermocline energy storage systems. Appl Energy 2015;142:283–92.

[192] Cascetta M, Serra F, Cau G, Puddu P. Comparison between experimental and numerical results of a packed-bed thermal energy storage system in continuous operation. Energy Procedia 2018;148:234–41.

[193] Cascetta M, Cau G, Puddu P, Serra F. A study of a packed-bed thermal energy storage device: Test rig, experimental and numerical results. Energy Procedia 2015;81:987–94.

[194] Esence T, Bruch A, Fourmigué JF, Stutz B. A versatile one-dimensional numerical model for packed-bed heat storage systems. Renew Energy 2019;133:190–204.

[195] Al-Azawii MMS, Theade C, Danczyk M, Johnson E, Anderson R. Experimental study on the cyclic behavior of thermal energy storage in an air-alumina packed bed. J Energy Storage 2018;18:239–49.

[196] Koçak B, Paksoy H. Packed-bed sensible thermal energy storage system using demolition wastes for concentrated solar power plants. E3S Web Conf 2019;113:1–9.

[197] Yang X, Yang X, Ding J, Shao Y, Qin FGF, Jiang R. Criteria for performance improvement of a molten salt thermocline storage system. Appl Therm Eng 2012;48:24–31.

[198] Anderson R, Shiri S, Bindra H, Morris JF. Experimental results and modeling of energy storage and recovery in a packed bed of alumina particles. Appl Energy 2014;119:521–9.

[199] Al-Azawii MMS, Theade C, Bueno P, Anderson R. Experimental study of layered thermal energy storage in an air-alumina packed bed using axial pipe injections. Appl Energy 2019;249:409–22.

[200] Keilany MA, Milhé M, Bézian JJ, Falcoz Q, Flamant G. Experimental evaluation of vitrified waste as solid fillers used in thermocline thermal energy storage with parametric analysis. J Energy Storage 2020;29:101285.

[201] Gautam A, Saini RP. Development of correlations for Nusselt number and friction factor of packed bed solar thermal energy storage system having spheres with pores as packing elements. J Energy Storage 2021;36:102362.

[202] Bruch A, Bourdon D, Dumas C, Blaise A, Chouvel-Saye A. Experimental characterization of a water/rock thermocline cold thermal energy storage for optimization of condenser cooling. J Energy Storage 2021;44:103426.

[203] Alonso E, Rojas E. Air solid packed-beds for high temperature thermal storage: practical recommendations for predicting their thermal behaviour. Appl Therm Eng 2022;202:117835.

[204] Xu C, Liu M, Jiao S, Tang H, Yan J. Experimental study and analytical modeling on the thermocline hot water storage tank with radial plate-type diffuser. Int J Heat Mass Transf 2022;186:122478.

[205] Li MJ, Li MJ, Tong ZX, Li D. Optimization of the packed-bed thermal energy storage with cascaded PCM capsules under the constraint of outlet threshold temperature. Appl Therm Eng 2021;186:116473.

[206] Elsayed Elfeky K, Gambo Mohammed A, Wang Q. Influence of inlet temperature on the performance

of cascade and hybrid storage tank for CSP plants. Appl Therm Eng 2022;206:118098.

[207] Taylor BN, Kuyatt CE. Guidelines for evaluating and expressing the uncertainty of NIST measurement results. Natl Inst Stand Technol Gaithersburg, MD 2001:D.1.1.2.

[208] He Z, Wang X, Du X, Amjad M, Yang L, Xu C. Experiments on comparative performance of water thermocline storage tank with and without encapsulated paraffin wax packed bed. Appl Therm Eng 2019;147:188–97.

[209] Stern F, Muste M, Beninati M, Eichinger WE. Summary of exerimental uncertainty assessmet methodology. 1999.

[210] Wang W, He X, Hou Y, Qiu J, Han D, Shuai Y. Thermal performance analysis of packed-bed thermal energy storage with radial gradient arrangement for phase change materials. Renew Energy 2021;173:768–80.

[211] International Energy Agency. Net Zero by 2050--A Roadmap for the Global Energy Sector 2021. https://www.iea.org/reports/net-zero-by-2050.

[212] Yildirim N, Bilir L. Evaluation of a hybrid system for a nearly zero energy greenhouse. Energy Convers Manag 2017;148:1278–90.

[213] Gross H, Annual W. CUAES Greenhouses - Energy Consumption and Equivalents CUAES Greenhouses - Energy Consumption and Equivalents 2014:3–6.

[214] Watanabe T, Kikuchi H, Kanzawa A. Enhancement of charging and discharging rates in a latent heat storage system by use of PCM with different melting temperatures. Heat Recover Syst CHP 1993;13:57–66.

[215] Farid MM, Kim Y, Kansawa A. Thermal performance of a heat storage module using PCM's with different melting temperature: Experimental. J Sol Energy Eng Trans ASME 1990;112:125–31.

[216] Peng H, Li R, Ling X, Dong H. Modeling on heat storage performance of compressed air in a packed bed system. Appl Energy 2015;160:1–9.

[217] Shamsi H, Boroushaki M, Geraei H. Performance evaluation and optimization of encapsulated cascade PCM thermal storage. J Energy Storage 2017;11:64–75.

[218] Alptekin E, Ezan MA. A systematic assessment on a solar collector integrated packed-bed single / multi-layered latent heat thermal energy storage system. J Energy Storage 2021;37:102410.

[219] Wang L, Lin X, Zhang H, Peng L, Zhang X, Chen H. Analytic optimization of Joule–Brayton cycle-based pumped thermal electricity storage system. J Energy Storage 2022;47:103663.

[220] Wu S, Yan T, Kuai Z, Pan W. Thermal conductivity enhancement on phase change materials for thermal energy storage: A review. Energy Storage Mater 2020;25:251–95.

[221] Xia L, Zhang P, Wang R. Numerical heat transfer analysis of the packed bed latent heat storage system based on an effective packed bed model. Energy 2010;35:2022–32.

[222] Serres P, Guerin P, Schaeffer E. Bilan énergétique global des besoins et des ressources, prédimensionnement des moyens de production et de stockage. Intern Rep 2021.

[223] Trevisan S, Jemmal Y, Guedez R, Laumert B. Packed bed thermal energy storage: A novel design methodology including quasi-dynamic boundary conditions and techno-economic optimization. J Energy Storage 2021;36:102441.

[224] Antoine Chatelain JL. Récupéré sur quelleenergie 2021. https://www.quelleenergie.fr/.

[225] Nazir H, Batool M, Isaza-Ruiz M, Xud X, Vignarooban K, Phelan P, et al. Recent developments in phase change materials for energy storage applications A review. Int J Heat Mass Transf 2019;129:419–523.

[226] Zalba B, Marın; JM, Mehling LFCH. Review on thermal energy storage with phase change: materials, heat transfer analysis and applications. vol. 704. 2012.

[227] Ukrainczyk N, Kurajica S, Šipušiæ J. Thermophysical comparison of five commercial paraffin waxes as latent heat storage materials 2010;c:129–37.

[228] Qureshi ZA, Ali HM, Khushnood S. Recent advances on thermal conductivity enhancement of phase change materials for energy storage system: A review. Int J Heat Mass Transf 2018;127:838–56.

[229] Matlab. Global optimization Toolbox 2022 n.d. https://www.mathworks.com/products/global-optimization.html.

[230] Justesen PD. Multi-objective Optimization using Evolutionary Algorithms Progress. Dep Comput Sci 2009;Confirmati:497.

[231] Arora JS. Chapter 16 - Genetic Algorithms for Optimum Design. In: Arora JSBT-I to OD (Third E, editor., Boston: Academic Press; 2012, p. 643–55.

[232] Yusoff Y, Ngadiman MS, Zain AM. Overview of NSGA-II for optimizing machining process parameters. Procedia Eng 2011;15:3978–83.

[233] Marler RT, Arora JS. Survey of multi-objective optimization methods for engineering. Struct Multidiscip Optim 2004;26:369–95.

Publication lists

[1] Xie B, Baudin N, Soto J, Fan Y, Luo L. Wall impact on efficiency of packed-bed thermocline thermal energy storage system. ***Energy*** 2022;247:123503.

[2] Xie B, Baudin N, Soto J, Fan Y, Luo L. Chapter 10 - Thermocline packed bed thermal energy storage system: a review. In: Jeguirim MBT-REP and D, editor. Adv. Renew. Energy Technol., vol. 1, ***Academic Press*** 2022, p. 325–85.

[3] Xie B, Baudin N, Soto J, Fan Y, Luo L. Experiment and numerical study of thermocline packed-bed water system with sensible heat fillers: diffuser and insulation. ***Renew Energy*** 2022. (Under review)

[4] Xie B, Baudin N, Soto J, Fan Y, Luo L. Optimization of thermocline packed-bed system with PCM fillers for greenhouse application. 2022. (Modifying)

Attended conferences lists

(1) Xie B, Baudin N, Soto J, Fan Y, Luo L. Wall impact on efficiency of packed-bed thermocline thermal energy storage system. ***Société Française de Thermique*** *(SFT2021)*, web-conference, 1-3 July, 2021. (Poster, Video presentation)

(2) Xie B, Baudin N, Soto J, Fan Y, Luo L. Wall Impact on Efficiency of Packed-bed Thermocline Thermal Energy Storage System. ***Global Summit and Expo on Sustainable and Renewable Energy*** *(GSESRE2022)*, Copenhagen, Denmark, 16-18 June, 2022. (Oral presentation, Online)

(3) Xie B, Baudin N, Soto J, Fan Y, Luo L. Thermocline packed-bed storage tank under impacts: inlet configuration and insulation. ***Journées Nationales de l'Energie Solaire*** *(JNES2022)*, Albi, France, 29 June-01 July, 2022. (Oral presentation)

(4) Xie B, Baudin N, Soto J, Fan Y, Luo L. Optimization of thermocline packed-bed system with PCM fillers for greenhouse application. ***International Conference on Solar Energy for Buildings and Industry*** *(EuroSun2022)*, Kassel, Germany 25-29 September, 2022. (Poster)

DOCTORAT BRETAGNE SCIENCES LOIRE POUR L'INGENIEUR

Nantes Université

Titre : Etude des systèmes de stockage thermique par thermocline avec garnissage

Mots clés : Stockage d'énergie thermique (TES), garnissage, stratification thermique, configuration de garnissage, média de stockage, optimisation multi-objectifs

Résumé : Un réservoir thermocline avec un garnissage constitué de matériaux pour du stockage thermique sensible et/ou latent est une solution prometteuse pour le stockage d'énergie thermique (TES). Les performances d'un tel réservoir sont très dépendantes de la configuration physique, et des matériaux du garnissage. Ainsi, il existe un optimum pour chaque cas d'usage même si quelques règles générales sont conservées. L'objectif de cette thèse consiste à d'abord étudier l'effet de ces différents paramètres géométriques, physiques et thermo-hydrauliques sur l'efficacité du stockage. Une étude d'optimisation est réalisée afin de déterminer la meilleure configuration des paramètres pour un objectif donné. La première partie du manuscrit traite de l'impact des parois sur l'évolution de la thermocline et sur l'efficacité globale de la charge/décharge du réservoir, au moyen d'un modèle numérique simplifié prenant en compte ces effets tout en restant rapide à résoudre. Ensuite, les effets de la configuration du diffuseur d'entrée/sortie, de l'isolation thermique et des paramètres de charge/décharge sont étudiés expérimentalement sur un banc de tests dédié. Cette expérience a permi également de valider le modèle numérique. Ce modèle numérique est ensuite utilisé pour mener une optimisation avec une configuration multi-couches et multi-matériaux du garnissage grâce à un algorithme génétique multi-objectifs pour différents types de cycles de charge/décharge. Cette méthodologie est notamment mise en œuvre pour une application de stockage thermique dédiée à une serre horticole . Le manuscrit décrit, enfin, des pistes à développer pour des travaux futurs.

Title : Thermocline study of packed-bed thermal energy storage system

Keywords : Thermal energy storage (TES), packed bed, thermocline, packing configuration, storage media, multi-objective optimization

Abstract : The thermocline packed-bed tank with sensible heat or latent heat fillers is a cost-effective option for thermal energy storage (TES). Its thermal performance is very dependent on the packing configurations to each fluid flow and temperature situation. The principal objective of this PhD dissertation is to study the influence factors for different configuration of fluid flow and tank design, and then to conduct multi-layered packing configuration optimization of the storage tank. It starts by exploring the wall impact on thermocline and global thermal performance in dynamic conditions. Then, various influences, including the inlet configuration, the insulation, the filler size, and the operating parameters, on the thermocline in radial and axial direction based on a basic sensible heat filler tank are investigated. After that, the multi-layered configuration optimization of phase change material storage tank using a multi-objective genetic algorithm in multiple cycling is carried out by integrating the tank into an agriculture greenhouse application. The thermal performance of optimal tanks in seasonal operations is studied to find the potential for improvement of future work.